New Modelling and Simulation Methods to Support Clean Marine Propulsion

by

Michael Grant
B.A.Sc. (Mech. Eng.), University of British Columbia Okanagan, 2012

A Thesis Submitted in Partial Fulfillment of the
Requirements for the Degree of

MASTER OF APPLIED SCIENCE

in the Department of Mechanical Engineering

New Modelling and Simulation Methods to Support Clean Marine Propulsion

by

Michael Grant
B.A.Sc. (Mech. Eng.), University of British Columbia Okanagan, 2012

Supervisory Committee

Dr. Z. Dong, Supervisor
(Department of Mechanical Engineering)

Dr. C. Crawford, Departmental Member
(Department of Mechanical Engineering)

ABSTRACT

The marine industry has increased its adoption of pure-electric, diesel-electric, and other non-traditional propulsion architectures to reduce ship emissions and fuel consumption. While these technologies can improve performance, the design of a propulsion system becomes challenging, given that no single technology is superior across all vessel types. Furthermore, even identical ships with different operating patterns may be better suited to different propulsion technologies. Addressing this problem, previous research has shown that if key elements of a vessel's operational profile are known, simulation and optimization techniques can be employed to evaluate multiple propulsion architectures and result in a better propulsion system design and energy management strategy for a given vessel. While these studies have demonstrated the performance improvements that can be achieved from optimizing clean marine propulsion systems, they rely on vessel operational profiles obtained through physical measurement from existing ships. From a practical point of view, the optimization of a vessel's propulsion system needs to occur prior to a vessel's construction and thus precludes physical measurement.

To this end, this thesis introduces a marine simulation platform for producing vessel operational profiles which enable propulsion system optimization during the ship design process. Core subsystem modules are constructed for simulating ship motions in 3 degrees of freedom and result in operational profile time-series, including propulsion power. Data is acquired from a benchmark vessel to validate the simulation. Results show the proposed approach strikes a balance between speed, accuracy, and complexity compared with other available tools.

Table of Contents

List of Tables

List of Figures

List of Abbreviations

CAD	computer aided drawing.
CFD	computaional-fluid dynamics.
DOF	degree-of-freedom.
ECEF	earth-centred, earth fixed.
ESS	energy storage system.
GPS	global positioning system.
HIL	hardware-in-loop.
LNG	liquid natural gas.
MBD	model-based design.
MMG	manoeuvring modelling group.
MV	motor vessel.
NED	north-east-down.
PST	Pacific Standard Time.
SIL	software-in-loop.
VDR	voyage data recorder.

Nomenclature

$\alpha_{advance}$	propeller inflow incidence angle $[rad]$
β	vessel drift angle $[rad]$
$\dot{\boldsymbol{\eta}}^n_{b/n}$	vessel velocity with respect to the North-East-Down frame expressed in the North-East-Down frame $[m/s \; and \; rad/s]$
$\boldsymbol{\eta}^n_{b/n}$	vessel position and orientation with respect to the North-East-Down frame expressed in the North-East-Down frame $[m \; and \; rad]$
$\boldsymbol{\nu}^b_{b/n}$	vessel velocity with respect to the North-East-Down frame expressed in the body-fixed frame $[m/s \; and \; rad/s]$
$\boldsymbol{\tau}^b_b$	forces and moments acting on the vessel expressed in the body-fixed frame $[N \; and \; Nm]$
$\boldsymbol{\tau}^{prop}_{prop}$	thrust forces produced by the propeller at o_{prop} in the propeller-fixed frame $[N]$
$\boldsymbol{\xi}^b_{b/n}$	vessel velocity with respect to the local ocean surface expressed in the body-fixed frame $[m/s \; and \; rad/s]$
$\boldsymbol{m_A}$	vessel 3x3 added mass-inertia matrix $[kg \; and \; kg \cdot m^2]$
$\boldsymbol{m}$	vessel 3x3 mass-inertia matrix $[kg \; and \; kg \cdot m^2]$
$\dot{\boldsymbol{\nu}}^b_{b/n}$	vessel acceleration with respect to the North-East-Down frame expressed in the body-fixed frame $[m/s^2 \; and \; rad/s^2]$
$\dot{\mathbf{p}}^e_{b/e}$	vessel velocity expressed in the Earth-Centred, Earth-Fixed frame $[m/s]$
$\dot{\psi}$	vessel true heading rate of change $[rad/s]$
$\dot{\theta}_{azi}$	azimuth thruster angle rate of change $[rad/s]$

$\dot{E}_{b/n}$	vessel velocity in the E-direction of the North-East-Down frame $[m/s]$
$\dot{E}_{c/n}$	ocean current velocity in the E-direction of the North-East-Down frame $[m/s]$
$\dot{N}_{b/n}$	vessel velocity in the N-direction of the North-East-Down frame $[m/s]$
$\dot{N}_{c/n}$	ocean current velocity in the N-direction of the North-East-Down frame $[m/s]$
$\dot{r}$	vessel acceleration in the yaw direction $[rad/s^2]$
$\dot{u}$	vessel acceleration in the surge direction $[m/s^2]$
$\dot{v}$	vessel acceleration in the sway direction $[m/s^2]$
$\dot{v}_G$	vessel acceleration in the sway direction at the ship's centre of gravity $[m/s^2]$
$\dot{x}_{b/e}$	vessel velocity in the x_e-direction of the Earth-Centred, Earth-Fixed frame $[m/s]$
$\dot{y}_{b/e}$	vessel velocity in the y_e-direction of the Earth-Centred, Earth-Fixed frame $[m/s]$
$\dot{z}_{b/e}$	vessel velocity in the z_e-direction of the Earth-Centred, Earth-Fixed frame $[m/s]$
ϵ_{data}	measured gauge strain $[-]$
$\eta_{gearbox}$	efficiency of the z-drive gearbox embedded within the azimuth tower $[-]$
η_{prop}	propeller efficiency $[-]$
γ_{data}	measured propeller shaft shear strain $[-]$
$\mathbf{\Theta}^e_{b/e}$	vessel position vector given by latitude and longitude expressed in the Earth-Centred, Earth-Fixed frame $[rad]$
$\mathbf{p}^e_{b/e}$	vessel position vector expressed in the Earth-Centred, Earth-Fixed frame $[m]$
μ	latitude $[rad]$
μ_0	initial latitude of the vessel $[rad]$
$\mu_{viscosity}$	fluid dynamic viscosity $[kg/(m \cdot s)]$
∇_{vessel}	vessel displacement $[m^3]$

$\overline{A}_{ij}$	element of the non-dimensionalized 6x6 added mass-inertia matrix output by WAMIT [−]
$\phi_{blade\,rotation}$	rotation angle of propeller blade about propeller's axis of rotation $[rad]$
ψ	vessel heading with respect to the North-East-Down frame $[rad]$
ψ_0	initial vessel heading with respect to the North-East-Down frame $[rad]$
ρ	fluid density $[kg/m^3]$
τ_{data}	measured propeller shaft shear stress $[Pa]$
θ_{azi}	azimuth thruster angle commanded by the helmsperson during manoeuvring $[rad]$
θ_{pp_i}	pitch angle at i-th propeller aerofoil contour $[rad]$
θ_{s_i}	skew angle to mid-chord point at i-th propeller aerofoil contour $[rad]$
$\vec{\mathbf{r}}^{\,b}_{azi/b}$	location of the azimuth thruster expressed in the vessel body-fixed frame$[m]$
$\vec{\mathbf{r}}^{\,b}_{prop/b}$	location of the propeller expressed in the vessel body-fixed frame $[m]$
$\vec{\mathbf{r}}^{\,n}_{b/n}$	vessel position with respect to the North-East-Down frame expressed in the North-East-Down frame $[m]$
$\vec{\mathbf{r}}^{\,b}_{CG/b}$	distance from the vessel's geometric centre at o_b to its centre of gravity $[m]$
$\{azi\}$	azimuth body-fixed reference frame [−]
$\{b\}$	vessel body-fixed reference frame [−]
$\{e\}$	Earth-Centred, Earth-Fixed reference frame [−]
$\{n\}$	North-East-Down reference frame [−]
$\{prop\}$	propeller body-fixed reference frame [−]
A_{ij}	element of the 6x6 added mass-inertia matrix output by WAMIT $[kg or kg{\cdot}m^2]$
$a_{resistance}$	resistance augmentation factor [−]
b_{vessel}	overall beam of vessel $[m]$
C_B	vessel block coefficient [−]

C_D	vessel superstructure air drag coefficient $[-]$
C_F	ITTC 1957 coefficient of frictional resistance $[-]$
c_{chord_i}	chord length of i-th propeller aerofoil contour $[m]$
CG	vessel centre of gravity $[-]$
CO	vessel geometric centre at the waterline $[-]$
D_{prop}	propeller diameter $[m]$
d_{vessel}	draught of vessel $[m]$
E	Young's modulus $[Pa]$
$E_{b/n\,0}$	initial vessel position in the E-direction of the North-East-Down frame $[m]$
$E_{b/n}$	vessel position in the E-direction of the North-East-Down frame $[m]$
E_{shafts}	total propulsion energy consumed across all propeller shafts $[J]$
E_{shaft}	propulsion energy consumed across one propeller shaft $[J]$
F_{PS}	force experience by shaft-mounted power supply housing $[N]$
Fr	Froude number $[-]$
Fr_∇	volume Froude number $[-]$
G	shear modulus $[Pa]$
g	acceleration due to gravity $[m/s^2]$
h_{sea}	height above sea-level $[m]$
i_{G_i}	rake distance at i-th propeller aerofoil contour $[m]$
I_{xx}	vessel mass moment of inertia about x_b–axis $[kg \cdot m^2]$
I_{yy}	vessel mass moment of inertia about y_b–axis $[kg \cdot m^2]$
I_{zz}	vessel mass moment of inertia about z_b–axis $[kg \cdot m^2]$
$J_{advance}$	propeller advance coefficient $[-]$
J_{shaft}	polar moment of inertia of the propeller shaft $[m^4]$

J_{zz}	vessel added moment of inertia about the z_b-axis $[kg \cdot m^2]$
k	dimensionalization coefficient for the added-mass matrix output by WAMIT $[-]$
K_{air}	vessel air resistance coefficient $[N/(m/s)^2]$
$k_{appendage}$	vessel hull appendage form-factor coefficient $[-]$
$K_{gearbox}$	gear ratio of the z-drive gearbox embedded within the azimuth tower $[-]$
$K_{hull_{fouling\,CFD}}$	hull resistance fouling correction factor for CFD derived resistances $[-]$
$K_{hull_{fouling\,empirical}}$	hull resistance fouling correction factor for empirically derived resistances $[-]$
$K_{hull_{fouling}}$	hull resistance fouling correction factor $[-]$
K_Q	propeller torque coefficient $[-]$
$K_{thrust_{fouling}}$	propeller thrust fouling correction factor $[-]$
$K_{thrust_{geometry}}$	propeller thrust modelling geometry correction factor $[-]$
$K_{torque_{fouling}}$	propeller torque fouling correction factor $[-]$
$K_{torque_{geometry}}$	propeller torque modelling geometry correction factor $[-]$
K_{Tx}	propeller axial thrust coefficient $[-]$
K_{Ty}	propeller transverse thrust coefficient $[-]$
l	longitude $[rad]$
l_0	initial longitude of the vessel $[rad]$
$L_{prop\,offset}$	offset distance between the azimuth thruster's axis of rotation and the propeller origin $[m]$
L_{ULEN}	characteristic length of the hull mesh geometry supplied to WAMIT $[-]$
L_{vessel}	overall length of vessel $[m]$
L_{wl}	length of vessel at the waterline $[m]$
lwl	water-level in calm water $[-]$

m	vessel mass $[kg]$
m_x	vessel added mass in the x_b-direction $[kg]$
m'_x	vessel dimensionless added mass in the x_b-direction $[-]$
m_y	vessel added mass in the y_b-direction $[kg]$
m'_y	vessel dimensionless added mass in the y_b-direction $[-]$
m_{PS}	mass of shaft-mounted power supply assembly $[kg]$
N^F_{MMG}	vessel hull resistance in yaw from MMG model corrected for fouling effects $[Nm]$
N^F_{prop}	propeller moment acting on the vessel about o_b in the yaw direction corrected for fouling effects $[Nm]$
N^F_{tower}	azimuth tower appendage resistance in yaw corrected for fouling effects $[Nm]$
N'_{MMG_r}	non-dimensionalized hull resistance in the yaw direction due to sway and yaw motion $[-]$
$N^{F,G}_{prop}$	propeller moment acting on the vessel about o_b in the yaw direction corrected for fouling effects and modelling geometry deviations $[Nm]$
N^F_{hull}	vessel total hull resistance in yaw corrected for fouling effects $[Nm]$
$N_{b/n\,0}$	initial vessel position in the N-direction of the North-East-Down frame $[m]$
$N_{b/n}$	vessel position in the N-direction of the North-East-Down frame $[m]$
n_{data}	measured propeller shaft speed $[rad/s]$
N_{e-n}	distance from o_n along the z_n-axis of the North-East-Down frame to the z_e-axis of the Earth-Centred, Earth-Fixed coordinate frame $[m]$
N_{hull}	total vessel hull resistance in yaw $[Nm]$
n_{limit}	minimum propeller speed to avoid division by zero $[rad/s]$
n_{max}	maximum propeller shaft speed $[rad/s]$
N_{MMG}	vessel hull resistance in yaw due to sway and yaw motion $[Nm]$

N_{moment}	sum of moments acting on the vessel about o_b in the yaw direction $[Nm]$
N_{props}	sum of propeller moments in the yaw direction $[Nm]$
n_{prop}	propeller angular velocity $[rad/s]$
N_{rudder}	sum of rudder moments in the yaw direction $[Nm]$
n_{shaft}	propeller shaft speed $[rad/s]$
N_{tower}	azimuth tower appendage resistance in the yaw direction $[Nm]$
o_b	origin of body-fixed vessel coordinate system $[-]$
o_{prop}	origin of propeller coordinate system $[-]$
P_{data}	measured propeller shaft power $[W]$
p_{prop_i}	pitch distance of the i-th propeller aerofoil contour $[m]$
P_{prop}	power at the propeller $[W]$
P_{shaft}	power at the propeller shaft $[W]$
q	vessel pitch rate $[rad/s]$
Q^F_{prop}	propeller torque corrected for fouling effects $[Nm]$
$Q^{F,G}_{prop}$	propeller torque corrected for fouling effects and modelling geometry deviations $[Nm]$
Q_{data}	measured propeller shaft torque $[Nm]$
Q_{prop}	propeller torque $[Nm]$
r	vessel angular velocity in the yaw direction $[rad/s]$
r'	vessel dimensionless angular velocity in the yaw direction $[-]$
R_e	Reynold's number $[-]$
r_{azi}	yaw rate at the azimuth thruster $[rad/s]$
$r_{contour_i}$	radius at i-th propeller aerofoil contour $[m]$
r_{major}	radius of the semi-major axis of the WGS-84 Earth reference ellipsoid

r_{minor}	radius of the semi-minor axis of the WGS-84 Earth reference ellipsoid
r_{PS}	radius from the centre of the propeller shaft to the shaft-mounted power supply assembly's centre of gravity $[m]$
r_{shaft}	radius of the propeller shaft $[m]$
$S_{appendage}$	surface area of a vessel hull appendage $[m^2]$
$S_{superstructure}$	vessel superstructure projected area perpendicular to the surge direction of travel $[m^2]$
$T^F_{prop_x}$	axial propeller thrust corrected for fouling effects $[N]$
$T^F_{prop_y}$	transverse propeller thrust corrected for fouling effects $[N]$
$T^{F,G}_{prop_x}$	axial propeller thrust corrected for fouling effects and modelling geometry deviations $[N]$
$T^{F,G}_{prop_y}$	transverse propeller thrust corrected for fouling effects and modelling geometry deviations $[N]$
$t_{deduction}$	thrust deduction factor $[-]$
T_{prop_x}	axial propeller thrust $[N]$
T_{prop_y}	transverse propeller thrust $[N]$
$T_{prop_{required}}$	theoretical thrust in surge required to propel a vessel at a desired forward speed $[N]$
U	vessel speed-over-ground $[m/s]$
u	vessel velocity in the surge direction $[m/s]$
u_c	ocean current velocity in the surge direction of the vessel body-fixed frame $[m/s]$
u_r	vessel velocity in the surge direction, relative to the local ocean surface $[m/s]$
u_{azi}	surge velocity at the azimuth thruster $[m/s]$
u_{design}	vessel design velocity $[m/s]$
U_{GPS}	recorded GPS vessel speed-over-ground $[m/s]$

v	vessel velocity in the sway direction $[m/s]$
v_c	ocean current velocity in the sway direction of the vessel body-fixed frame $[m/s]$
v_G	vessel velocity in the sway direction at the ship's centre of gravity $[m/s]$
v_r	vessel velocity in the sway direction, relative to the local ocean surface $[m/s]$
$V_{advance_{aft}}$	advance velocity at aft propellers $[m/s]$
$V_{advance_{fore}}$	advance velocity at fore propellers $[m/s]$
$V_{advance}$	propeller advance velocity $[m/s]$
v_{azi}	sway velocity at the azimuth thruster $[m/s]$
$v_{poisson}$	Poisson's ratio $[-]$
w	vessel velocity in the heave direction $[m/s]$
W_A	vessel wake fraction at aft propellers $[-]$
W_F	vessel wake fraction at fore propellers $[-]$
X_0^A	vessel hull resistance in surge from CFD corrected with the resistance augmentation factor $[N]$
X_{MMG}^A	vessel hull resistance in surge from MMG model corrected with the resistance augmentation factor $[N]$
X_{tower}^A	azimuth tower appendage resistance in surge corrected with the resistance augmentation factor $[N]$
X_0^F	vessel hull resistance in surge from CFD corrected for fouling effects $[N]$
X_{MMG}^F	vessel hull resistance in surge from MMG model corrected for fouling effects $[N]$
X_{prop}^F	propeller force acting on the vessel at o_b in the surge direction corrected for fouling effects $[N]$
X_{tower}^F	azimuth tower appendage resistance in surge corrected for fouling effects $[N]$

X'_{MMG_r} non-dimensionalized hull resistance in the surge direction due to sway and yaw motion $[-]$

$X_0^{F,A}$ vessel hull resistance in surge from CFD corrected with the resistance augmentation factor and corrected for fouling effects $[N]$

$X_{hull\,design}^{F,A}$ vessel total hull resistance in surge at design velocity corrected with the resistance augmentation factor and corrected for fouling effects $[N]$

$X_{hull}^{F,A}$ vessel total hull resistance in surge corrected with the resistance augmentation factor and corrected for fouling effects $[N]$

$X_{MMG}^{F,A}$ vessel hull resistance in surge from MMG model corrected with the resistance augmentation factor and corrected for fouling effects $[N]$

$X_{tower}^{F,A}$ azimuth tower appendage resistance in surge corrected with the resistance augmentation factor and corrected for fouling effects $[N]$

$X_{prop}^{F,G}$ propeller force acting on the vessel at o_b in the surge direction corrected for fouling effects and modelling geometry deviations $[N]$

X'_0 non-dimensionalized hull resistance in the surge direction due to pure surge motion $[-]$

x_G distance from the vessel's geometric centre at o_b to its centre of gravity in the x_b-direction $[m]$

x'_G non-dimensionalized distance from the vessel's geometric centre at o_b to its centre of gravity in the x_b-direction $[-]$

X_0 vessel hull resistance in surge due to pure surge motion $[N]$

X_{air} vessel air resistance in surge $[N]$

$x_{azi/b}$ x-coordinate of the azimuth thruster in the vessel body-fixed frame $[m]$

x_{azi} x-axis of the azimuth coordinate system $[-]$

$x_{b/e\,0}$ initial x-coordinate of vessel in the Earth-Centred, Earth-Fixed frame $[m]$

$x_{b/e}$ x-coordinate of vessel in the Earth-Centred, Earth-Fixed frame $[m]$

x_b x-axis of vessel body-fixed coordinate system $[-]$

$x_{c/2_i}$	x-coordinate of i-th propeller aerofoil contour mid-chord point $[m]$
x_e	x-axis of the Earth-Centred, Earth-Fixed coordinate system $[-]$
X_{force}	sum of forces acting on the vessel at o_b in the surge direction $[N]$
X_{hull}	total vessel hull resistance in surge $[N]$
x_{LE_i}	x-coordinate of i-th propeller aerofoil contour leading-edge point $[m]$
X_{MMG}	vessel hull resistance in surge due to sway and yaw motion $[N]$
x_n	x-axis of the North-East-Down coordinate system $[-]$
X_{props}	sum of propeller forces in the surge direction $[N]$
x_{prop}	x-axis of propeller coordinate system $[-]$
X_{rudder}	sum of rudder forces in the surge direction $[N]$
X_{tank}	hull resistance in surge obtained through tow-tank experiments $[N]$
x_{TE_i}	x-coordinate of i-th propeller contour trailing-edge point $[m]$
X_{tower}	azimuth tower appendage resistance in the surge direction $[N]$
Y^F_{MMG}	vessel hull resistance in sway from MMG model corrected for fouling effects $[N]$
Y^F_{prop}	propeller force acting on the vessel at o_b in the sway direction corrected for fouling effects $[N]$
Y^F_{tower}	azimuth tower appendage resistance in sway corrected for fouling effects $[N]$
Y'_{MMG_r}	non-dimensionalized hull resistance in the sway direction due to sway and yaw motion $[-]$
$Y^{F,G}_{prop}$	propeller force acting on the vessel at o_b in the sway direction corrected for fouling effects and modelling geometry deviations $[N]$
Y^F_{hull}	vessel total hull resistance in sway corrected for fouling effects $[N]$
y_G	distance from the vessel's geometric centre at o_b to its centre of gravity in the y_b-direction $[m]$

$y_{azi/b}$	y-coordinate of the azimuth thruster in the vessel body-fixed frame $[m]$
y_{azi}	y-axis of the azimuth coordinate system $[-]$
$y_{b/e\,0}$	initial y-coordinate of vessel in the Earth-Centred, Earth-Fixed frame $[m]$
$y_{b/e}$	y-coordinate of vessel in the Earth-Centred, Earth-Fixed frame $[m]$
y_b	y-axis of vessel body-fixed coordinate system $[-]$
$y_{c/2_i}$	y-coordinate of i-th propeller aerofoil contour mid-chord point $[m]$
y_e	y-axis of the Earth-Centred, Earth-Fixed coordinate system $[-]$
Y_{force}	sum of forces acting on the vessel at o_b in the sway direction $[N]$
Y_{hull}	total vessel hull resistance in sway $[N]$
y_{LE_i}	y-coordinate of i-th propeller aerofoil contour leading-edge point $[m]$
Y_{MMG}	vessel hull resistance in sway due to sway and yaw motion $[N]$
y_n	y-axis of the North-East-Down coordinate system $[-]$
Y_{props}	sum of propeller forces in the sway direction $[N]$
y_{prop}	y-axis of propeller coordinate system $[-]$
Y_{rudder}	sum of rudder forces in the sway direction $[N]$
y_{TE_i}	y-coordinate of i-th propeller contour trailing-edge point $[m]$
Y_{tower}	azimuth tower appendage resistance in the sway direction $[N]$
z_G	distance from the vessel's geometric centre at o_b to its centre of gravity in the z_b-direction $[m]$
z_{azi}	z-axis of the azimuth coordinate system $[-]$
$z_{b/e\,0}$	initial z-coordinate of vessel in the Earth-Centred, Earth-Fixed frame $[m]$
$z_{b/e}$	z-coordinate of vessel in the Earth-Centred, Earth-Fixed frame $[m]$
z_b	z-axis of vessel body-fixed coordinate system $[-]$
$z_{c/2_i}$	z-coordinate of i-th propeller aerofoil contour mid-chord point $[m]$

z_e	z-axis of the Earth-Centred, Earth-Fixed coordinate system $[-]$
z_{LE_i}	z-coordinate of i-th propeller aerofoil contour leading-edge point $[m]$
z_n	z-axis of the North-East-Down coordinate system $[-]$
z_{prop}	z-axis of propeller coordinate system $[-]$
z_{TE_i}	z-coordinate of i-th propeller contour trailing-edge point $[m]$

ACKNOWLEDGEMENTS

I would like to thank:

Dr. Zuomin Dong, for providing invaluable guidance

Mostafa Rahimpour, Haijia Zhu, Anthony Truelove,

and Kevin Anderson for their collaborations that made this work possible.

My family for their unwavering support.

DEDICATION

This thesis is dedicated to my family.

Chapter 1

Introduction

1.1 General Background

As the effects of climate change become increasingly disruptive, members of industry, government, and academia continue to explore avenues of reducing the impacts of human activities through the adoption of new technologies and through influencing behavioural changes.

Much of the effort to date has been concentrated on land-based transportation, building efficiency, agricultural practices, and energy infrastructure. Until recently, one area that had received considerably less attention was marine based transportation.

The International Maritime Organization (IMO) reported in 2014 that marine shipping accounted for an average of 3.1% of annual global CO_2 emissions between 2007-2012 [1] and in 2021 the IMO released a subsequent report that projected the absolute annual CO_2 emissions from marine shipping would increase 90%-130% over 2008 levels by the year 2050 [2]. With these statistics and projections, marine transportation is certainly an area worthy of further study and one that has been drawing increased attention.

1.2 Research Problem

There are several emission reduction technologies being investigated across a variety of marine applications, with no technology seemingly superior in all situations or across all vessel types. Of these technologies, hybrid electric marine propulsion is one of the forefront solutions with broad application potential and is the chosen focus of this thesis.

From the automotive industry, it is known that the extent of fuel and emissions reduction that can be obtained using a hybrid electric powertrain is very much application specific and in certain cases, a hybrid electric powertrain may not always be the superior choice [3].

To this end, naval architects and marine engineers who are considering a hybrid electric propulsion system for a new vessel design need tools that can assess the suitability of a chosen propulsion architecture for each unique vessel and its expected drive-cycle(s) and which allows for a comparison of environmental impact, performance and cost.

One constraint that complicates this problem is the need optimize the design of a propulsion system prior to a vessel's construction, and thus many solutions that involve physical systems and measurement are not feasible.

1.3 Proposed Approach

In order to assess the suitability of a hybrid electric propulsion system for a new vessel design and its projected drive-cycle(s), a marine simulation platform is introduced which enables the simulation of a virtual vessel transiting along a given drive-cycle, which in turn generates a vessel operational profile that includes propulsion power demand.

The resulting vessel operational profile provides a means to assess the suitability of a selected propulsion architecture and allows for the optimization of powertrain components and energy management strategies during the vessel design phase.

1.4 Outline of Thesis

The proposed approach and accompanying details are presented in the following order:

- Chapter 2 establishes research motivations in greater detail by introducing the concept of model-based design (MBD) and demonstrating how it can be applied to produce superior hybrid electric propulsion system designs
- Chapter 3 details the acquisition of key operational data from a benchmark vessel for the purpose of validating the proposed simulation and assessing the accuracy of its embedded models
- Chapter 4 describes a new computationally efficient hybrid approach to hull and propeller modelling for the calculation of vessel motion and propulsion power during simulation
- Chapter 5 constructs the core subsystems of a modular MBD marine simulation platform which are used for simulating the benchmark vessel's operational profile

- Chapter 6 presents and discusses the simulation results which are compared with the recorded benchmark vessel data
- Chapter 7 concludes this work an outline of research contributions and recommendations

Chapter 2

Research Motivations

2.1 Introduction to Hybrid Electric Marine Propulsion

The primary emission reducing technology targeted by this work is hybrid electric propulsion which will be defined as consisting of one or more internal combustion engines which are paired with one or more electric machines that are in turn connected with an energy storage system (ESS) comprised of batteries, ultra-capacitors or similar.

While these hybrid electric drive solutions have a high probability of reducing well-to-propeller emissions over a vessel's life-cycle, deriving an economic benefit can be sensitive to a vessel's operational profile and the chosen technology [4, 5]. For some vessels, a poorly selected emission reduction strategy can prove more expensive than using a traditional internal combustion engine propulsion system.

To illustrate how hybrid electric technology can reduce a vessel's emissions and operating costs, first consider that an internal combustion engine's fuel consumption and emission rates are sensitive to the engine's operating point as illustrated by the fuel consumption and emission rate maps in Figure 2.1.

Note that fuel consumption is correlated to, but not directly linked to the emission rates. If a particular driving task allows for operational flexibility, this can pose a dilemma of whether to operate at a more fuel (and cost) efficient operating point, or at an operating point with fewer emissions.

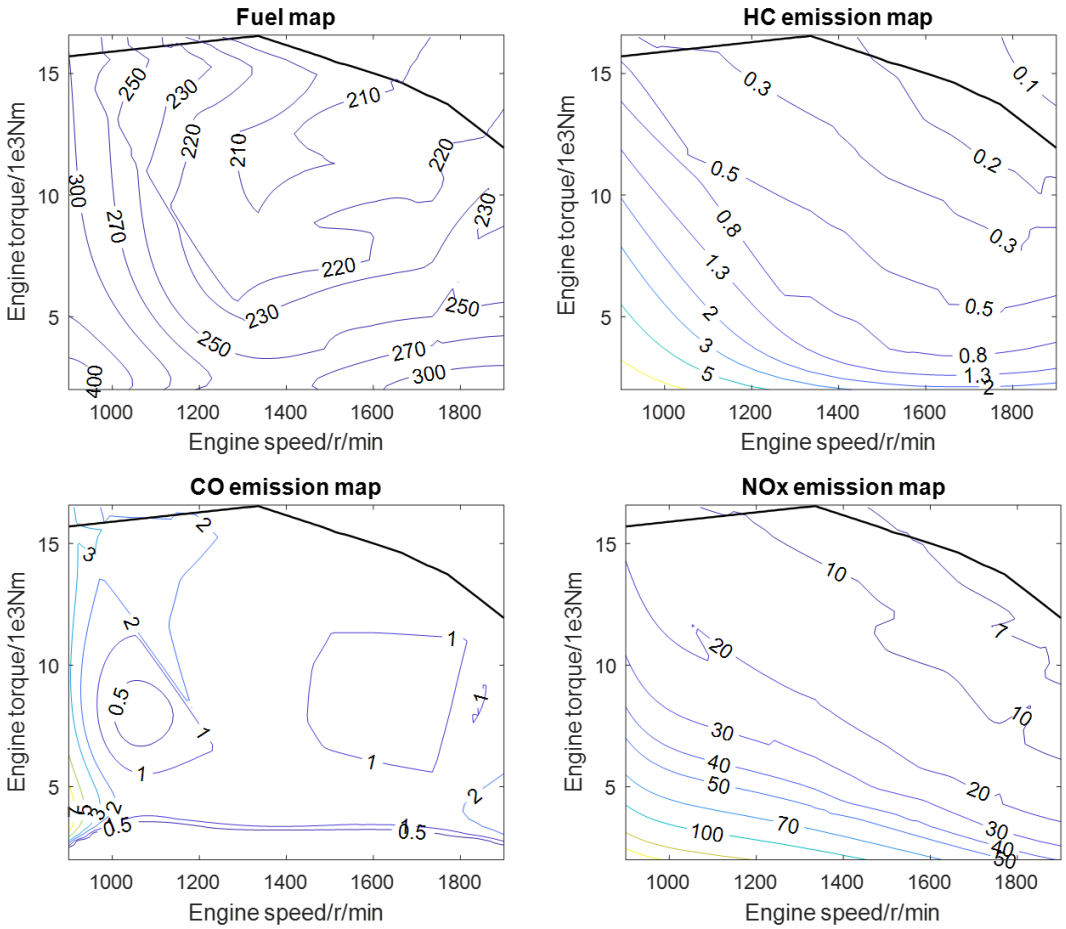

Figure 2.1: Fuel Consumption and Emission Maps – Generic Diesel Engine
Source: Reproduced with permission from Feng and Dong [6]

By pairing an internal combustion engine with an electric motor and ESS, the engine can often operate at a more preferable loading condition, and if certain hybrid configurations are used, the engine can be shutdown entirely during periods of low load. To visualize how this can be accomplished, first examine the simplified hybrid electric marine propulsion schematic in Figure 2.2.

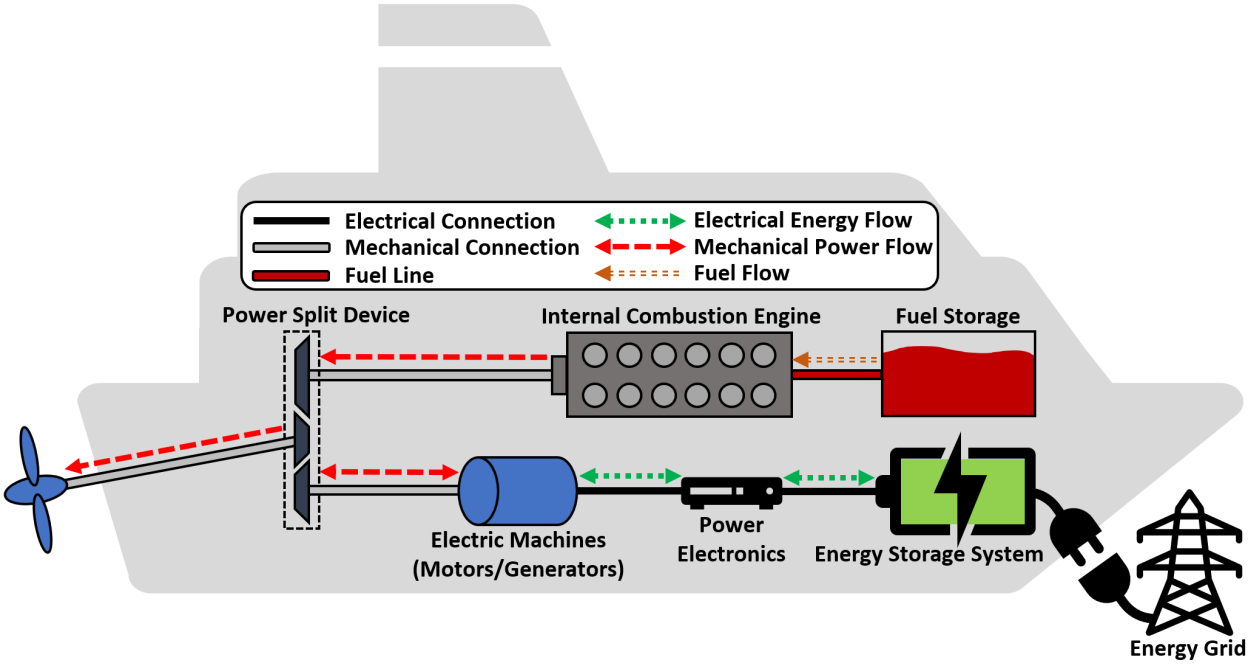

Figure 2.2: Simplified Hybrid Electric Marine Propulsion Schematic

A hybrid architecture similar to that shown above can provide a wide range of operational flexibility. During periods of low to moderate propulsion demand, the internal combustion engine can be shutdown while the electric machines provide the necessary propulsion power, or alternatively, the engine can generate excess power at an efficient operating point while the electric machines act as generators to recharge the ESS.

During periods of high propulsion system demand, the internal combustion engine can work in parallel with the electric machines which in turn draw energy from the ESS to meet propulsion demand. Additionally, plug-in hybrid functionality can allow a ship to replenish its ESS from a land-based energy grid, further reducing the fuel consumed and emissions generated onboard.

In each of the above operating scenarios, the hybrid electric powertrain is governed by a sophisticated energy management system that dictates the flow of power and energy to arrive at a more efficient operating condition. This includes an attempt to keep the engine's operating point in a preferred region as illustrated in Figure 2.3.

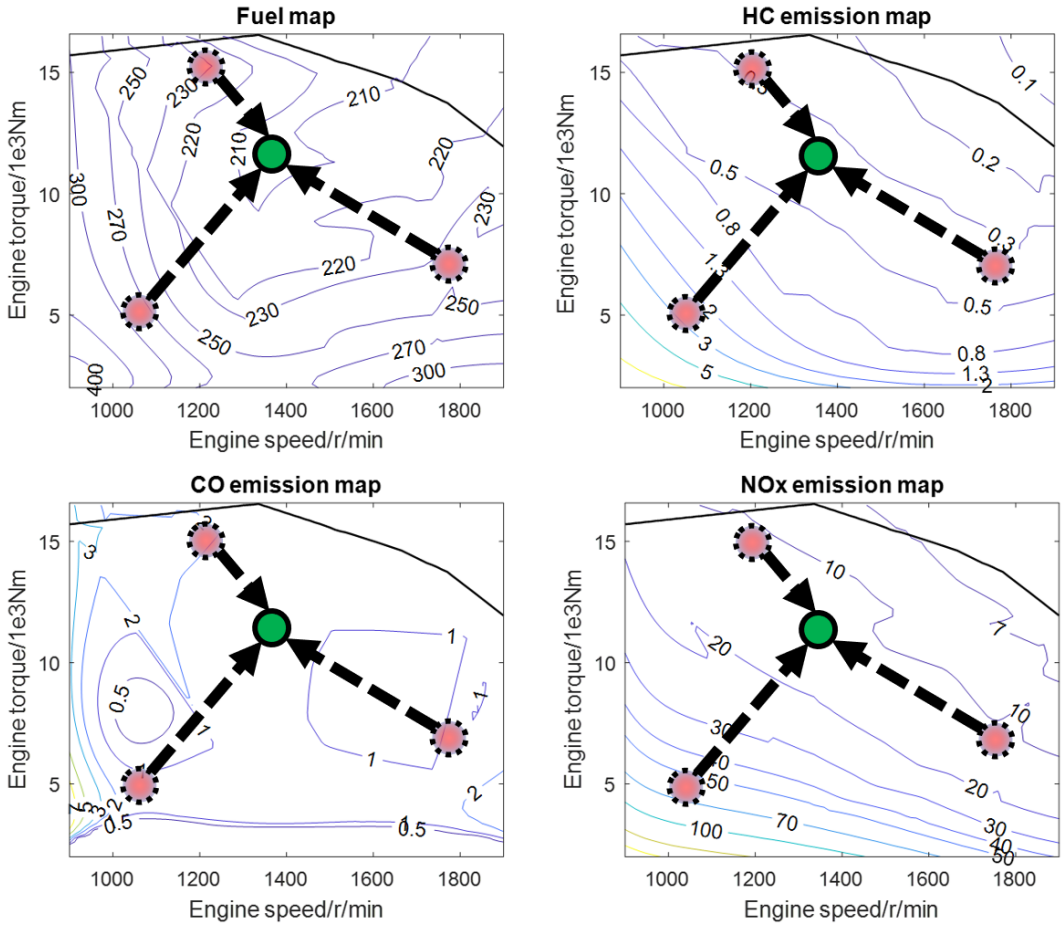

Figure 2.3: Control of the Engine Operating Point – Generic Diesel Engine
Source: Reproduced and modified with permission from Feng and Dong [6]

This is just one vision for a hybrid propulsion system, of which there are many possible architectures with limitless variations, each with its own benefits and drawbacks that may be suitable for a particular ship while unsuitable for another ship or another operation profile.

To demonstrate the importance of selecting a hybrid architecture and components that are appropriately sized for a vessel's operations, consider the example of a recently converted diesel-electric hybrid vessel that was found to have an ESS grossly oversized for its daily mission cycle. On this particular vessel, the hybrid system was limited to driving a seldom used bow thruster and the ESS's state-of-charge remained between 97% and 100% nearly all of the time, and was rarely depleted to less than 95% of its total capacity. In addition, awkward placement of the bow thruster controls led to many helmspersons avoiding its use entirely, exacerbating this component selection mismatch.

A hybrid vessel that is poorly designed for its unique operation profile can come at a large expense to its owner, who foots the bill for disappointing performance. Perhaps even more

damaging, a vessel with a less-than-optimal hybrid implementation can serve as a deterrent and slow down the adoption of these emission reducing technologies across the entire marine industry.

In order to design well-rounded, high performance hybrid electric systems, the automotive industry has turned to an MBD method. This approach uses detailed models and virtual drive-cycle simulations to predict a vehicle's power demand which in turn allows for optimization of powertrain components and energy management strategies during the design phase.

Porting these concepts from the automotive industry to the marine industry, Zhu [7], Manouchehrinia [4], and Chen [5] employ MBD methodologies to study hybrid electric propulsion systems for marine vessels. Using optimization techniques, they propose hybrid architectures and energy management strategies that are tuned for their respective vessels and find they significantly reduce emissions and provide economic benefits for their studied marine applications [4, 5, 7].

Key vessel design considerations addressed by their optimization processes include:

1) What is the best propulsion system architecture for a particular ship under its operational profile?
    a) traditional diesel engine
    b) diesel electric hybrid
    c) liquid natural gas (LNG) electric hybrid
    d) hybrid electric with fuel cells
    e) pure electric
    f) etc.
2) What is the best source of fuel and/or energy storage?
    a) lithium-ion batteries
    b) ultra-capacitors
    c) hydrogen
    d) etc.
3) What is the optimal size and number of each powertrain component?
    a) engine(s)
    b) motor(s)

c) ESS(s)

d) power-split device(s)

e) etc.

4) What is an efficient energy management strategy?

a) should pure electric mode be utilized?

b) should engine and motor power be combined to meet propulsion demands?

c) should the ESS be charged?

d) etc.

The issue herein is that these optimization approaches were executed using vessel operational profiles and power time-series data that were physically acquired from the *existing* vessels that the propulsion systems were optimized for (albeit as a proof-of-concept). From a practical point of view, the design and optimization of a vessel's hybrid electric propulsion system needs to occur prior to the vessel being constructed, which inherently excludes the possibility of obtaining a power time-series profile through physical measurement.

Turning again to the automotive industry for inspiration, one finds that automotive engineers utilize detailed virtual vehicle models to simulate a vehicle navigating along a standardized drive-cycle that consists of a vehicle's velocity over time and is derived from statistical data. This process results in a simulated operational profile for the vehicle with power time-series data that can be used for the optimization of hybrid electric powertrain designs and energy management strategies.

2.2 Vessel Operational Profiles

The successful implementation of MBD methods for marine applications hinges on the capability of being able to produce *accurate* vessel operational profiles by simulating a virtual ship transiting along a given drive-cycle such that the optimization of its propulsion architecture can occur during the design phase (prior to its construction).

A vessel operational simulation should take in a given drive-cycle and result in an operational profile that consists of a variety of metrics including propeller speed, power, and energy consumption as shown in Figure 2.4.

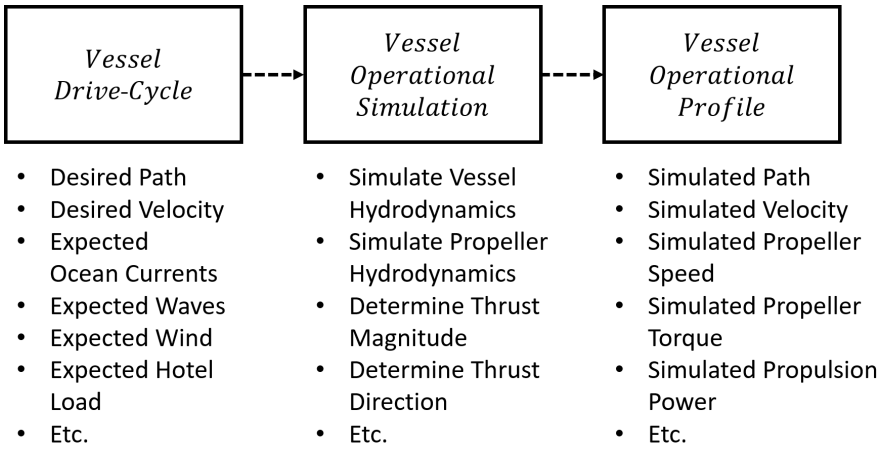

Figure 2.4: Vessel Drive Cycle and Operational Profile

The concept of the resulting operational profile and its application to hybrid propulsion design will be illustrated by focusing on the aforementioned power time-series.

Consider Figure 2.5 which provides a simplified representation of propulsion system demand which will be assumed to have already been obtained through a virtual vessel simulation. Neglecting efficiency losses for the sake of simplicity, the fulfillment of the propulsion demand will come entirely from an internal combustion engine when a traditional propulsion design is employed.

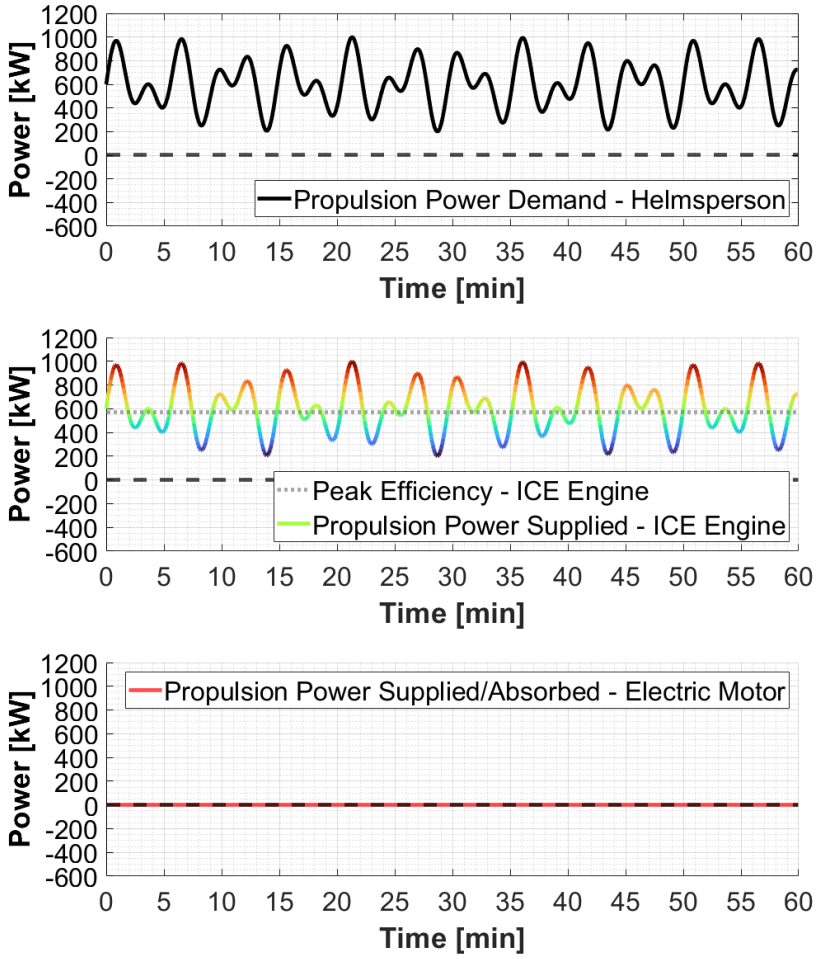

Figure 2.5: Simplified Power Demand – Traditional Propulsion (Large Engine)

When considering the above power time-series alongside the engine fuel consumption and emissions maps that were previously discussed, it is apparent that a traditional propulsion system can result in an engine running for long periods outside of its desirable operating region.

Now consider how propulsion demand can be met if the load is distributed between an internal combustion engine and an electric machine. The electric machine, which has a wider range of efficient operation, can meet the fluctuating portion of load demand, while the smaller internal combustion engine that uses less fuel can operate steadily within a more efficient region.

By incorporating models of propulsion system components (motors, engines, ESS, power electronics) and energy management strategies into a subsequent MBD simulation, the performance of a proposed hybrid propulsion system can be simulated such as in Andersen, Zhu, Lui, Chen, and Manouchehrinia [4, 5, 7–9], and may result in an output similar to that illustrated in Figure 2.6.

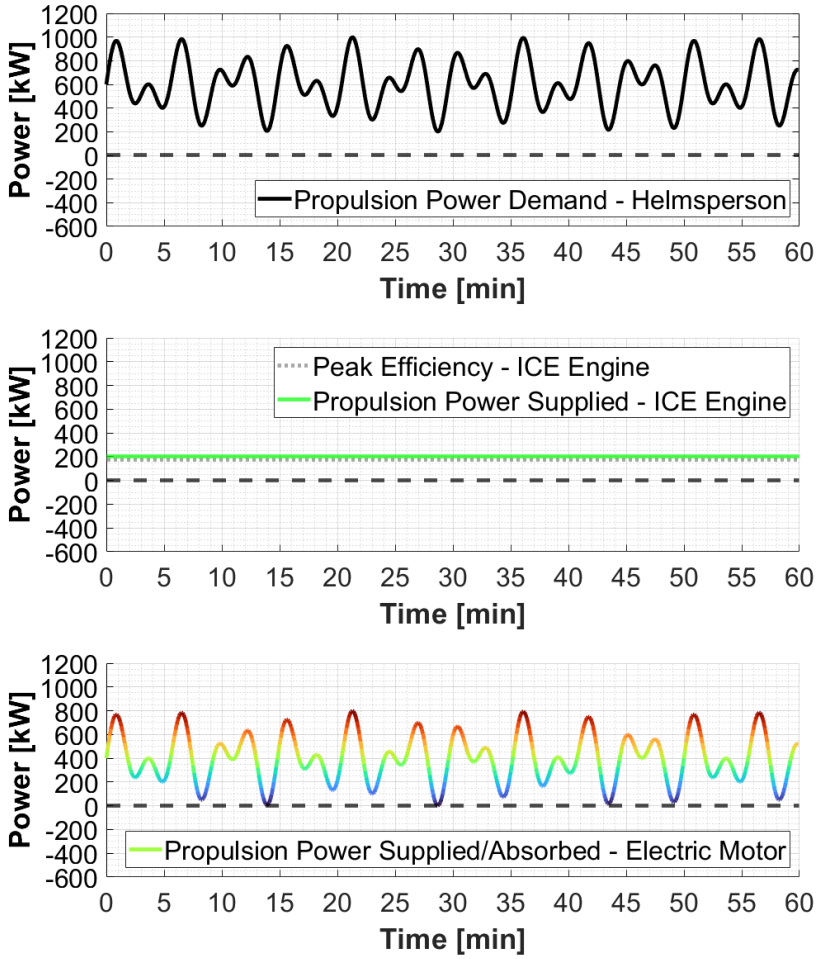

Figure 2.6: Simplified Power Demand – Hybrid Electric Propulsion (Small Engine)

A subsequent analysis of this first-pass MBD result might reveal that the initial engine selection was too small, which in turn required too large of an electric machine and ESS, or perhaps required too high of a discharge rate that would accelerate the degradation of battery cells. Using this information, the next iteration of the propulsion system design may incorporate a larger engine and lead to the result shown in Figure 2.7.

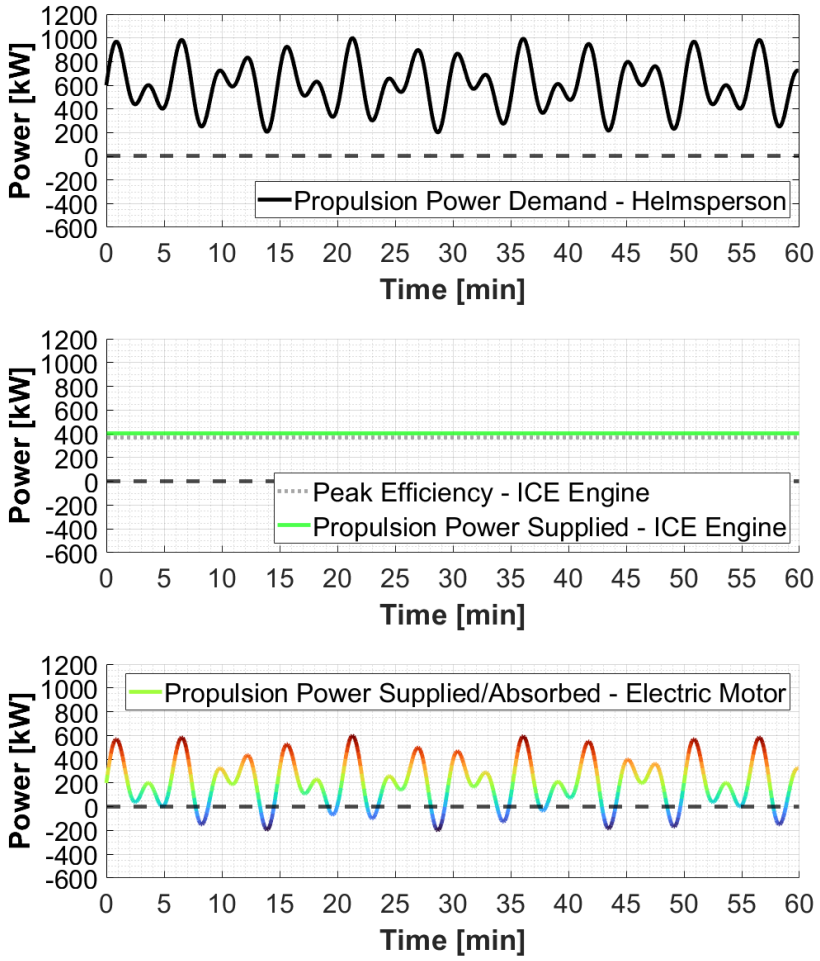

Figure 2.7: Simplified Power Demand – Hybrid Electric Propulsion (Medium Engine)

Analysis of this subsequent MBD result may reveal further deficiencies and the design of the hybrid propulsion system will continue to evolve until sufficient performance is achieved in simulation. For obvious reasons, it is vastly more preferable to iterate through virtual ship designs than it would be to construct multiple ships and powertrains!

In reality, propulsion component sizing and energy management strategies will be tuned using constrained optimization in conjunction with a MBD simulation, however the above example of design iteration serves to provide an illustration of how obtaining a ship's operational profile, including its power time-series, can lead to a better propulsion system design.

In other words, MBD design and optimization cannot occur without having first obtained a vessel's operational profile through virtual vessel simulation.

Finally, as hybrid systems thrive when propulsion demand fluctuates, the previous exam-

ple should have demonstrated that it is not sufficient to consider time-averaged propulsion demand for hybrid-propulsion system design. As can be seen in Figure 2.8, due to the efficiency and conversion losses associated with hybrid systems, a traditional internal combustion engine that is sized to operate at or near its most efficient region for long periods, would in many cases be indicated as the superior solution if the predicted propulsion demand was steady and if there was infrequent access to plug-in shore power.

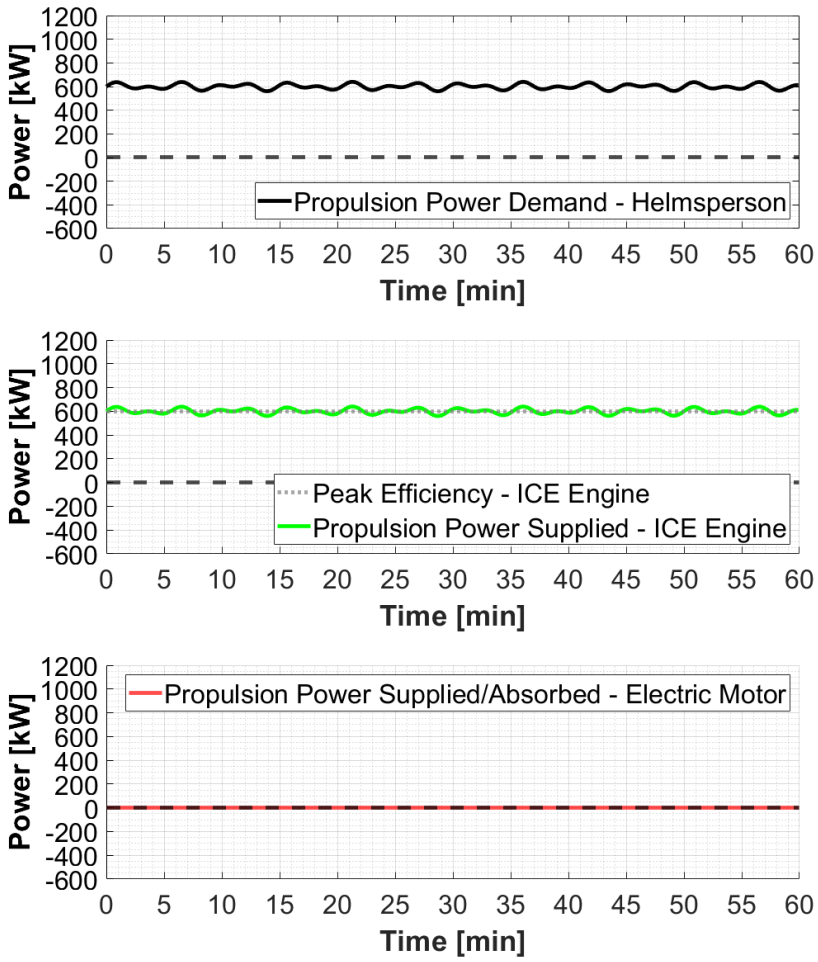

Figure 2.8: Simplified Power Demand – Steady Power Demand

2.3 Modular MBD Marine Simulation Platform

The preceding sections have presented the motivation for producing vessel operational profiles through virtual vessel simulation while demonstrating an application thereof and introducing the concept of MBD.

While a specific application of MBD was presented, MBD is a broad concept that encompasses the shift of engineering activities and product development processes such as design

iteration, system testing, and software debugging, from a physical-based platform to a virtual simulation platform in which the whole of, or portions of, a physical system are represented by mathematical models.

MBD unlocks advanced product development processes that would not be feasible on physical-based platforms, for example, the optimization of a hybrid electric propulsion system may iterate through 10^5 design variations before arriving at a satisfactory solution.

The flow-chart in Figure 2.9 depicts where the proposed virtual vessel simulation would be implemented within an overall MBD framework. The secondary links establish some of the advanced processes enabled through MBD including: energy management optimization, hybrid powertrain optimization, the development of autonomous ship control strategies, as well as hardware and software in loop simulation (HIL, SIL).

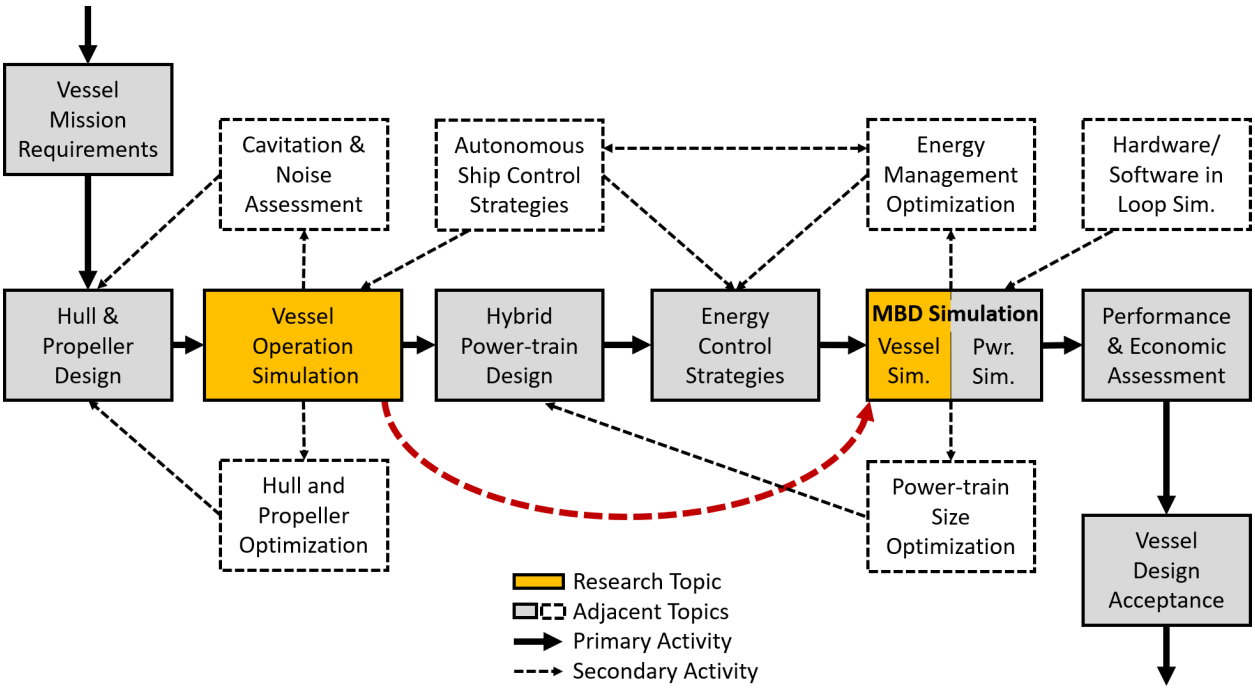

Figure 2.9: MBD Flow Chart

Expanding on the progression within the proposed MBD framework, the virtual vessel simulation, which is by definition a MBD simulation itself, may only involve hull, propeller, helmsperson and environment subsystems which serve to develop the initial vessel operational profile.

The resulting vessel operational profile with power time-series would in turn be used in a subsequent MBD configuration that isolates hybrid propulsion subsystems as shown in Figure 2.10. This subsequent simulation would be used to optimize the hybrid powertrain and energy management strategy as demonstrated by Zhu, Manouchehrinia, and Chen [4, 5, 7].

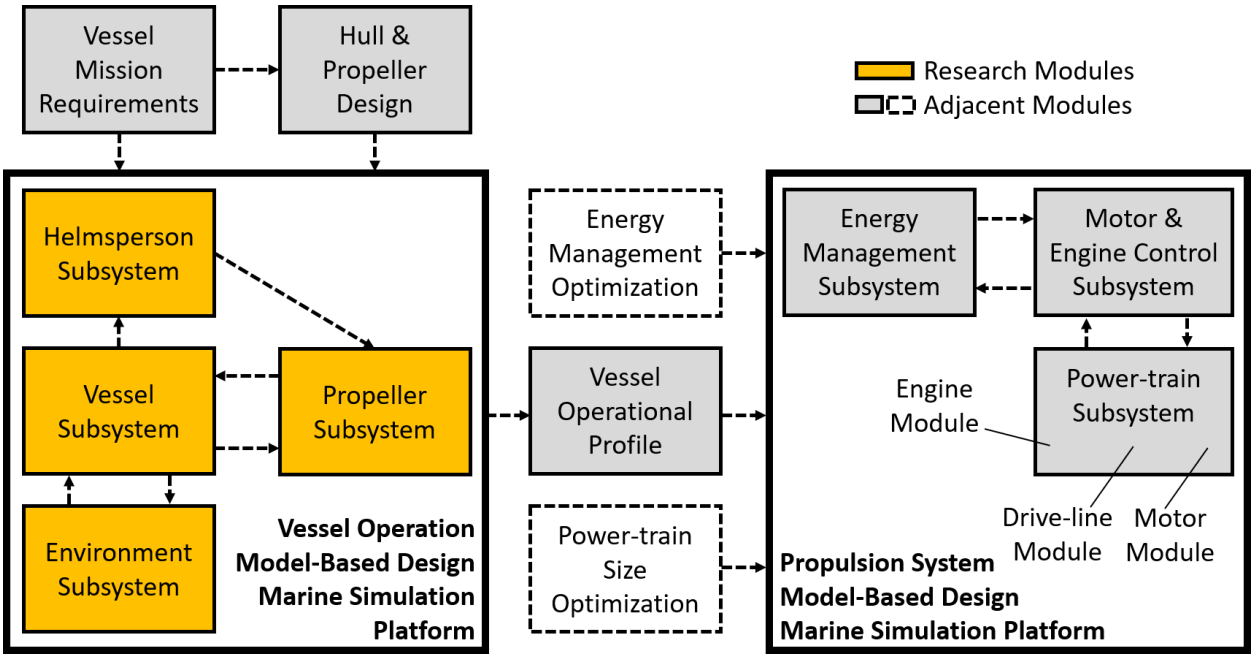

Figure 2.10: MBD Platform – Isolated Subsystems

As a vessel design enters mature stages, the scope of a MBD simulation can broaden to incorporate ever more subsystems to capture the complex interactions that can occur between them and to enable advanced processes as shown in Figure 2.11.

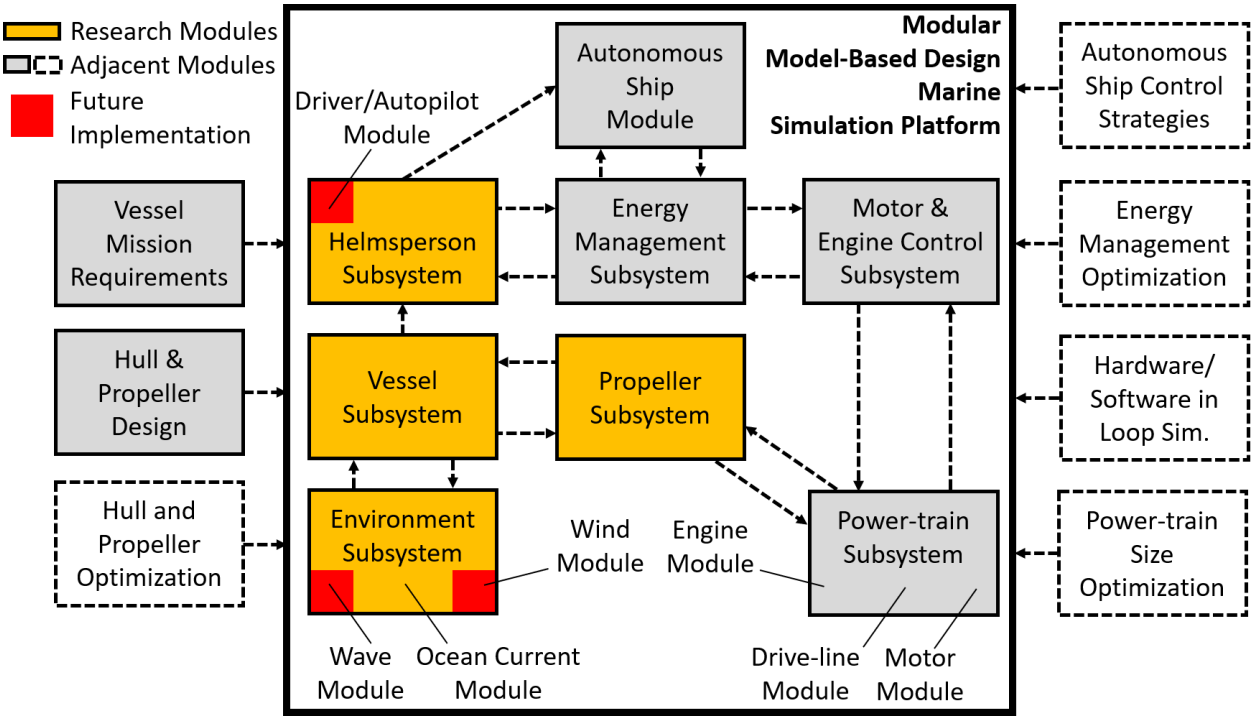

Figure 2.11: MBD Platform – Modular Marine Simulation

In order to adapt with the fluid and changing needs of the design process, Chen [5] proposes a modular MBD platform that can be configured to isolate specific subsystems which target focused engineering objectives, and which can also be reconfigured to capture the system as a whole.

The remainder of this work focuses on new modelling approaches that are incorporated into the development of vessel, propeller, helmsperson and environmental subsystems that form core subsystems of the modular MBD marine simulation platform.

The selected subsystems are sufficient for generating a vessel's operational profile early on in a vessel's design progression and are developed with computational efficiency in mind such that they are *compatible* with later MBD optimization processes.

2.4 Related Work

There are numerous works in the literature that explore vessel manoeuvring simulations, however many of these publications use computationally expensive CFD methods that are unsuitable for use with the MBD optimization processes that require rapid iteration.

Andersen [8] and Liu [9] present MBD simulation platforms that make use of compatible 1 degree-of-freedom (DOF) manoeuvring models for simulating vessel operational profiles. While their codes are computationally efficient and the accuracy of their resulting operational profiles are satisfactory, both researchers concede that the 1 DOF approach can introduce large errors during dynamic manoeuvring sequences and suggest that this can only be remedied through the use of higher DOF manoeuvring models.

Truelove [10] employs a 3 DOF manoeuvring model to generate vessel operational profiles while opting to substitute accurate hull surface models with mathematically generated pseudo-hull geometries. The elegance of this approach is that it can be employed rapidly and without the use of computer-aided-drawing and computational-fluid-dynamics software. Truelove's approach produces promising results, but he was unable to thoroughly validate the manoeuvring accuracy during dynamic sequences due to variations between the actual vessel's control input and the simulated vessel's control input.

While the works mentioned above build their 1 and 3 DOF manoeuvring models around the works of Fossen [11], the approach herein introduces a new hybrid manoeuvring model built around the so-called Manoeuvring Modelling Group (MMG) model. Also setting this work apart is an alternate approach to validation that focuses heavily on the accuracy of predicted hull and propeller performance through the use of directly recorded control inputs.

Chapter 3

Data Acquisition for Drive-Cycle Development and Simulation Validation

3.1 Motivation for Acquiring Vessel Drive-Cycle and Operational Data

Data acquisition can be an essential component of any research project where it is necessary or prudent to validate results using physically measured data. In this work, data acquisition serves three purposes:

1) The first being to record actual helmsperson control actions that govern the magnitude and direction of applied thrust. These helmsperson actions are used as control inputs during simulation and allow for a more rigorous assessment of simulation accuracy.

2) The second purpose of data acquisition is to generate a drive-cycle that a simulated virtual ship is expected to transit along during simulation. For a new ship in the design phase, this recorded drive-cycle would be replaced with a user-generated drive-cycle, which at a minimum would consist of a series of georeferenced waypoints that define a ship's intended path and velocity.

3) The third purpose of data acquisition is to provide benchmark data used for the validation of the simulation and for assessing the accuracy of the resulting vessel operational profile including the simulated power time-series.

The following sections introduce the benchmark vessel this work is centred around and then proceed to outline the processes implemented for acquiring the necessary data.

3.2 Benchmark Vessel: BC Ferries' M.V. *Skeena Queen*

The modelling efforts within this work are focused on the motor vessel (M.V.) *Skeena Queen*, a roll-on/roll-off (ro-ro) vehicle and passenger ferry that was built in 1997 and which is owned and operated by British Columbia Ferry Services Inc. (BC Ferries). As is common with many ferry designs, the M.V. *Skeena Queen* makes use of a bi-directional hull and features a large open vehicle deck. The M.V. *Skeena Queen*'s vehicle deck is flanked on either side by passenger lounges while the bridge is located amidships and is raised above the vehicle deck as shown in Figures 3.1–3.2.

Figure 3.1: M.V. *Skeena Queen* Arriving at Swartz Bay
Source: Reproduced with permission from P. Grant and J. Grant [12]

Figure 3.2: M.V. *Skeena Queen* at Dry Dock

The M.V. *Skeena Queen* currently services a ferry route on the West Coast of British Columbia, Canada, transiting between Swartz Bay on Vancouver Island to Fulford Harbour on Salt Spring Island. This popular route is approximately 35 minutes one-way and all 16 daily scheduled crossings are serviced by the *Skeena Queen*. Further details regarding the general particulars of the vessel, including dimensions and capacity, are listed in Table 3.1.

Table 3.1: M.V. *Skeena Queen* Vessel Particulars
Source: MV Skeena Queen: Trim and Stability Booklet, Our Fleet: Skeena Queen, and Specification Sheets of S6U-MPTK Engine [13–15]

Property	**Description**
Year built	1997 (Vancouver, BC)
Length (overall)	110.0 m
Length (waterline)	104.0 m
Beam (overall)	24.0 m
Draft (design)	2.723 m
Maximum speed	15.3 kn
Displacement (design)	2942 tonnes
Crew compliment	7
Passenger capacity	450
Vehicle capacity	92
Continuous power (main engines)	4476 kW

Unlike traditional ships that rely on fixed propellers and rudders for propulsion and steering, the M.V. *Skeena Queen's* thrust is provided by four z-drive azimuth thrusters that can rotate 360° to direct thrust in any direction as shown in Figure 3.3. Each azimuth thruster is mechanically driven by a 1119 kW diesel engine [15] that runs through a single stage gearbox with clutch. The ship's AC grid is powered separately by two diesel generators while a third emergency generator provides redundancy. A simplified propulsion schematic is provided in Figure 3.4.

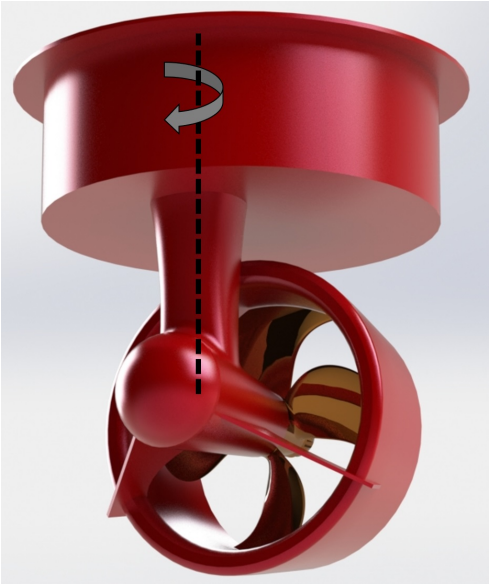

Figure 3.3: M.V. *Skeena Queen* Azimuth Thruster

With the M.V. *Skeena Queen* serving as the benchmark vessel for validating the proposed MBD marine simulation platform, the following sections document the processes implemented for acquiring the necessary data from this ship.

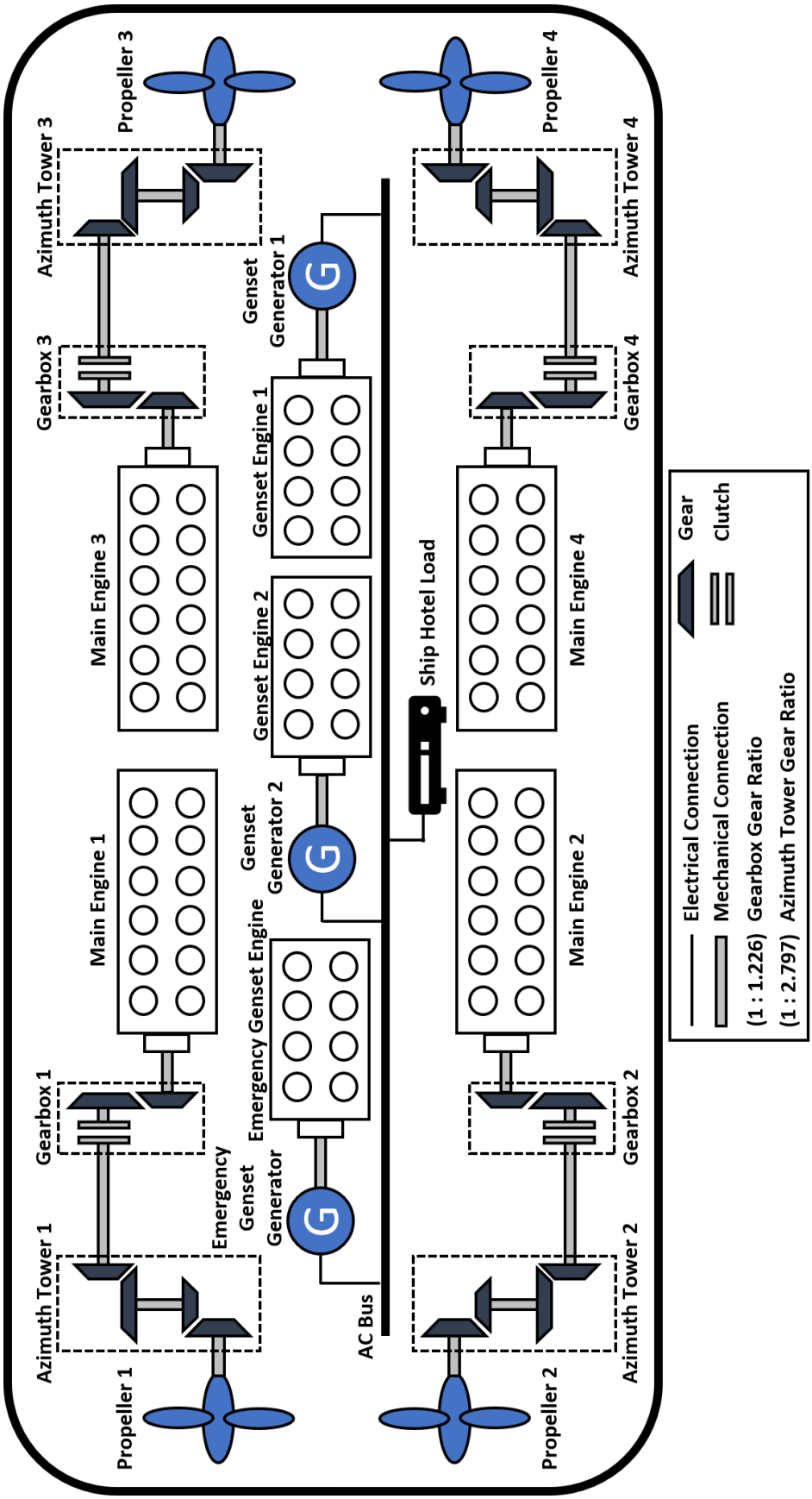

Figure 3.4: M.V. *Skeena Queen* Propulsion Schematic

3.3 Scope and Plan of Data Acquisition

Obtaining recorded vessel mission data from the M.V. *Skeena Queen* was crucial to this work as it provided a means to validate the vessel simulation platform and assess the accuracy of its embedded models.

The M.V. *Skeena Queen* data was acquired as part of a larger effort that involved a team of researchers from the University of Victoria (UVic), each with their own interest in collecting data from the ship.

During a review of the M.V. *Skeena Queen*'s systems, it was discovered that the vessel had been equipped with a voyage data recorder (VDR) which stored several signals of interest, including ship position, speed-over-ground, and heading. Although direct access was forbidden, the VDR could be accessed by BC Ferries personnel who in turn could send requested data to researchers at UVic.

In addition to the signals available on the VDR, the team installed an off-the-shelf measurement system from BeeData to measure the power transmitted from the main engines through the propeller shafts. As two of the four propeller shafts were located at the opposite end of the ship, a separate BeeData system was required at each end as depicted in the data acquisition system schematic (Figure 3.5).

The remaining data acquisition module, a standalone anemometer, was installed on the upper bridge deck to obtain wind speed and wind direction.

While a centralized all-in-one data recording solution would have provided superior data synchronization, the research group applied a modular approach to reduced cost, development time, and complexity. This approach required the data to be synchronized during post-processing, which introduced an un-quantified synchronization error into the data.

The signals collected by the three data acquisition modules were all recorded at 1 Hz and are listed in Table 3.2.

Table 3.2: M.V. *Skeena Queen* Data Acquisition Signals

Signal	**Source**
Shaft strain	BeeData module
Shaft speed	BeeData module
Shaft torque (calculated)	BeeData module
Shaft power (calculated)	BeeData module
Wind speed	Anemometer module
Wind direction	Anemometer module
Position (Latitude/Longitude)	VDR module
Speed-over-ground	VDR module
Heading (true)	VDR module
Turn rate	VDR module
Thruster angle (command)	VDR module
Thruster angle (response)	VDR module
Engine speed (command)	VDR module
Engine speed (response)	VDR module

A schematic of the overall data acquisition system architecture is provided in Figure 3.5 and the following subsections provide further details of each module.

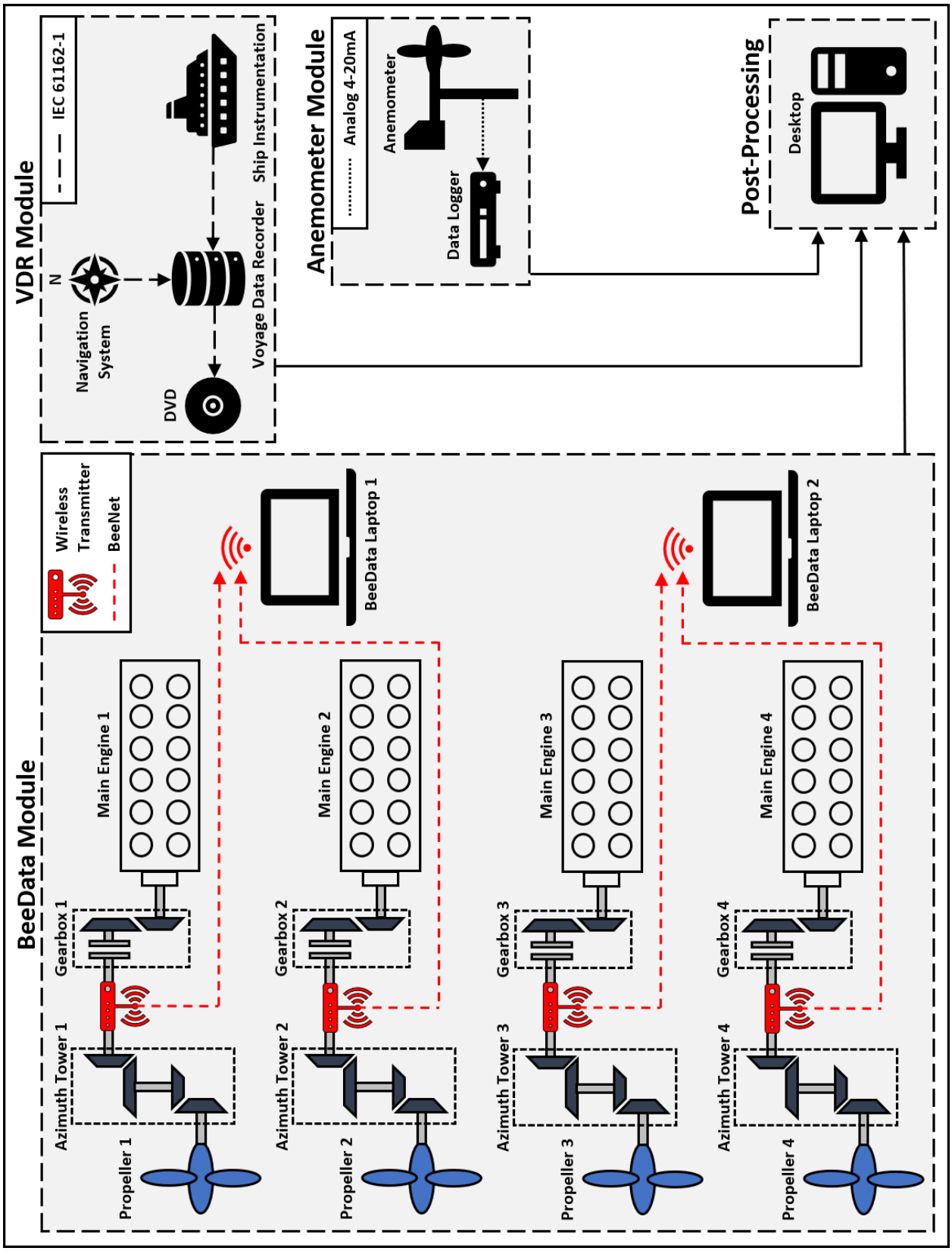

Figure 3.5: M.V. *Skeena Queen* Data Acquisition System Architecture

3.4 BeeData Shaft Speed and Torque Measurement Module

To assess the accuracy of the propulsion power predicted by the simulation, it was critical to compare the ship's simulated power with measured power. To accomplish this, an off-the-shelf system was purchased from BeeData to measure the power being transmitted from the main engines to the azimuth thrusters through the propeller shafts.

The BeeData measurement system makes use of shaft-mounted sensors that measure both shaft strain and shaft speed while a wireless transmitter sends the data to a nearby laptop running BeeData software.

The shaft speed, n_{data}, was measured with a shaft-mounted hall-effect sensor that generated a pulse each time it rotated past a stationary magnet. As each Hall effect sensor pulse corresponded with a full revolution, counting the number of pulses within a given time window allowed the BeeData software to determine the angular shaft speed.

The shaft torque, Q_{data}, was obtained using a full-bridge strain gauge that was adhered to the shaft. An illustration of the shaft mounted BeeData instrumentation is provided in Figure 3.6.

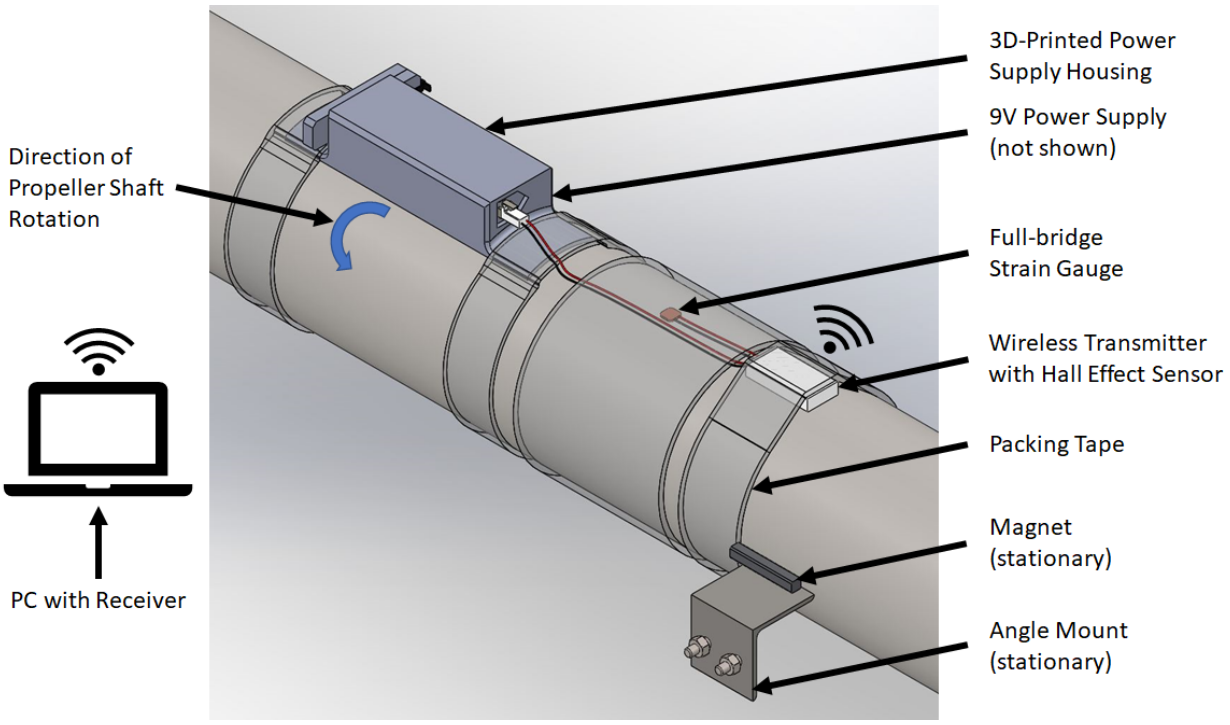

Figure 3.6: Propeller Shaft Strain and Angular Velocity Measurement Setup

The power measured at the shaft is calculated from:

$$P_{data} = Q_{data} n_{data} \tag{3.1}$$

where P_{data} is the shaft power, Q_{data} is the measured torque, and n_{data} is the measured shaft speed.

As a strain gauge does not measure torque directly, the strain measurements must be converted to torque using the known material and geometric properties of the shaft.

This process begins by converting the actual voltage measured across the strain gauge sensor into measured strain. To accomplish this, the BeeData software required inputs to account for the gauge's form-factor (full-bridge) and sensitivity which were provided by the gauge manufacturer and were input into the software as per the BeeData manual [16].

The subsequent conversion of measured strain into shaft torque requires an additional conversion factor. The calculation of this subsequent conversion factor begins with the relation between the shaft's shear stress and shear strain:

$$\tau_{data} = G \gamma_{data} \tag{3.2}$$

where τ_{data} is shear stress, γ_{data} is shear strain, and G is the shear modulus of the shaft material.

The shaft's shear stress is also related to torque with:

$$\tau_{data} = \frac{Q_{data} r_{shaft}}{J_{shaft}} \tag{3.3}$$

where Q_{data} is the shaft torque, r_{shaft} is the shaft radius, and J_{shaft} is the polar moment of inertia of the *solid* propeller shaft given by:

$$J_{shaft} = \frac{\pi}{2} r_{shaft}^4 \tag{3.4}$$

The propeller shaft's shear modulus is related to Young's modulus with:

$$G = \frac{E}{2\left(1 + v_{poisson}\right)} \tag{3.5}$$

where E is Young's modulus, and $v_{poisson}$ is the Poisson ratio of the shaft material.

Combining equations (3.2) to (3.5) and re-arranging results in an expression that relates

shaft torque to shaft shear strain:

$$Q_{data} = \gamma_{data} \frac{E}{2\,(1 + v_{poisson})} \left(\frac{\pi}{2} r_{shaft}^{3} \right) \tag{3.6}$$

Taking into consideration that the strain gauge provides a measurement of the normal strain experienced by the strain gauge, and not the shear strain on the shaft, an additional expression that relates the two strains is required. With the gauges aligned at 45° to the shaft, the gauge normal strain is related to shaft shear strain with:

$$\epsilon_{data} = \frac{\gamma_{data}}{2} \tag{3.7}$$

where ϵ_{data} is the measured gauge strain.

Substituting equation (3.7) into equation (3.6) results in the expression used by the BeeData software to convert measured gauge strain to shaft torque:

$$Q_{data} = \epsilon_{data} \frac{E}{(1 + v_{poisson})} \left(\frac{\pi}{2} r_{shaft}^{3} \right) \tag{3.8}$$

It should be noted that error is introduced into the torque measurement through the estimation of point values for E and $v_{poisson}$ which were chosen from a given range for the specified shaft material.

3D-Printed Power Supply Housing Design

The BeeData shaft-mounted instrumentation for measuring strain and speed was installed underneath existing protective shaft guards at locations designated by BC Ferries personnel. The instrumentation locations on shafts 1 and 2 are shown in Figure 3.7 while the sensors on shafts 3 and 4 were installed at identical locations at the opposite end of the ship.

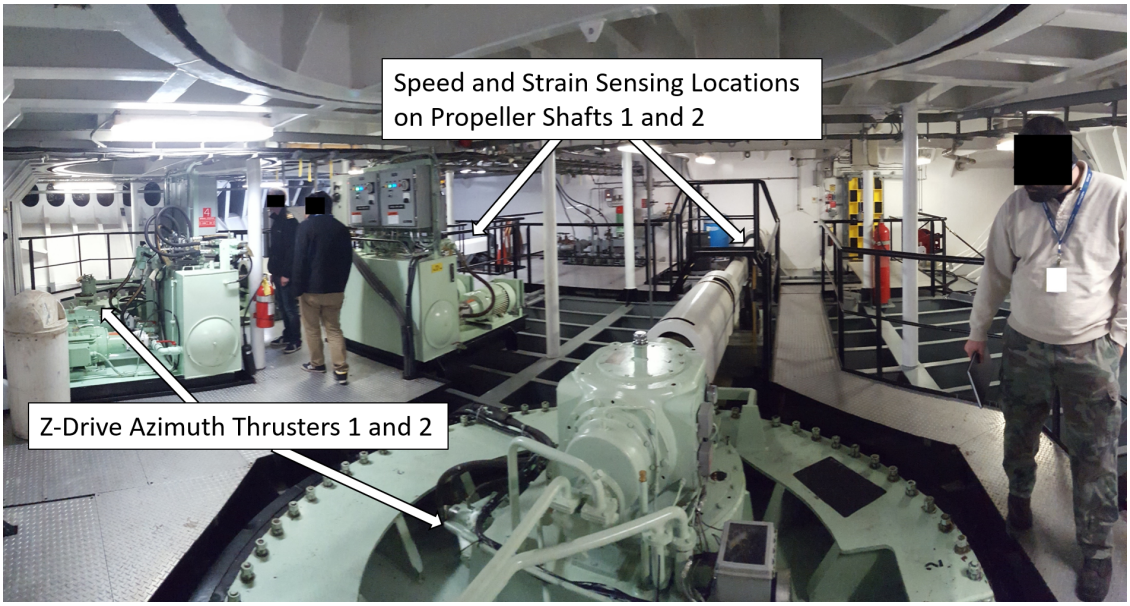

Figure 3.7: Shaft Speed and Strain Sensing Locations on Propeller Shafts 1 and 2

When planning the BeeData installation, it was discovered that the process of removing and replacing the shaft guards on all four shafts exceeded 90 minutes. This posed a conflict as the shaft-mounted instrumentation was powered by shaft-mounted batteries which needed to be changed periodically. To avoid any disruption to the regularly scheduled ferry service, it became evident that the batteries would need to be replaced without removing the shaft guards.

The solution implemented to resolve this conflict was to design and produce four 3D-printed power supply housings that allowed BC Ferries crew to quickly access and change the batteries through an opening at the bottom of the shaft guard as shown in 3.8.

By incorporating a sliding-tray into the 3D-printed housing design, BC Ferries crew members were able to change the batteries in less than 3 minutes per shaft with a simple process:

- Cut a zip-tie that restrained a sliding tray
- Unplug the tray connector
- Remove the sliding tray and replace the batteries
- Re-insert the sliding tray
- Plug-in the tray connector
- Install a new zip-tie to secure the tray

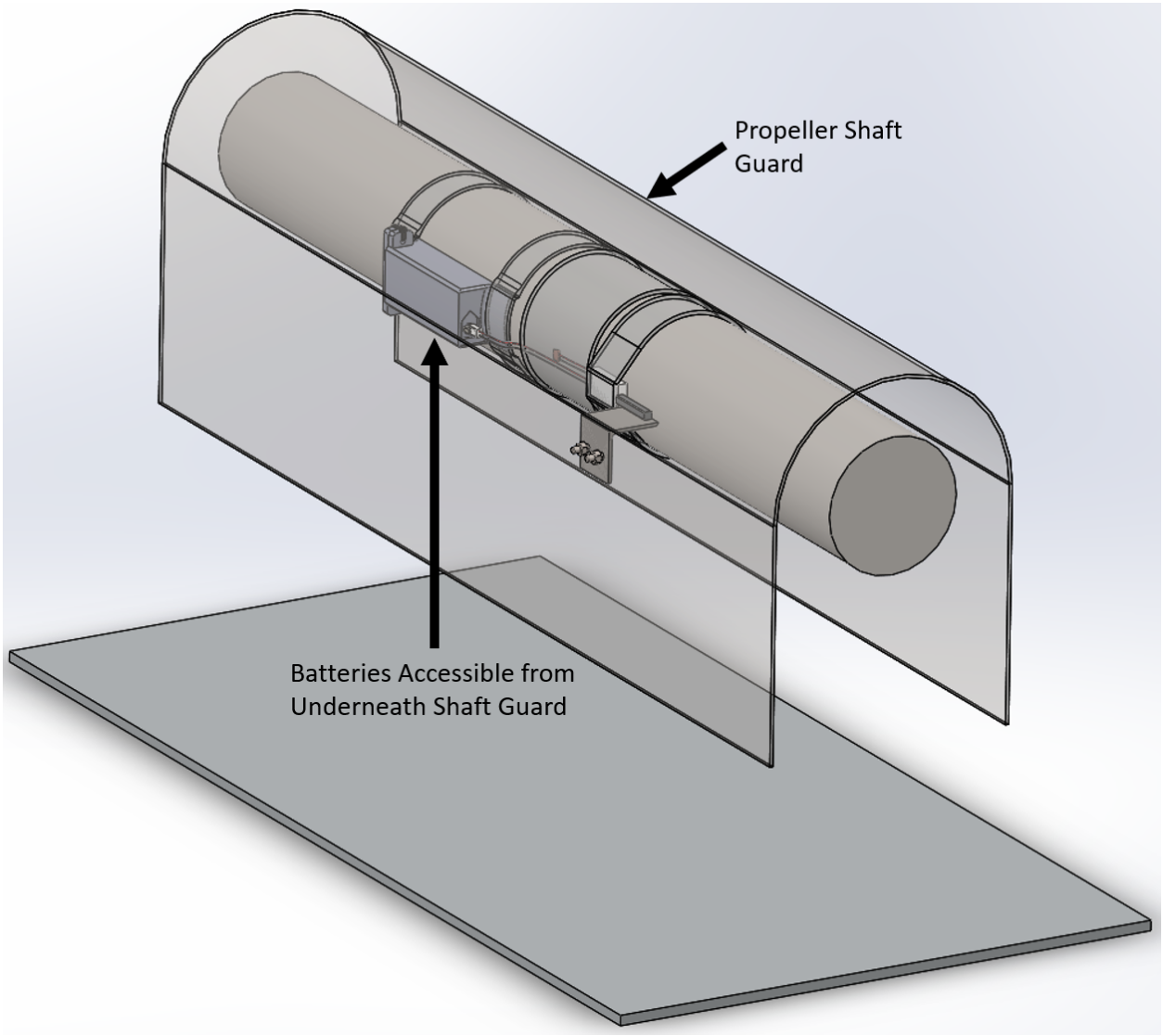

Figure 3.8: Power Supply Accessibility

The sliding tray housed two 9V batteries that were connected with snap-on 9V battery connectors. The lead wires from the snap-on 9V battery connectors were soldered in parallel to a tray mounted connector that extended power to the shaft-mounted instrumentation. Some of the design features of the 3D-printed power supply housing are highlighted in Figure 3.9 and Figure 3.10.

To ensure that the power supply housing was capable of withstanding the forces it would experience while rotating at high speed, it was subjected to a static load test.

The force experienced by the power supply housing at constant maximum shaft speed was estimated as:

$$F_{PS} = m_{PS} r_{PS} n_{max}^2 \tag{3.9}$$

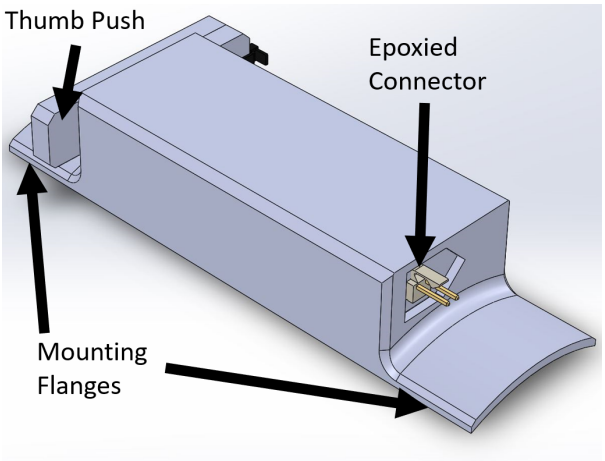

Figure 3.9: Power Supply Housing – Closed

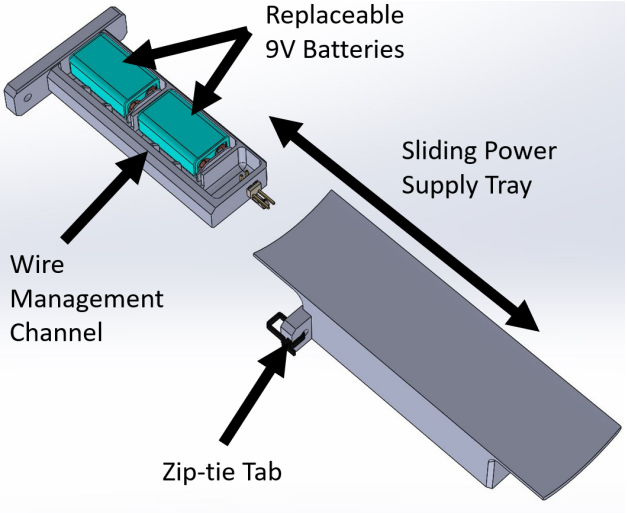

Figure 3.10: Power Supply Housing – Open

where F_{PS} is the load applied to the power-supply housing, m_{PS} is the mass of the power-supply assembly including the batteries, r_{PS} is the radius to the power-supply assembly's centre of gravity, and n_{max} is the maximum shaft speed.

One of the 3D-printed power-supply housings was tested with a static load that was 2.5 times larger than the estimated maximum force, a value which was assumed to provide sufficient allowance for shaft angular acceleration.

In summary, the BeeData module measured strain and angular speed at the propeller shafts to provide recorded power time-series that were compared with simulated power time-series to assess the accuracy of the simulation platform.

3.5 Anemometer Module

Wind speed and direction data were recorded with an anemometer that was mounted on the *Skeena Queen*'s upper bridge deck by UVic researcher Haijia Zhu. This data was intended to support the inclusion of wind-resistance within the simulation, but it was not implemented due to a lack of detailed information regarding the M.V. *Skeena Queen*'s superstructure geometry.

For the analyzed crossings, the recorded wind speed was approximately the same speed as the vessel, indicating that the apparent wind velocity was mostly due to the motion of the ship itself and implying that the wind speed was negligible during many of the analyzed crossings.

3.6 VDR Module

The M.V. *Skeena Queen* is equipped with a VDR that is analogous to an aircraft's "black box" and which records an array of important ship operational data. During the data acquisition system planning phase, BC Ferries agreed to extract VDR data during periods of interest, remove any sensitive data such as bridge audio recordings, and provide a copy of the remaining data to the research group. The VDR logs, encoded in NMEA 0183 format, were later provided on a DVD to UVic researcher Haijia Zhu. Zhu wrote a Python script to extract and decode the VDR signals which he then distributed to the research group in spreadsheet format.

The VDR signals used in this work were:

- Latitude and longitude
- Ship speed-over-ground
- Ship true heading
- Azimuth thruster angle

3.7 Data Post-Processing

Once the data files had been obtained from the three data acquisition modules, a script was written in MATLAB to synchronize and combine the data.

Prior to the data collection effort, it was acknowledged that the data from the separate modules would need to be synchronized during post-processing and so differences between the system clock times were noted using a stopwatch. With the differences in system clock times noted, the datasets from the BeeData module and Anemometer module were time-shifted during post-processing to align with the VDR module data. The estimated synchronization error after the time-shift operation was approximately ± 1 second.

After the data had been synchronized, it was split into data subsets that represented individual ferry crossings. Each data subset began with the M.V. *Skeena Queen* departing from its berth and terminated when the ferry arrived at the berth on the opposite side. The periods of time between ferry crossings, when the passengers and vehicles were loaded and unloaded, were cut from the data subsets.

The plots in Figure 3.11 to Figure 3.18 illustrate a complete series of subset data for a single ferry crossing.

The first plot shows the *Skeena Queen*'s recorded path between Swartz Bay and Fulford Harbour which is generated by overlaying global positioning system (GPS) latitude and longitude data on top of a georeferenced satellite image made available by National Resources Canada [17, 18].

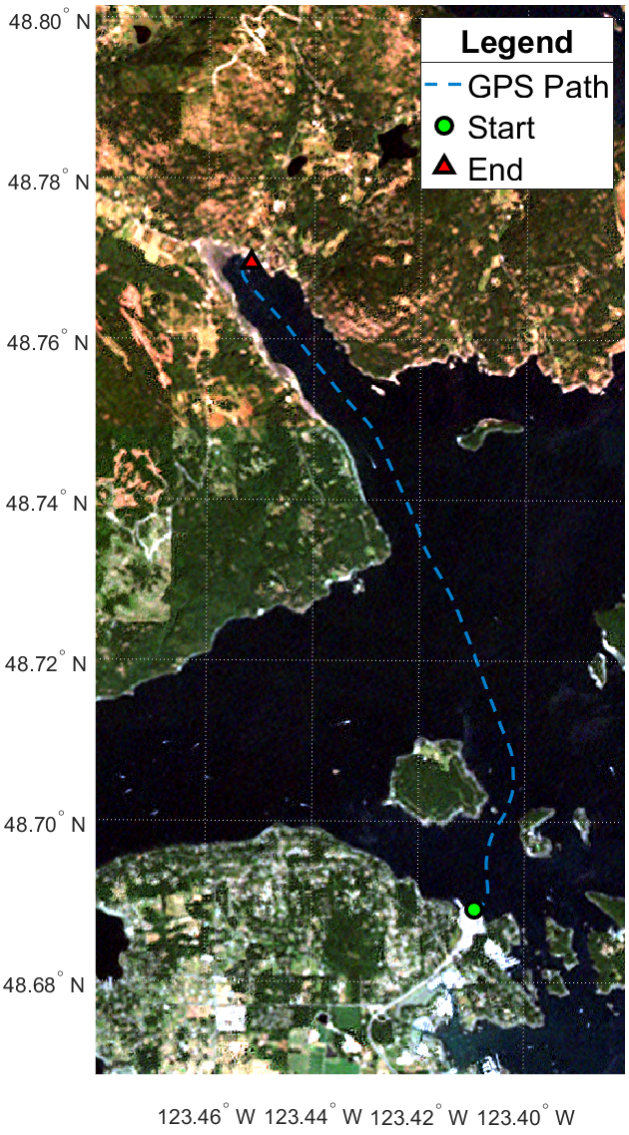

Figure 3.11: Recorded GPS Path from Swartz Bay to Fulford Harbour (VDR Module) Source: Satellite imagery reproduced with permission from National Resources Canada [17, 18].

Figure 3.12 depicts the M.V. *Skeena Queen*'s speed-over ground as measured by the ship's onboard GPS. The ship speed ramps up after departure from Swartz Bay, remains semi-constant during transit, and then ramps down as it approaches Fulford Harbour.

The ship speed fluctuates somewhat noticeably near the beginning of the journey as the

vessel manoeuvres between the islands near Swartz Bay. This fluctuation may be caused by stronger drag forces that arise during manoeuvring, and/or by chaotic ocean currents that can occur between these islands. While the ocean current speeds can be estimated using a current atlas [19], the resolution between the islands is not sufficient to confirm the cause of the vessel's speed fluctuation.

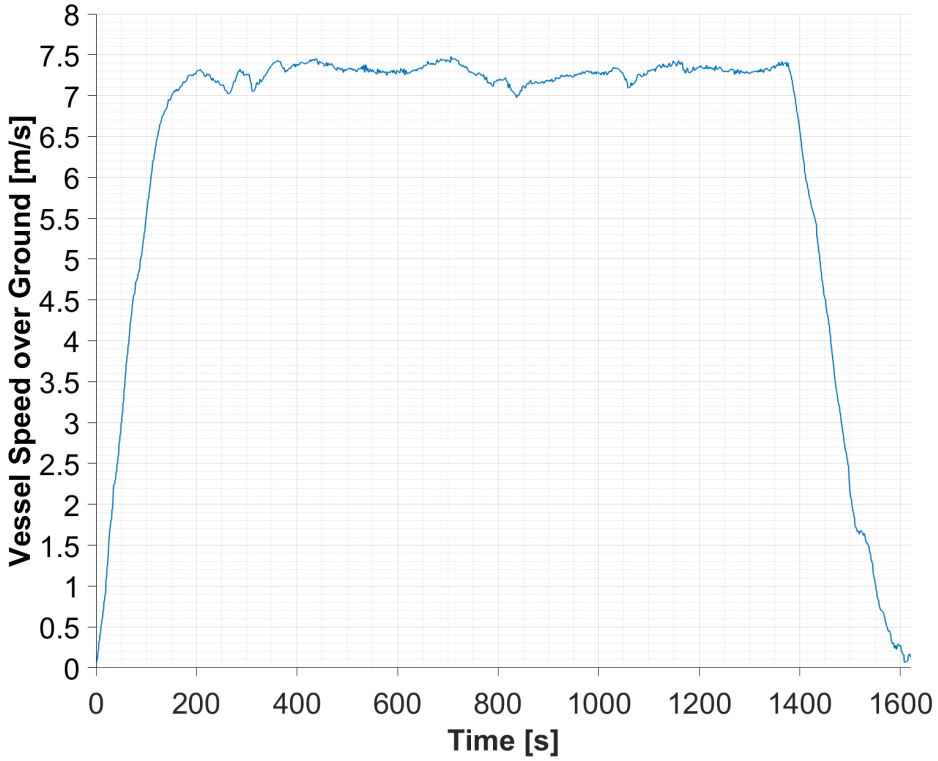

Figure 3.12: Recorded Ship Speed-over-Ground (VDR Module)

Figure 3.13 is a plot of the recorded azimuth angles from the four azimuth thrusters.

When transiting from Swartz Bay to Fulford Harbour, azimuth thrusters 1 and 2 are located at the bow of the ship while azimuth thrusters 3 and 4 are located at the stern. Thanks to the *Skeena Queen*'s bi-directional design, the opposite is true when the ship travels in the other direction from Fulford Harbour to Swartz Bay. Near the end of the ferry crossing when the *Skeena Queen* is approaching the berth at Fulford Harbour, it can be seen that both fore thrusters are rotated 180° to provide braking thrust that slows the ship down.

Figure 3.14 depicts the *Skeena Queen*'s recorded true compass heading and yaw rate. Note that the plots for azimuth thruster angle (−180° to 180°) and vessel heading (0° to 360°) are plotted in degrees such that visual discontinuities occur when the angles wrap around a full circle.

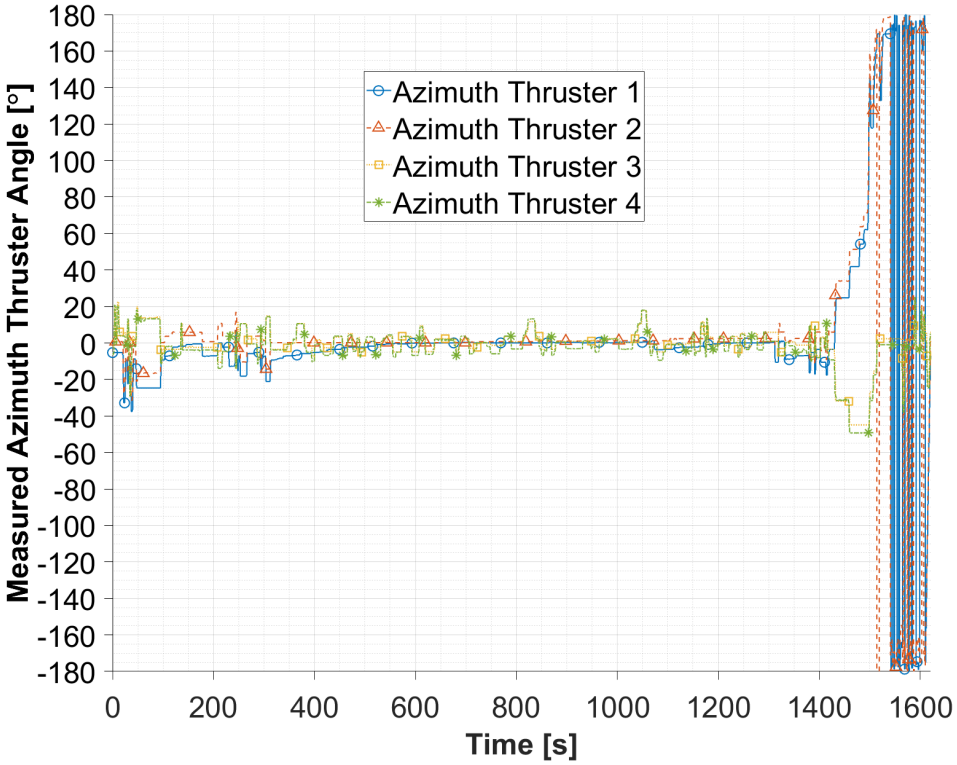

Figure 3.13: Recorded Azimuth Thruster Response Angle (VDR Module)

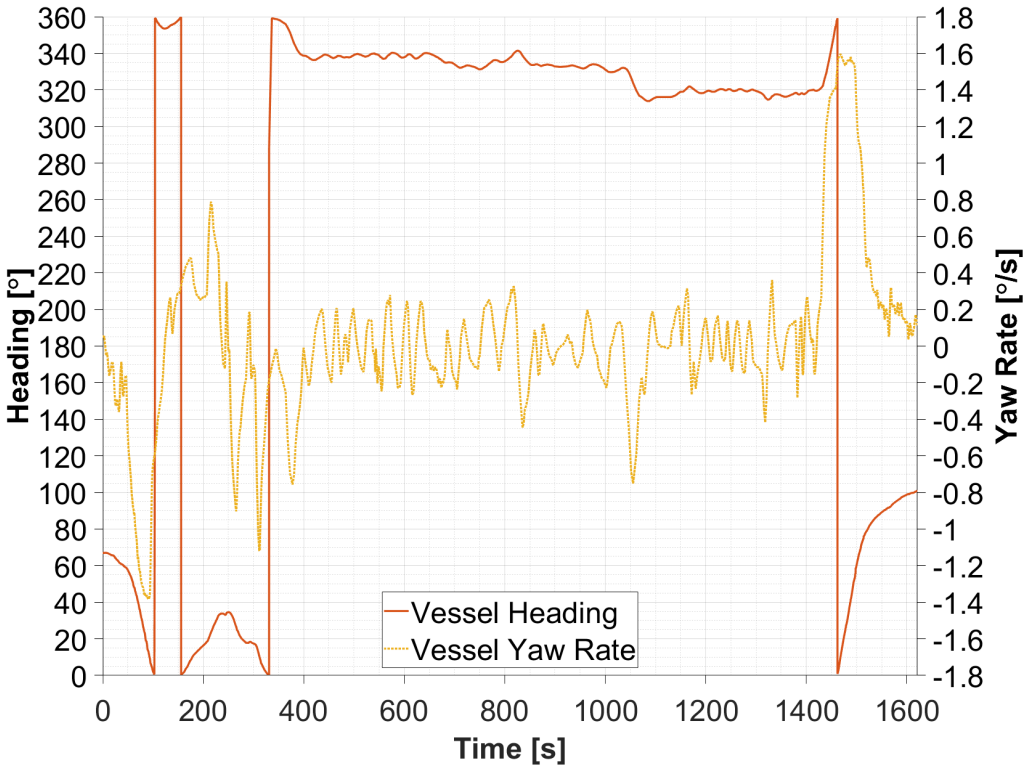

Figure 3.14: Recorded Ship Heading and Yaw Rate (VDR Module)

Recorded wind speed is shown in Figure 3.15. Examination of this plot reveals that relative wind speed is slightly less than the ship's speed-over-ground, indicating that forward ship speed is likely contributing to most of the apparent wind velocity during this crossing.

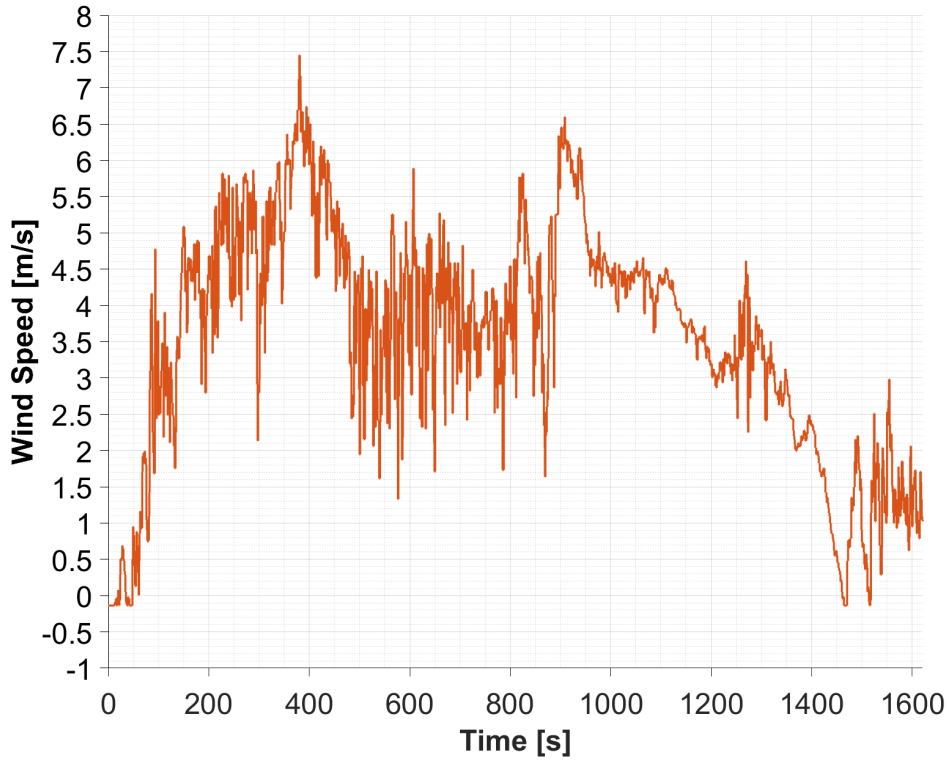

Figure 3.15: Recorded Wind Speed (Anemometer Module)

Recorded propeller shaft speed and torque plots are shown in Figure 3.16 and Figure 3.17 respectively.

Upon review of these plots, it can be observed that during the near steady-state portion of the crossing between 200 and 1300 seconds, all of the shaft speeds are nearly uniform.

As all of the azimuth thrusters feature identical powertrains and drivelines, a nearly uniform torque reading across all shafts was also expected. It can be observed however, that the torque on shaft 4 trends significantly lower than the torque measured on the other shafts. When considering that the accuracy of a strain gauge is sensitive to the installation process, this variance can likely be attributed to a poor strain gauge installation on shaft 4.

The under-reported torque reading on shaft 4 cascades into an under-reported power reading on shaft 4 which can be observed in Figure 3.18.

When comparing the recorded shaft power data with independent shaft power measurements from a *Skeena Queen* sea-trial report, the power data was shown to be in close agreement, with the exception of power measured on shaft 4 [20].

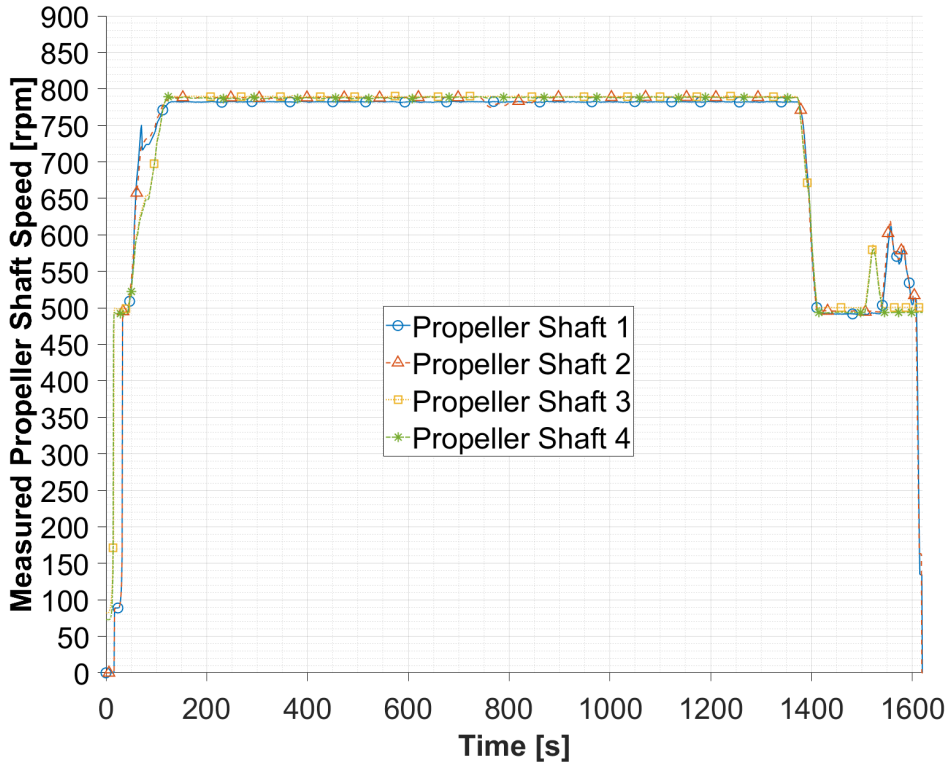

Figure 3.16: Recorded Shaft Speed (BeeData Module)

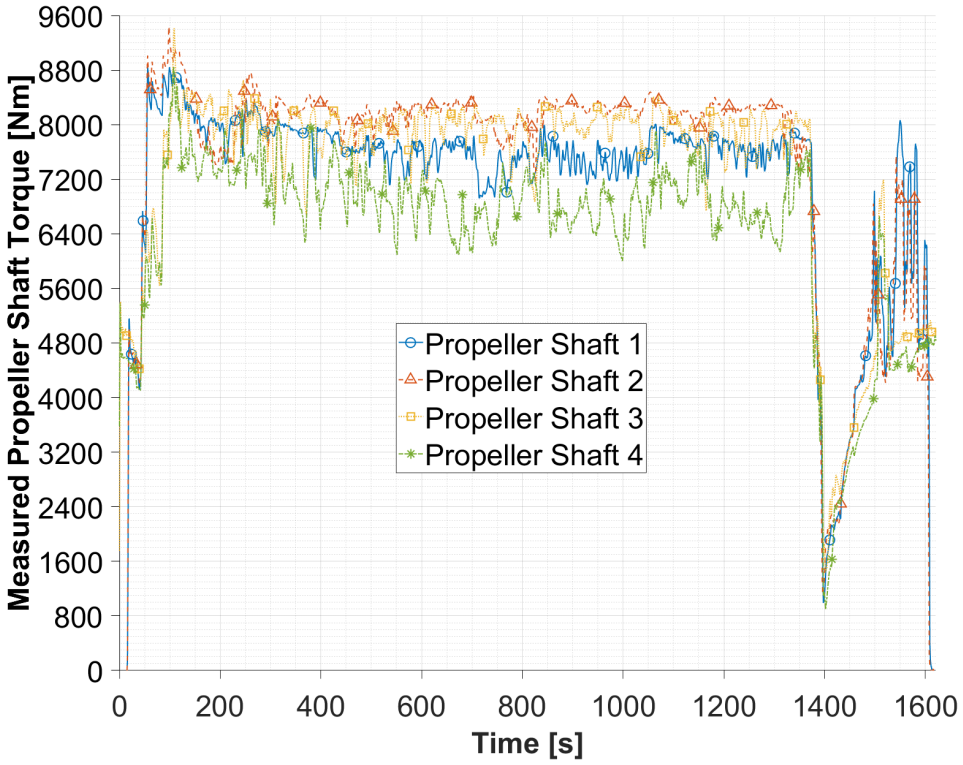

Figure 3.17: Recorded Shaft Torque (BeeData Module)

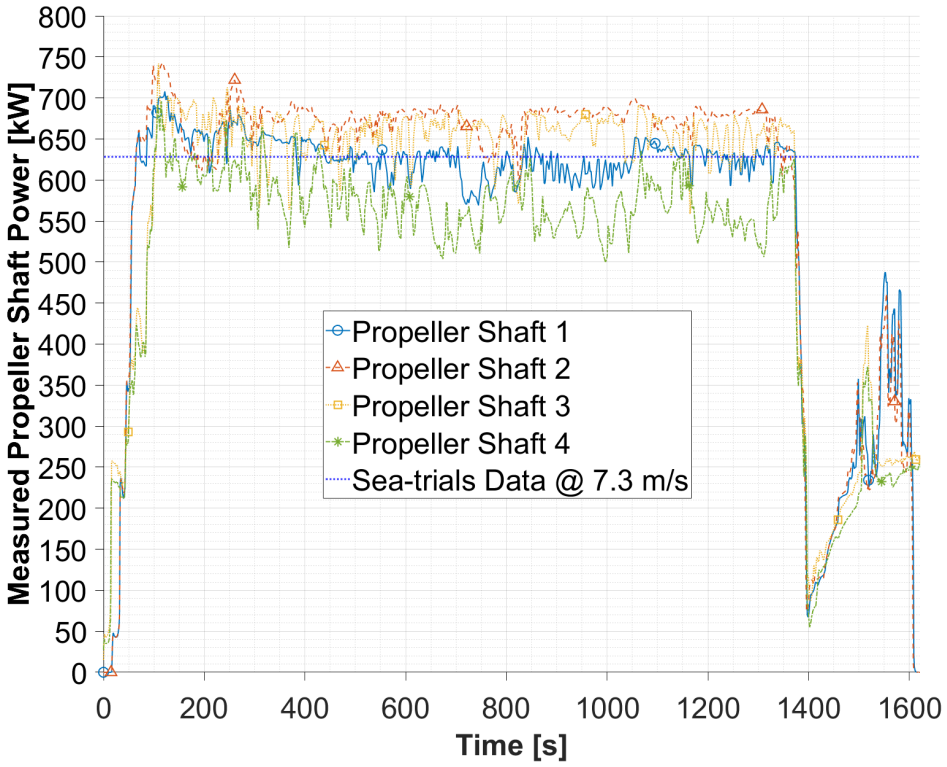

Figure 3.18: Recorded Shaft Power (BeeData Module)

It should be noted that as the ship was near-new when the sea-trial report was issued 20 years prior, the sea-trial reference power measurement does not factor in the effects of coating degradation, increased surface roughness, and fouling that lead to increased power requirements over-time.

This concludes the description of the data collection effort which provided a means to validate and assess the accuracy of the proposed vessel simulation platform.

Chapter 4

Marine Vessel Modelling for Propulsion Power Prediction

4.1 Propulsion Power Prediction for New Vessels

For the purposes of this work, marine vessel modelling pertains to the forces, moments, and accelerations that arise as a result of a ship's hull and propeller(s) interacting with a fluid (seawater). Marine vessel modelling within this work consists of *i*) modelling the resistance of the ship hull as it moves through the water, and *ii*) modelling the thrust and torque of the propeller(s) (Figure 4.1).

It can be said that the resistance of the hull moving through the water and the thrust required to overcome resistance and propel the ship to the desired velocity are inextricably linked to propulsion power, the dominant source of a vessel's power consumption while underway. When recalling that a key objective of this work is to predict a vessel's power time-series over the course of a voyage, it becomes clear that marine vessel modelling is integral to this effort.

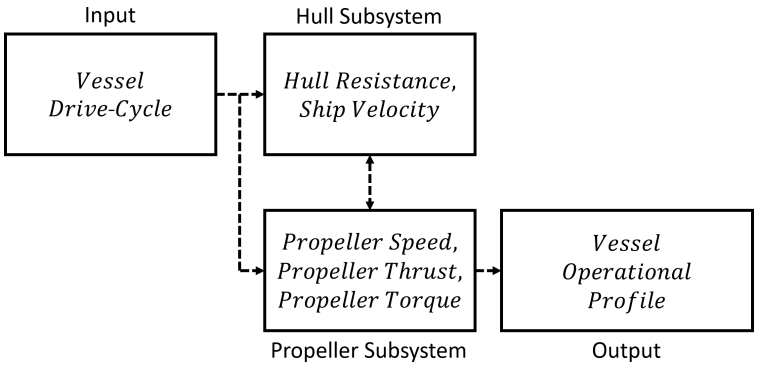

Figure 4.1: Obtaining Vessel Operational Profile and Propulsion Power

While there are a variety of approaches for simulating marine vessels, they need to be considered alongside the issue of computational demand, a real and persistent problem for marine systems modelling that is not likely to abate in the near-term.

The most precise simulation results are currently achievable through high-quality self-propelled computational fluid dynamics (CFD) based simulations which generally require a tremendous amount of super-computing power and extensive run-times that are incompatible with iterative MBD optimization processes. In effect, CFD methods are precluded from integration with MATLAB/Simulink based MBD tools due to excessive computational demand.

The approach in this work aims to strike a balance between simulation accuracy and computational effort in order to produce actionable results that are sufficient for analyzing real-world engineering problems. This is achieved by running a limited number of simplified CFD analyses at selected conditions within the vessel's operating envelope and using the results to build pre-computed hull and propeller hydrodynamic look-up tables.

By simulating vessel dynamics with pre-computed kinetics, the resistance of the hull, as well as the torque and thrust of the propeller can be estimated nearly instantaneously from the look-up tables at the expense of some accuracy during highly dynamic manoeuvres.

The CFD analyses used to build out these look-up tables were run at quasi steady state (i.e. constant ship forward velocity, or constant propeller speed) and therefore an inherent assumption of this approach is that any transient developments in flow caused by acceleration can be neglected. While this steady-state assumption introduces error, it is imperative for reducing the number of operating conditions analyzed with CFD, while simultaneously reducing the computational demand of each analysis.

The accuracy of this approach is investigated for a medium-speed vessel with a displacement hull design that operates in sheltered coastal waters and thus any extension of this work to dynamic high-speed vessels and/or higher sea states may lead to increases in error and should be approached with care.

The following sections describe a process for developing propeller and hull mathematical models, including the construction of pre-computed hull and propeller look-up tables, which are later incorporated into a MBD marine simulation platform.

Finally, and as noted in later sections, it is acknowledged with great appreciation that all of the CFD analyses in this work were run by Rahimpour [24, 36].

4.2 Propeller Modelling

Describing the process of propeller modelling necessitates a brief introduction to the conventions used in this work.

The origin of the propeller coordinate system, o_{prop}, lies on the propeller's axis of rotation with the x_{prop}-axis aligned with the propeller's axis of rotation and positive towards the leading edges of the blades. The y_{prop}-axis is positive to starboard while the z_{prop}-axis is positive downwards as shown in Figure 4.2.

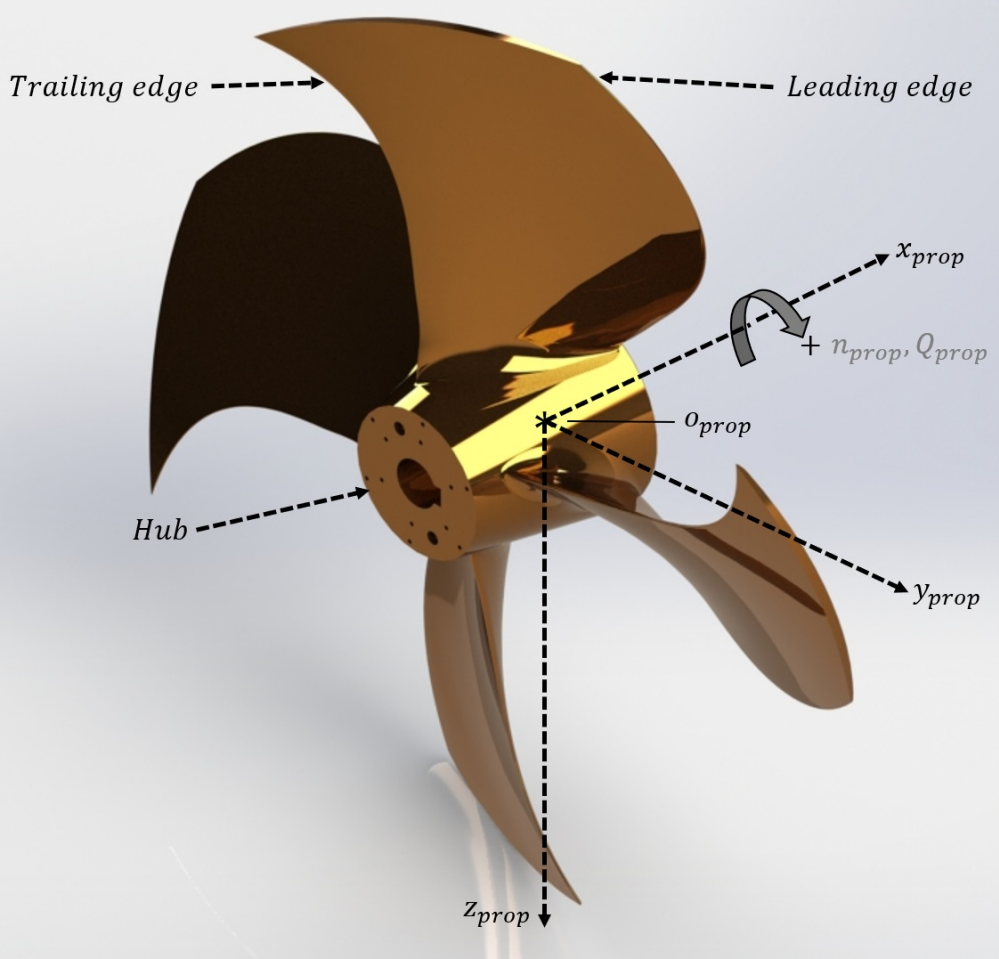

Figure 4.2: Propeller Coordinate System – Orthographic View

In the proposed 3 DOF MBD marine simulation platform, propeller calculations are limited to the x_{prop}–y_{prop} plane, and therefore thrust is only quantified in the x_{prop}-direction (T_{prop_x}), and in the y_{prop}-direction (T_{prop_y}) as shown in Figure 4.3.

The advance velocity, $V_{advance}$, is defined as the propeller's velocity relative to the water at the inlet of the propeller and is primarily dependant on the forward speed of the vessel. The angle $\alpha_{advance}$ defines the incidence angle of the flow at the inlet of the propeller and is

positive clockwise from the propeller's x_{prop}-axis. The propeller's speed or angular velocity, n_{prop}, is measured about the x_{prop}-axis, as is propeller torque, Q_{prop}.

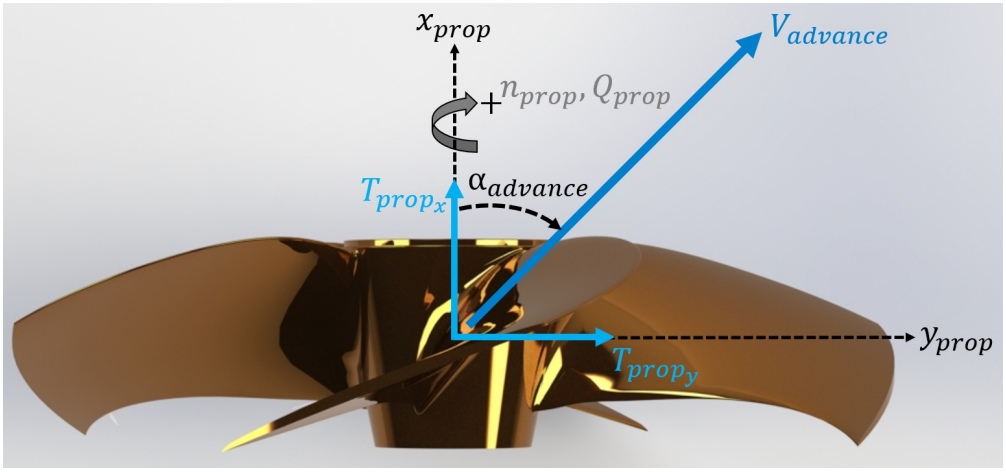

Figure 4.3: Propeller Coordinate System – Top View

In naval architecture it is customary to define a propeller's performance characteristics using several non-dimensional terms that are a product of the propeller's design geometry. The non-dimensional propeller terms found within this work are the advance coefficient, $J_{advance}$, thrust coefficient, K_T, and torque coefficient, K_Q.

The advance coefficient, $J_{advance}$, is defined as:

$$J_{advance} = \frac{V_{advance}}{\left(\frac{1}{2\pi} n_{prop}\right) D_{prop}} \tag{4.1}$$

where n_{prop} and D_{prop} are the angular velocity of the propeller and the diameter of the propeller respectively, and $V_{advance}$ is the aforementioned advance velocity.

The propeller axial and transverse thrust coefficients being K_{Tx} and K_{Ty} respectively, are defined as:

$$\begin{aligned} K_{Tx} &= \frac{T_{prop_x}}{\rho \left(\frac{1}{2\pi} n_{prop}\right)^2 D_{prop}^4} \\ K_{Ty} &= \frac{T_{prop_y}}{\rho \left(\frac{1}{2\pi} n_{prop}\right)^2 D_{prop}^4} \end{aligned} \tag{4.2}$$

where T_{prop_x} and T_{prop_y} are axial thrust and transverse thrust respectively, and ρ is the density of the fluid.

The propeller torque coefficient, K_Q, is defined as:

$$K_Q = \frac{Q_{prop}}{\rho \left(\frac{1}{2\pi} n_{prop}\right)^2 D_{prop}^5} \tag{4.3}$$

where Q_{prop} is propeller torque.

It is typical to find a propeller's axial thrust and torque coefficients plotted against the advance coefficient as shown in Figure 4.4. Note that the torque coefficient is scaled by a factor of 10 as is customary.

A general takeaway from this plot is that *i*) peak thrust is provided at the bollard pull condition (when the ship is stationary), and *ii*) if propeller speed is held constant, the provided thrust will decrease as the ship's speed and corresponding advance ratio, $J_{advance}$, increase. The resulting decrease in thrust force will eventually equalize with increasing hull resistance, leading to a quasi steady-state operating point (steady forward ship speed).

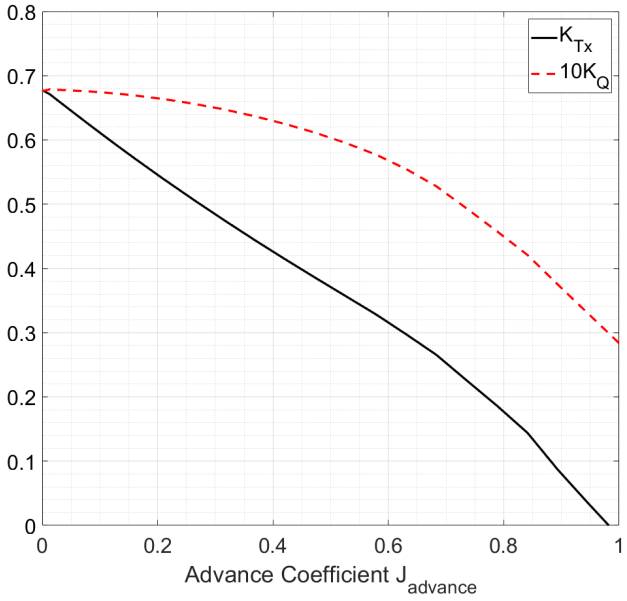

Figure 4.4: Axial Thrust (K_{Tx}) and Torque (K_Q) Coefficients vs. Advance Coefficient ($J_{advance}$)

As mentioned at the beginning of this chapter, the development of pre-computed hull and propeller hydrodynamic look-up tables are integral to the MBD marine simulation platform in this work. Propeller look-up tables are generated for *i*) axial thrust coefficient (K_{Tx}), *ii*) transverse thrust coefficient (K_{Ty}), and *iii*) torque coefficient (K_Q), each of which are defined as a function of *i*) advance coefficient ($J_{advance}$), and *ii*) the incidence angle of the flow into the propeller ($\alpha_{advance}$).

The flowchart in Figure 4.5 is a simplified representation of the propeller subsystem within the simulation platform and depicts how the integrated look-up tables are used to calculate propeller thrust and torque at each time-step. Upon review of the flowchart, it should be apparent that the propeller subsystem makes use of equation (4.1), and rearranged forms of equations (4.2) and (4.3) to solve for thrust and torque (T_{prop_x}, T_{prop_y}, Q_{prop}).

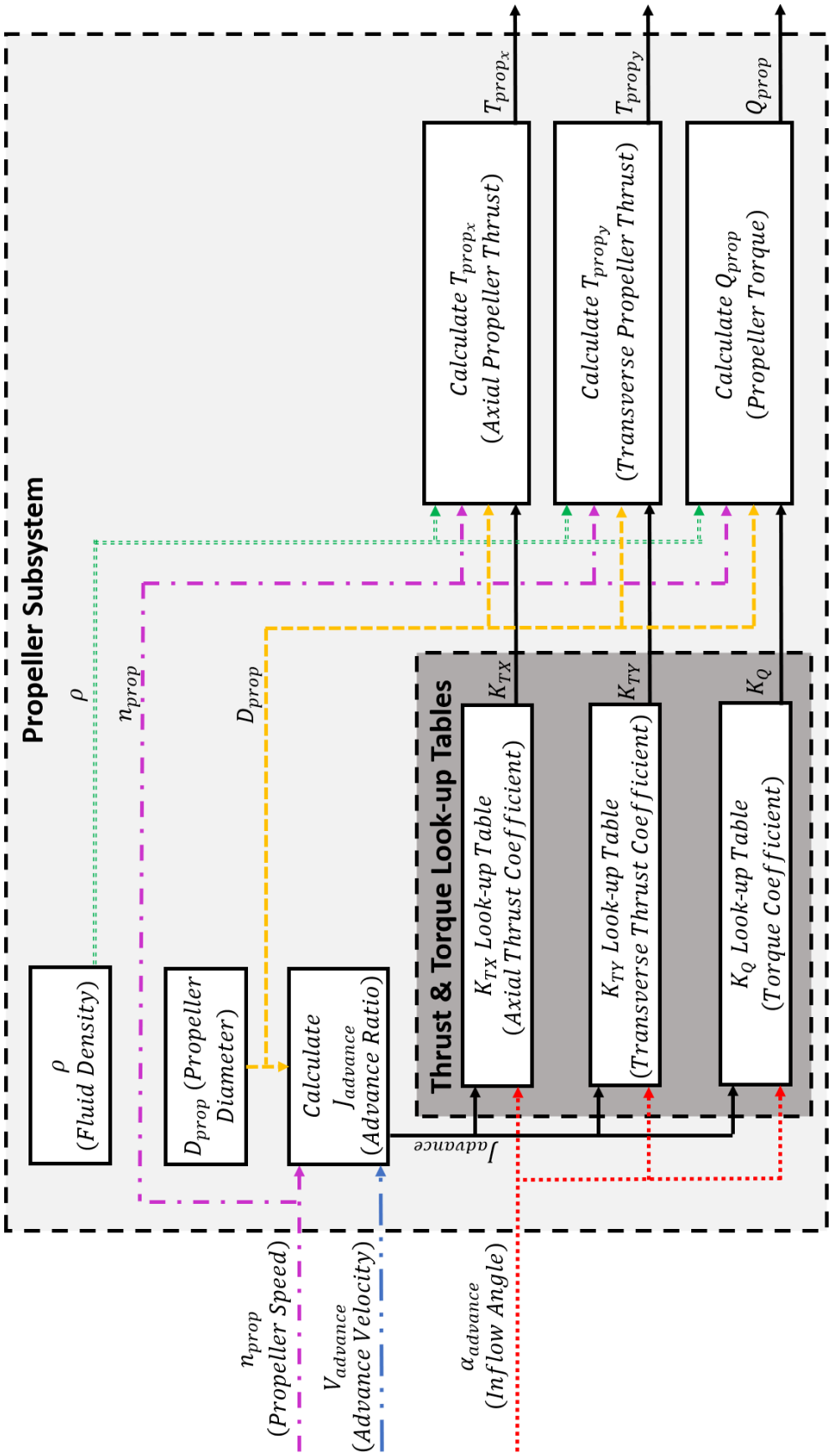

Figure 4.5: Integration of Propeller Subsystem Module Look-up Tables

The sequential procedure developed to generate propeller thrust and torque coefficient look-up tables was as follows:

1) Propeller 3D surface modelling
    a) Develop a 3D surface model of a propeller using computer-aided drafting (CAD) software
2) Propeller CFD analyses
    a) Import the generated 3D surface model into CFD software
    b) Run CFD analyses while methodically varying two parameters
        i. Inflow angle ($\alpha_{advance}$)
        ii. Advance ratio ($J_{advance}$)
3) Propeller thrust and torque look-up tables
    a) Extract CFD results to build out propeller look-up tables
        i. Thrust coefficients (K_{Tx}, K_{Ty})
        ii. Torque coefficient (K_Q)
    b) Incorporate the look-up tables into the propeller subsystem within the MBD marine simulation platform

The following sections provide a detailed description of the aforementioned procedure.

4.2.1 Propeller 3D Surface Model

The goal of modelling a propeller surface in 3D is to generate an accurate representation of propeller geometry that can in turn be analyzed with CFD to generate the propeller thrust and torque coefficient look-up tables. While there are specialized software packages for designing propellers such as PropCad by Hydrocomp, the approach in this work makes use of standard CAD commands that should be compatible with commonly available CAD software.

With recently built vessels, or vessels that are still in the design stage, a naval architect will often have developed a 3D surface model of the vessel's propeller that can be readily imported into CFD software with little to no modification. In the case of older ships that were designed prior to the widespread adoption of 3D modelling, or when propeller designs are the proprietary property of a third-party, a 3D model of the propeller is not always available. In

the case of the M.V. *Skeena Queen*, BC Ferries supplied a copy of the propeller's 2D design drawing as illustrated in Figure 4.6.

As the propeller's geometry was provided in a 2D format, a procedure was developed to translate the *Skeena Queen*'s 2D propeller drawing into a 3D surface which was largely based on the work of Andersen [8] who described a similar process and refers to Carlton [21] for necessary theory.

The most difficult and perhaps the most critical part of this procedure is to accurately recreate the complex surfaces of the propeller's blades. A single blade can be conceptualized as a series of aerofoil contours that are of infinitesimal thickness, stacked one on-top of another, curled concentrically around the propeller's axis of rotation. The 2D propeller design drawing defines a number of these aerofoil contours at selected radii which have been uncurled and flattened onto the drawing. A key objective of the process described herein is to translate these flattened aerofoil contours into 3D space as shown in Figure 4.7, all the while accounting for pitch, rake, skew and curl.

The work of Carlton [21] derives equations that define the Cartesian coordinates of an aerofoil contour's leading-edge, trailing-edge, and mid-chord points in respect to an origin that is located at the propeller's axis of rotation. The chord-line of an aerofoil section is defined as a line that runs between the leading-edge and trailing-edge of the aerofoil contour. The mid-chord point is hence located at the middle of the chord-line (Figure 4.7).

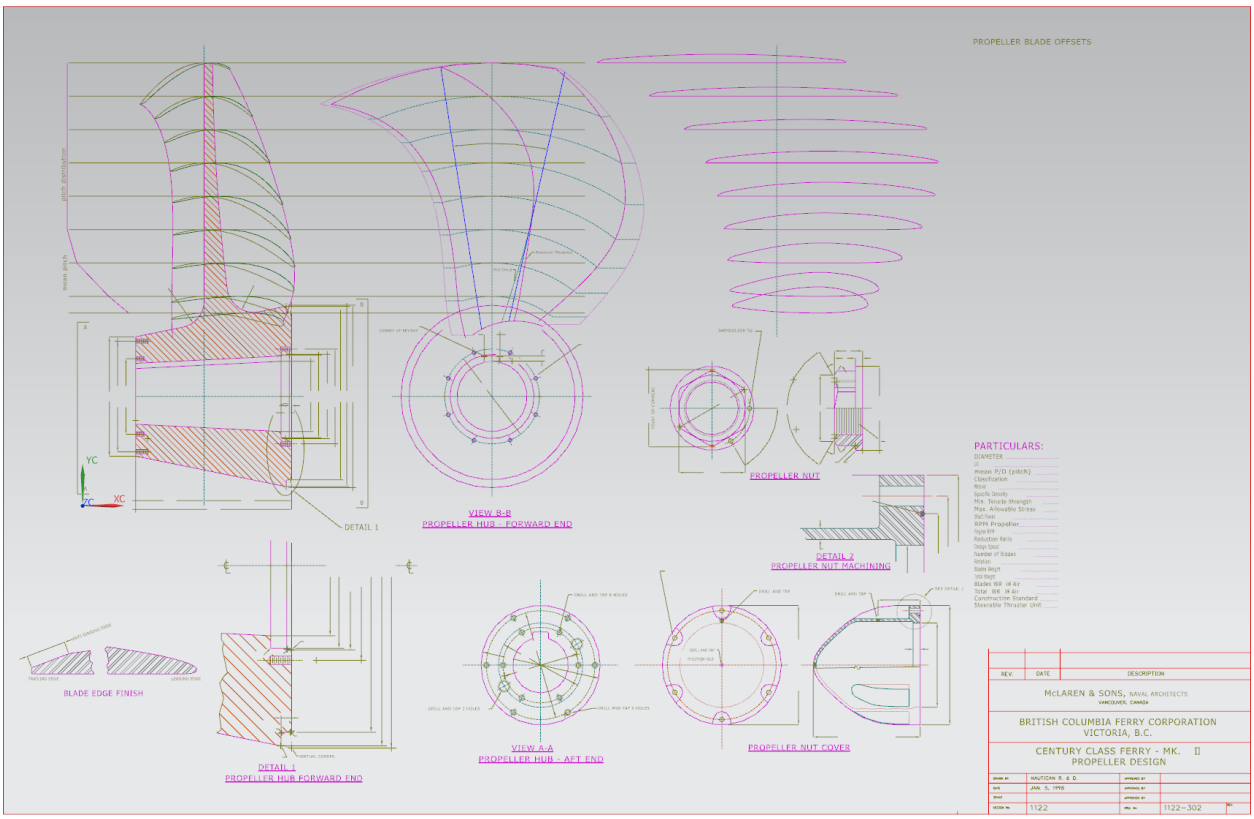

Figure 4.6: M.V. *Skeena Queen* Propeller Drawing (Dimensions Redacted)
Source: reproduced from Century Class Ferry – MK II Propeller Design [22]

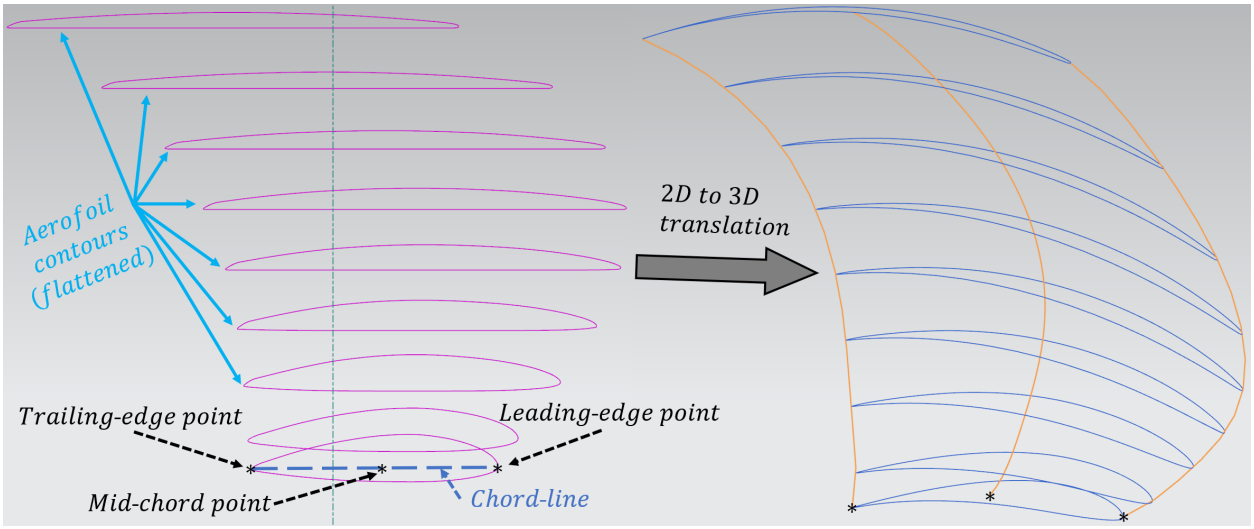

Figure 4.7: Translation of 2D Propeller Aerofoil Contours into 3D Space

Before presenting the equations that locate the aerofoil contours in 3D space, some terms relating to propeller geometry need to be introduced.

The angle, $\phi_{blade\,rotation}$, adjusts for the position of the propeller as it rotates about the propeller's axis of rotation. The position of the propeller is considered to be static during the development of the 3D propeller surface and is fixed at π due to user preference as shown in Figure 4.8.

The i-th skew angle, θ_{s_i}, is defined in the plane of y_{prop}-z_{prop} prior to the propeller rotation ($\phi_{blade\,rotation} = 0$), and is the angle between the z_{prop}-axis and a line drawn from the origin to the i-th mid-chord point (Figure 4.8).

To define the i-th rake distance, i_{G_i}, first consider a cross-section that slices through the middle of the propeller in the plane of x_{prop}-z_{prop} as shown in Figure 4.8. The rake distance is the lateral distance (measured in the x_{prop}-direction) between the z_{prop}-axis to the hind edge of the blade cross-section and is positive towards the rear face of the propeller hub. The M.V. *Skeena Queen*'s propeller is an example of the special case where the hind-edge of the cross-section is in-line with the z_{prop}-axis and therefore it has zero rake.

The i-th pitch angle, θ_{pp_i} is related to the angle of attack of the i-th aerofoil contour. To define the pitch angle, consider the i-th aerofoil contour to be lying on a cylinder of radius $r_{contour_i}$ that is concentric with the propeller's axis of rotation, the x_{prop}-axis. The cylinder is rotated about the propeller's axis of rotation until the mid-chord point of the i-th aerofoil contour is coincident with the plane of x_{prop}-z_{prop}. The cylinder is then unwrapped such that the mid-chord point is still coincident with the plane of x_{prop}-z_{prop} as shown in Figure 4.9. The pitch angle, θ_{pp_i}, can then be defined as the angle formed between the y_{prop}-axis and the chord-line of the i-th aerofoil section as shown in Figure 4.9. The pitch distance, p_{prop_i}, can be defined as the opposite side of the right-angle triangle formed by the unfurled cylinder circumference, $2\pi r_{contour_i}$, and the pitch angle, θ_{pp_i} (Figure 4.9).

Propeller drawings often provide pitch distance in place of pitch angle with relation between the two being:

$$\theta_{pp_i} = tan^{-1}\left(\frac{p_{prop_i}}{2\pi r_{contour_i}}\right) \tag{4.4}$$

where p_{prop_i} is the pitch distance of the i-th aerofoil contour at the given radius, $r_{contour_i}$.

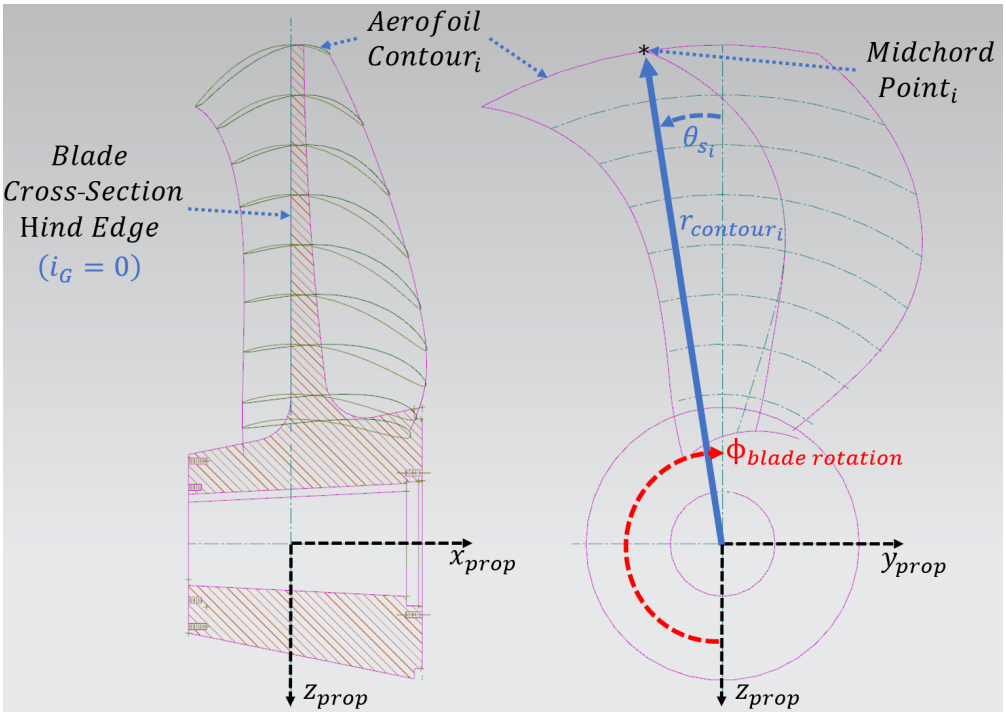

Figure 4.8: Propeller Rake (i_{G_i}), Skew (θ_{s_i}), and Rotation ($\phi_{blade\ rotation}$)
Source: adapted from Century Class Ferry – MK II Propeller Design [22]

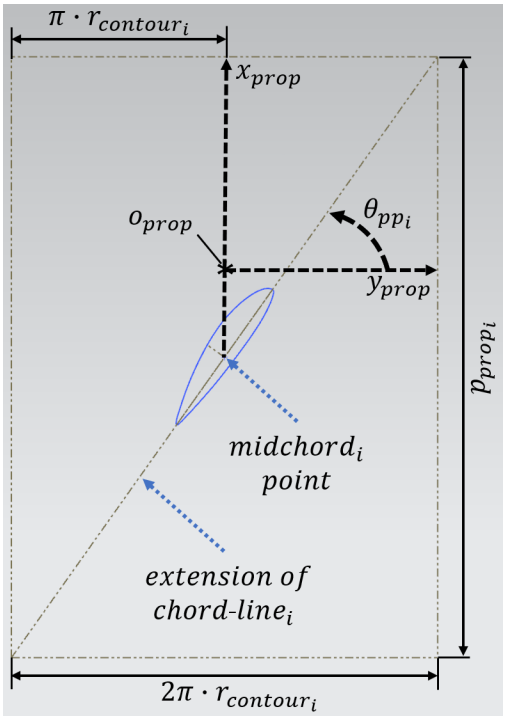

Figure 4.9: Propeller Pitch Angle (θ_{pp_i}) and Pitch Distance (p_{prop_i})

Now that the required propeller terms have been introduced, the equations that locate the aerofoil contours in 3D space can be presented. The location of the i-th aerofoil contour's mid-chord point is given by Carlton [21] as:

$$\begin{aligned} x_{c/2_i} &= -\left[i_{G_i} + r_{contour_i}\theta_{s_i}\tan(\theta_{pp_i})\right] \\ y_{c/2_i} &= -r_{contour_i}\sin\left[\phi_{blade\,rotation} - \theta_{s_i}\right] \\ z_{c/2_i} &= r_{contour_i}\cos\left[\phi_{blade\,rotation} - \theta_{s_i}\right] \end{aligned} \tag{4.5}$$

where $x_{c/2_i}$, $y_{c/2_i}$, $z_{c/2_i}$ give the Cartesian coordinates of the i-th aerofoil contour's mid-chord point that is defined at a given radius, $r_{contour_i}$, from the propeller's axis of rotation.

Similarly, Carlton [21] defines the coordinates of the i-th aerofoil contour's leading-edge point with:

$$\begin{aligned} x_{LE_i} &= -\left[i_{G_i} + r_{contour_i}\theta_{s_i}\tan(\theta_{pp_i})\right] + \frac{c_{chord_i}}{2}\sin(\theta_{pp_i}) \\ y_{LE_i} &= -r_{contour_i}\sin\left[\phi_{blade\,rotation} - \theta_{s_i} + \frac{90c_{chord_i}\cos(\theta_{pp_i})}{\pi r}\right] \\ z_{LE_i} &= r_{contour_i}\cos\left[\phi_{blade\,rotation} - \theta_{s_i} + \frac{90c_{chord_i}\cos(\theta_{pp_i})}{\pi r}\right] \end{aligned} \tag{4.6}$$

where x_{LE_i}, y_{LE_i}, z_{LE_i} give the coordinates of the i-th aerofoil contour's leading-edge point, and c_{chord_i} is the length of the chord-line of the given aerofoil contour.

Finally, Carlton [21] defines the coordinates of the i-th aerofoil contour's trailing-edge point with:

$$\begin{aligned} x_{TE_i} &= -\left[i_{G_i} + r_{contour_i}\theta_{s_i}\tan(\theta_{pp_i})\right] - \frac{c_{chord_i}}{2}\sin(\theta_{pp_i}) \\ y_{TE_i} &= -r_{contour_i}\sin\left[\phi_{blade\,rotation} - \theta_{s_i} - \frac{90c_{chord_i}\cos(\theta_{pp_i})}{\pi r}\right] \\ z_{TE_i} &= r_{contour_i}\cos\left[\phi_{blade\,rotation} - \theta_{s_i} - \frac{90c_{chord_i}\cos(\theta_{pp_i})}{\pi r}\right] \end{aligned} \tag{4.7}$$

where x_{TE_i}, y_{TE_i}, z_{TE_i} give the coordinates of the i-th aerofoil contour's trailing-edge point.

The 2D propeller drawing provided by BC Ferries contained all of the necessary information for parameterizing equation groups (4.5) to (4.7). The mid-chord, leading-edge, and trailing-edge points were generated in 3D space and then fit with curves to provide an outline of the blade as shown in Figure 4.10.

In order to prepare for the later step of wrapping the aerofoil contours about the propeller's axis of rotation, a series of cylindrical surfaces were generated concentric with the propeller's axis of rotation and coincident with the mid-chord points as shown in Figure 4.11.

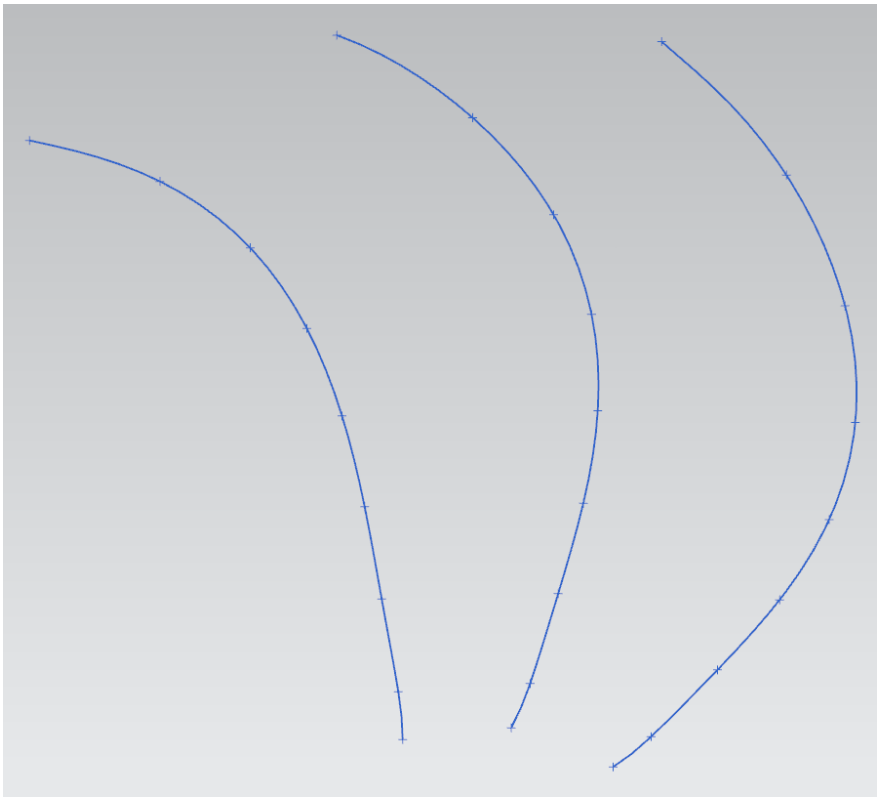

Figure 4.10: Propeller Mid-chord, Leading-edge and Trailing Edge Points

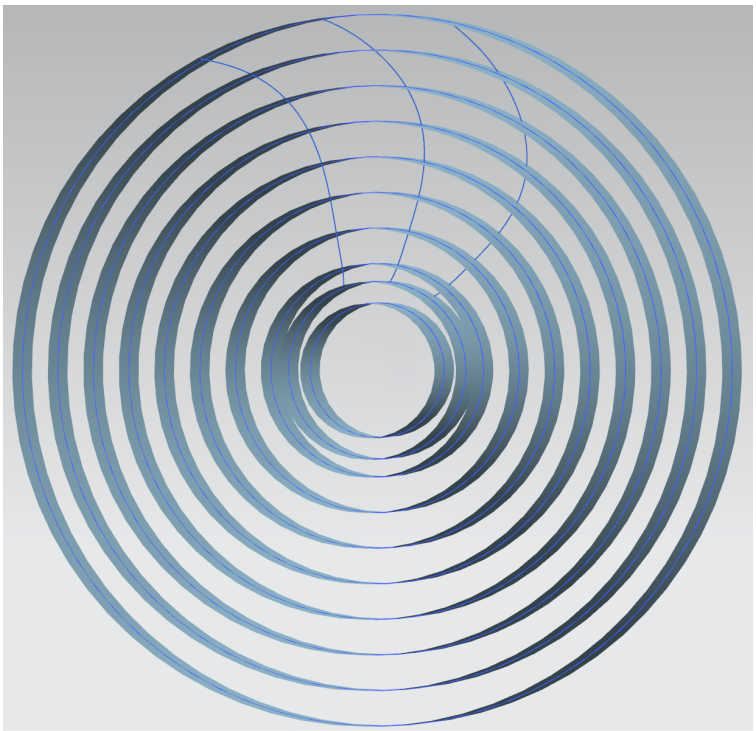

Figure 4.11: Cylindrical Surfaces at Key Propeller Radii

A corresponding series of planes were then added tangent to each of the cylindrical surfaces and coincident with the mid-chord points as shown in Figure 4.12.

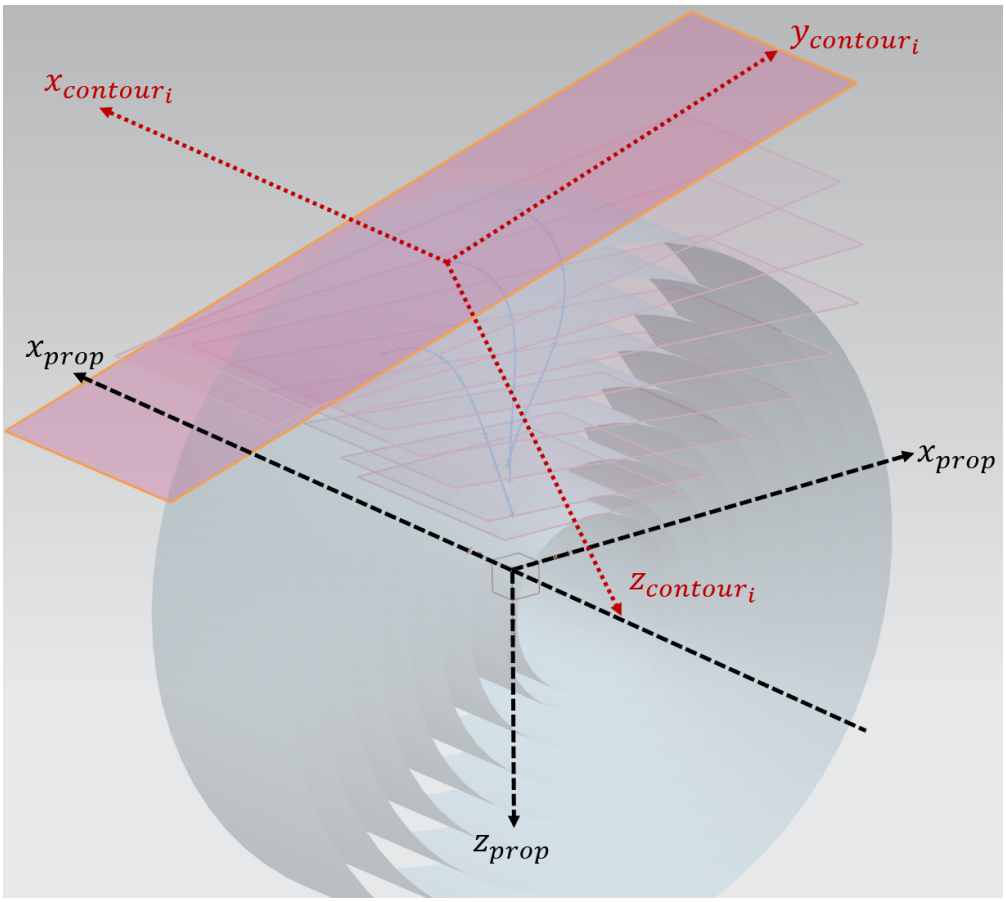

Figure 4.12: Tangent Planes at Key Propeller Radii

The next step in the procedure was to initiate a sketch on each of the planes. The origin of each sketch was made coincident with the corresponding mid-chord point that was generated from with the equations in Cartlon [21]. The sketch coordinate system was oriented such that the x-axis, $x_{contour_i}$, lay parallel to x_{prop}, the y-axis, $y_{contour_i}$ lay parallel to the plane of y_{prop}-z_{prop}. The z-axis, $z_{contour_i}$, was orthogonal to x_{prop} as shown in Figure 4.12.

After importing the 2D propeller drawing into the CAD software and scaling it to size, each 2D flattened aerofoil contour was extracted and transferred to a corresponding sketch. The mid-chord points of the aerofoil contours were placed coincident with the mid-chord points generated by the equations in Carlton [21] and then rotated to account for pitch angle as shown in Figure 4.13.

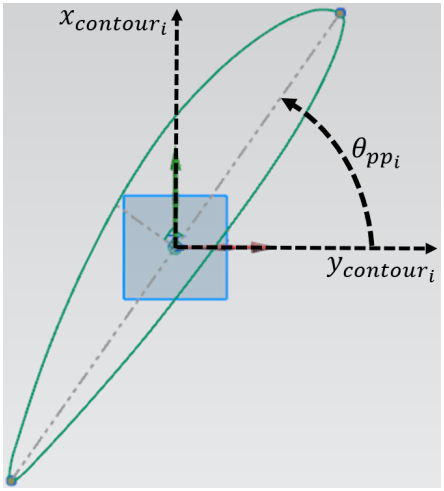

Figure 4.13: Aerofoil Contour Pitch Angle (θ_{pp_i})

Figure 4.14 shows the flat aerofoil contours after they have been correctly positioned.

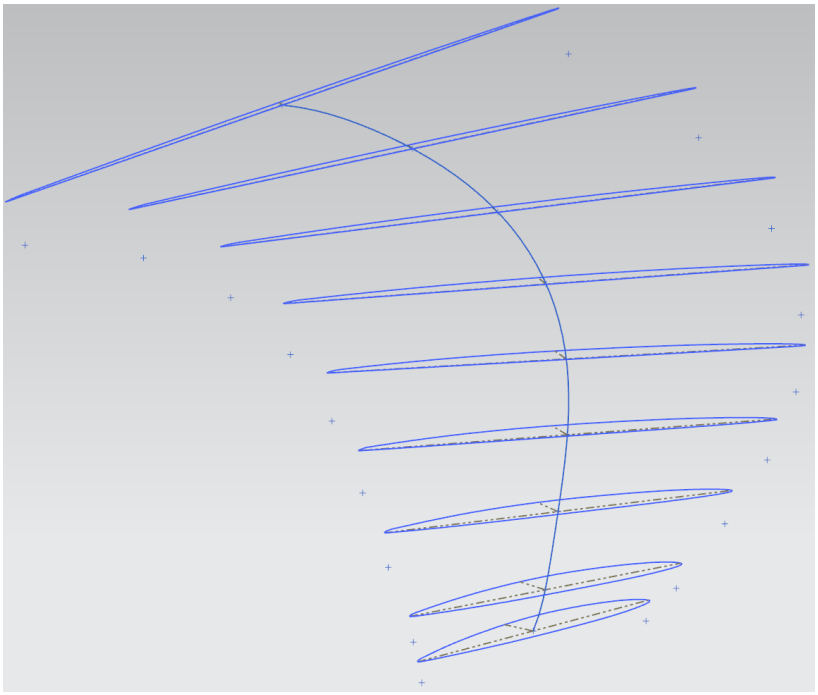

Figure 4.14: Flattened Propeller Aerofoil Contours

The aerofoil contours were then curled over their corresponding cylindrical surfaces using the software's "wrap surface" command as shown in Figure 4.15. The wrapping process can be thought of as analogous to the application of a decal over a curved surface where the aerofoil "decal" is curled without the possibility of stretching or wrinkling.

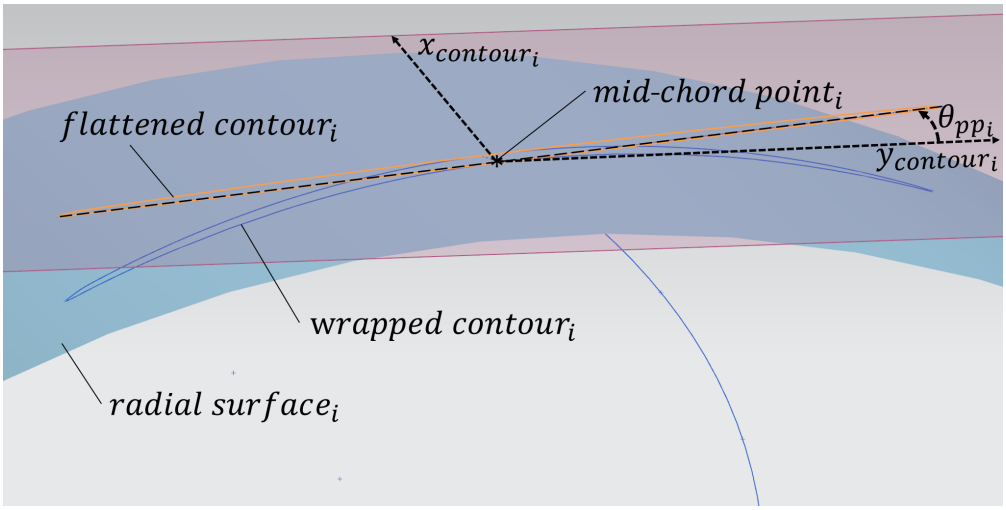

Figure 4.15: Propeller Aerofoil Contour Wrapping Process

Figure 4.16 shows all of the propeller blade contours after they have been wrapped about their respective cylindrical surfaces. The leading-edges and trailing-edges of the wrapped aerofoil contours coincided almost perfectly with the *independently* created leading-edge and trailing-edge points generated from the equations in Carlton [21]. Small differences in position of less than $5.0 \times 10^{-5} mm$ were attributed to errors arising from numerical precision.

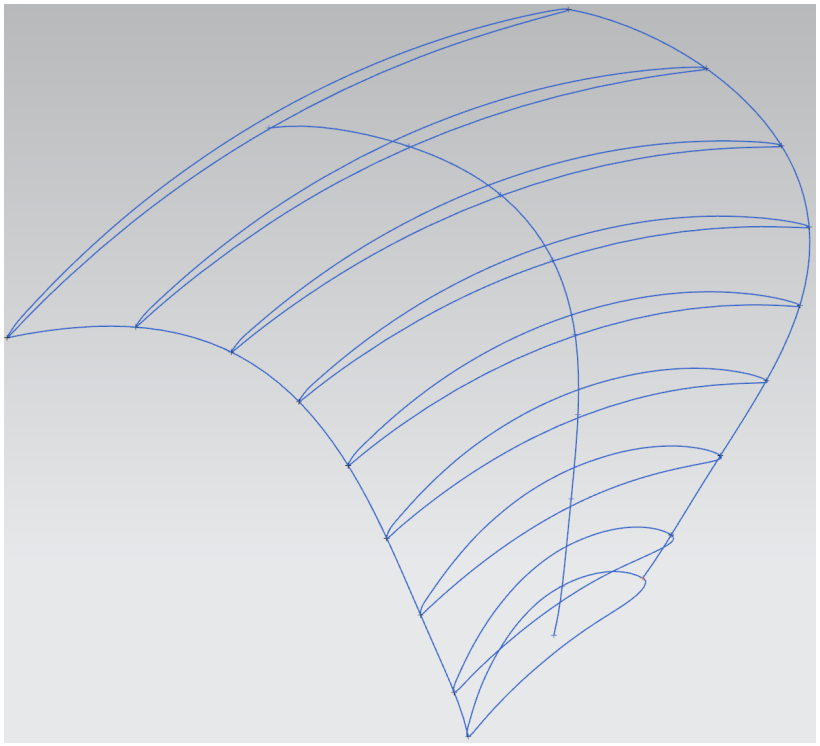

Figure 4.16: Wrapped Propeller Aerofoil Contours

The wrapped aerofoil contours became the framework for forming the blade's surface. A surface was fit over the aerofoil contours by allowing the software to determine the best fit as shown in Figure 4.17. It should be noted that a more accurate surface fit was later achieved through the use of guide curves, but unfortunately this was not implemented on the surface model that was analyzed in CFD to generate the thrust and torque look-up tables.

The hub was then revolved as a solid and merged with the blade as shown in Figure 4.18. Finally, the completed blade was patterned around the propeller's axis of rotation to reproduce the required number of additional blades.

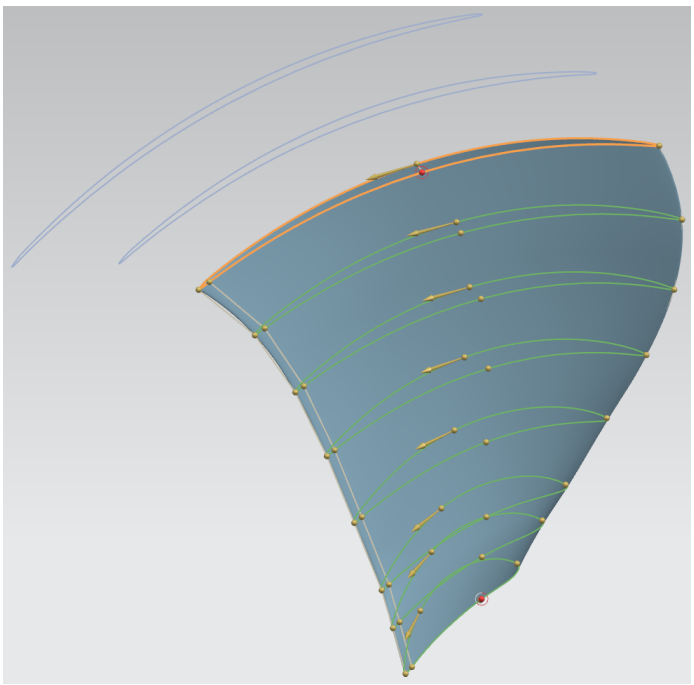

Figure 4.17: Propeller Blade Surfacing

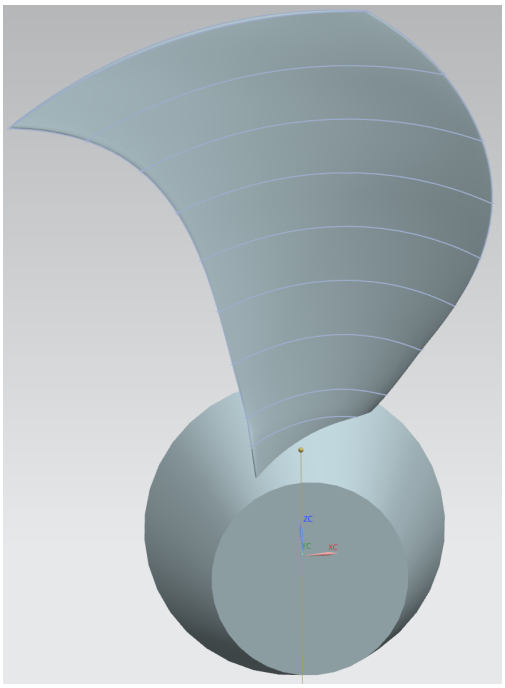

Figure 4.18: Blade Merged to Hub

The hub's bore and several tapped hole features were added to facilitate a mass comparison between the recreated 3D propeller model and the weight listed on the propeller's drawing as shown in Figure 4.19. Assigning the density of the brass alloy listed on the drawing, the 3D model had a calculated mass of approximately 1.64% less than the mass listed on the drawing, indicating a good, but not perfect reproduction.

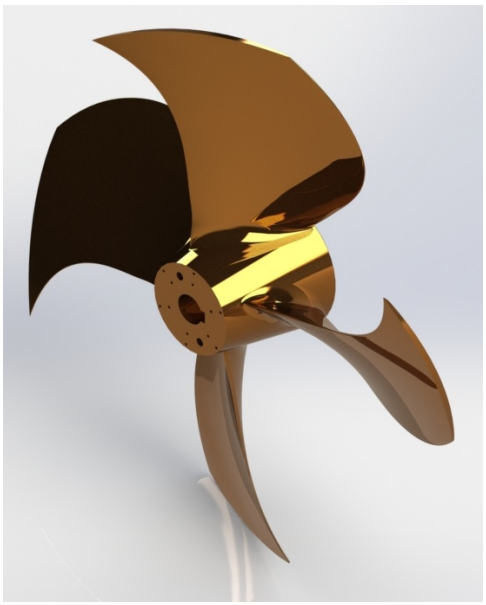

Figure 4.19: Completed Propeller

Figure 4.20: Azimuth Thruster Assembly

After mass calculations, the bore and tapped hole features were suppressed prior to the CFD analyses.

Azimuth Tower and Propeller Duct Modelling

The azimuth tower and propeller duct geometries shown in Figure 4.20 were generated from an additional *Skeena Queen* shafting arrangement drawing provided by BC Ferries as shown in Figure 4.21. The azimuth tower and duct dimensions on this supplementary drawing were only approximations of the actual geometries for the purpose of communicating the general layout. With this in mind, the resulting azimuth tower and duct CAD surfaces are not considered to be highly accurate.

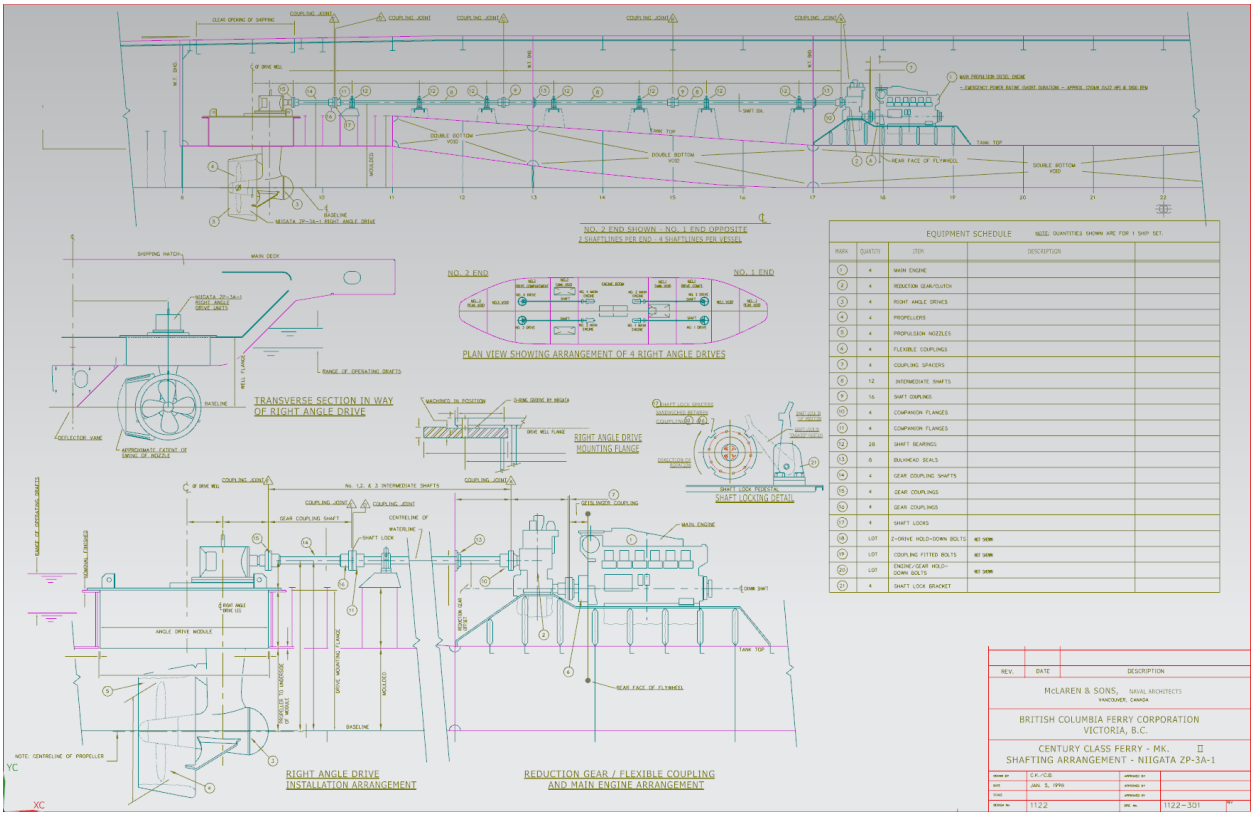

Figure 4.21: M.V. *Skeena Queen* Shaft Arrangement Drawing (Dimensions Redacted)
Source: reproduced from Century Class Ferry – MK II Shafting Arrangement [23]

Considering that the azimuth tower and propeller duct surfaces were generated using relatively trivial CAD commands, their development processes are not described in further detail.

Once the azimuth tower and propeller duct models were developed, they were assembled with the propeller for CFD analyses.

4.2.2 Propeller CFD Analyses

To ensure the robustness and accuracy of the propeller module within the MBD simulation, the propeller thrust and torque coefficient look-up tables were constructed to encompass the entire operating envelope of the propeller during a simulated voyage.

To accomplish this, several propeller CFD analyses were run by Rahimpour [24] at varying advance ratios ($J_{advance}$) and flow incidence angles ($\alpha_{advance}$). In each subsequent CFD case, propeller speed was held constant at the propeller's design speed while the advance velocity ($V_{advance}$) was incrementally increased.

After running through all advance ratios at a single incidence angle, the flow incidence

angle was incremented by 15° and the process was repeated at the new incidence angle. This process was repeated for several angles beginning with the propeller generating thrust in the same direction as advance velocity ($\alpha_{advance} = 0°$) and ending with the propeller generating thrust in the opposing direction of advance velocity ($\alpha_{advance} = 180°$) as illustrated in Figure 4.22.

The results for negative flow incidence angles (0° to −180°) were assumed to mirror the results of the positive incident angles (0° to 180°) and therefore the cases for negative incident angles were not run. It should be noted however that this assumption neglects the imbalances introduced by the rotational direction of the propeller and several works have found non-negligible differences in torque and thrust at positive vs. negative incidence angles [25–27]. Future implementations can be improved by running CFD cases for both positive and negative incidence angles.

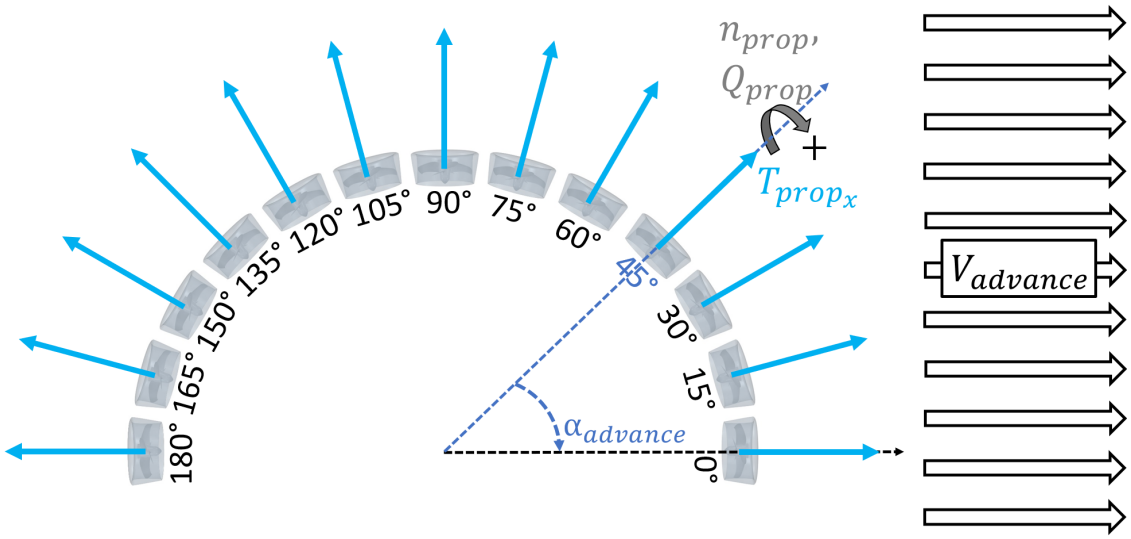

Figure 4.22: Propeller CFD Incidence Angle Schematic

As is common in industry, the propeller CFD analyses were "open-water" analyses, meaning that the geometry of the ship hull was absent throughout the process. The open-water approach requires a correction for "wake fraction" which is discussed in Section 4.2.4. Prior to running these analyses, Rahimpour simplified the propeller geometry by removing the azimuth tower and duct struts as shown in Figure 4.23. The frictional resistance of the removed geometry was later accounted for by augmenting hull resistance with empirical appendage resistance, but it is unclear how removing the tower assembly and duct struts affected the computed thrust and torque CFD results.

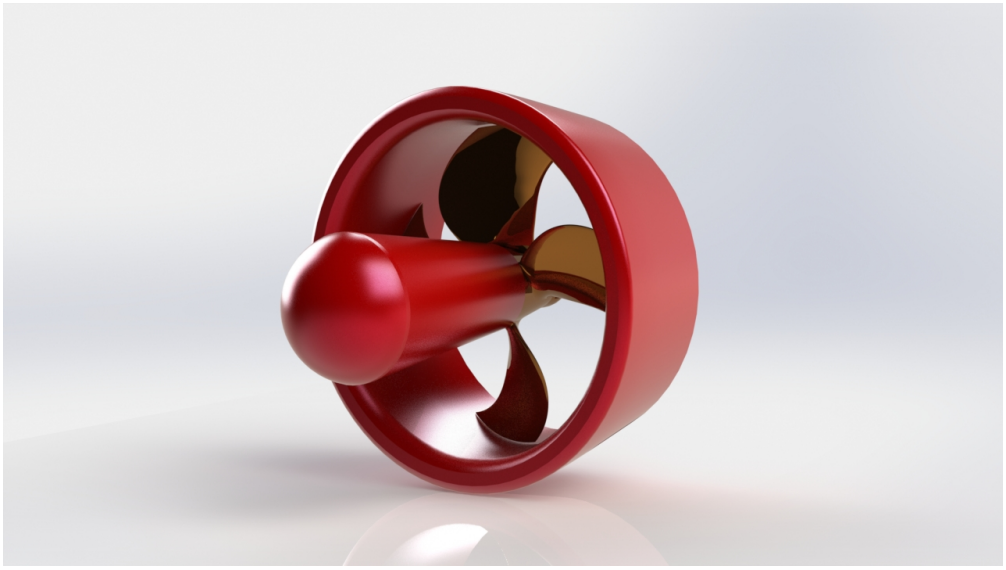

Figure 4.23: Propeller CFD Assembly

Some basic parameters used in the CFD analyses are provided in Table 4.1.

Table 4.1: Propeller CFD Case Parameters
Source: Rahimpour [24]

Parameter	**Value(s)**
Propeller speed $[rad/s]$	32.36
Fluid incidence angle [°]	0, 15, 30, 45, 60, 75, 90, 105, 120, 135, 150, 165, 180
Advance velocity $[m/s]$	0.129, 0.257, 0.386, 0.514, 0.772, 1.029, 1.286, 1.543, 2.058, 2.572, 3.087, 3.601, 4.116, 4.630, 5.144, 5.659, 6.173, 6.688, 7.202, 7.717, 8.231, 8.746, 9.260, 9.774, 10.289

After each CFD case, the software calculated the sum of the forces acting on the propeller assembly's surfaces, *including* the drag forces acting on the duct. The sum of the forces were output with respect to the propeller's coordinate system and decomposed into T_{prop_x}, and T_{prop_y} components.

Similarly, to determine propeller torque, Q_{prop}, the CFD software calculated the sum of the moments acting on the propeller's surfaces about the propeller's axis of rotation, this time *excluding* the forces acting on the duct.

The absence of empirical thrust and torque measurements for the *Skeena Queen*'s propeller prohibited a direct validation of the CFD results, but Rahimpour and Andersen had previously used the same CFD technique on a Kaplan Ka4-70 propeller with 19A duct and produced results that closely matched published empirical data [8].

4.2.3 Propeller Thrust and Torque Look-up Tables

After running the all of the propeller CFD cases, Rahimpour [24] extracted the results for axial thrust coefficient (K_{Tx}) and torque coefficient (K_Q) as a function of advance coefficient ($J_{advance}$) and inflow angle ($\alpha_{advance}$).

While these parameters were initially considered to be sufficient, early results from the MBD marine simulation revealed significant error between the *Skeena Queen*'s simulated motion and the recorded GPS motion. An investigation into the source(s) of error led to the works of Piaggio et al. [28], Islam et al. [25], and Xingrong and Yuejin [27]. These researchers describe experiments with podded propulsors and find that propellers generate significant transverse thrust (T_{prop_y}) while operating in oblique flow ($|\alpha_{advance}| > 0$).

This finding is particularly relevant for azimuth thrusters and podded propulsors which are frequently rotated relative to incoming flow during turning manoeuvres. As a result of this investigation, the transverse thrust coefficient (K_{Ty}) was retroactively extracted from the stored CFD data so that transverse thrust (T_{prop_y}) could be introduced into the propeller subsystem for improved accuracy.

The CFD results for axial thrust coefficient (K_{Tx}), transverse thrust coefficient (K_{Ty}), and torque coefficient (K_Q) vs. advance coefficient ($J_{advance}$) are provided in Figures 4.24–4.26.

It can be seen that many of the thrust coefficient curves with flow incidence angles of 90° and greater (dashed lines) are generally more chaotic than the thrust coefficient curves at flow incidence angles of 75° and less (solid lines). Further study is needed to assess the root cause(s) of this observation, but one possible explanation is that the CFD analyses were less accurate when modelling the more complex flow at high incident angles while using the same mesh size and time-step initially determined at 0°.

The axial thrust and transverse thrust coefficients are plotted using the same scale to facilitate visual comparison. For inflow angles between 0° to 60° it can be seen that the axial thrust coefficient (K_{Tx}) decreases as advance ratio increases, while conversely the absolute value of the transverse thrust coefficient (K_{Ty}) increases as advance ratio increases. A takeaway from this observation is that transverse thrust becomes more significant while manoeuvring at higher advance ratios.

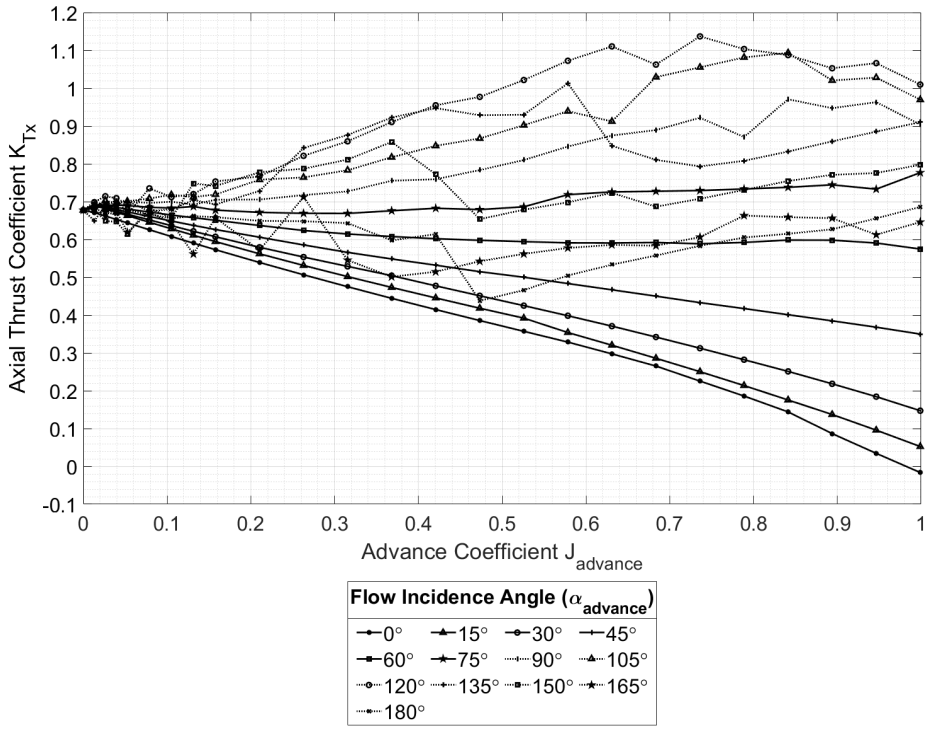

Figure 4.24: Axial Thrust Coefficient vs. Advance Coefficient Results

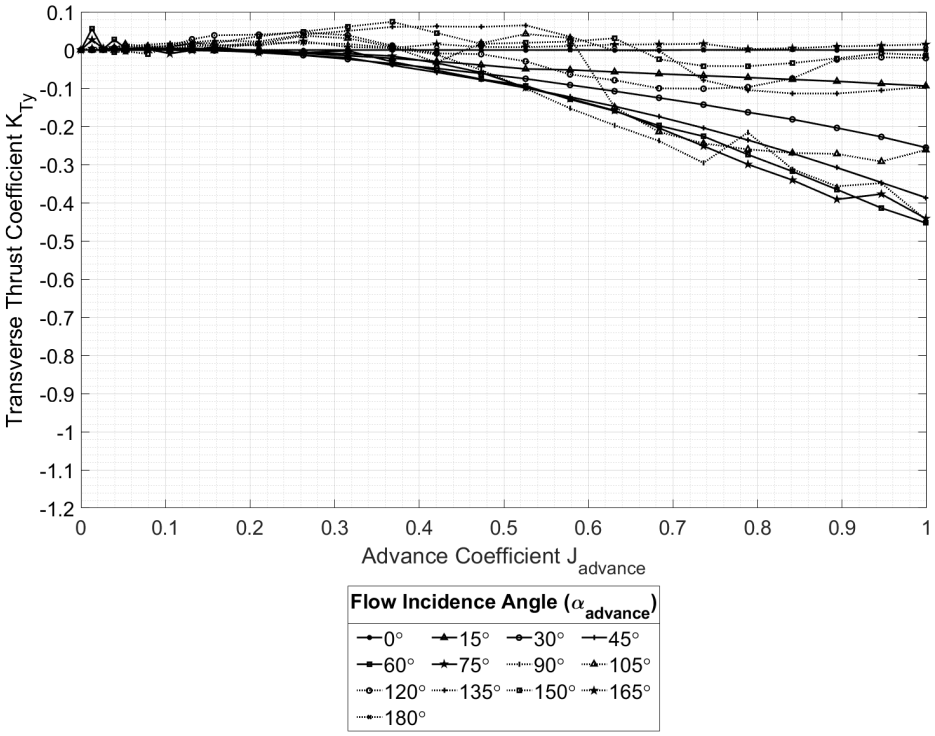

Figure 4.25: Transverse Thrust Coefficient vs. Advance Coefficient Results

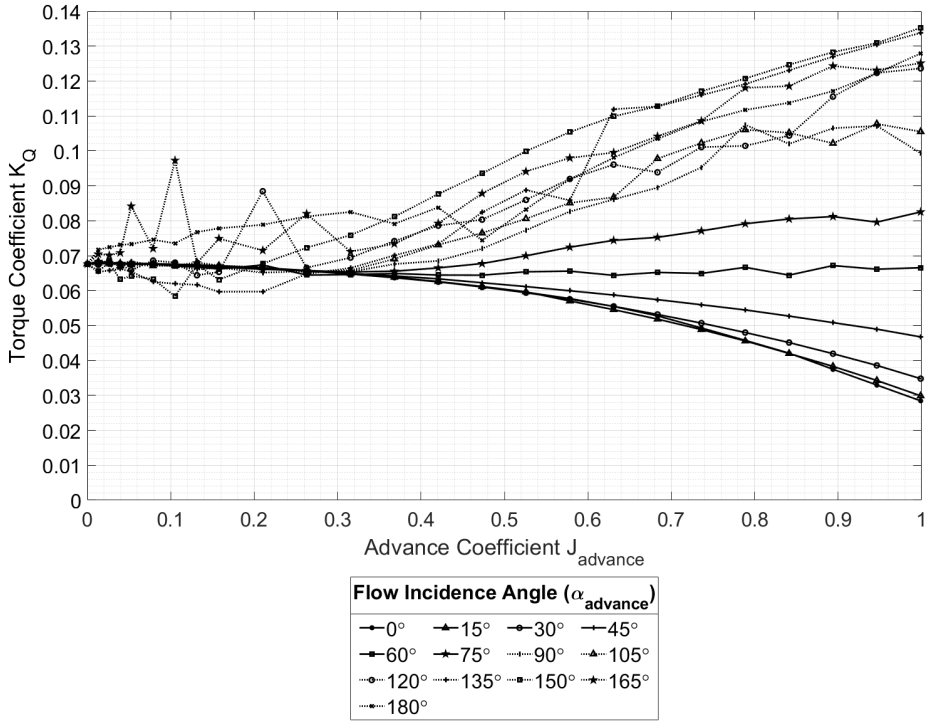

Figure 4.26: Torque Coefficient vs. Advance Coefficient Results

The axial thrust coefficient (K_{Tx}), transverse thrust coefficient (K_{Ty}), and torque coefficient (K_Q) can also be represented as surfaces as shown in Figures 4.27–4.29. It is these surfaces that were incorporated into the propeller subsystem of the MBD marine simulation platform, and as the *Skeena Queen*'s four identical propellers are all right-handed models, they all share the same look-up surfaces.

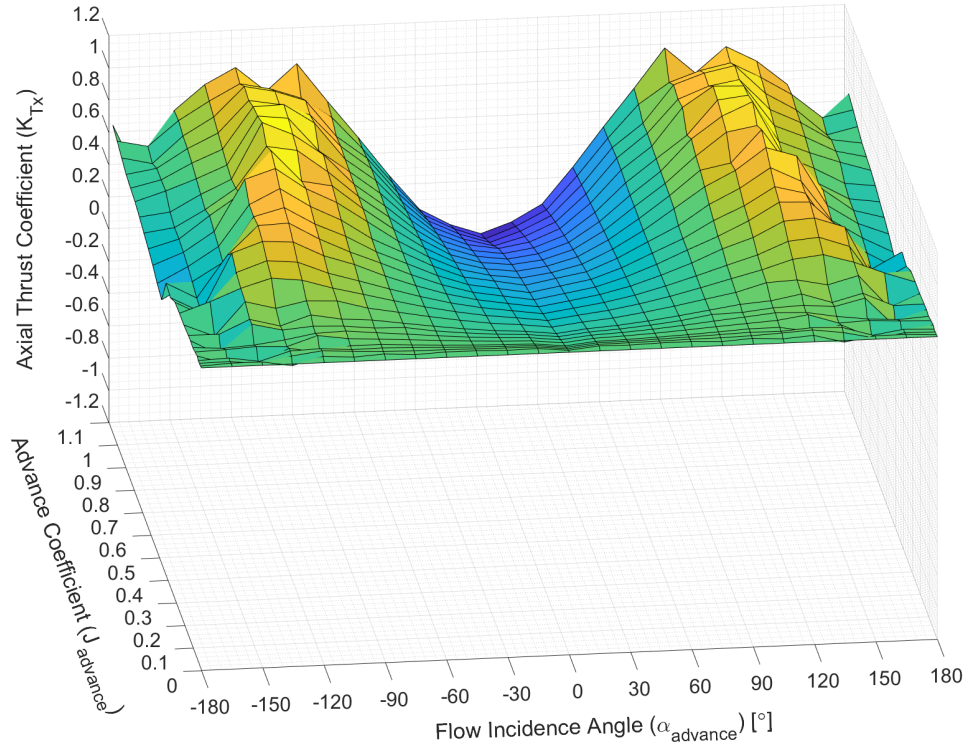

Figure 4.27: Axial Thrust Coefficient Look-up Surface K_{Tx}

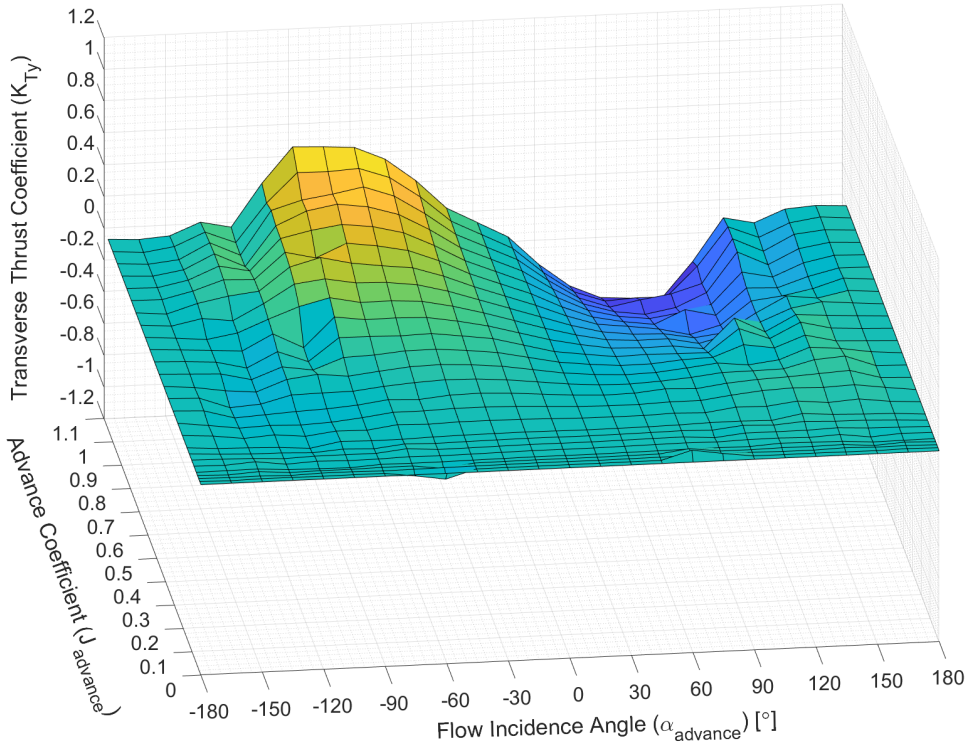

Figure 4.28: Transverse Thrust Coefficient Look-up Surface K_{Ty}

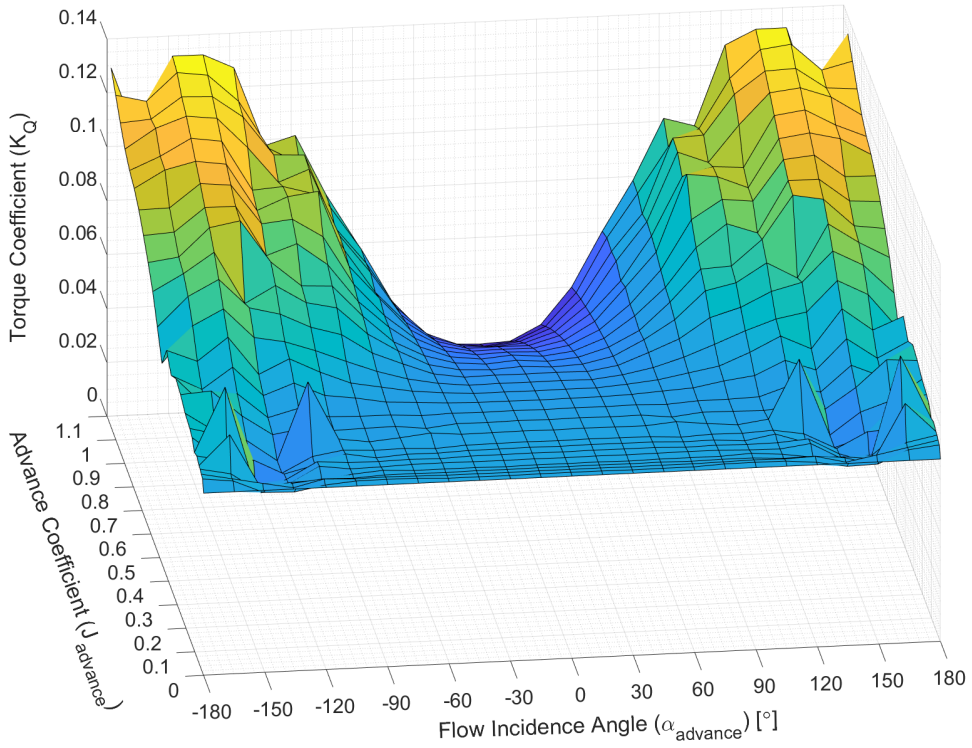

Figure 4.29: Torque Coefficient Look-up Surface K_Q

4.2.4 Propeller Thrust and Torque Correction Factors

Once the thrust and torque look-up surfaces had been obtained, a series of correction factors were worked into the simulation structure to account for effects not captured with CFD.

Wake Fraction

As previously mentioned, the propeller CFD analyses were open-water analyses, meaning that the geometry of the ship hull was absent throughout the process. It is important to make this distinction because while under-way, the presence of the ship hull alters the velocity of the flow into the propeller ($V_{advance}$) [21, 29, 30], which in turn alters the advance ratio ($J_{advance}$) and resulting thrust and torque (T_{prop_x}, T_{prop_y}, Q_{prop}). This change in velocity is accounted for with the introduction of the so-called wake fraction. The wake fractions at the fore and aft propellers are defined as:

$$\begin{aligned} W_F &= 1 - \frac{V_{advance_{fore}}}{u_r} \\ W_A &= 1 - \frac{V_{advance_{aft}}}{u_r} \end{aligned} \tag{4.8}$$

where u_r is the relative forward speed of the ship and $V_{advance_{fore}}$ and $V_{advance_{aft}}$ are the advance velocities at the fore and aft propellers respectively. W_F and W_A are the wake fractions at the fore and aft propellers.

Many references provide empirical estimations for wake fraction [21,30], but in this work, the fore and aft wake fractions were estimated during hull CFD analyses discussed later in Section 4.3.2. This was accomplished by strategically placing virtual velocity probes that measured the inflow velocity at the *Skeena Queen*'s propeller locations ($V_{advance_{fore}}$ and $V_{advance_{aft}}$) to facilitate a comparison against the ship's relative velocity (u_r).

As the CFD results for wake fraction were velocity dependant, the wake fractions are incorporated into the MBD marine simulation platform as look-up tables which output wake fraction as a function of ship velocity as shown in Figure 4.30. These look-up tables are used to adjust the advance velocities seen by the fore and aft propellers during simulation with a re-arranged form of equation group (4.8).

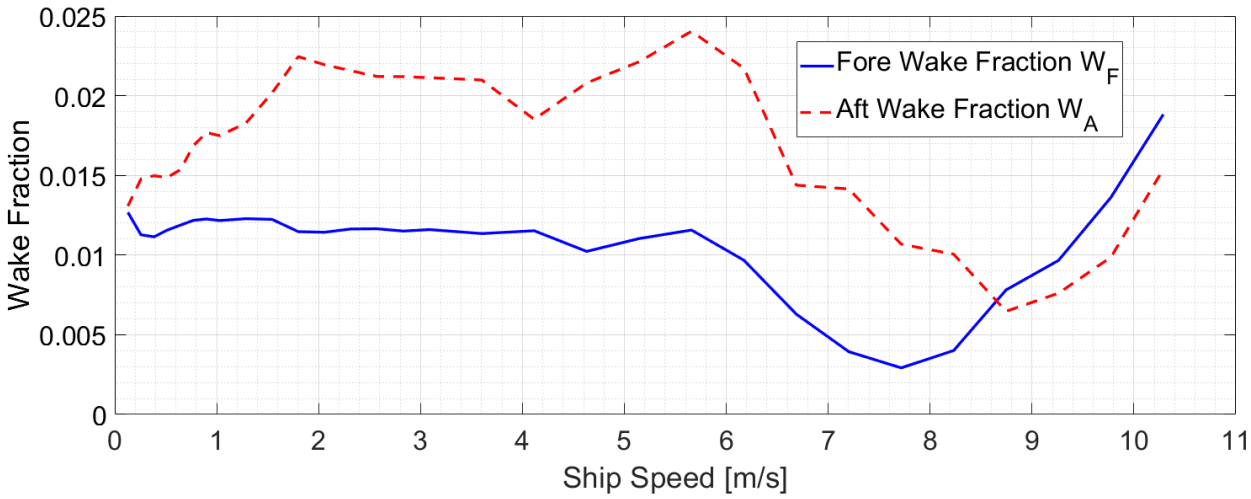

Figure 4.30: Fore and Aft Propeller Wake Fraction vs. Speed

Thrust Deduction Factor

See *resistance augmentation factor* in Section 4.3.6.

Propeller Fouling Factors

As the propeller CFD analyses were run for hydraulically smooth surfaces, they did not account for the effects of surface roughness and fouling due to marine growth.

Owen et al. [31] used CFD to estimate correction factors for 6 stages of fouling beginning with an as-applied anti-fouling coating and progressing up to heavy calcareous fouling.

The fouling correction factor for propeller thrust is implemented as follows:

$$\begin{aligned} T^F_{prop_x} &= T_{prop_x} \cdot K_{thrust_{fouling}} \\ T^F_{prop_y} &= T_{prop_y} \cdot K_{thrust_{fouling}} \end{aligned} \tag{4.9}$$

where $T^F_{prop_x}$ and $T^F_{prop_y}$ are the axial and transverse thrusts obtained after correcting for fouling, and $K_{thrust_{fouling}}$ is the fouling correction factor for propeller thrust.

Similarly, the fouling correction factor for propeller torque is applied as follows:

$$Q^F_{prop} = Q_{prop} \cdot K_{torque_{fouling}} \tag{4.10}$$

where Q^F_{prop} is the propeller torque after correcting for fouling, and $K_{torque_{fouling}}$ is the fouling correction factor for propeller torque.

Owen et al. [31] give the thrust and torque correction factors as a function of advance ratio as shown in Table 4.2. The "deteriorated coating/light slime" condition was assumed when simulating the *Skeena Queen*.

Table 4.2: Propeller Fouling Factors for Deteriorated Coating/Light Slime Condition
Source: Owen et. al. [31]

Advance ratio	**Thrust correction factor**	**Torque correction factor**
$J_{advance} <= 0.6$	$K_{thrust_{fouling}} = 0.9683$	$K_{torque_{fouling}} = 1.0074$
$J_{advance} = 0.8$	$K_{thrust_{fouling}} = 0.9575$	$K_{torque_{fouling}} = 1.0066$
$J_{advance} = 1.0$	$K_{thrust_{fouling}} = 0.9392$	$K_{torque_{fouling}} = 1.0068$
$J_{advance} >= 1.2$	$K_{thrust_{fouling}} = 0.9000$	$K_{torque_{fouling}} = 1.0036$

The propeller fouling correction factors were incorporated into the simulation as look-up tables which output $K_{thrust_{fouling}}$ and $K_{torque_{fouling}}$ as a function of $J_{advance}$ as shown in Figures 4.31–4.32.

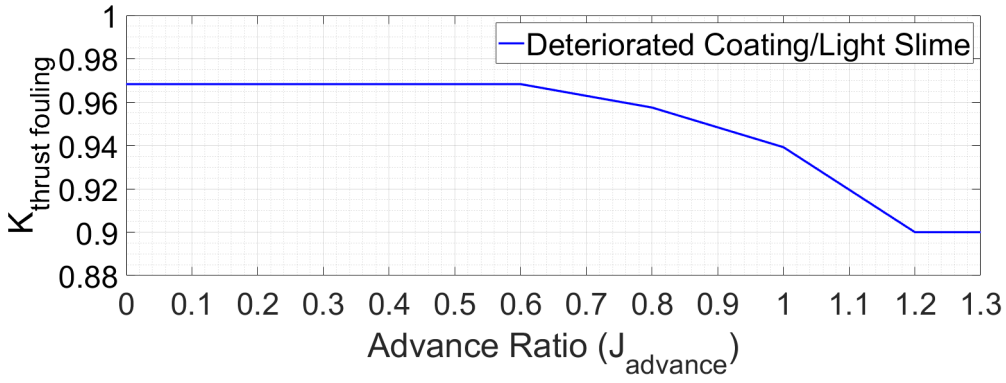

Figure 4.31: Propeller Fouling Thrust Correction Factor Look-up Table

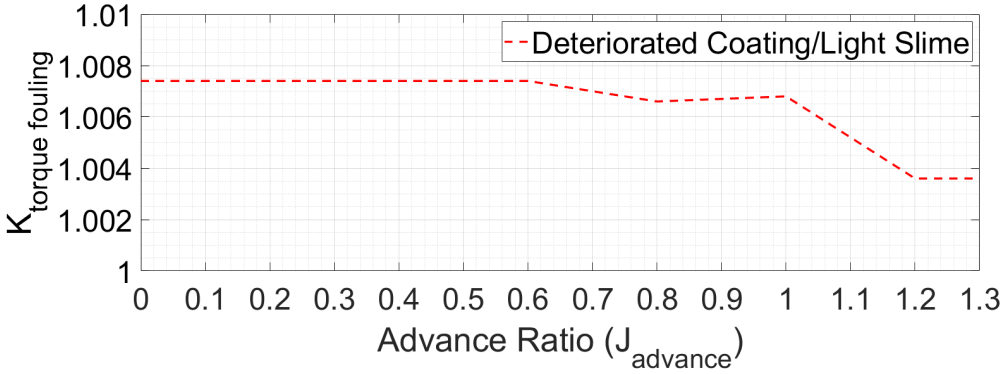

Figure 4.32: Propeller Fouling Torque Correction Factor Look-up Table

This concludes the description of the procedure used to generate the thrust and torque look-up surfaces as well as the propeller correction factors that were incorporated into the MBD marine simulation platform.

4.3 Ship Hull Modelling

Describing the process of ship hull modelling necessitates a brief introduction to the conventions and terminology used in this work. The overall length and beam of the vessel are represented by L_{vessel} and b_{vessel} respectively. The origin of the vessel's body-fixed coordinate system, o_b, is placed mid-beam, $b_{vessel}/2$, halfway along the length of the waterline, $L_{wl}/2$, and coincident with a horizontal plane that represents the water-level in calm water, lwl. The x_b-axis is positive towards the bow of the ship, the y_b-axis is positive to starboard, and the z_b-axis is positive downwards as is typical in naval architecture. The vessel's draught is d_{vessel}.

The MBD marine simulation platform simulates vessel motions in 3 DOF and accounts for the vessel's velocity, U, and yaw rate, r. The ship's velocity, U, is composed of a surge component, u, and a sway component, v, as shown in Figure 4.33. The M.V. *Skeena Queen*'s bi-directional hull results in near-symmetry across two-planes and therefore its centre of gravity, CG, is located nearly directly above o_b as shown in Figure 4.34. The distance from o_b to CG is $\vec{\mathbf{r}}^{\,b}_{CG/b} = [x_G, y_G, z_G]^{\mathsf{T}}$.

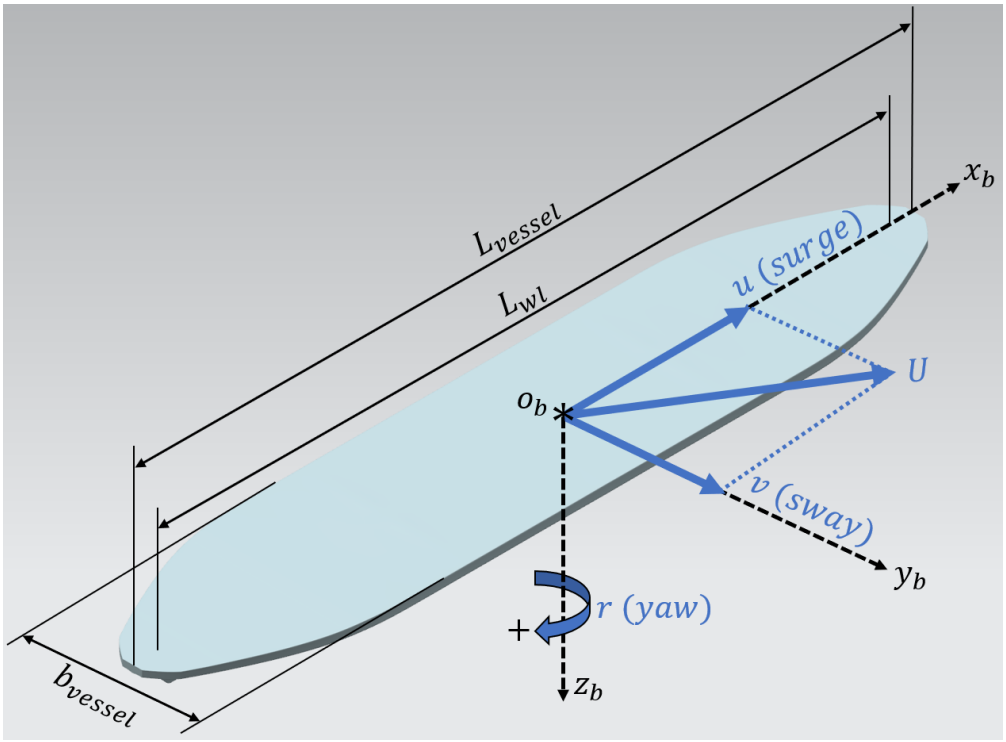

Figure 4.33: Ship Coordinate System – Orthographic View

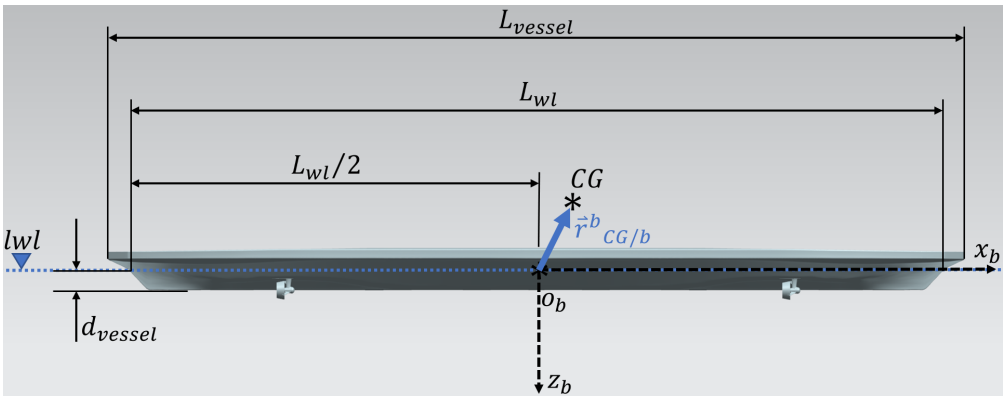

Figure 4.34: Ship Coordinate System – Right View

As mentioned at the beginning of this chapter, the development of a pre-computed hull resistance look-up table is integral to this work. The hull resistance look-up table is generated with CFD for resistance in pure surge, X_0, as a function of relative surge velocity, u_r. In this work, resistance in pure surge is taken to mean the resistance of the hull in the surge direction when the ship's course is in a straight line ($v_r = 0$, $r = 0$), during which the ship's angle of attack and resistance are unaffected by turning manoeuvres. The term relative velocity describes ship speed relative to the local ocean surface and allows for the introduction of

ocean currents into the model. Ship speed relative to the water is often referred to as speed-over-water, while ship speed relative to an earth-fixed coordinate system is referred to as speed-over-ground. Note that speed-over-ground is equal to speed-over-water if ocean current is zero.

The hull resistance look-up table is generated for resistance in pure surge because it is typically the dominant component of hull resistance while a vessel is underway. This CFD generated resistance is then augmented with additional resistances that arise from motions in sway and yaw using a modified version of the widely known MMG model as envisioned by Yoshimura and Masumoto [32].

With X_{hull}, Y_{hull}, N_{hull} denoting the vessel's hull resistance in surge, sway and yaw respectively, the total resistance in the surge direction is the sum of both CFD and MMG components:

$$X_{hull} = X_0 + X_{MMG} \tag{4.11}$$

where X_0 is the hull's resistance in surge due to motion in pure surge, and X_{MMG} is the hull's added resistance in surge due to sway and yaw motions during manoeuvring.

The sway and yaw components of hull resistance come solely from the MMG model:

$$Y_{hull} = Y_{MMG} \tag{4.12}$$

$$N_{hull} = N_{MMG} \tag{4.13}$$

where Y_{MMG} and N_{MMG} are the sway and yaw components of resistance that are computed with the MMG model.

The flowchart in Figure 4.35 provides a simplified representation of the hybrid MMG model within the MBD marine simulation platform and depicts how the integrated look-up table is used to calculate hull resistance at each time-step.

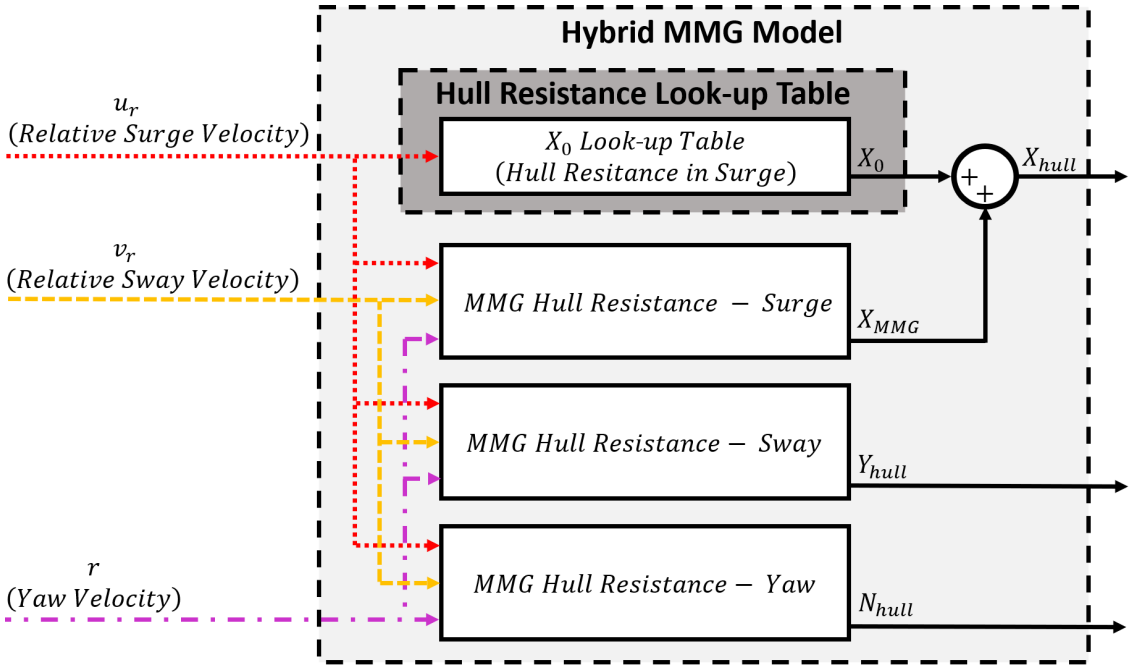

Figure 4.35: Integration of the Hull Resistance Look-up Table within the Hybrid MMG Model

The sequential procedure that was developed for generating the hull resistance look-up table is as follows:

1) Ship hull 3D surface modelling
    a) Develop a 3D surface model of a ship hull using CAD software
2) Ship hull CFD analyses
    a) Import the previously generated 3D hull model into CFD software
    b) Run CFD analyses while methodically varying the vessel's speed
        i. Relative surge velocity (u_r)
3) Ship hull resistance look-up table
    a) Extract CFD results to build out the hull resistance look-up table
        i. Vessel hull resistance in surge (X_0) as a function of relative surge velocity (u_r)
    b) Incorporate the look-up table into the simulation platform within the vessel sub-system module

The following sections provide a detailed description of the aforementioned procedure.

4.3.1 Hull 3D Surface Model

The goal of modelling a ship hull surface in 3D is to generate an accurate representation of the hull geometry that can in turn be analyzed with CFD to generate a hull resistance look-up table. While there are specialized software packages for designing ship hulls, the approach in this work makes use of standard CAD commands that should be compatible with commonly available CAD software.

With recently built vessels, or vessels that are still in the design stage, a naval architect will have often developed a 3D model of the vessel's hull that can be readily imported into CFD software with little to no modification. In the case of older ships that were designed prior to the widespread adoption of 3D modelling, a model is not always available. In the case of the M.V. *Skeena Queen*, BC Ferries was able to provide a 3D lines-plan but not a 3D hull surface.

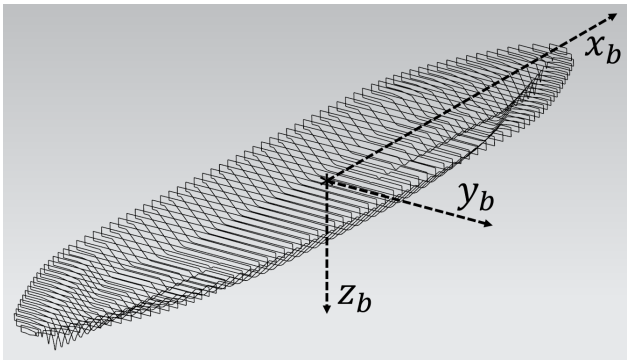

Figure 4.36: Vessel Lines-plan – Ortho. View

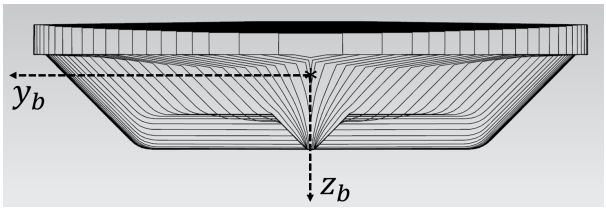

Figure 4.37: Vessel Lines-plan – Front View

As can be seen in Figures 4.36–4.37, the provided 3D lines-plan consists of the vessel's geometry from the bottom of the keel up to the main vehicle deck and lacks the vessel's superstructure. Fortunately, the CFD analyses only required the vessel's wetted surfaces (all surfaces that are in contact with the water) to compute hull resistance which is the dominant source of a vessel's resistance. If a vessel's superstructure is present, its resistance in air can also be estimated with CFD and typically represents 4%–8% of a ship's total resistance while underway in calm conditions with no wind [33, 34]. Due to the lack of superstructure geometry in CAD, The M.V. *Skeena Queen*'s air resistance is estimated empirically (see Section 5.8).

The procedure that was developed to translate the *Skeena Queen*'s 3D lines-plan into a 3D hull surface began with importing the provided lines-plan into CAD software.

Initially, the import process resulted in hull contour curves that were self-intersecting and which could not be fit directly with a surface. This issue was resolved by fitting each

contour with a series of points and then fitting the points with continuous splines as shown in Figure 4.38. The curve fitting process resulted in a maximum deviation of 0.11% when compared with overall beam width and is shown highly magnified in Figure 4.39.

A hull surface was fit through the newly created contours as shown in Figure 4.40. Making use of the M.V. *Skeena Queen*'s symmetry, the process was completed for half of the hull and then mirrored across the y_b-z_b plane to generate the complete hull.

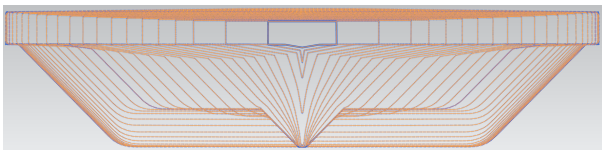

Figure 4.38: Fitted Hull Contours

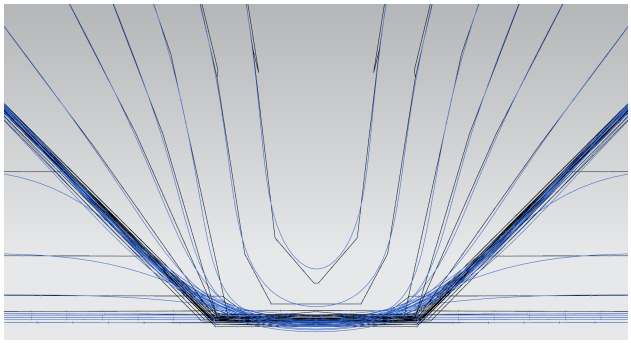

Figure 4.39: Fitted Hull Contour Deviation

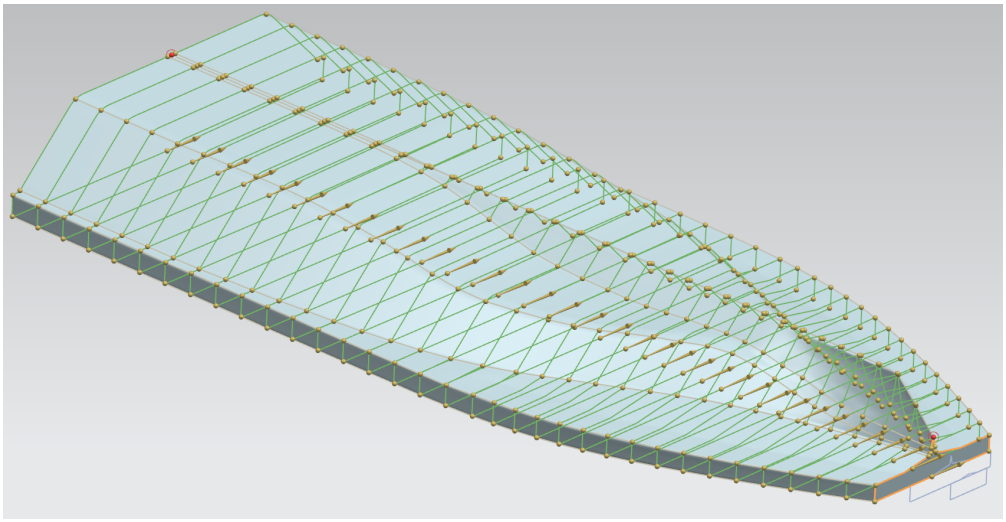

Figure 4.40: Hull Contours Fitted with Surface

Once the *Skeena Queen*'s bare hull surface had been developed, the model was exported from CAD to CFD analyses.

As an after-thought, the hull model was later assembled with the azimuth thruster towers and propeller ducts with the intention of re-running the CFD analyses to account for the additional appendage resistance as shown in Figure 4.41. Since these revised analyses were not run, the appendage resistance was estimated empirically (see Section 4.3.6).

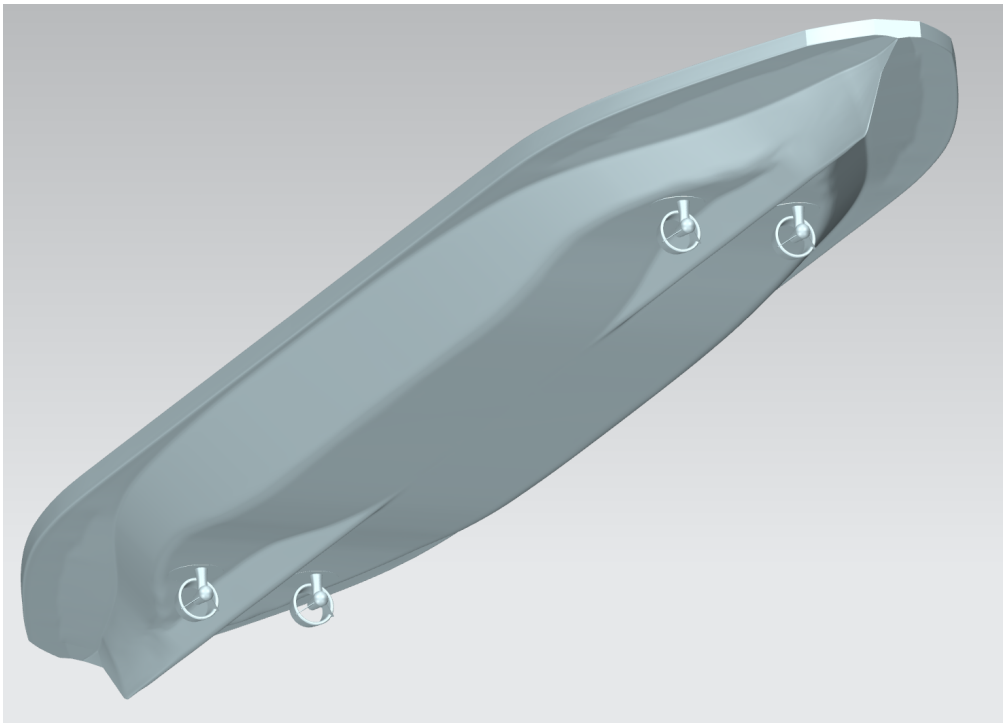

Figure 4.41: Skeena Queen Assembly with Azimuth Towers and Ducts

Vessel Mass and Moment of Inertia Estimation

Before running the CFD analyses, it was important to obtain estimates relating to the vessel's mass. As the ship's CAD model lacked details regarding the ship's interior, superstructure and distribution of mass, the vessel's mass, centre of gravity, and moments of inertia were established by other means.

Key mass parameters were obtained from the M.V. *Skeena Queen*'s stability book which contained empirical measurements of the vessel's mass and the location of its centre of gravity for various loading conditions. While the stability book provided detailed mass information for various loading scenarios, a single static loading condition was selected in the interest of limiting the number of CFD cases. The stability book listed the mass of the ship's heaviest operating condition as being 19% greater than its lightest operating condition, with the difference being attributed to vehicle load, passenger load, as well as fuel, potable water, and sewage tank levels [13]. With the knowledge that the simulation was to be validated with data collected during a period of high demand, the static loading condition was chosen to be about 16.8% greater than the lightest operating condition, or about 2.0% lighter than the heaviest operating condition. The chosen operating condition neglects any shifts in equipment, vehicles, and passengers, as well as variations in water and fuel tank levels that may slightly shift the centre of gravity.

The vessel's mass moments of inertia were estimated according to International-Tow-Tank-Conference (ITTC) guidelines: [35]

$$\begin{aligned} I_{xx} &= m\left(0.4 \cdot b_{vessel}\right)^2 \\ I_{yy} &= m\left(0.25 \cdot L_{vessel}\right)^2 \\ I_{zz} &= m\left(0.25 \cdot L_{vessel}\right)^2 \end{aligned} \tag{4.14}$$

where I_{xx}, I_{yy}, and I_{zz} are the mass moments of inertia about the vessel's x_b-, y_b-, and z_b-axes respectively. m is the mass of the ship, b_{vessel} is the width of the beam, and L_{vessel} is the length of the ship between perpendiculars.

As the CFD analyses were run for the ship transiting along a straight-line course, the vessel's motions in CFD were constrained to allow only forward motion (surge), vertical motion (heave) and rotation about the y_b-axis (pitch). The moment of inertia about the y_b–axis, I_{yy}, was required for computing pitch motions while I_{xx} and I_{zz} were excluded due to the absence of roll and yaw.

Similarly, in the MBD marine simulation platform, the moment of inertia about the z_b–axis, I_{zz}, is used for computing yaw motion while I_{xx} and I_{yy} are excluded due to the absence of roll and pitch.

Due to the motion constraints in both the CFD analyses and the MBD simulation, I_{xx} is not utilized in either scenario.

It should be noted that adding additional DOF require a vessel's products of inertia and can be essential for accurately simulating vessel motions during certain manoeuvres or during higher sea-states. One such example would be a tight radius turn at high speed where there is a strong coupling of yaw and roll (a vessel tends to keel-over during these manoeuvres). The decision to restrict the model to 3 DOF is supported by the reality that the M.V. *Skeena Queen*'s roll angle is usually small due to its barge-like hull, its operations that are restricted to sheltered waters, and because it performs gentle manoeuvres that prioritize passenger comfort.

After the vessel's mass, centre of gravity, and moments of inertia had been estimated, the details were fed into the CFD analyses.

4.3.2 Hull Resistance CFD Analyses

The CFD analyses for ship hull resistance were run with the ship transiting along a straight-line course and were constrained to motions in surge, heave and pitch, where surge is motion in the x_b-direction, heave is motion in the z_b-direction and pitch is rotation about the y_b-axis as shown in Figure 4.42.

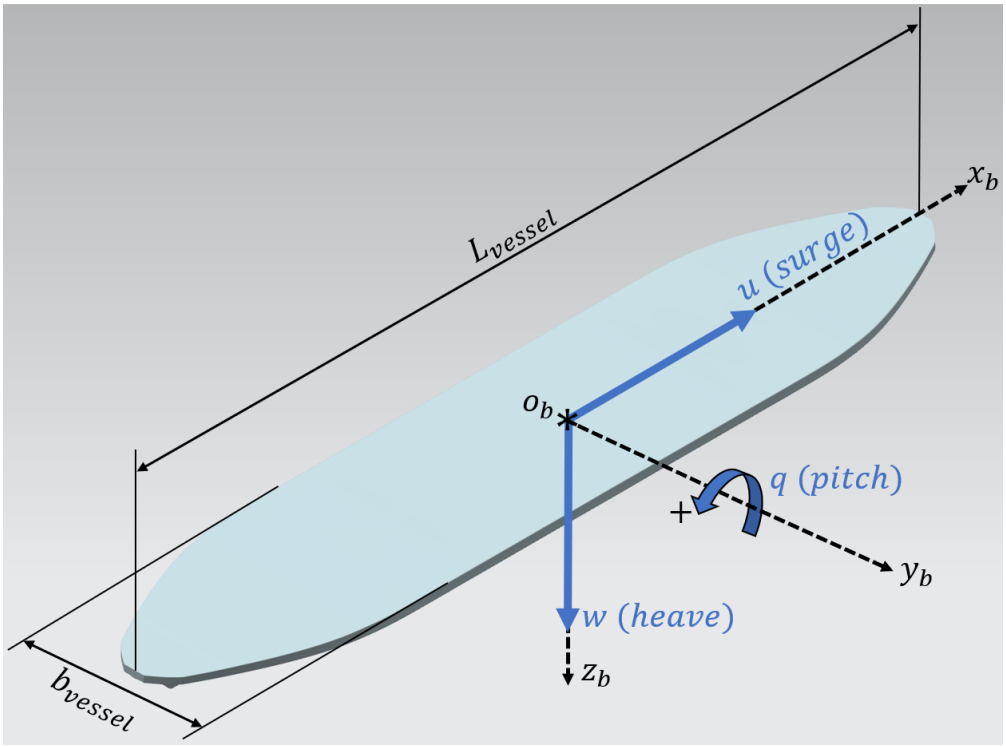

Figure 4.42: Ship Hull CFD Motions

The constrained motions allowed the CFD analyses to take advantage of the ship's symmetry across its x_b-z_b plane and reduce the computations to the starboard half of the ship, contributing to a significant reduction in computational demand.

In this work, the CFD analyses for hull resistance were run by Rahimpour [36] and were designed to mimic model tow-tank experiments that are used in naval architecture to assess the resistance of a hull at various surge speeds. To accomplish this, Rahimpour [36] ran several CFD cases for multiple surge speeds (u) in calm water conditions. The surge speed was incrementally increased in each subsequent CFD case until the vessel's entire range of speed was covered as shown in Table 4.3.

Table 4.3: Ship Hull CFD Case Parameters
Source: Rahimpour [36]

Parameter	**Value(s)**
Vessel Surge Speed $[m/s]$	0.129, 0.257, 0.386, 0.514, 0.643, 0.772, 0.900, 1.029, 1.286, 1.543, 1.801, 2.058, 2.315, 2.572, 2.829, 3.087, 3.601, 4.116, 4.630, 5.144, 5.659, 6.173, 6.688, 7.202, 7.717, 8.231, 8.746, 9.260, 9.774, 10.289

After each CFD case, the software calculated the sum of the forces acting on the starboard

half of the hull which was then doubled to compute total hull resistance. As the analyses were dynamic, they resulted in periodic motion and the forces were averaged over the duration of one period. The total resistance was output with respect to the ship's coordinate system and the X_0 component was extracted to build the resistance look-up table used in the MBD marine simulation platform. Finally, it should be mentioned that owing to the use of dynamic simulation, the affect of the vessel's trim is accounted for within the resistance results and is captured by the given loading condition inputs (mass, centre of gravity, and moments of inertia).

It should also be noted that the hull CFD analyses were not "self-propelled", meaning that the propellers were not present and generating thrust during the computations. It is important to make this distinction because while under-way, the propeller increases the local flow velocity which in turn reduces pressure at the surface of the hull and leads to increased resistance [21,29,30]. The typical convention in naval architecture is to represent this increase in hull resistance with an equivalent reduction in thrust using the "thrust deduction factor". In the MBD marine simulation platform, the "augmented resistance factor" (see Section 4.3.6) is used in-place of the "thrust reduction factor" and is integrated within the vessel subsystem.

The other propeller-hull interaction that was discussed previously is wake fraction (Section 4.2.4). While underway, the presence of the ship hull alters the velocity of the flow into the propeller ($V_{advance}$) [21, 29, 30], which in turn alters the resulting propeller thrust and torque (T_{prop_x}, T_{prop_y}, Q_{prop}).

To obtain an estimate for the wake fraction at the propellers, virtual velocity probes were distributed around the regions where the propellers would normally have been located so that velocity measurements could be taken during the CFD analyses.

The resulting wake fraction measurements at fore and aft propeller locations are plotted vs. surge velocity in Figure 4.43.

4.3.3 Hull Resistance Look-Up Table

After completing the hull CFD analyses, Rahimpour [36] extracted the results for hull resistance in the surge direction (X_0) as a function of relative surge velocity (u_r) which is plotted in Figure 4.44. Note that the CFD hull resistance results are later corrected for appendage and fouling resistance as discussed in Section 4.3.6.

As a ship moves through the water, it emits a wake-system consisting of a bow wave, a forward shoulder wave, an aft shoulder wave, and a stern wave [34]. A ship's resistance curve can contain local peaks and troughs caused by the interference of these waves, during

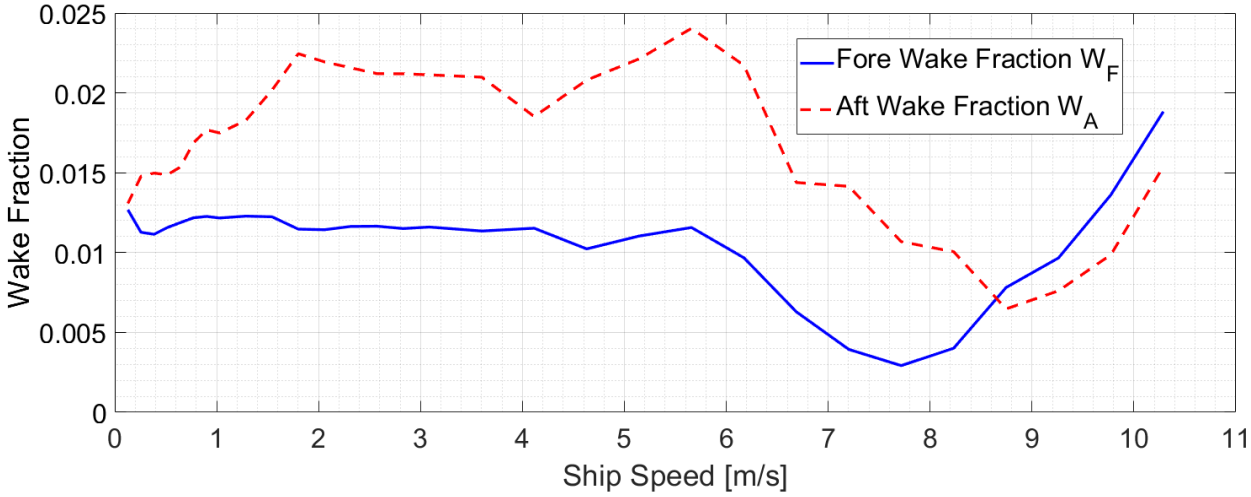

Figure 4.43: Fore and Aft Propeller Wake Fraction vs. Speed

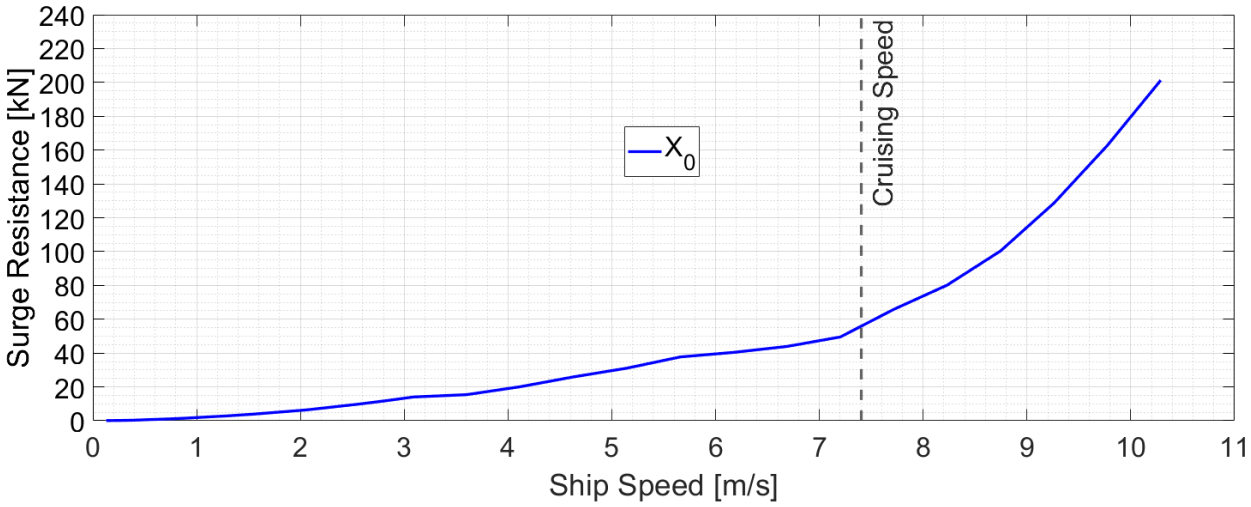

Figure 4.44: Hull Surge Resistance vs. Speed

which they act to reinforce or cancel one another, increasing or reducing hull resistance respectively. It is interesting to note that there is a change in slope in the *Skeena Queen*'s hull resistance plot between $6-7\,m/s$ which may signify a reduction in resistance caused by wave cancellation.

This concludes the description of the procedure used to generate the hull resistance look-up table that was incorporated into the MBD simulation platform.

4.3.4 Hull Added Mass

As a vessel accelerates through a fluid, it cannot simultaneously occupy the same space as the fluid, and therefore must accelerate some volume of fluid out of its way as it passes

through. This is relevant for assessing a ship's power requirements because the ship must provide enough thrust to move both the ship and the volume of water it is displacing. The mass of the fluid that the ship displaces is often referred to as "added mass".

The MBD marine simulation platform assumes constant added mass that is represented by the so-called zero-frequency added mass, a common assumption in marine vessel modelling [11].

In this work, the software program called WAMIT was used to compute the M.V. *Skeena Queen*'s zero-frequency added mass and interested readers are directed to the software's manual for in-depth details regarding the background theory and calculation methods [37].

As WAMIT relies on a 3D panel method for its calculations, it required an alternate meshed version of the ship hull that was created with Rhinoceros 5 CAD software. After initial WAMIT runs terminated with errors stemming from a poor-quality mesh, the 3rd party plug-in "Grasshopper" was used to significantly increase the hull mesh density. The final version of the meshed hull is shown in Figure 4.45.

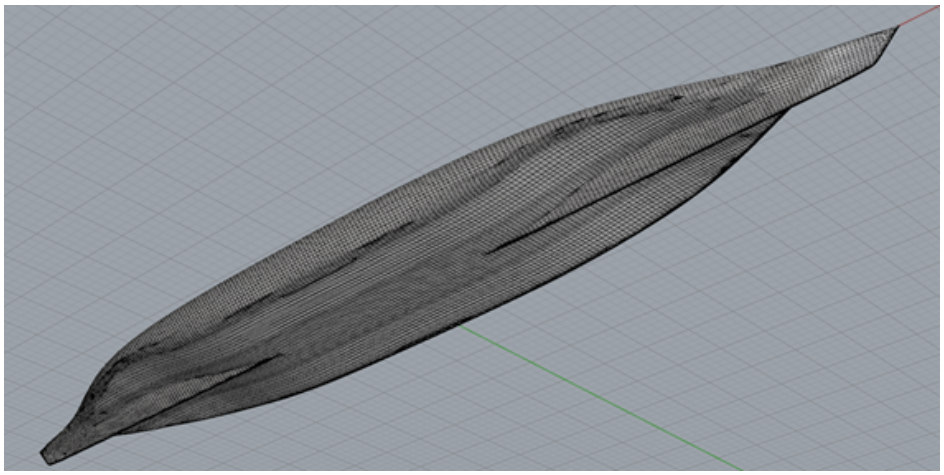

Figure 4.45: M.V. *Skeena Queen* Meshed Hull for WAMIT Analysis

To ensure consistency, the same vessel mass and moments of inertia were used in both the CFD analyses and WAMIT analyses. As the products of inertia were unknown, they were set to zero within WAMIT.

WAMIT outputs a $6x6$ added-mass matrix in non-dimensional form. The added-masses were extracted for surge (m_x), sway (m_y) and yaw (J_{zz}), which correspond to the $i, j = 1$, $i, j = 2$, and $i, j = 6$ elements of the added-mass matrix respectively. Before extraction, these added-masses were dimensionalized with [37]:

$$A_{ij} = \overline{A}_{ij} \cdot \rho \cdot L_{ULEN}^{k} \tag{4.15}$$

$$k = 3 \text{ for } i, j = 1, 2, \text{ and } k = 5 \text{ for } i, j = 6$$

where A_{ij} is the dimensionalized added mass element, $\overline{A}_{ij}$ is the non-dimensionalized added mass element, and L_{ULEN} is the characteristic length of the hull mesh geometry specified in the WAMIT input file.

The dimensionalized added-masses were used within the hybrid MMG model to compute vessel acceleration as discussed in the following section.

4.3.5 Hybrid MMG Model

While hull resistance in the surge direction due to surge velocity is the dominant source of ship's resistance while underway, accounting for resistances due to motion in other directions is essential for accurately simulating a vessel's motion while manoeuvring. These additional resistances are estimated using a modified version of the MMG model as envisioned by Yoshimura and Masumoto [32].

The inclusion of the MMG model allows for the estimation of hull forces in additional DOF while avoiding the expansion of the CFD analyses to 3 or 6 DOF which would require a significant growth in the number of CFD cases, computational demand, and knowledge of a vessel's products of inertia.

The adopted MMG model assumes port-starboard symmetry which is true of many vessels and begins with the following vessel equations of motion [32]:

$$\begin{aligned} (m + m_x)\,\dot{u} - (m + m_y)\,v_G r &= X_{force} \\ (m + m_y)\,\dot{v}_G + (m + m_x)\,ur &= Y_{force} \\ (I_{zz} + J_{zz})\,\dot{r} &= N_{moment} - x_G Y_{force} \end{aligned} \tag{4.16}$$

where $\dot{u}$, $\dot{v_G}$, and $\dot{r}$ are the vessel's accelerations at its centre of gravity in surge, sway and yaw respectively. m is the vessel's mass, I_{zz} is the yaw moment of inertia, and m_x, m_y, and J_{zz} are the added masses and added yaw moment of inertia respectively. v_G is the sway component of velocity at the ship's centre of gravity and x_G is distance from o_b to CG in the x_b-direction.

X_{force}, Y_{force}, and N_{moment} are the sum of the forces and moments acting on the hull at o_b which can be decomposed into hull, propeller and rudder forces:

$$\begin{aligned} X_{force} &= X_{hull} + X_{props} + \cancelto{0}{X_{rudder}} \\ Y_{force} &= Y_{hull} + Y_{props} + \cancelto{0}{Y_{rudder}} \\ N_{moment} &= N_{hull} + N_{props} + \cancelto{0}{N_{rudder}} \end{aligned} \tag{4.17}$$

where X_{hull}, Y_{hull}, and N_{hull} are the resistance forces and moments acting on the hull and X_{props}, Y_{props}, and N_{props} are propeller forces and moments acting about o_b respectively. X_{rudder}, Y_{rudder}, and N_{rudder} are the rudder forces and moments respectively, but as the *Skeena Queen* has no rudder, they were removed from the model.

The original MMG model as presented by Yoshimura and Masumoto [32] was built for a traditional single rudder, single propeller ship with a propeller located on the ship's centre-line. The original model does not contain Y_{props}, or N_{props} because it assumes the single propeller's line of action is passing through o_b. In order to adequately model the motion of the *Skeena Queen*, the addition of Y_{props}, and N_{props} were necessary to account for the additional forces and moments generated by the offset azimuth thrusters.

The MMG model estimates hydrodynamic forces acting on the hull using a series of non-dimensionalized hydrodynamic derivatives that are presented as a function of drift angle and dimensionless turning rate [32].

The drift angle is defined as:

$$\beta = -\sin^{-1}(v_r/U_r) \tag{4.18}$$

where β is the drift angle, v_r is the vessel's relative sway velocity at o_b, and U_r is the vessel's overall relative velocity at o_b.

The dimensionless yaw or turning rate is defined as:

$$r' = r\,(L_{wl}/U_r) \tag{4.19}$$

where r' is the dimensionless turning rate and L_{wl} is the length of the vessel at the waterline.

The MMG model's dimensionless added masses are:

$$\begin{aligned} m'_x &= \frac{m_x}{(\rho/2)\,L_{wl}d_{vessel}} \\ m'_y &= \frac{m_y}{(\rho/2)\,L_{wl}d_{vessel}} \end{aligned} \tag{4.20}$$

where m'_x and m'_y are the dimensionless added masses in surge and sway respectively while m_x and m_y are the zero-frequency dimensionalized added masses in surge and sway that were obtained through WAMIT.

The dimensionless distance from o_b to CG is defined as x'_G, and is given as:

$$x'_G = x_G/L_{wl} \tag{4.21}$$

Finally, the MMG model's hydrodynamic forces are non-dimensionalized by $\left[\frac{\rho}{2}L_{wl}d_{vessel}U^2\right]$,

while moments are non-dimensionalized by $\left[\frac{\rho}{2}L_{wl}^2 d_{vessel}U^2\right]$.

Yoshimura and Masumoto construct hydrodynamic derivatives using polynomials of β and r'. The hydrodynamic derivatives in surge make use of 2nd and 4th order terms while 1st and 3rd order terms appear in sway and yaw as follows [32]:

$$
\begin{aligned}
&X_{hull} + m_y v_G r = \\
&\qquad \left[\frac{\rho}{2}L_{wl}d_{vessel}U^2\right] \cdot \left[X'_0 + X'_{\beta\beta}\beta^2 + \left(X'_{\beta r} - m'_y\right)\beta r' + \left(X'_{rr} + x'_G m'_y\right) r'^2 + X'_{\beta\beta\beta\beta}\beta^4\right] \\
&Y_{hull} - m_x u r = \\
&\qquad \left[\frac{\rho}{2}L_{wl}d_{vessel}U^2\right] \cdot \left[Y'_\beta\beta + \left(Y'_r - m'_x\right) r' + Y'_{\beta\beta\beta}\beta^3 + Y'_{\beta\beta r}\beta^2 r' + Y'_{\beta rr}\beta r'^2 + Y'_{rrr}r'^3\right] \\
&N_{hull} = \\
&\qquad \left[\frac{\rho}{2}L_{wl}^2 d_{vessel}U^2\right] \cdot \left[N'_\beta\beta + N'_r r' + N'_{\beta\beta\beta}\beta^3 + N'_{\beta\beta r}\beta^2 r' + N'_{\beta rr}\beta r'^2 + N'_{rrr}r'^3\right]
\end{aligned}
\tag{4.22}
$$

Noting that X'_0 represents the hull's non-dimensionalized straight-line resistance [38], this term was pulled out and replaced with the straight-line resistance look-up table computed with CFD and marks one of the major modifications that differentiates the hybrid MMG model used in this work.

For convenience, the non-dimensionalized forces and moments are grouped in surge, sway and yaw as X'_{MMG}, Y'_{MMG}, and N'_{MMG} respectively:

$$
\begin{aligned}
X_{hull} =& \underbrace{X_0}_{CFD} - m_y v_G r \\
&+ \left[\frac{\rho}{2}L_{wl}d_{vessel}U^2\right] \cdot \underbrace{\left[X'_{\beta\beta}\beta^2 + \left(X'_{\beta r} - m'_y\right)\beta r' + \left(X'_{rr} + x'_G m'_y\right) r'^2 + X'_{\beta\beta\beta\beta}\beta^4\right]}_{X'_{MMG}} \\
Y_{hull} =& m_x u r \\
&+ \left[\frac{\rho}{2}L_{wl}d_{vessel}U^2\right] \cdot \underbrace{\left[Y'_\beta\beta + \left(Y'_r - m'_x\right) r' + Y'_{\beta\beta\beta}\beta^3 + Y'_{\beta\beta r}\beta^2 r' + Y'_{\beta rr}\beta r'^2 + Y'_{rrr}r'^3\right]}_{Y'_{MMG}} \\
N_{hull} =& \\
&\left[\frac{\rho}{2}L_{wl}^2 d_{vessel}U^2\right] \cdot \underbrace{\left[N'_\beta\beta + N'_r r' + N'_{\beta\beta\beta}\beta^3 + N'_{\beta\beta r}\beta^2 r' + N'_{\beta rr}\beta r'^2 + N'_{rrr}r'^3\right]}_{N'_{MMG}}
\end{aligned}
\tag{4.23}
$$

In Yoshimura and Masumoto's MMG model, the hydrodynamic forces and moments are given about o_b, while vessel accelerations are given at the ship's centre of gravity, making their formulation slightly cumbersome [32]. Conveniently, Yasukawa and Yoshimura [38] later propose a standardization of the MMG model where both the hydrodynamic forces

and vessel accelerations are given at the vessel's geometric centre, o_b.

Combining equations (4.16), (4.17) and (4.23), and substituting $v_G = v + x_G r$ [38] results in the following equations of motion about o_b:

$$\begin{aligned}
(m+m_x)\,\dot{u} &= X_0 + \left(\frac{\rho}{2} L_{wl} d_{vessel} U^2\right) X'_{MMG} + m\left(vr + x_g r^2\right) + X_{props} \\
(m+m_y)\,\dot{v} &= \left(\frac{\rho}{2} L_{wl} d_{vessel} U^2\right) Y'_{MMG} - (m+m_y)\,x_G \dot{r} - mur + Y_{props} \\
\left(I_{zz} + J_{zz} + (m+m_y)x_G^2\right)\dot{r} &= \left(\frac{\rho}{2} L_{wl}^2 d_{vessel} U^2\right) N'_{MMG} - (m+m_y) x_G \dot{v} - x_G mur + N_{props}
\end{aligned} \tag{4.24}$$

The equations of motion in (4.24) are slightly different than the form proposed by Yasukawa and Yoshimura in order to maintain compatibility with a dimensionless hydrodynamic derivative database constructed by Yoshimura and Masumoto.

Accounting for ocean currents, the vessel's relative surge and sway velocities become $u_r = u - u_c$, and $v_r = v - v_c$ respectively, where u_c and v_c are the ocean current velocities in surge and sway. With the assumption that the ocean currents are constant and irrotational, the yaw rate remains unchanged with $r_r = r - \cancelto{0}{r_c}$, as do the acceleration terms with $\dot{u}_r = \dot{u} - \cancelto{0}{\dot{u}_c}$, $\dot{v}_r = \dot{v} - \cancelto{0}{\dot{v}_c}$, and $\dot{r}_r = \dot{r} - \cancelto{0}{\dot{r}_c}$ [11]. Making these substitutions into equation (4.24) results in:

$$\begin{aligned}
(m+m_x)\,\dot{u} &= X_0 + \underbrace{\left(\frac{\rho}{2} L_{wl} d_{vessel} U_r^2\right) X'_{MMG_r} + m\left(v_r r + x_g r^2\right)}_{X_{MMG}} + X_{props} \\
(m+m_y)\,\dot{v} &= \underbrace{\left(\frac{\rho}{2} L_{wl} d_{vessel} U_r^2\right) Y'_{MMG_r} - (m+m_y)\,x_G \dot{r} - mu_r r}_{Y_{MMG}} + Y_{props} \\
\left(I_{zz} + J_{zz} + (m+m_y)x_G^2\right)\dot{r} &= \underbrace{\left(\frac{\rho}{2} L_{wl}^2 d_{vessel} U_r^2\right) N'_{MMG_r} - (m+m_y) x_G \dot{v} - x_G mu_r r}_{N_{MMG}} + N_{props}
\end{aligned} \tag{4.25}$$

It is worthwhile to point out that the drift angle, β, and the dimensionless yaw rate, r', used in the calculation of the non-dimensionalized MMG forces and moments, X'_{MMG_r}, Y'_{MMG_r}, N'_{MMG_r}, are now also computed with relative velocity to account for ocean current.

For convenience, equation (4.25) is re-written as:

$$\begin{aligned}
(m+m_x)\,\dot{u} &= X_0 + X_{MMG} + X_{props} \\
(m+m_y)\,\dot{v} &= Y_{MMG} + Y_{props} \\
\left(I_{zz} + J_{zz} + (m+m_y)x_G^2\right)\dot{r} &= N_{MMG} + N_{props}
\end{aligned} \tag{4.26}$$

One of the key contributions of Yoshimura and Masumoto's publication is an empirical hydrodynamic derivative database which is built using experimental results from 13 medium

speed ships.

The hydrodynamic derivatives within Yoshimura and Masumoto's database were obtained using two tests for each vessel: an oblique towing test and a circular motion test. Each of the measured hydrodynamic derivatives were then normalized by geometric properties including L_{wl}, b_{vessel}, d_{vessel} and C_B, where C_B is the vessel's block coefficient given by:

$$C_B = \frac{\nabla_{vessel}}{L_{wl} d_{vessel} b_{vessel}} \tag{4.27}$$

with ∇_{vessel} being the vessel's displacement.

Yoshimura and Masumoto performed a regression analysis across the combined, normalized results, and from the fitted results, they formulate a set of empirical equations that estimate each of the non-dimensional hydrodynamic derivatives terms as found in Table 4.4.

Table 4.4: Empirical Formulas for Dimensionless Hydrodynamic Derivatives
Source: Yoshimura and Masumoto [32]

Hydrodynamic Derivative	**Hybrid MMG Value**
X_0	CFD Resistance
$X'_{\beta\beta}$	$1.15C_b/\left(L_{wl}/b_{vessel}\right) - 0.18$
$\left(X'_{\beta r} - m'_y\right)$	$-1.19C_b/\left(L_{wl}/b_{vessel}\right) + 0.08$
$\left(X'_{rr} + x'_g m'_y\right)$	$-0.085C_b/\left(L_{wl}/b_{vessel}\right) + 0.008$
$X'_{\beta\beta\beta\beta}$	$-6.68C_b/\left(L_{wl}/b_{vessel}\right) + 1.10$
Y'_β	$\pi d_{vessel}/L_{wl} + 1.4C_b/(L_{wl}/b_{vessel})$
$(Y'_r - m'_x)$	$0.5C_b/(L_{wl}/b_{vessel})$
$Y'_{\beta\beta\beta}$	$0.185\left(L_{wl}/b_{vessel}\right) + 0.48$
$Y'_{\beta\beta r}$	-0.75
$Y'_{\beta rr}$	$0.26\left(1 - C_b\right)\left(L_{wl}/b_{vessel}\right) + 0.11$
Y'_{rrr}	-0.051
N'_β	$2d_{vessel}/L_{wl}$
N'_r	$0.54 \cdot 2d_{vessel}/L_{wl} + \left(2d_{vessel}/L_{wl}\right)^2$
$N'_{\beta\beta\beta}$	$-0.69C_b + 0.66$
$N'_{\beta\beta r}$	$1.55C_b/\left(L_{wl}/b_{vessel}\right) - 0.76$
$N'_{\beta rr}$	$0.075\left(1 - C_b\right)\left(L_{wl}/b_{vessel}\right) - 0.098$
N'_{rrr}	$0.25C_b/\left(L_{wl}/b_{vessel}\right) - 0.056$

While all of the vessels in the regression analysis were single-rudder, single-propeller ships, the hydrodynamic hull forces were separated from the propeller and rudder interactions allowing the empirical formulas to be used with other ship configurations. Yoshimura and Masumoto suggest that the presented hydrodynamic derivative equations are valid for medium speed displacement vessels such as fishing vessels and ferries [32].

A vessel can be classified as a displacement hull if its Froude number is less than 0.4 at its maximum service speed using the well-known equation for Froude number [11]:

$$Fr = \frac{u_r}{\sqrt{gL_{wl}}} \tag{4.28}$$

where g is acceleration due to gravity.

Using the values found in Table 3.1, the M.V. *Skeena Queen's* Froude number evaluates to approximately 0.246, placing it firmly in the displacement hull category and indicating that it is compatible with the database.

In conclusion, the empirical equations presented by Yoshimura and Masumoto in Table 4.4 are used to estimate the M.V. *Skeena Queen*'s hydrodynamic derivatives and calculate the vessel's motion using the hybrid MMG model.

4.3.6 Hull Correction Factors

Once preliminary estimates for the hull forces and moments had been obtained, a series of correction factors were worked into the simulation to account for effects not captured with CFD or with the MMG model.

Appendage Resistance

Considering that the four azimuth towers were not included in either the propeller or hull CFD analyses, their contribution to hull resistance needed to be approximated.

As azimuth tower appendage resistance is proportional to velocity, the first step is to compute the velocity at each of the azimuth towers locations while accounting for the ship's yaw rate with:

$$\begin{bmatrix} u_{azi} \\ v_{azi} \\ r_{azi} \end{bmatrix} = \begin{bmatrix} u_r \\ v_r \\ r \end{bmatrix} + \left(\begin{bmatrix} 0 \\ 0 \\ r \end{bmatrix} \times \begin{bmatrix} x_{azi/b} \\ y_{azi/b} \\ 0 \end{bmatrix} \right) \tag{4.29}$$

where u_{azi}, v_{azi}, and r_{azi} are the surge, sway and yaw velocities respectively at the azimuth thruster in the vessel's body-fixed frame. The variables $x_{azi/b}$, and $y_{azi/b}$ are the distances in the x_b-, and y_b-directions from o_b to the azimuth thruster at o_{azi}.

Holtrop and Mennen [39] assert that an appendage's contribution to hull resistance in surge can be determined from:

$$X_{tower} = 0.5\rho u_{azi}^2 S_{appendage} \left(1 + k_{appendage}\right) C_F \tag{4.30}$$

where X_{tower} is the azimuth tower appendage resistance, $S_{appendage}$ is the surface area of the appendage, and $k_{appendage}$ is the appendage form-factor coefficient. C_F is the ITTC 1957 coefficient of frictional resistance given by:

$$C_F = \frac{0.075}{\left(\log_{10} R_e - 2\right)^2} \tag{4.31}$$

with R_e being Reynold's number:

$$R_e = \frac{\rho u_r L_{wl}}{\mu_{viscosity}} \tag{4.32}$$

and $\mu_{viscosity}$ being the dynamic viscosity.

Holtrop and Mennen provide a table of experimentally obtained appendage coefficients for common ship appendages. Considering that there was no experimental appendage coefficient for an azimuth tower, each azimuth tower was approximated as a rudder with an appendage coefficient of $k_{appendage} = 2.0$ [39].

After computing appendage resistance in surge, the methodology was extended to sway with:

$$Y_{tower} = 0.5\rho v_{azi}^2 S_{appendage} \left(1 + k_{appendage}\right) C_F \tag{4.33}$$

where Y_{tower} is the azimuth tower appendage resistance in sway.

The resulting surge (X_{tower}) and sway (Y_{tower}) appendage resistances are plotted vs. the surge (u_{azi}) and sway (v_{azi}) relative velocities at the azimuth tower location in Figure 4.46.

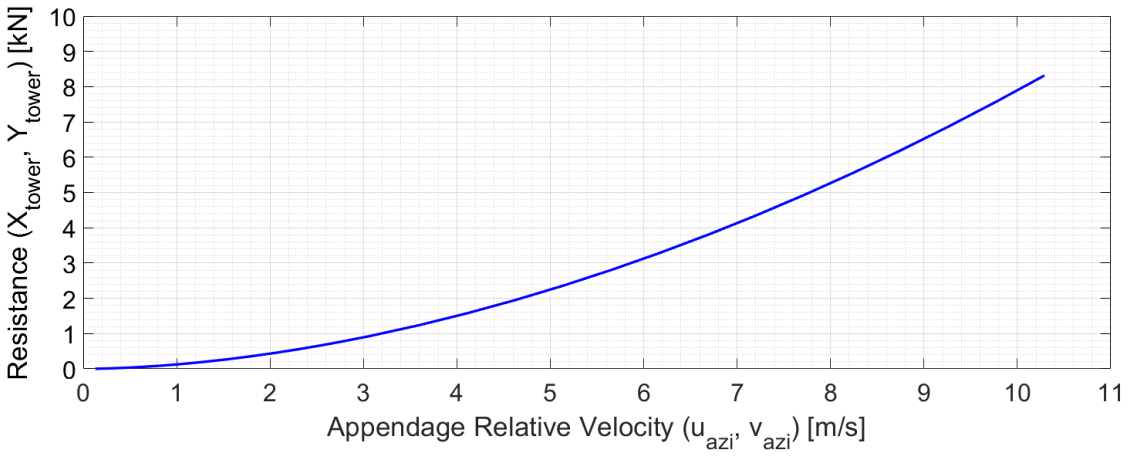

Figure 4.46: Appendage Resistance in Surge and Sway vs. Speed

Finally, the moment induced about the vessel at o_b by the azimuth tower appendage resistance is calculated with:

$$\begin{bmatrix} 0 \\ 0 \\ N_{tower} \end{bmatrix} = \begin{bmatrix} x_{azi/b} \\ y_{azi/b} \\ 0 \end{bmatrix} \times \begin{bmatrix} X_{tower} \\ Y_{tower} \\ 0 \end{bmatrix} \tag{4.34}$$

where N_{tower} is the moment induced by the appendage resistances.

Hull Fouling

As the CFD analyses for determining hull resistance were run on a hydraulically smooth hull surface, they did not account for the effects of surface roughness and fouling from marine growth. Additionally, an assumption is made that the MMG model resistances as well as the ITTC 1957 appendage friction resistance were determined empirically using un-fouled surfaces.

Schultz [40] provides fouling correction factors for 6 stages of fouling beginning with an as-applied anti-fouling coating and progressing up to heavy calcareous fouling as listed in Table 4.5. The fouling correction factors in Schultz are given for a naval frigate travelling at a cruising velocity of $7.7m/s$, which is similar to the *Skeena Queen*'s cruising speed of about $7.3m/s$.

Table 4.5: Hull Fouling Factors for Various Hull Conditions
Source: Adapted from Schultz [40]

Hull Condition	$\mathbf{K_{hull_{fouling}}}$ $(7.7m/s)$
Hydraulically Smooth Surface	–
Typical as applied AF coating	0.02
Deteriorated coating or light slime	0.11
Heavy slime	0.20
Small calcareous fouling or weed	0.34
Medium calcareous fouling	0.52
Heavy calcareous fouling	0.80

A hull fouling correction factor is introduced into the MBD marine simulation platform model and is approximated as a constant, irrespective of ship velocity. The fouling correction

factor for hull resistance was implemented as follows:

$$X_0^F = X_0 \left(1 + K_{hull_{fouling\,CFD}}\right)$$

$$\begin{aligned} X_{tower}^F &= X_{tower} \left(1 + K_{hull_{fouling\,empirical}}\right) \\ Y_{tower}^F &= Y_{tower} \left(1 + K_{hull_{fouling\,empirical}}\right) \\ N_{tower}^F &= N_{tower} \left(1 + K_{hull_{fouling\,empirical}}\right) \end{aligned} \tag{4.35}$$

$$\begin{aligned} X_{MMG}^F &= X_{MMG} \left(1 + K_{hull_{fouling\,empirical}}\right) \\ Y_{MMG}^F &= X_{MMG} \left(1 + K_{hull_{fouling\,empirical}}\right) \\ N_{MMG}^F &= X_{MMG} \left(1 + K_{hull_{fouling\,empirical}}\right) \end{aligned}$$

where X_0^F is the fouling corrected surge resistance from CFD. X_{tower}^F, Y_{tower}^F, and N_{tower}^F are the fouling corrected surge, sway and yaw azimuth tower resistances. X_{MMG}^F, Y_{MMG}^F, and N_{MMG}^F are the fouling corrected surge, sway and yaw MMG model resistances.

When analyzing the *Skeena Queen*, the "deteriorated coating or light slime" condition was assumed. A correction factor of $K_{hull_{fouling\,CFD}} = 0.11$ was applied to X_0 to transition from the "hydraulically smooth surface" condition to the "deteriorated coating or light slime" condition. As the appendage resistance and MMG model resistance were obtained from physical systems, a correction factor of $K_{hull_{fouling\,empirical}} = (1.11/1.02 - 1) = 0.088$ was applied to X_{tower}^F, Y_{tower}^F, N_{tower}^F, X_{MMG}^F, Y_{MMG}^F, and N_{MMG}^F to transition from the "typical as applied AF coating" condition to the "deteriorated coating or light slime" condition.

Resistance Augmentation Factor

During the ship design process, it is common to tow a propeller-less model of a ship through a tow-tank to assess its hull resistance. This procedure does not account for the effects of propeller-hull interaction and therefore the measured resistance must later be augmented with a correction factor.

As a propeller rotates underneath a ship hull, it increases the velocity of the flow at the local surface of the hull which in turn reduces pressure [21]. This drop in pressure leads to increased hull resistance when compared to the propeller-less model pulled through the tow-tank, or in the case of this work, the propeller-less model analyzed with CFD.

The propeller-hull interaction is often accounted for using the resistance augmentation

factor which is defined as: [21]

$$T_{prop_{required}} = X_{tank}\,(1 + a_{augmented}) \tag{4.36}$$

where $T_{prop_{required}}$ is the thrust required to propel the ship to a desired forward speed. X_{tank} is the hull resistance in surge obtained through tow-tank experiments for the propeller-less hull, and $a_{augmented}$ is the resistance augmentation factor that adjusts for the increase in resistance caused by propeller-hull interaction.

An alternate method of accounting for the propeller-hull interaction is by replacing the resistance augmentation factor with an equivalent thrust deduction factor that is defined as [21]:

$$X_{tank} = T_{prop_{required}}\,(1 - t_{deduction}) \tag{4.37}$$

where $t_{deduction}$ is the thrust deduction factor.

The thrust deduction factor works well when simulating a ship that is moving ahead conventionally with its hull resistance acting in the opposing direction of propeller thrust. In this work however, the resistance augmentation factor is preferred because the M.V. *Skeena Queen* rotates its fore thrusters 180° to provide braking thrust as it approaches berth. During this manoeuvre, the hull resistance is acting in the same direction as propeller thrust and the use of a thrust deduction factor would result in higher vessel speed due to under-predicted braking thrust.

As the literature typically provides empirical estimates for thrust deduction factor rather than resistance augmentation factor, it is useful to have the conversion between the two [21]:

$$a_{augmented} = \left(\frac{t_{deduction}}{1 - t_{deduction}}\right) \tag{4.38}$$

Flikkema et al. provide an empirical relation that estimates the thrust deduction factor for podded propulsors as follows [41]:

$$t_{deduction} = 0.21593 + 0.099768C_B - 0.56056\frac{D_{prop}}{\sqrt{b_{vessel}d_{vessel}}} \tag{4.39}$$

Applying this empirical equation from Flikkema et al. to the *Skeena Queen* gives $t_{deduction} = 0.12$.

Similarly, Molland provides a range of thrust deduction factors for propellers that are paired with round bilge semi-displacement hulls. These deduction factors are defined by

volume Froude number:

$$Fr_{\nabla} = \frac{u_r}{\sqrt{g\nabla_{vessel}^{1/3}}} \tag{4.40}$$

where Fr_{∇} is the volume Froude number.

The *Skeena Queen* typically travels at $Fr_{\nabla} \approx 0.6$, for which Molland gives $t_{deduction} = 0.15$ [34].

In this work the thrust deduction factor for each azimuth thruster is estimated to be $t_{deduction} = 0.12$ which converts to $a_{augmented} = 0.1364$ for a single thruster, and as the M.V. *Skeena Queen* has four thrusters, the hull resistance in surge becomes:

$$\begin{aligned} X_0^A &= X_0 \left(1 + 4 \cdot a_{augmented}\right) \\ X_{tower}^A &= X_{tower} \left(1 + 4 \cdot a_{augmented}\right) \\ X_{MMG}^A &= X_{MMG} \left(1 + 4 \cdot a_{augmented}\right) \end{aligned} \tag{4.41}$$

where X_0^A, X_{tower}^A, and X_{MMG}^A are the CFD, azimuth tower, and MMG model surge resistances which have been corrected with the resistance augmentation factor.

4.3.7 Hull Resistance with Correction Factors

The consolidation of the aforementioned hull resistance correction factors results in the following modified hull resistance components:

$$\begin{aligned} X_0^{F,A} =& X_0 \left(1 + K_{hull_{fouling\,CFD}}\right) \left(1 + 4 \cdot a_{augmented}\right) \\ X_{tower}^{F,A} =& X_{tower} \left(1 + K_{hull_{fouling\,empirical}}\right) \left(1 + 4 \cdot a_{augmented}\right) \\ X_{MMG}^{F,A} =& X_{MMG} \left(1 + K_{hull_{fouling\,empirical}}\right) \left(1 + 4 \cdot a_{augmented}\right) \end{aligned}$$

$$\begin{aligned} Y_{tower}^{F} =& Y_{tower} \left(1 + K_{hull_{fouling\,empirical}}\right) \\ Y_{MMG}^{F} =& Y_{MMG} \left(1 + K_{hull_{fouling\,empirical}}\right) \end{aligned} \tag{4.42}$$

$$\begin{aligned} N_{tower}^{F} =& N_{tower} \left(1 + K_{hull_{fouling\,empirical}}\right) \\ N_{MMG}^{F} =& N_{MMG} \left(1 + K_{hull_{fouling\,empirical}}\right) \end{aligned}$$

Combining the modified hull resistance components from equation group (4.42) results

in:

$$X_{hull}^{F,A} = X_0^{F,A} + \sum_{i=1}^{4} X_{tower_i}^{F,A} + X_{MMG}^{F,A}$$

$$Y_{hull}^{F} = \sum_{i=1}^{4} Y_{tower_i}^{F} + Y_{MMG}^{F} \tag{4.43}$$

$$N_{hull}^{F} = \sum_{i=1}^{4} N_{tower_i}^{F} + N_{MMG}^{F}$$

where $X_{hull}^{F,A}$, Y_{hull}^{F}, and N_{hull}^{F} are the total surge, sway and yaw resistances acting on the hull after application of the resistance augmentation factor and fouling correction factor.

Air Resistance

A vessel's air-resistance is defined in this work as the resistance of a vessel's superstructure in calm air, absent the effects of wind. Molland et al. provide the following relation for air resistance:

$$X_{air} = 0.5\rho_{air} C_D S_{superstructure} u_r^2 \tag{4.44}$$

where X_{air} is the vessel's air resistance in surge, ρ_{air} is the density of air, C_D is the superstructure's air drag coefficient, $S_{superstructure}$ is the superstructure's projected area perpendicular to the surge direction of travel and u_r is the ship's velocity in surge.

Considering that the provided vessel CAD model was without the vessel's superstructure, the Skeena Queen's air drag needed to be estimated.

Molland et al. provide a table with empirical values of air drag as a percentage of the vessel's total resistance for a variety of vessels. The air drag for a similar sized ferry (650 passengers, 150 cars) was given as 4% of the vessel's overall resistance [34].

Assuming that the 4% value was provided at the vessel's design speed, and noting that X_{air} is proportional to u^2, the air-drag resistance is estimated as:

$$X_{air} = \underbrace{\left(\frac{0.04}{1-0.04}\right) \cdot \left(\frac{X_{hull\ design}^{F,A}}{u_{design}^2}\right)}_{K_{air}} \cdot u^2 \tag{4.45}$$

where u_{design} is the vessel's design velocity and $X_{hull\ design}^{F,A}$ is the hull resistance at the design velocity after correcting for appendages, fouling, and propeller-hull interactions. The constants in equation (4.45) were grouped into an air resistance coefficient K_{air} which is then

multiplied by the vessel's relative surge velocity squared to compute air resistance during simulation.

Note that when $u = u_{design}$, the air-resistance is simply 4% of the vessel's total surge resistance, or $X_{air} = \left(\frac{0.04}{1-0.04}\right) X^{F,A}_{hull\ design}$.

Revised Equations of Motion

After incorporating the hull appendage resistance, hull correction factors and air resistance into equation (4.26), and noting that propeller thrust is also corrected for fouling as shown in equation (4.9), the revised equations of motion in the hybrid MMG model become:

$$\begin{aligned} (m + m_x)\,\dot{u} &= X^{F,A}_{hull} + X_{air} + X^{F}_{props} \\ (m + m_y)\,\dot{v} &= Y^{F}_{hull} + Y^{F}_{props} \\ \left(I_{zz} + J_{zz} + (m + m_y)x_G^2\right)\dot{r} &= N^{F}_{hull} + N^{F}_{props} \end{aligned} \tag{4.46}$$

Chapter 5

Simulation for Obtaining Vessel Operational Profiles

5.1 Structure Overview

As one of the key objectives of this work was to accurately predict a vessel's power time-series over the course of a voyage, a MBD simulation was built within the MATLAB/Simulink environment to predict a vessel's motion and calculate propulsion power throughout a simulated journey. The modelling groundwork that was laid out in Chapter 4 serves as the foundation of the simulation structure which in turn consists of the following subsystems:

- Helmsperson Subsystem
- Propeller Subsystem
- Vessel Subsystem
- Environment Subsystem
- Visualization Subsystem

A simplified representation of the MBD marine simulation architecture is provided in Figure 5.1.

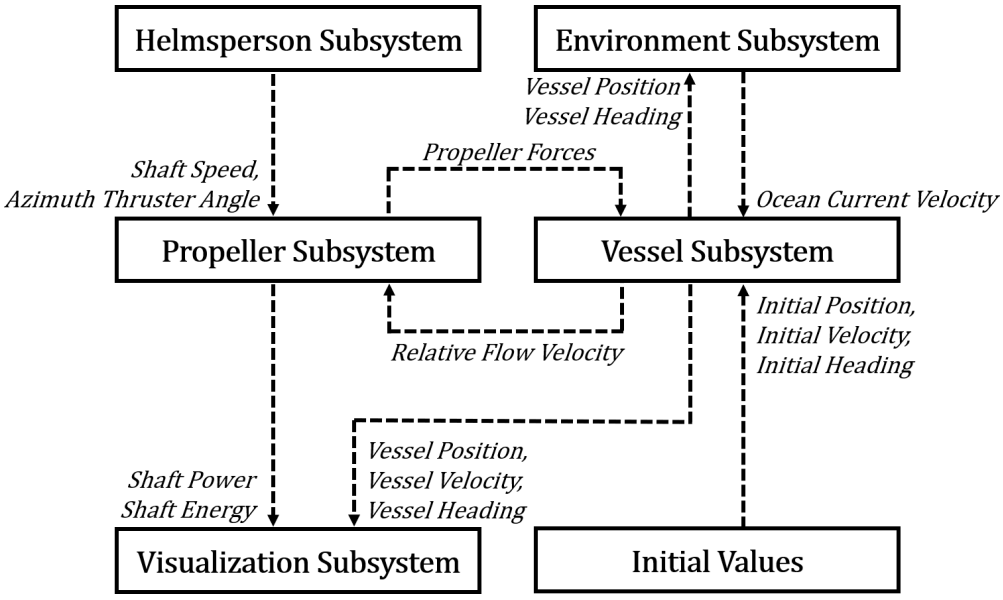

Figure 5.1: MBD Marine Simulation Architecture

The following sections provide further details of the MBD marine simulation platform and its subsystems. Once the simulation structure has been laid out, the Chapter concludes with a more detailed simulation flow diagram that is provided in Figure 5.24.

5.2 Reference Frames

Several frames of references are used within the simulation to compute the motion of the vessel and describe its position.

Body-Fixed Frame

The body-fixed reference frame, $\{b\}$, is fixed to the vessel with its origin, o_b, lying at the vessel's geometric centre at the waterline, CO (see Section 4.3). The x_b-axis points to the vessel's bow, the y_b-axis points to starboard, and the z_b–axis points downward into the Earth.

Azimuth-Fixed Frame

The azimuth-fixed frames, $\{azi_{1,2,3,4}\}$, are fixed to the four azimuth towers with their origins, $o_{azi_{1,2,3,4}}$, lying on the azimuth thruster axes of rotation. The $\{azi_{1,2,3,4}\}$ frames are fixed with respect to the body-fixed frame, $\{b\}$, such that the x_{azi}-axes are parallel with the x_b-axis, and the y_{azi}-axes are parallel with the y_b-axis as show in Figure 5.2. The z_{azi}-axes point downwards into the Earth.

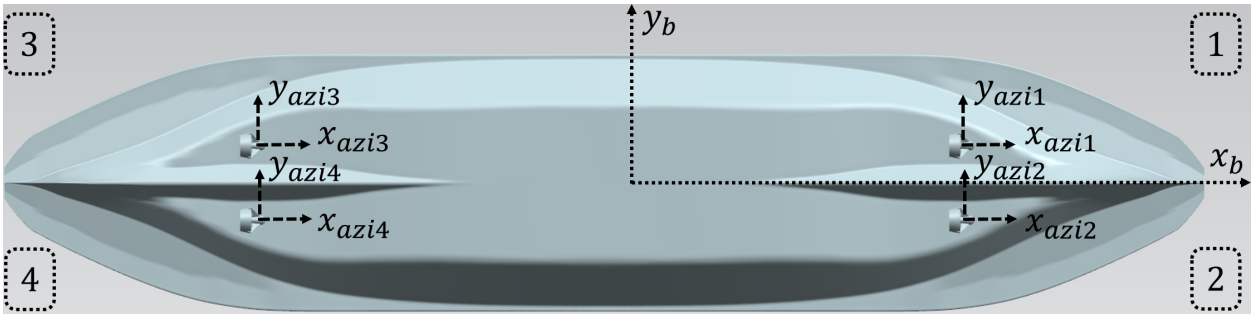

Figure 5.2: Body and Azimuth Reference Frames – Bottom View

Propeller-Fixed Frame

The propeller-fixed frames, $\{prop_{1,2,3,4}\}$, are fixed to the four propellers with their origins, $o_{prop_{1,2,3,4}}$, laying at the origins of the propellers as defined by the propeller design drawing. The $\{prop_{1,2,3,4}\}$ frames rotate with respect to the azimuth frames, $\{azi_{1,2,3,4}\}$, by the azimuth angles, $\theta_{azi_{1,2,3,4}}$, which are commanded by the helmsperson during manoeuvring (Figure 5.3). The propeller frames are fixed to the propellers such that the x_{prop}-axes are aligned with the x_{azi}-axes, and the y_{prop}-axes are parallel with the y_{azi}-axes when the azimuth angles of rotation are zero ($\theta_{azi_{1,2,3,4}} = 0$). The z_{prop}-axes point downward into the Earth.

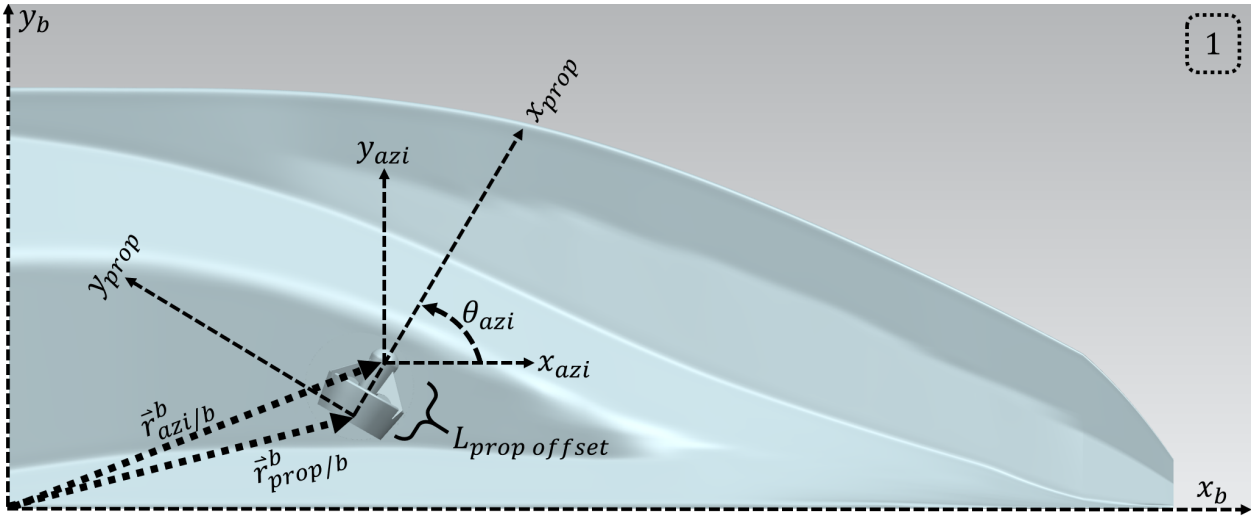

Figure 5.3: Body, Propeller and Azimuth Reference Frames – Bottom View

North-East-Down Frame

The North-East-down (NED) reference frame, $\{n\}$, is a plane that lies tangent to the Earth's surface with its origin, o_n, coincident to the Earth's surface near the location of the vessel. The frame's x_n-axis points North, its y_n-axis points East, and its z_n-axis points downward

into the Earth.

Earth-Centred, Earth-Fixed Frame

The Earth-centred, Earth-fixed (ECEF) reference frame is denoted by $\{e\}$, and its origin, o_e, lies at the centre of the Earth. The frame rotates with the Earth and is fixed such that its x_e-axis intersects the Earth's prime meridian, and its z_e-axis intersects the Geographic North Pole.

5.3 Simulation States and Transformations

Simulation states are used to describe and track the state of the vessel throughout a simulation while transformations allow for a simulation state described in particular frame to be expressed in an alternate frame.

States and Transformations in the Body-Fixed Frame

The linear and angular velocities of the ship at o_b with respect to the NED frame $\{n\}$ expressed in the body-fixed frame $\{b\}$ are:

$$\boldsymbol{\nu}^b_{b/n} = [u, v, r]^\mathsf{T}$$

The linear and angular accelerations of the ship at o_b with respect to the NED frame $\{n\}$, expressed in the body-fixed frame $\{b\}$ are:

$$\dot{\boldsymbol{\nu}}^b_{b/n} = [\dot{u}, \dot{v}, \dot{r}]^\mathsf{T}$$

The linear and angular velocities of the ship at o_b relative to the local ocean surface (to account for ocean currents) expressed in the body-fixed frame $\{b\}$ are:

$$\boldsymbol{\xi}^b_{b/n} = [u_r, v_r, r]^\mathsf{T}$$

Similarly, the total forces and moments acting on the vessel at o_b expressed in the body-fixed frame $\{b\}$ are given by:

$$\boldsymbol{\tau}^b_b = [X_{force}, Y_{force}, N_{moment}]^\mathsf{T}$$

States and Transformations in the Azimuth-Fixed and Propeller-Fixed Frames

The location of an azimuth thruster origin, o_{azi}, expressed in the body-fixed frame, is constant with respect to o_b and is given by:

$$\vec{\mathbf{r}}^{\,b}_{azi/b} = [x_{azi/b}, y_{azi/b}, 0]^\mathsf{T}$$

Due to the offset between the propeller and the azimuth thruster's axis of rotation, the location of the propeller, o_{prop}, as expressed in the body-fixed frame, varies with θ_{azi} and is given by:

$$\vec{\mathbf{r}}^{\,b}_{prop/b} = \vec{\mathbf{r}}^{\,b}_{azi/b} + \begin{bmatrix} -L_{prop\,offset} \cdot \cos(\theta_{azi}) \\ -L_{prop\,offset} \cdot \sin(\theta_{azi}) \\ 0 \end{bmatrix}$$

where the propeller offset is denoted by $L_{prop\,offset}$ as shown in Figure 5.4.

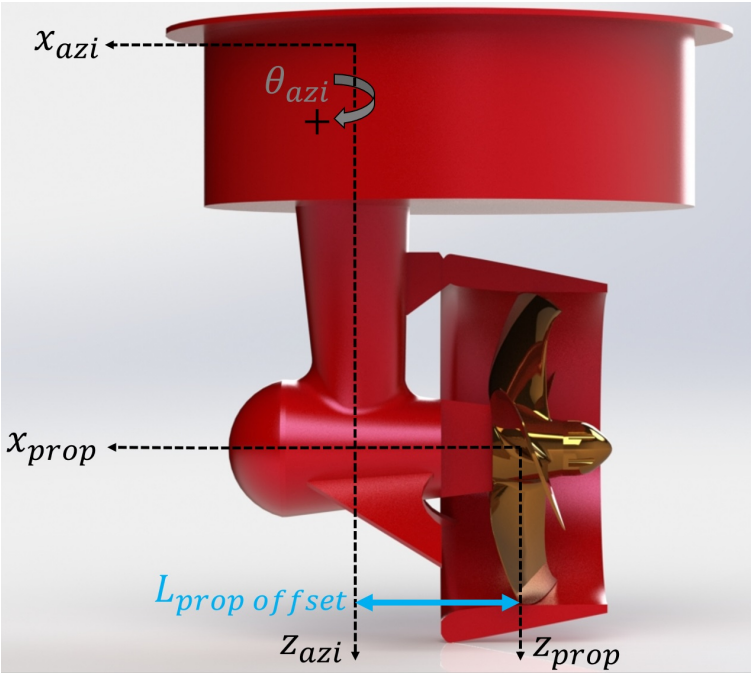

Figure 5.4: Offset between Azimuth Thruster and Propeller – Right View

The thrust forces produced by the propeller at o_{prop}, expressed in the propeller-fixed frame are given by:

$$\boldsymbol{\tau}^{prop}_{prop} = [T_{prop_x}, T_{prop_y}, 0]^\mathsf{T}$$

The propeller forces and velocities can be transformed from the propeller-fixed frame, $\{prop\}$, to the body-fixed frame, $\{b\}$ with a rotation between $\{prop\}$ and $\{b\}$.

The rotation matrix from the propeller-fixed frame to the body-fixed frame is $\mathbf{R}^b_{prop}$, which in 3 DOF reduces to:

$$\mathbf{R}^b_{prop} = \begin{bmatrix} \cos(\theta_{azi}) & -\sin(\theta_{azi}) & 0 \\ \sin(\theta_{azi}) & \cos(\theta_{azi}) & 0 \\ 0 & 0 & 1 \end{bmatrix} \tag{5.1}$$

where θ_{azi} is the azimuth thruster angle as previously described. Conversely, the rotation matrix from the body-fixed frame to the propeller-fixed frame is $\mathbf{R}^{prop}_b = \mathbf{R}^{b\mathsf{T}}_{prop}$.

States and Transformations in North-East-Down Frame

The location of a vessel in the NED frame $\{n\}$, is given by:

$$\vec{\mathbf{r}}^n_{b/n} = [N_{b/n}, E_{b/n}, 0]^\mathsf{T}$$

The vessel's heading with respect to true North, ψ, is the angle between the NED frame's x_n-axis and the vessel's x_b-axis as shown in Figure 5.5.

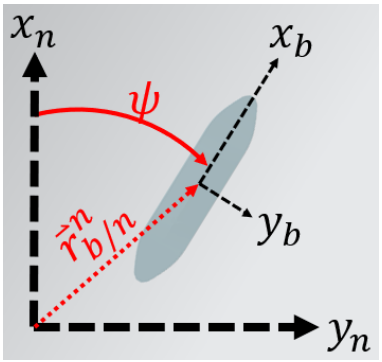

Figure 5.5: NED and Body Reference Frames
Source: adapted from Fossen [11]

A vessel's combined position and orientation state in the NED frame is given by:

$$\boldsymbol{\eta}^n_{b/n} = [N_{b/n}, E_{b/n}, \psi]^\mathsf{T}$$

The velocity of the ship with respect to the NED frame can be transformed from the body-fixed frame, $\{b\}$, to the NED frame, $\{n\}$ with:

$$\dot{\boldsymbol{\eta}}^n_{b/n} = \mathbf{R}^n_b \boldsymbol{\nu}^b_{b/n} \tag{5.2}$$

where $\mathbf{R}_b^n$ is a rotation matrix from the body-fixed frame to the NED frame, and where $\mathbf{R}_b^n = \mathbf{R}_n^{b\mathsf{T}}$. In 3 DOF, $\mathbf{R}_n^b$ reduces to [11]:

$$\mathbf{R}_n^b = \begin{bmatrix} \cos(\psi) & -\sin(\psi) & 0 \\ \sin(\psi) & \cos(\psi) & 0 \\ 0 & 0 & 1 \end{bmatrix} \tag{5.3}$$

Given an initial position and heading, $[N_{b/n\,0}, E_{b/n\,0}, \psi_0]^\mathsf{T}$, and noting that in 3 DOF, the ship's angular velocity in $\{n\}$ is simply equal to the vessel's yaw rate ($\dot{\psi} \approx r$), a ship's position $\boldsymbol{\eta}_{b/n}^n$ can be updated by numerically integrating the vessel's motion, $\dot{\boldsymbol{\eta}}_{b/n}^n$, over the course of a journey with:

$$\boldsymbol{\eta}_{b/n}^n(t) = \int_0^t \dot{\boldsymbol{\eta}}_{b/n}^n(t)\, dt \tag{5.4}$$

States and Transformations in Earth-Centred-Earth-Fixed Frame

A vessel's position on the surface of the Earth can be described in ECEF Cartesian coordinates where position is given by:

$$\mathbf{p}_{b/e}^e = [x_{b/e}, y_{b/e}, z_{b/e}]^\mathsf{T}$$

or alternatively by two angles:

$$\boldsymbol{\Theta}_{b/e}^e = [\mu, l]^\mathsf{T}$$

where μ, and l, are the well-known angles of latitude and longitude respectively.

Figure 5.6 shows the ECEF frame and the location of a NED frame at the Earth's surface given by latitude and longitude.

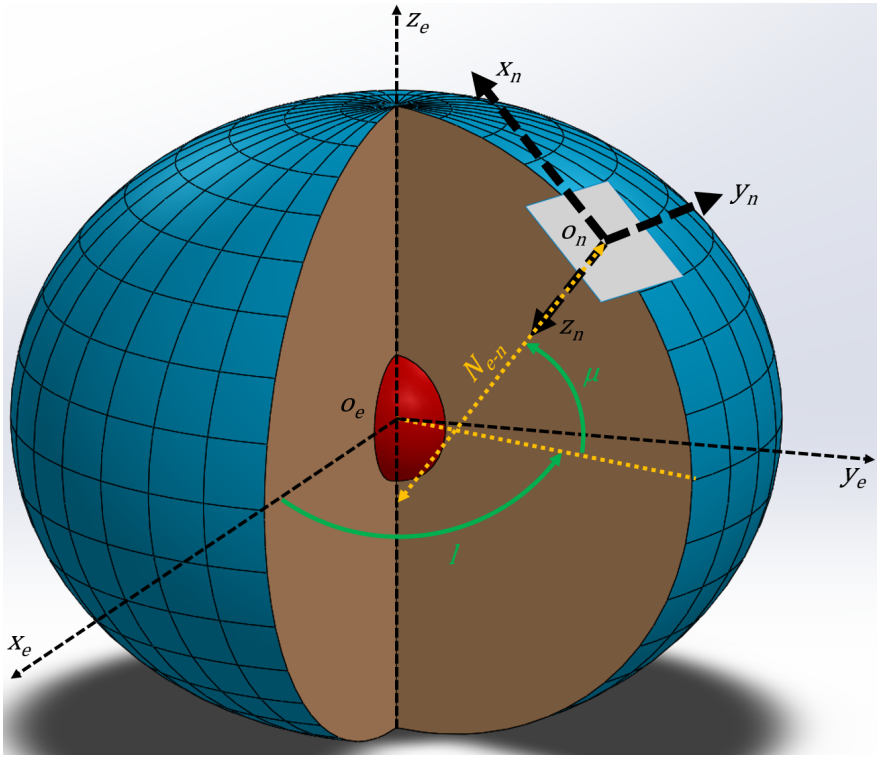

Figure 5.6: ECEF and NED Reference Frames (Ellipse Proportions Exaggerated)

While ship heading, ψ, is given in $\{n\}$, global navigation necessitates that position be given with respect to $\{e\}$. The velocity of the ship in the $\{n\}$ frame, $\dot{\boldsymbol{\eta}}^n_{b/n}$ can be transformed to the $\{e\}$ frame with:

$$\dot{\mathbf{p}}^e_{b/e} = \mathbf{R}^e_n \dot{\boldsymbol{\eta}}^n_{b/n} \tag{5.5}$$

where $\mathbf{R}^e_n$ is a rotation matrix between ECEF and NED [11] given by:

$$\mathbf{R}^e_n = \begin{bmatrix} -\cos(l)\sin(\mu) & -\sin(l) & -\cos(l)\cos(\mu) \\ -\sin(l)\sin(\mu) & \cos(l) & -\sin(l)\cos(\mu) \\ \cos(\mu) & 0 & -\sin(\mu) \end{bmatrix} \tag{5.6}$$

Combining equations (5.2) and (5.5), the velocity of a vessel in the body-fixed frame, $\{b\}$, can be transformed directly to $\{e\}$ with:

$$\dot{\mathbf{p}}^e_{b/e} = \mathbf{R}^e_n \mathbf{R}^n_b \boldsymbol{\nu}^b_{b/n} \tag{5.7}$$

Given an initial position in ECEF ($\mathbf{p}^e_{b/e} = [x_{b/e\,0}, y_{b/e\,0}, z_{b/e\,0}]$), the vessel's velocity $\dot{\mathbf{p}}^e_{b/e}$ can be numerically integrated over the course of a journey to update the vessel's position in

ECEF with:

$$\mathbf{p}^e_{b/e}(t) = \int_0^t \dot{\mathbf{p}}^e_{b/e}(t)\, dt \tag{5.8}$$

A transformation from ECEF coordinates, $\mathbf{p}^e_{b/e} = [x_{b/e}, y_{b/e}, z_{b/e}]^T$, to latitude and longitude, can be accomplished with the following equations [11]:

Longitude is found with:

$$l = tan^{-1}\left(\frac{y_{b/e}}{x_{b/e}}\right) \tag{5.9}$$

Latitude is computed by:

$$\mu = tan^{-1}\left(\frac{z_{b/e}}{\sqrt{x^2_{b/e} + y^2_{b/e}}}\left[1 - \left(1 - \frac{r_{minor}}{r_{major}}\right)\frac{N_{e-n}}{N_{e-n} + h_{sea}}\right]^{-1}\right) \tag{5.10}$$

where h_{sea} is the height above sea-level given with:

$$h_{sea} = \frac{\sqrt{x^2_{b/e} + y^2_{b/e}}}{\cos(\mu)} - N_{e-n} \tag{5.11}$$

The length N_{e-n} is calculated using:

$$N_{e-n} = \frac{r^2_{major}}{\sqrt{r^2_{major}\cos^2(\mu) + r^2_{minor}\sin^2(\mu)}} \tag{5.12}$$

where r_{major} and r_{minor} are the radii of the semi-major and semi-minor axes of the WGS-84 Earth reference ellipsoid.

As these equations are implicit, they are solved iteratively until reaching a specified level of tolerance. Fossen [11] cites an algorithm in Hofmann-Wellenhof et al. [42] that computes position as follows:

1) Compute an approximate value for latitude, μ_0, with:

$$\mu_0 = tan^{-1}\left(\frac{z_{b/e}}{\sqrt{x^2_{b/e} + y^2_{b/e}}}\left(\frac{r_{minor}}{r_{major}}\right)^{-1}\right)$$

2) Compute an approximate value of N_{e-n} with:

$$N_{e-n} = \frac{r^2_{major}}{\sqrt{r^2_{major}\cos^2(\mu_0) + r^2_{minor}\sin^2(\mu_0)}}$$

3) Compute height:

$$h_{sea} = \frac{\sqrt{x_{b/e}^2 + y_{b/e}^2}}{\cos(\mu)} - N_{e-n}$$

4) Compute an updated value for latitude:

$$\mu = tan^{-1}\left(\frac{z_{b/e}}{\sqrt{x_{b/e}^2 + y_{b/e}^2}}\left[1 - \left(1 - \frac{r_{minor}}{r_{major}}\right)\frac{N_{e-n}}{N_{e-n} + h_{sea}}\right]^{-1}\right)$$

5) Check if the difference between the estimated and computed latitude is within tolerance:

   a) If $|\mu - \mu_0| \geq tolerance$, set $\mu_0 = \mu$ and continue from Step 2, otherwise,

   b) If $|\mu - \mu_0| < tolerance$, no further iteration is required

Within the MBD simulation, it is the location of the ship that is of interest, and seeing that the origin of the vessel o_b is assumed to always be at sea-level, the height above sea-level is then also always be zero. With $h_{sea} = 0$, latitude simply becomes:

$$\mu = tan^{-1}\left(\frac{z_{b/e}}{\sqrt{x_{b/e}^2 + y_{b/e}^2}}\left(\frac{r_{minor}}{r_{major}}\right)^{-1}\right) \tag{5.13}$$

and no iterative algorithm is required.

If a position is given in latitude, longitude and height above sea level, it can also be converted back to ECEF Cartesian coordinates. After finding N_{e-n} using equation (5.12), the position $\mathbf{p}_{b/e}^e = [x_{b/e}, y_{b/e}, z_{b/e}]^T$ is found with [11]:

$$\begin{aligned} x_{b/e} &= (N_{e-n} + h_{sea})\cos(\mu)\cos(l) \\ y_{b/e} &= (N_{e-n} + h_{sea})\cos(\mu)\sin(l) \\ z_{b/e} &= \left[N_{e-n}\left(\frac{r_{minor}}{r_{major}}\right)^2 + h_{sea}\right]\sin(\mu) \end{aligned} \tag{5.14}$$

5.4 Initial Values

Initial values are provided to initialize the state of the system at time zero of the simulation. These values are provided to the vessel subsystem module as shown in Figure 5.7.

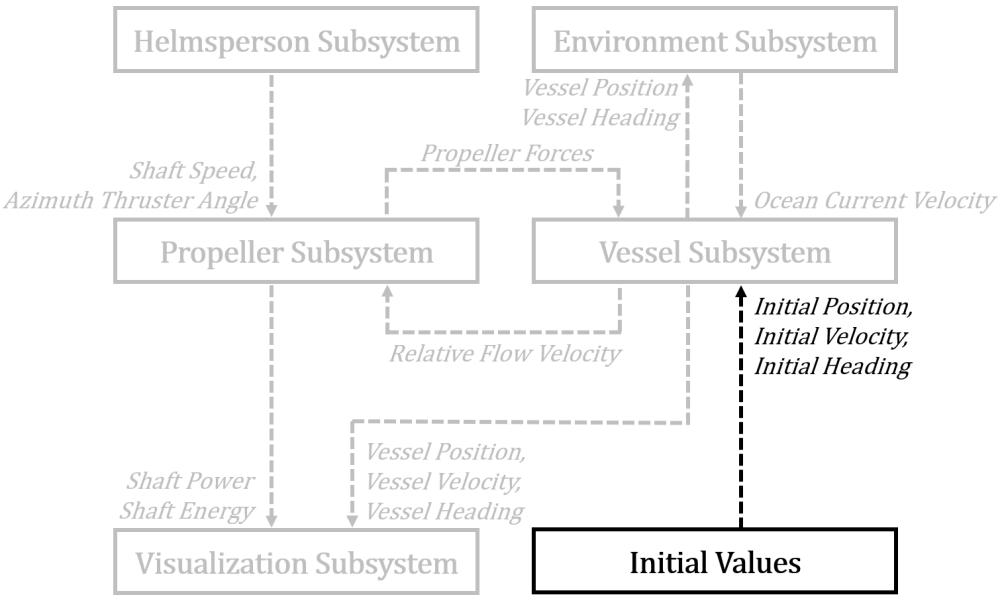

Figure 5.7: MBD Marine Simulation Architecture – Initial Values

The initial velocity of the *Skeena Queen* at berth in the body-fixed frame is given as:

$$\boldsymbol{\nu}^b_{b/n\,0} = [0, 0, 0]^\mathsf{T}$$

The initial position and orientation of the ship in the NED frame is given as:

$$\boldsymbol{\eta}^n_{b/n} = [0, 0, \psi_0]^\mathsf{T}$$

where the heading ψ_0 is estimated from the geographical orientation of the ferry terminal and the initial trajectory of the recorded vessel path.

The initial latitude and longitude is extracted from the *Skeena Queen*'s recorded GPS data and given as:

$$\boldsymbol{\Theta}^e_{b/e} = [\mu_0, l_0]^\mathsf{T}$$

Finally, the initial position of the vessel in the ECEF frame is given by converting $[\mu_0, l_0]^\mathsf{T}$ to ECEF coordinates using equation group (5.14), and results in:

$$\mathbf{p}^e_{b/e} = [x_{b/e\,0}, y_{b/e\,0}, z_{b/e\,0}]^\mathsf{T}$$

5.5 Helmsperson Subsystem

The helmsperson subsystem module is intended to mimic the control actions performed by a helmsperson steering a ship. In the case of the M.V. *Skeena Queen*, the helmsperson controls the motion of the ship by varying engine speed (which in turn varies propeller speed), and by rotating the angle of the four azimuth thrusters to direct thrust in the desired direction.

In this work, the helmsperson inputs are supplied directly from time-series data that were recorded during M.V. *Skeena Queen* ferry crossings. The simulated vessel is driven by feeding recorded shaft speeds ($n_{shaft_{1,2,3,4}}$) and recorded azimuth thruster angles ($\theta_{azi_{1,2,3,4}}$) into the propeller subsystem as depicted in Figure 5.8. The simulation then calculates the resulting propeller forces and moments and computes the motion of the vessel.

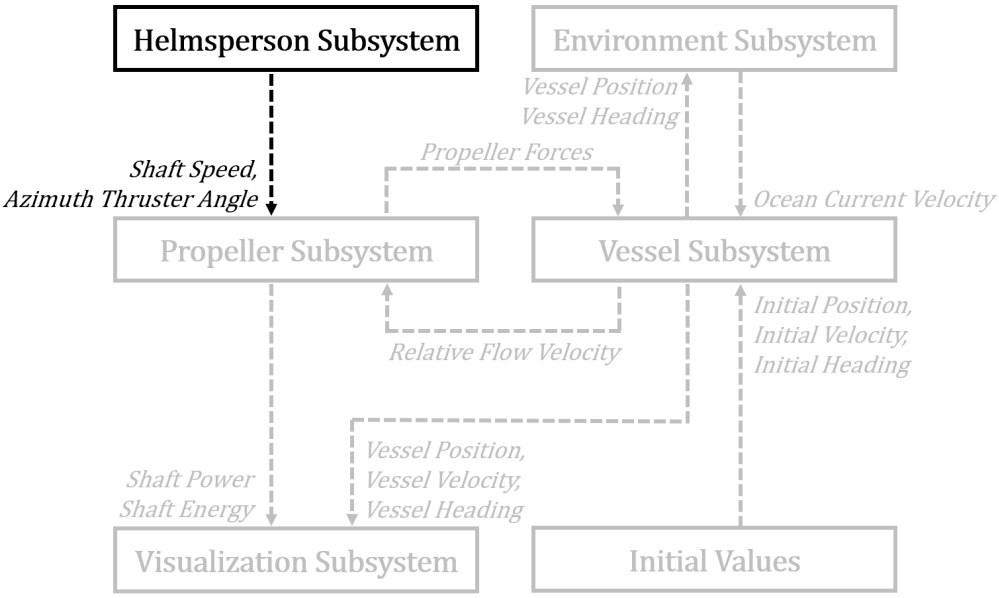

Figure 5.8: MBD Marine Simulation Architecture – Helmsperson Subsystem

The use of recorded helmsperson inputs is essential for assessing the accuracy of the simulation as is discussed in Chapter 6. However, as the intention of this work is to pave the way for the generation of power time-series using virtual ships that are still in the design phase, it should be noted that recorded helmsperson inputs will not be available for this intended purpose.

Future expansions of the helmsperson subsystem will need to include guidance, navigation and control capabilities, or essentially an autopilot that is capable of piloting a vessel along a user defined trajectory. With this addition, a user would define georeferenced waypoints consisting of latitude, longitude and ship speed, and the autopilot would guide the ship along the path to generate virtual drive-cycle data. In the case of the M.V. *Skeena Queen*,

the autopilot would need to solve for the shaft speeds and azimuth angles commanded to the four azimuth thrusters, a non-trivial problem that has been addressed by Fossen and Perez [43] who present a general approach to the thrust allocation control problem for ships with multiple azimuthing thrusters.

5.6 Propeller Subsystem

The propeller subsystem receives the shaft speed and azimuth angle inputs from the helmsperson subsystem, as well as relative flow velocity from the vessel subsystem. The propeller subsystem is responsible for calculating propeller thrust and power as shown in Figure 5.9.

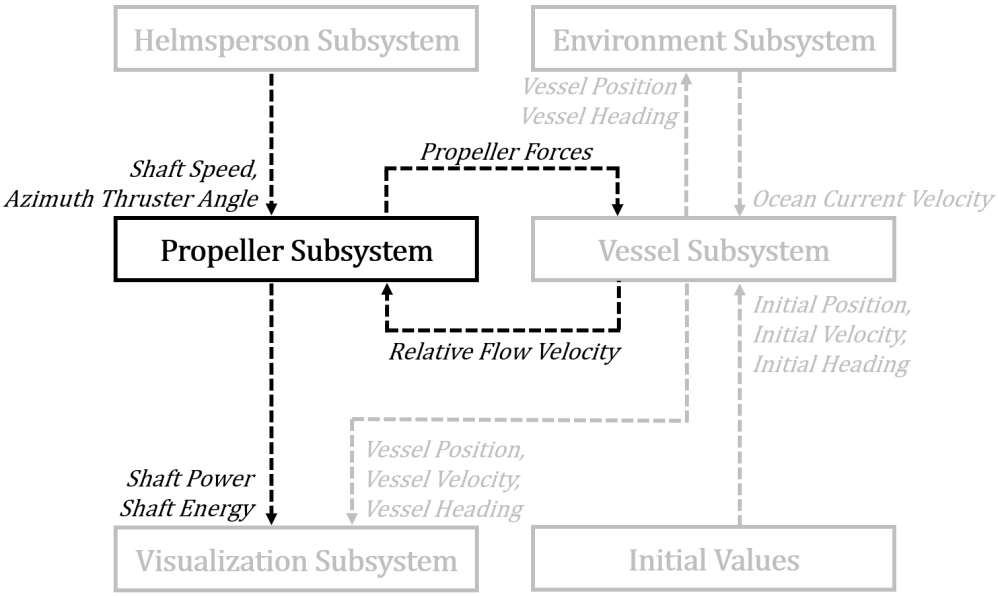

Figure 5.9: MBD Marine Simulation Architecture – Propeller Subsystem

The azimuth angles ($\theta_{azi_{1,2,3,4}}$) received from the helmsperson subsystem are utilized as-is, but the shaft speeds, $n_{shaft_{1,2,3,4}}$, are converted to propeller speeds, $n_{prop_{1,2,3,4}}$, by applying the gear ratio embedded within the azimuth thruster tower:

$$n_{prop} = n_{shaft} K_{gearbox} \tag{5.15}$$

where K_{gear} is the gear ratio between the shaft and the propeller.

The relative velocity of the ship received from the vessel subsystem module, $\boldsymbol{\xi}^b_{b/n} = [u_r, v_r, r]^\mathsf{T}$, is used to find the relative velocity at the location of the propeller after factoring in wake fraction.

The fore and aft wake fractions are computed by feeding ship relative velocity into the 1D

wake fraction look-up tables that were built with CFD velocity measurements (see Section 4.2.4). The look-up tables output the fore and aft wake fractions as shown in Figure 5.10.

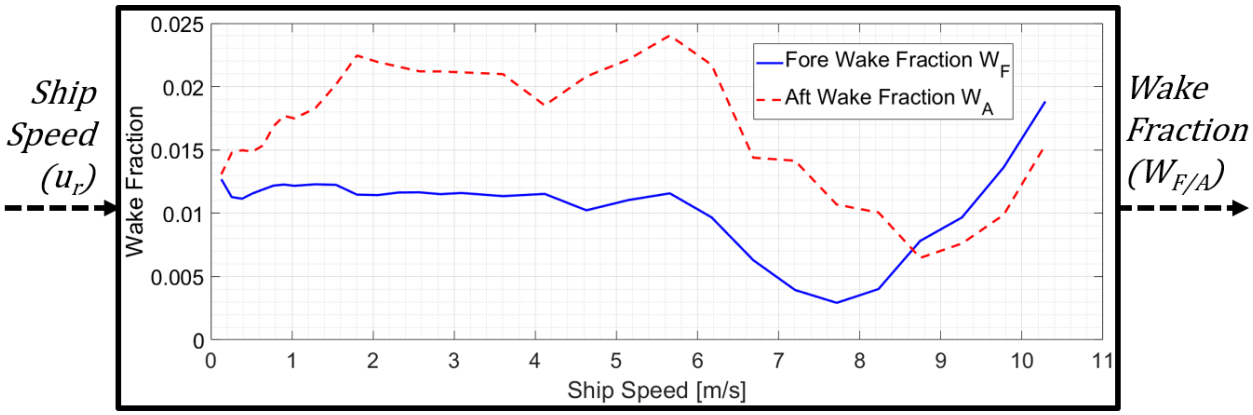

Figure 5.10: Fore and Aft Wake Fraction Look-up Table Inputs and Output

The relative velocity at the propeller, o_{prop}, expressed in the body-fixed frame is then calculated with:

$$\begin{bmatrix} u_{prop} \\ v_{prop} \\ 0 \end{bmatrix}_{\{b\}} = \begin{bmatrix} u_r(1 - W_{F/A}) \\ v_r \\ 0 \end{bmatrix}_{\{b\}} + \begin{bmatrix} 0 \\ 0 \\ r \end{bmatrix}_{\{b\}} \times \vec{\mathbf{r}}^{\,b}_{prop/b}(\theta_{azi}) \tag{5.16}$$

where the notation $\vec{\mathbf{r}}^{\,b}_{prop/b}(\theta_{azi})$ is to signify that the distance from o_b to o_{prop} is a function of the azimuth angle, θ_{azi}. Note that equation (5.16) accounts for relative velocity at the propeller induced by the ship's yaw rate (r), and also that wake fraction is not applied to the relative sway velocity, v_r, as wake fraction in this direction was not measured in CFD and is assumed to be negligible.

As the M.V. *Skeena Queen*'s helmsperson changes the direction of a thruster, the propeller swings about the azimuth tower's axis of rotation (o_{azi}) at a maximum tangential velocity of $[L_{prop\,offset} \cdot \dot{\theta}_{azi}]$, a motion which contributes to the relative velocity at the propeller's location. Due to poor results when attempting to differentiate the recorded azimuth angle position, θ_{azi}, the contribution of $\dot{\theta}_{azi}$ to the relative velocity at the propeller was ignored. After reviewing the thruster's maximum rotation speed [20], the largest possible contribution from $\dot{\theta}_{azi}$ was confirmed to be minimal for this case study.

As the propeller thrust and torque look-up tables were generated with respect to the propeller-fixed reference frame $\{prop\}$, the relative velocity of the propeller as expressed in the vessel's body-fixed frame is rotated so that it is expressed in the propeller-fixed frame

with:

$$\begin{bmatrix} u_{prop} \\ v_{prop} \\ 0 \end{bmatrix}_{\{prop\}} = \mathbf{R}_b^{prop}(\theta_{azi}) \begin{bmatrix} u_{prop} \\ v_{prop} \\ 0 \end{bmatrix}_{\{b\}} \tag{5.17}$$

where the notation $\mathbf{R}_b^{prop}(\theta_{azi})$ is to signify that the rotation matrix from o_b to o_{prop} is a function of azimuth angle, θ_{azi} as illustrated in Figure 5.11.

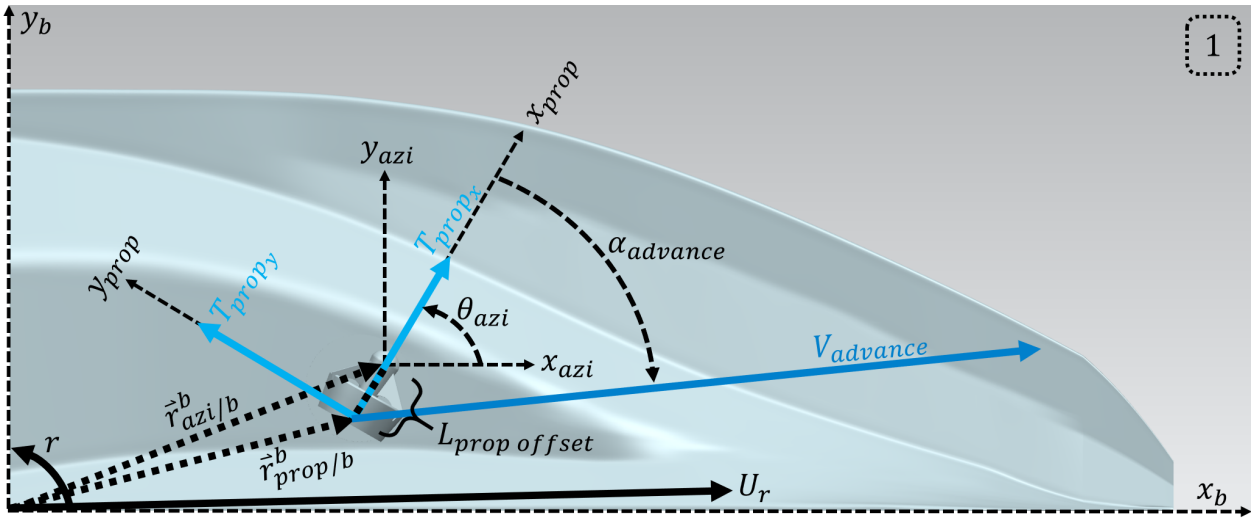

Figure 5.11: Body, Propeller and Azimuth Reference Frames with Thrust – Bottom View

The advance velocity and advance angle at the propeller are then calculated using the relative velocities expressed in the propeller-fixed frame:

$$\begin{aligned} V_{advance} &= \sqrt{u_{prop}^2 + v_{prop}^2} \\ \alpha_{advance} &= atan2\left(\frac{v_{prop}}{u_{prop}}\right) \end{aligned} \tag{5.18}$$

and the advance ratio is calculated with:

$$J_{advance} = \frac{V_{advance}}{\left(\frac{1}{2\pi} n_{prop}\right) D_{prop}} \tag{5.19}$$

where n_{prop} is the propeller speed fed into the simulation through the helmsperson subsystem and D_{prop} is the propeller diameter.

To avoid division by zero, a nominal lower limit for propeller speed is set such that if $|n_{prop}| \leq n_{limit}$, then $n_{prop} = \pm n_{limit}$, where n_{limit} is the lower limit for propeller speed.

Computing Propeller Thrust with CFD Look-up Tables

Once the propeller advance ratio and inflow angle have been calculated, they are fed into the thrust look-up tables which output pre-computed thrust coefficients as shown in Figure 5.12.

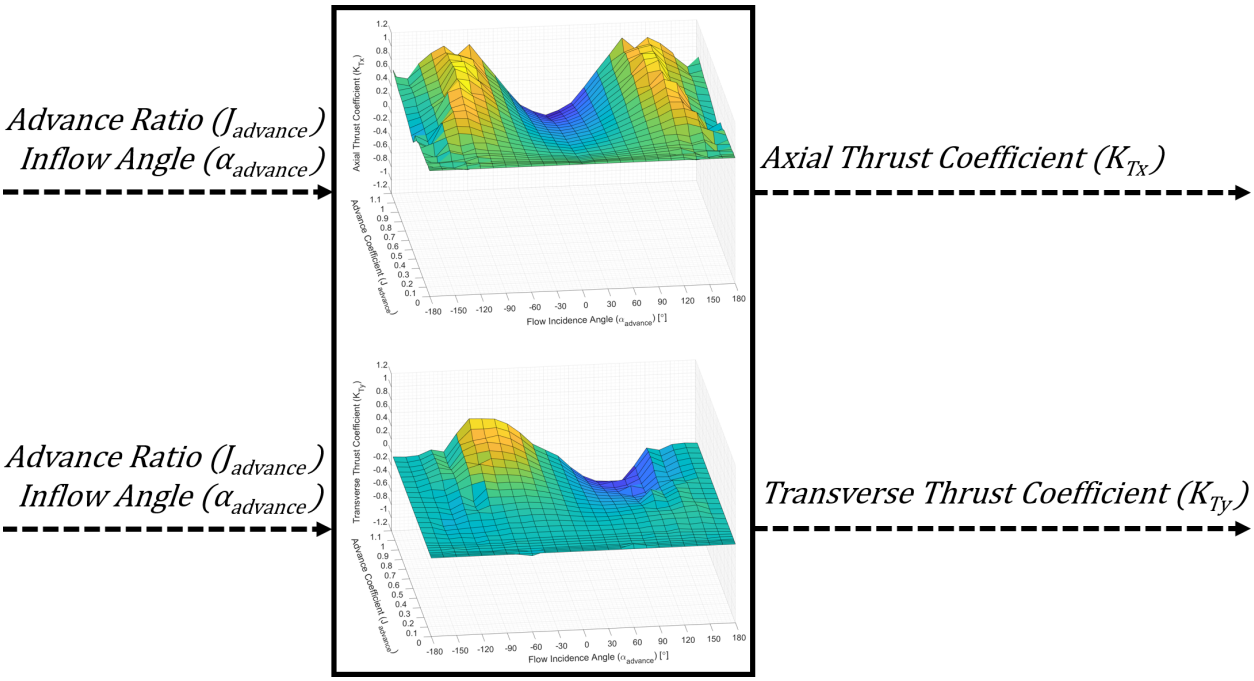

Figure 5.12: Propeller Thrust and Torque Look-up Table Inputs and Outputs

In parallel, the propeller advance ratio is also fed into the fouling correction look-up table which outputs the fouling thrust correction factor as shown in Figure 5.13.

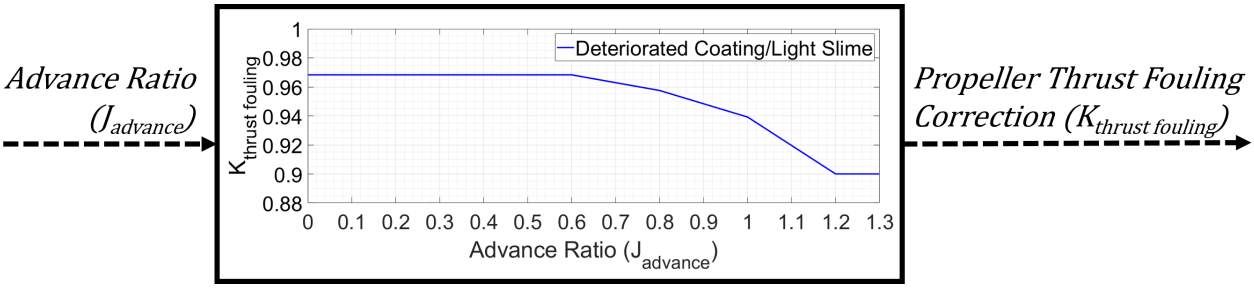

Figure 5.13: Propeller Fouling Thrust Correction Factor Look-up Table Input and Output

Re-arranging equation group (4.2), propeller thrust is calculated with the thrust coeffi-

cients and fouling correction factor as follows:

$$\begin{aligned} T^F_{prop_x} &= K_{Tx} \cdot \rho \left(\frac{1}{2\pi} n_{prop} \right)^2 D^4_{prop} \cdot K_{thrust_{fouling}} \\ T^F_{prop_y} &= K_{Ty} \cdot \rho \left(\frac{1}{2\pi} n_{prop} \right)^2 D^4_{prop} \cdot K_{thrust_{fouling}} \end{aligned} \tag{5.20}$$

The resulting propeller forces acting at o_{prop} are expressed in the propeller-fixed frame. These propeller forces are then expressed in the vessel's body-fixed frame with:

$$\begin{bmatrix} T^F_{prop_x} \\ T^F_{prop_y} \\ 0 \end{bmatrix}_{\{b\}} = \mathbf{R}^b_{prop}(\theta_{azi}) \begin{bmatrix} T^F_{prop_x} \\ T^F_{prop_y} \\ 0 \end{bmatrix}_{\{prop\}} \tag{5.21}$$

With the propeller thrust forces at o_{prop} now expressed in the vessel's body-fixed frame, the thrust forces and moments acting about the vessel's origin o_b can be calculated by appending the thrust induced moment as follows:

$$\begin{bmatrix} X^F_{prop} \\ Y^F_{prop} \\ N^F_{prop} \end{bmatrix}_{\{b\}} = \begin{bmatrix} T^F_{prop_x} \\ T^F_{prop_y} \\ 0 \end{bmatrix}_{\{b\}} + \vec{\mathbf{r}}^b_{prop/b}(\theta_{azi}) \times \begin{bmatrix} T^F_{prop_x} \\ T^F_{prop_y} \\ 0 \end{bmatrix}_{\{b\}} \tag{5.22}$$

As this process is repeated for each of the four azimuth thrusters, the forces and moments are summed into total propeller forces and moments such that:

$$\begin{bmatrix} X^F_{props} \\ Y^F_{props} \\ N^F_{props} \end{bmatrix}_{\{b\}} = \sum_{i=1}^{4} \begin{bmatrix} X^F_{prop\,i} \\ Y^F_{prop\,i} \\ N^F_{prop\,i} \end{bmatrix}_{\{b\}} \tag{5.23}$$

With equation (5.23) resulting in the total propeller forces and moments that are provided to the vessel subsystem to calculate the motion of the vessel.

Computing Propeller Torque and Power with CFD Look-up Tables

In parallel to the thrust calculation, the advance ratio and inflow angle are also fed into the propeller torque look-up table to output a pre-computed torque coefficient as shown in Figure 5.14.

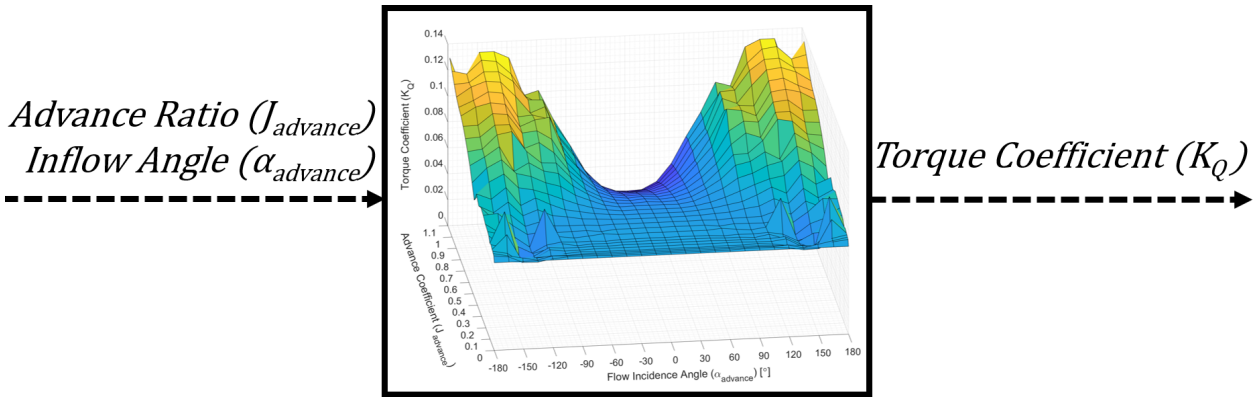

Figure 5.14: Propeller Torque Look-up Table Input and Output

Simultaneously, the propeller advance ratio is also fed into the fouling correction look-up table which outputs the fouling torque correction factor as shown in Figure 5.15.

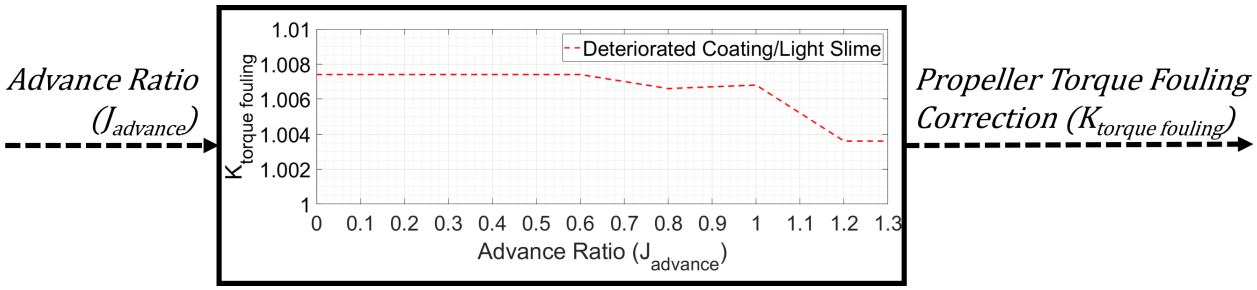

Figure 5.15: Propeller Fouling Torque Correction Factor Look-up Table Input and Output

By re-arranging equation (4.3), propeller torque is calculated using the torque coefficient and fouling correction factor as follows:

$$Q^F_{prop} = K_Q \cdot \rho \left(\frac{1}{2\pi} n_{prop}\right)^2 D^5_{prop} \cdot K_{torque_{fouling}} \tag{5.24}$$

In order to generate the vessel's power time-series, the power at the propeller is calculated from torque and speed with:

$$P_{prop} = Q^F_{prop} n_{prop} \tag{5.25}$$

where P_{prop} is the power at the propeller.

To assess the accuracy of predicted power (see Chapter 6), power data was measured from the *Skeena Queen*'s propeller shafts which are upstream of the azimuth thruster tower's z-drive gearbox. In order to facilitate a comparison between the simulated *propeller* power and the recorded *shaft* power, an allowance needed to be made for the efficiency losses of

the z-drive gearbox as follows:

$$P_{shaft} = P_{prop} \frac{1}{\eta_{gearbox}} \tag{5.26}$$

where $\eta_{gearbox} < 1$ is the efficiency of the z-drive gearbox embedded within the azimuth tower and is assumed to be constant at $\eta_{gearbox} = 0.95$ [8].

Finally, the energy consumed by the propulsion system at a single shaft is found by numerically integrating shaft power over the duration of the simulation with:

$$E_{shaft} = \int_0^t P_{shaft}(t)\, dt \tag{5.27}$$

with the total propulsion system energy being given as the sum of the four individual shafts energies:

$$E_{shafts} = \sum_{i=1}^{4} E_{shaft\,i} \tag{5.28}$$

Propeller State Visualization and Analysis

The propeller subsystem exports the following propeller time-series to the visualization subsystem for post-processing, data analysis and visualization:

1) Power
    - Estimated shaft power ($P_{shaft_{1,2,3,4}}$)
2) Energy
    - Estimated total propulsion energy (E_{shafts})

5.7 Vessel Subsystem

Commencing from a set of initial conditions set by the user (vessel position, vessel heading, and vessel velocity), the vessel subsystem is responsible for calculating the motion of the vessel throughout a simulation.

In order to calculate the various states of the vessel in the body-fixed, NED, and ECEF reference frames, the vessel subsystem receives propeller forces and moments from the propeller subsystem, as well as ocean current velocity from the environment subsystem as shown in Figure 5.16.

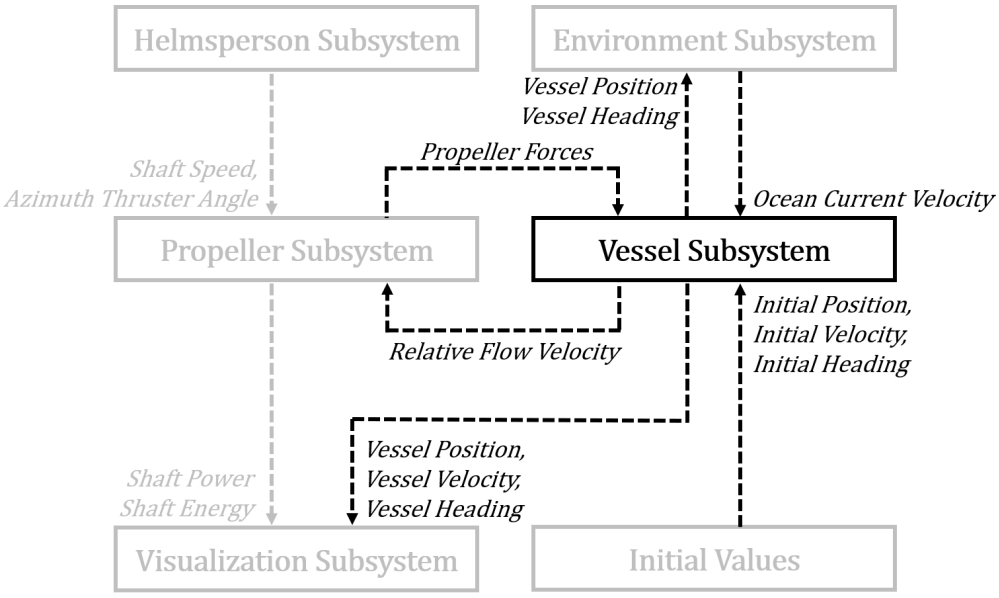

Figure 5.16: MBD Marine Simulation Architecture – Vessel Subsystem

In addition to the propeller forces and moments that are provided by the propeller subsystem, the hydrodynamic forces and moments that act on the ship's hull are computed within the vessel subsystem using the hybrid MMG model.

During simulation, the ship's motion is governed by equation (4.46) which is re-arranged to solve for acceleration and re-written in matrix form as:

$$\begin{bmatrix} \dot{u} \\ \dot{v} \\ \dot{r} \end{bmatrix}_{\{b\}} = (\boldsymbol{m} + \boldsymbol{m_A})^{-1} \begin{bmatrix} X^{F,A}_{hull} + X_{air} + X^{F}_{props} \\ Y^{F}_{hull} + Y^{F}_{props} \\ N^{F}_{hull} + N^{F}_{props} \end{bmatrix}_{\{b\}} \tag{5.29}$$

where $(\boldsymbol{m} + \boldsymbol{m_A})$ is the vessel's combined mass and added mass matrix that is assumed to be constant, and which has been re-written for brevity from:

$$(\boldsymbol{m} + \boldsymbol{m_A}) = \begin{bmatrix} m + m_x & 0 & 0 \\ 0 & m + m_y & 0 \\ 0 & 0 & I_{zz} + J_{zz} + (m + m_y)x_G^2 \end{bmatrix} \tag{5.30}$$

Reviewing equation (5.29), it can be seen that once the forces and moments on the right-hand side are known, the vessel's accelerations can be solved for.

Ship Acceleration

At the initial time-step, the ship's relative velocity has been set to zero such that the hydrodynamic forces are also zero and the only contributions to the vessel's acceleration are from the propeller forces and moments. Using the propeller forces and moments received from the propeller subsystem, equation (5.29) is solved for initial vessel acceleration with respect to the NED frame, $\dot{\boldsymbol{\nu}}^b_{b/n} = [\dot{u}, \dot{v}, \dot{r}]^\mathsf{T}$, which is expressed in the body-fixed frame.

At each remaining time-step, vessel hydrodynamic forces and moments are present when the simulation re-computes vessel acceleration.

Ship Velocity and Position

Considering that the hydrodynamic forces and moments acting on the ship hull and superstructure are velocity dependant, the vessel subsystem first assesses the ship's velocity with respect to the NED frame (speed-over-ground), and also with respect to the local ocean surface (speed-over-water).

Using the vessel's acceleration that was obtained previously, the result is integrated numerically to find the vessel's velocity with respect to the NED frame expressed in the body fixed frame, $\boldsymbol{\nu}^b_{b/n} = [u, v, r]^\mathsf{T}$ which happens to be the vessel's speed-over-ground.

Having already obtained the vessel's speed-over-ground, the computation of the vessel's relative velocity is somewhat more involved and begins with expressing the vessel's velocity in the NED frame with:

$$\begin{bmatrix} \dot{N}_{b/n} \\ \dot{E}_{b/n} \\ \dot{\psi} \end{bmatrix}_{\{n\}} = \mathbf{R}^n_b(\psi) \begin{bmatrix} u \\ v \\ r \end{bmatrix}_{\{b\}} \tag{5.31}$$

where the notation $\mathbf{R}^n_b(\psi)$ is used to signify that the rotation matrix from $\{b\}$ to $\{n\}$ is a function of vessel heading, ψ.

The vessel's velocity expressed in the NED frame is then integrated numerically to compute the vessel's position in the NED frame, $\boldsymbol{\eta}^n_{b/n} = [N_{b/n}, E_{b/n}, \psi]^\mathsf{T}$, which allows for the vessel's true heading, ψ, and the rotation matrix, $\mathbf{R}^n_b(\psi)$, to be updated throughout the simulation.

After obtaining both the position and velocity expressed in the NED frame, the vessel subsystem proceeds to calculate the vessel's velocity expressed in the ECEF frame with:

$$\begin{bmatrix} \dot{x}_{b/e} \\ \dot{y}_{b/e} \\ \dot{z}_{b/e} \end{bmatrix}_{\{e\}} = \mathbf{R}^e_n(\mu,\, l)\mathbf{R}^n_b(\psi) \begin{bmatrix} u \\ v \\ r \end{bmatrix}_{\{b\}} \tag{5.32}$$

where the notation $\mathbf{R}_n^e(\mu,\, l)$ is used to signify that the rotation matrix from $\{n\}$ to $\{e\}$ is a function of latitude and longitude.

Having obtained the vessel's velocity expressed in the ECEF frame, the result is integrated numerically to compute the vessel's position in the ECEF frame, $\boldsymbol{p}_{b/n}^n = [x_{b/e}, y_{b/e}, z_{b/e}]^\mathsf{T}$.

Recalling that one can convert ECEF Cartesian coordinates to latitude and longitude with equation (5.9) and (5.13), the vessel's latitude and longitude are computed such that μ and l, and the rotation matrix, $\mathbf{R}_n^e(\mu,\, l)$, can be updated throughout the simulation.

The vessel's computed heading, latitude, and longitude (ψ, μ, and l) are then sent to the environment subsystem (see Section 5.8) which uses the geographic location of the vessel to determine ocean current velocity at the ship's location. The environment subsystem returns the ocean current velocity relative to the NED frame at the ship's location, $[u_c, v_c, 0]^\mathsf{T}$, which is expressed in the vessel's body-fixed frame.

Finally, the vessel's relative velocity, or speed-over-water can be calculated with:

$$\begin{bmatrix} u_r \\ v_r \\ r \end{bmatrix}_{\{b\}} = \begin{bmatrix} u \\ v \\ r \end{bmatrix}_{\{b\}} - \begin{bmatrix} u_c \\ v_c \\ 0 \end{bmatrix}_{\{b\}} \tag{5.33}$$

With the vessel's velocity ($\boldsymbol{\nu}_{b/n}^b = [u, v, r]^\mathsf{T}$), acceleration ($\dot{\boldsymbol{\nu}}_{b/n}^b = [\dot{u}, \dot{v}, \dot{r}]^\mathsf{T}$), and relative velocity ($\boldsymbol{\xi}_{b/n}^b = [u_r, v_r, r]^\mathsf{T}$) now obtained, the velocity dependant hull and air resistances can be calculated.

Computing Hull Resistance with the CFD Look-up Table

To compute the dominant source of the vessel's hull resistance, the vessel's relative surge velocity (u_r) is fed into the CFD hull resistance look-up table (see Section 4.3.3) which outputs a pre-computed surge resistance value as shown in Figure 5.17.

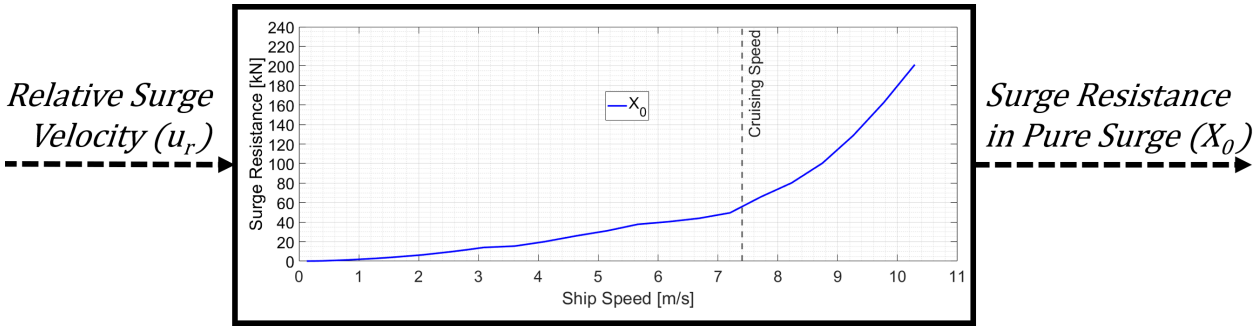

Figure 5.17: Hull Resistance Look-up Table Input and Output

The given surge resistance is then corrected with the resistance augmentation factor as

well as the hull fouling factor with:

$$X_0^{F,A} = X_0(1 + K_{hull_{foulingCFD}})(1 + 4 \cdot a_{augmented}) \tag{5.34}$$

As previously mentioned, the surge resistance $X_0^{F,A}$ is typically the dominant source of a vessel's resistance while underway, but it needs to be supplemented with hull resistances induced by motions in sway and yaw to better predict the vessel's motion in 3 DOF.

Computing Hull Resistance with the Hybrid MMG model

Hull forces and moments that arise due to sway and yaw motions are computed within the vessel subsystem using the modified MMG model and make use of the hydrodynamic derivatives estimated with Yoshimura and Masumoto's [32] empirical formulas (see Section 4.3.5).

Solving for the vessel's acceleration in equation (5.29) requires all of the forces and moments acting on the vessel to be known which raises a conflict as the forces in the hybrid MMG model are dependent on the acceleration terms themselves. In order to resolve this, the sway force and yaw moment computed by the MMG model are approximated with vessel accelerations calculated in the previous time-step such that:

$$\begin{bmatrix} \dot{u}_{(t)} \\ \dot{v}_{(t)} \\ \dot{r}_{(t)} \end{bmatrix}_{\{b\}} = (\boldsymbol{m} + \boldsymbol{m_A})^{-1} \underbrace{\begin{bmatrix} X_{hull}^{F,A} + X_{air} + X_{props}^{F} \\ Y_{hull}^{F}\left(\dot{r}_{(t-1)}\right) + Y_{props}^{F} \\ N_{hull}^{F}\left(\dot{v}_{(t-1)}\right) + N_{props}^{F} \end{bmatrix}_{\{b\}}}_{\boldsymbol{\tau}_b^b} \tag{5.35}$$

where $\dot{u}_{(t)}$, $\dot{v}_{(t)}$, and $\dot{r}_{(t)}$ denote the vessel accelerations being solved for at the present time-step, and $Y_{hull}^{F}\left(\dot{r}_{(t-1)}\right)$, and $N_{hull}^{F}\left(\dot{v}_{(t-1)}\right)$ are the sway force and yaw moment calculated with vessel accelerations from the previous time-step. When simulating the M.V. *Skeena Queen*'s motion, the components of Y_{hull}^{F}, and N_{hull}^{F} that depend on $\dot{r}_{(t-1)}$, and $\dot{v}_{(t-1)}$ were found to be small when compared with the other terms in equation (4.24), indicating that this approximation likely had a negligible effect.

During simulation, the vessel's relative velocity and acceleration are fed into the hybrid MMG model which computes the sway and yaw induced hull forces and moments as detailed in Section 4.3.5. A representation of the simulation flow is provided in Figure 5.18.

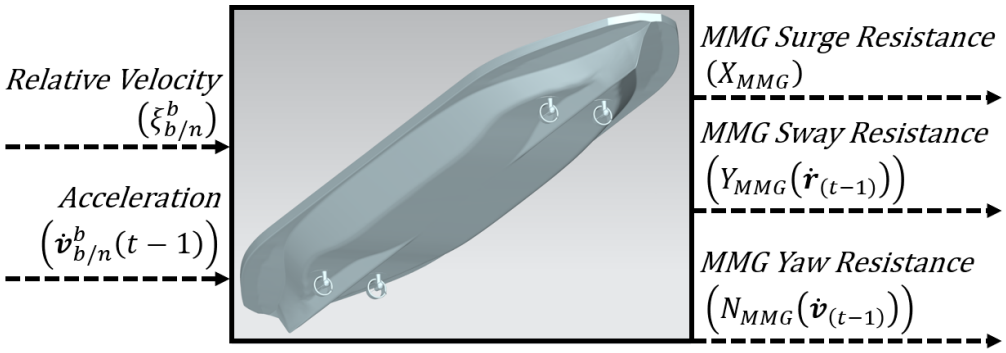

Figure 5.18: Hybrid MMG Model Inputs and Outputs

The hull forces and moments that are output from the MMG model are then corrected with the resistance augmentation factor and hull fouling factor as follows:

$$\begin{aligned} X^{F,A}_{MMG} &= X_{MMG}(1 + K_{hull_{foulingempirical}})(1 + 4 \cdot a_{augmented}) \\ Y^{F}_{MMG} &= Y_{MMG}(1 + K_{hull_{foulingempirical}}) \\ N^{F}_{MMG} &= N_{MMG}(1 + K_{hull_{foulingempirical}}) \end{aligned} \tag{5.36}$$

Computing Appendage Resistance

As the four azimuth towers were not present in either the hull or propeller CFD analyses, their contribution to hull resistance is estimated empirically.

Starting with the vessel's relative velocity, $\boldsymbol{\nu}^b_{b/n}$, the relative velocity at an azimuth tower, o_{azi}, expressed in the body-fixed frame is calculated with:

$$\begin{bmatrix} u_{azi} \\ v_{azi} \\ 0 \end{bmatrix}_{\{b\}} = \begin{bmatrix} u_r \\ v_r \\ 0 \end{bmatrix}_{\{b\}} + \begin{bmatrix} 0 \\ 0 \\ r \end{bmatrix}_{\{b\}} \times \vec{\mathbf{r}}^b_{azi/b} \tag{5.37}$$

where it is noted that equation (5.37) accounts for the relative velocity at the azimuth tower induced by the ship's yaw rate (r).

The relative velocity at the azimuth tower is fed into a look-up table that outputs azimuth tower appendage resistances in surge and sway acting at the location of the azimuth tower, o_{azi}, as illustrated in Figure 5.19.

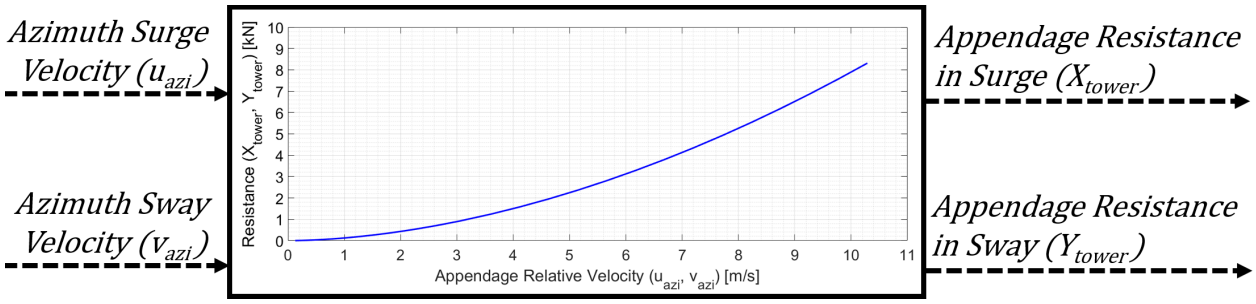

Figure 5.19: Appendage Resistance Look-up Table Inputs and Outputs

The appendage resistance acting about the vessel's origin, o_b, is obtained by appending the appendage induced moment as follows:

$$\begin{bmatrix} X_{tower} \\ Y_{tower} \\ N_{tower} \end{bmatrix}_{\{b\}} = \begin{bmatrix} X_{tower} \\ Y_{tower} \\ 0 \end{bmatrix}_{\{b\}} + \vec{\mathbf{r}}^{\,b}_{azi/b} \times \begin{bmatrix} X_{tower} \\ Y_{tower} \\ 0 \end{bmatrix}_{\{b\}} \tag{5.38}$$

As this process is repeated for each of the four azimuth thruster towers, the forces and moments are summed into total appendage resistance such that:

$$\begin{bmatrix} X_{towers} \\ Y_{towers} \\ N_{towers} \end{bmatrix}_{\{b\}} = \sum_{i=1}^{4} \begin{bmatrix} X_{tower\,i} \\ Y_{tower\,i} \\ N_{tower\,i} \end{bmatrix}_{\{b\}} \tag{5.39}$$

with X_{towers}, Y_{towers}, and N_{towers} representing the total azimuth tower appendage resistance in surge, sway and yaw respectively.

The resulting appendage forces and moments are then corrected with the resistance augmentation factor and hull fouling factor as follows:

$$\begin{aligned} X^{F,A}_{towers} &= X_{towers}(1 + K_{hull_{foulingempirical}})(1 + 4 \cdot a_{augmented}) \\ Y^{F}_{towers} &= Y_{towers}(1 + K_{hull_{foulingempirical}}) \\ N^{F}_{towers} &= N_{towers}(1 + K_{hull_{foulingempirical}}) \end{aligned} \tag{5.40}$$

Computing Air Resistance

Unlike the previous hull resistance components, air resistance is computed from the vessel's speed-over-ground velocity ($\boldsymbol{\nu}^b_{b/n} = [u, v, r]^\mathsf{T}$) instead of the vessel's velocity relative to the ocean surface. The air resistance in surge is given as:

$$X_{air} = K_{air} u^2 \tag{5.41}$$

where K_{air} is estimated using the methodology discussed in Section 4.3.7.

Computing the Sum of Forces and Moments

Once the hull and air resistances have been calculated and the associated correction factors have been applied, the resistances are summed with the propeller forces and moments such that:

$$\underbrace{\begin{bmatrix} X^{F,A}_{hull} + X_{air} + X^{F}_{props} \\ Y^{F}_{hull}\left(\dot{r}_{(t-1)}\right) + Y^{F}_{props} \\ N^{F}_{hull}\left(\dot{v}_{(t-1)}\right) + N^{F}_{props} \end{bmatrix}_{\{b\}}}_{\boldsymbol{\tau}^{b}_{b}} = \begin{bmatrix} X^{F,A}_{0} \\ 0 \\ 0 \end{bmatrix}_{\{b\}} + \begin{bmatrix} X^{F,A}_{MMG} \\ Y^{F}_{MMG}\left(\dot{r}_{(t-1)}\right) \\ N^{F}_{MMG}\left(\dot{v}_{(t-1)}\right) \end{bmatrix}_{\{b\}} + \begin{bmatrix} X^{F,A}_{towers} \\ Y^{F}_{towers} \\ N^{F}_{towers} \end{bmatrix}_{\{b\}} + \begin{bmatrix} X_{air} \\ 0 \\ 0 \end{bmatrix}_{\{b\}} + \begin{bmatrix} X^{F}_{props} \\ Y^{F}_{props} \\ N^{F}_{props} \end{bmatrix}_{\{b\}} \tag{5.42}$$

Re-computing Ship Acceleration

With the sum of forces and moments acting on the vessel known, they are fed back into the equation of motion (5.35) to solve for the vessel's acceleration at the next time-step:

$$\begin{bmatrix} \dot{u}_{(t)} \\ \dot{v}_{(t)} \\ \dot{r}_{(t)} \end{bmatrix}_{\{b\}} = (\boldsymbol{m} + \boldsymbol{m_A})^{-1}\boldsymbol{\tau}^{b}_{b}$$

The simulation proceeds to loop back to computing the vessel's velocity and position at the next time-step and repeats this process until the end of the simulation.

Vessel State Visualization and Analysis

The vessel subsystem exports the following vessel state time-series to the visualization subsystem for post-processing, data analysis and visualization:

1) Vessel position
    - Position in Latitude (μ) and Longitude (l)
2) Vessel orientation
    - Heading with respect to the NED frame (ψ)

3) Vessel velocity

- Speed-over-ground velocity with respect to the NED frame ($\boldsymbol{\nu}^b_{b/n} = [u, v, r]^\mathsf{T}$)

These vessel subsystem outputs are presented and discussed in Chapter 6.

5.8 Environment Subsystem

The environment subsystem exists to account for external forces and disturbances acting on the vessel that arise from ocean currents, wind, and waves.

With the current implementation of the subsystem only accounting for ocean currents, the environment subsystem receives the ship's position and heading from the vessel subsystem and returns the ocean current velocity with respect to the ship's body-fixed frame at the vessel's geographic location as illustrated in Figure 5.20.

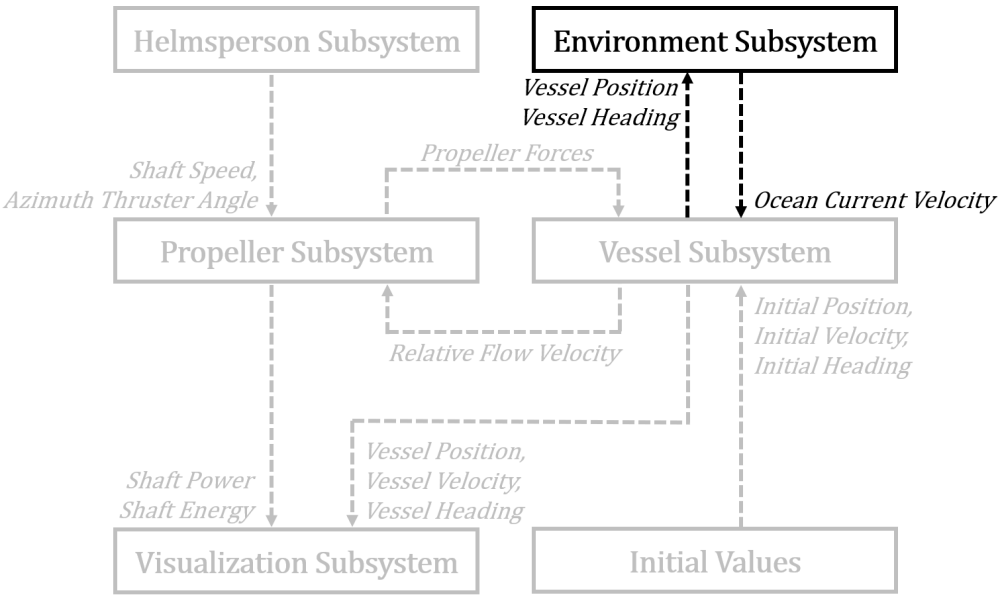

Figure 5.20: MBD Marine Simulation Architecture – Environment Subsystem

Ocean Current

Ocean currents can have a significant influence on a ship's power and energy requirements and thus are an important consideration for the prediction of a vessel's power time-series.

In this work, ocean currents are assumed to be constant and irrotational such that the ocean current velocities given with respect to the NED frame $\{n\}$, expressed in the NED frame are:

$$[N_{c/n}, E_{c/n}, 0]^\mathsf{T}$$

where $N_{c/n}$ and $E_{c/n}$ are the North and East components of ocean current velocity respectively.

With the common assumption that ocean currents are constant [11], the acceleration of ocean current is:

$$[\cancelto{0}{\dot{N}_{c/n}}, \cancelto{0}{\dot{E}_{c/n}}, 0]^{\mathsf{T}}$$

where $\dot{N}_{c/n}$ and $\dot{E}_{c/n}$ represent acceleration of ocean current in the North and East directions respectively.

The ocean currents that were present during the *Skeena Queen*'s crossings were estimated using the "*Current Atlas: Juan de Fuca Strait to Strait of Georgia*" by the Canadian Hydrographic Service [19].

The current atlas conveys the strength of ocean currents with a field of vector arrows that are of varying thicknesses and which are overlaid on top of a chart. Each chart in the referenced current atlas covers the same geographic area, but the strength and direction of the currents vary with time due to ocean tides.

To identify the correct current atlas chart that is relevant for the time of a specific journey, the "Canadian Tide and Current Tables", also by the Canadian Hydrographic Service [44], must be cross-referenced. The cross-referencing procedure uses tidal information from nearby Point Atkinson to compute the correct page of the current atlas. An example tide table from Point Atkinson on a day of *Skeena Queen* data acquisition is provided in Table 5.1.

Table 5.1: Point Atkinson Tide Table
Source: Reproduced with permission from the Canadian Hydrographic Service [44]

Day	**Time**	**Metres**	**Feet**
8	0338	4.0	13.1
	1104	0.9	3.0
SA	1834	4.4	14.4
SA	2343	3.4	11.2

Note: Times are given in Pacific Standard Time (PST).

After cross-referencing the tide table to find the correct current atlas chart, the local ocean currents were estimated for each M.V. *Skeena Queen* validation crossing.

As the *Skeena Queen*'s crossings are generally in the North-South direction, ocean currents were implemented within the simulation using latitudinal current zones, with each zone having its own magnitude and direction of current as shown in Figure 5.21.

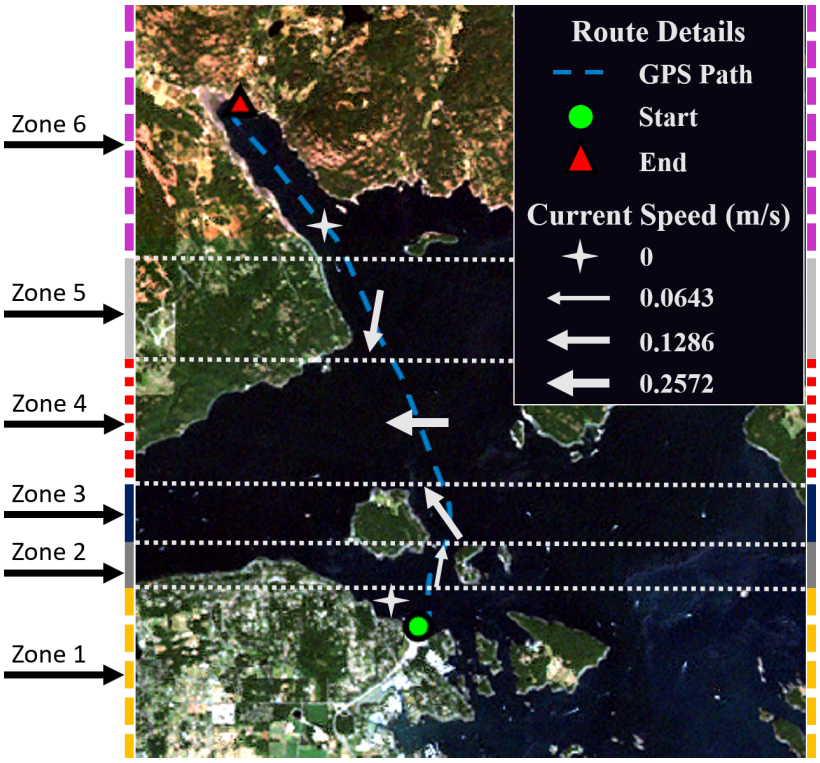

Figure 5.21: Swartz Bay to Fulford Harbour with Estimated Current Speeds
Source: Satellite imagery reproduced with permission from National Resources Canada [17, 18]. Current speeds estimated from Current Atlas: Juan de Fuca Strait to Strait of Georgia [19].

For passages with larger East-West movements, the ocean current field could be generated with East-West gradients.

The environment subsystem receives the latitude and longitude of the ship (μ, l) from the vessel subsystem which it feeds into 2D look-up tables that output the $N_{c/n}$ and $E_{c/n}$ components of ocean current velocity as shown in Figure 5.22.

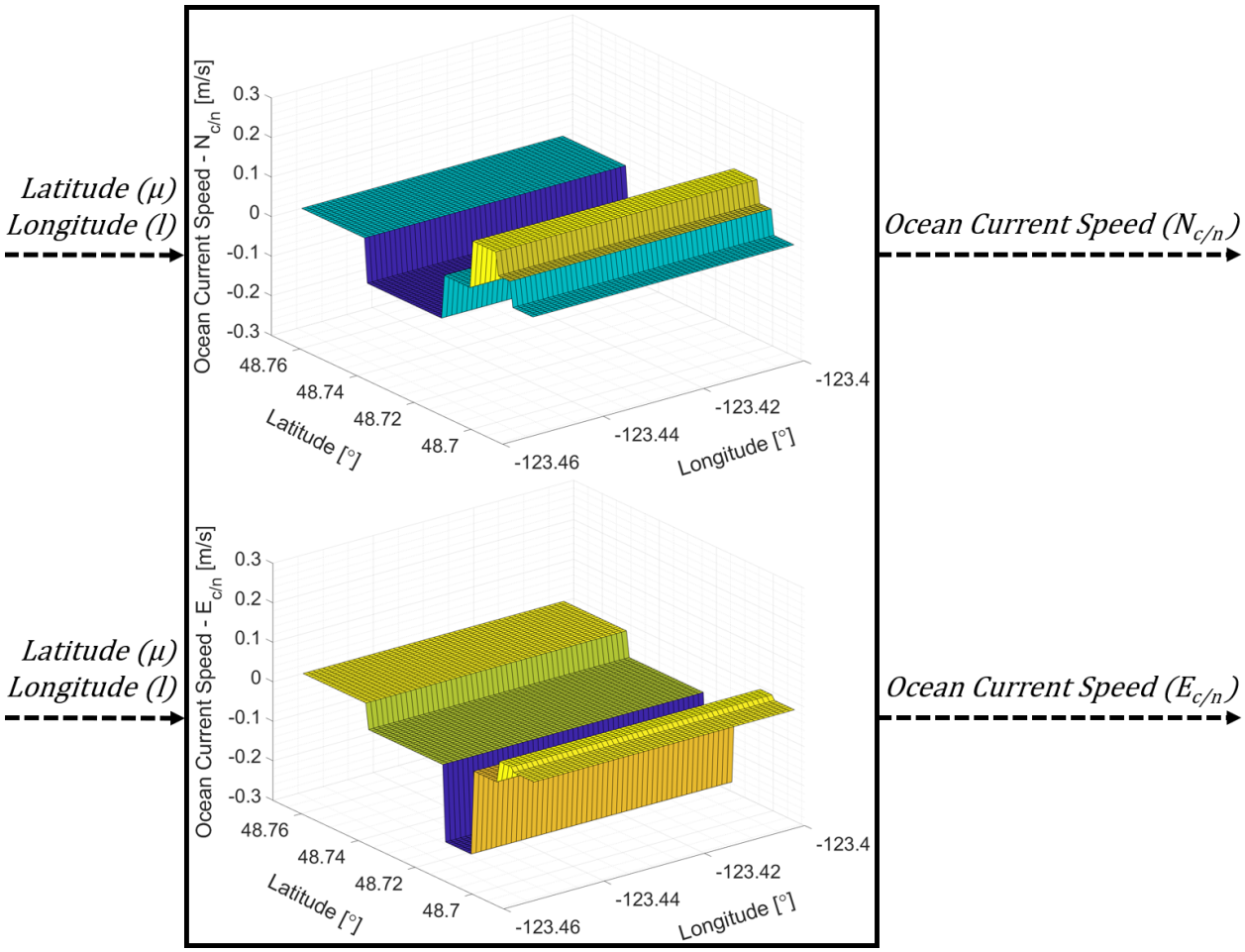

Figure 5.22: Ocean Current Speed Look-up Table Inputs and Outputs

The ocean currents which are expressed in the NED frame are then transformed to the body-fixed frame with:

$$\begin{bmatrix} u_c \\ v_c \\ 0 \end{bmatrix}_{\{b\}} = \mathbf{R}_n^b(\psi) \begin{bmatrix} N_{c/n} \\ E_{c/n} \\ 0 \end{bmatrix}_{\{n\}} \tag{5.43}$$

where the notation $\mathbf{R}_n^b(\psi)$ is to signify that the rotation matrix from $\{n\}$ to $\{b\}$ is a function of vessel heading, ψ.

The computed ocean current velocity is then sent back to the vessel subsystem where it is used to calculate the vessel's velocity relative to the water ($\boldsymbol{\xi}_{b/n}^b = [u_r, v_r, r]^\mathsf{T}$) with:

$$\begin{bmatrix} u_r \\ v_r \\ r \end{bmatrix}_{\{b\}} = \begin{bmatrix} u \\ v \\ r \end{bmatrix}_{\{b\}} - \begin{bmatrix} u_c \\ v_c \\ 0 \end{bmatrix}_{\{b\}} \tag{5.44}$$

Wind

Wind forces are absent from the current implementation of the environment subsystem. Although the vessel's air resistance in still-air is estimated to be 4% of the vessel's total resistance, this value can increase meaningfully with a strong headwind and should be included in future implementations.

Waves

Wave forces are also absent from the current implementation of the environment subsystem. Although the M.V. *Skeena Queen* operates in relatively sheltered waters, wave forces will be an important addition to future implementations of the modelling platform.

5.9 Visualization and Analysis Subsystem

The visualization and analysis subsystem consolidates multiple signals that it receives from the other subsystems as shown in Figure 5.23.

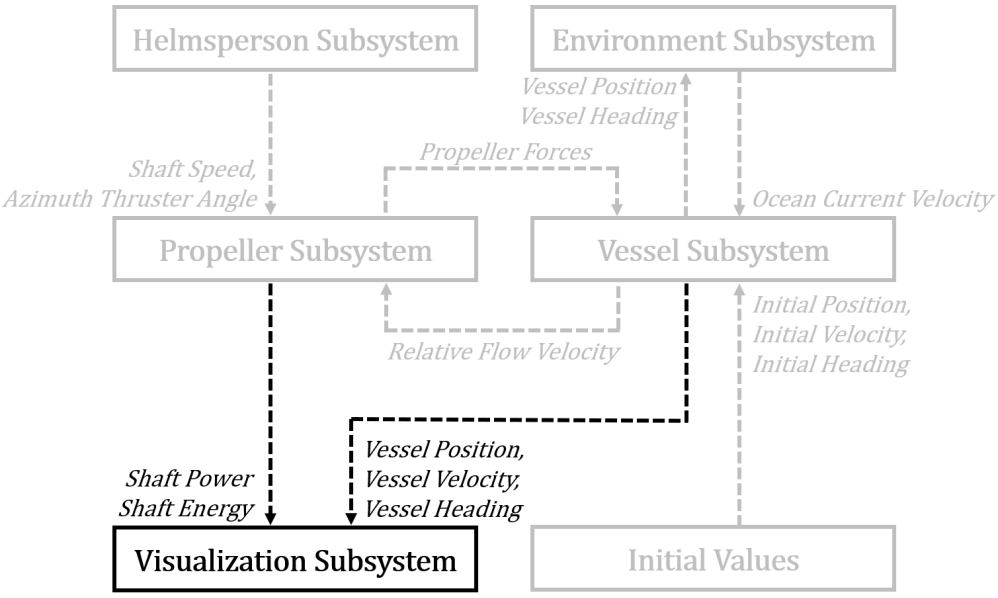

Figure 5.23: MBD Marine Simulation Architecture – Vis. & Anal. Subsystem

This subsystem is responsible for facilitating data analysis and visualization of the following simulation metrics:

1) Power

   - Estimated shaft power ($P_{shaft_{1,2,3,4}}$)

2) Energy

   - Cumulative propulsion energy (E_{shafts})

3) Vessel position

   - latitude (μ) and longitude (l)

4) Vessel orientation

   - Heading (ψ) with respect to the NED frame

5) Vessel velocity

   - Speed-over-ground ($U = \sqrt{u^2 + v^2}$)

The results produced by the visualization and analysis subsystem are presented in Chapter 6 for further discussion.

Simulation Flow Diagram

Now that a complete description has been given for each of the individual simulation subsystems, a simulation flow diagram is provided in Figure 5.24 to visualize the connections between each subsystem. With this, the description of the MBD marine simulation structure concludes.

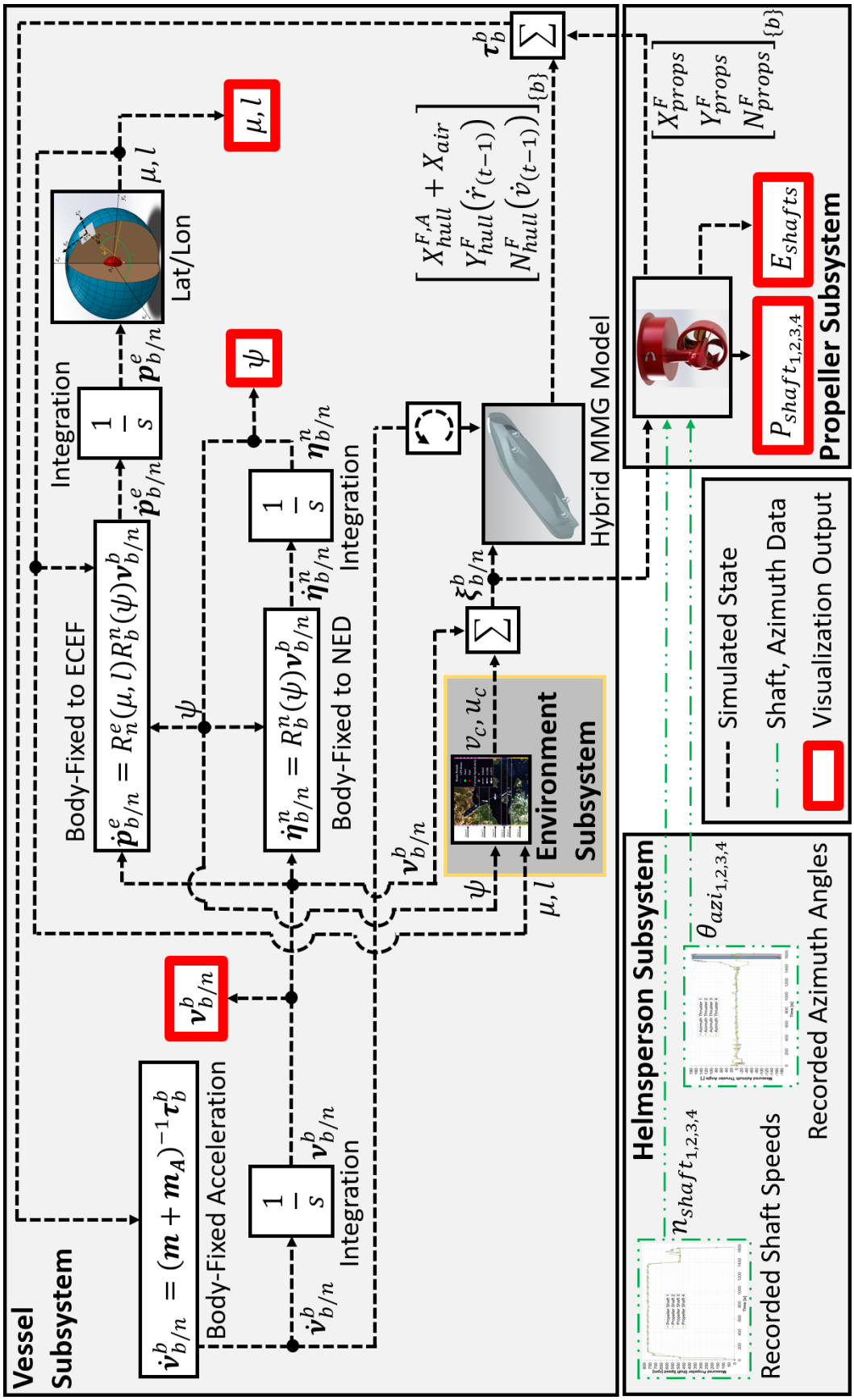

Figure 5.24: MBD Marine Simulation Flow Diagram

Chapter 6

Vessel Operational Profile Results and Discussion

In order to validate and assess the accuracy of the MBD marine simulation platform that was laid out in the previous chapters, simulation results were compared with data that was recorded during M.V. *Skeena Queen* crossings. The findings are documented in the following sections.

6.1 Simulation Results: Free-Running, Initial

The first simulation run of the M.V. *Skeena Queen* travelling from Swartz Bay to Fulford Harbour is termed "free-running" because the ship is driven solely by recorded shaft speed and azimuth angle inputs such that the vessel's velocity, position, and orientation are computed entirely by the simulation platform.

Recalling that the simulation platform outputs latitude and longitude (μ, l) coordinates at each time-step, the ship's simulated path can be shown by overlaying the latitude and longitude data on top of georeferenced satellite imagery. Figure 6.1 depicts the ship's simulated path shown alongside the ship's recorded GPS path.

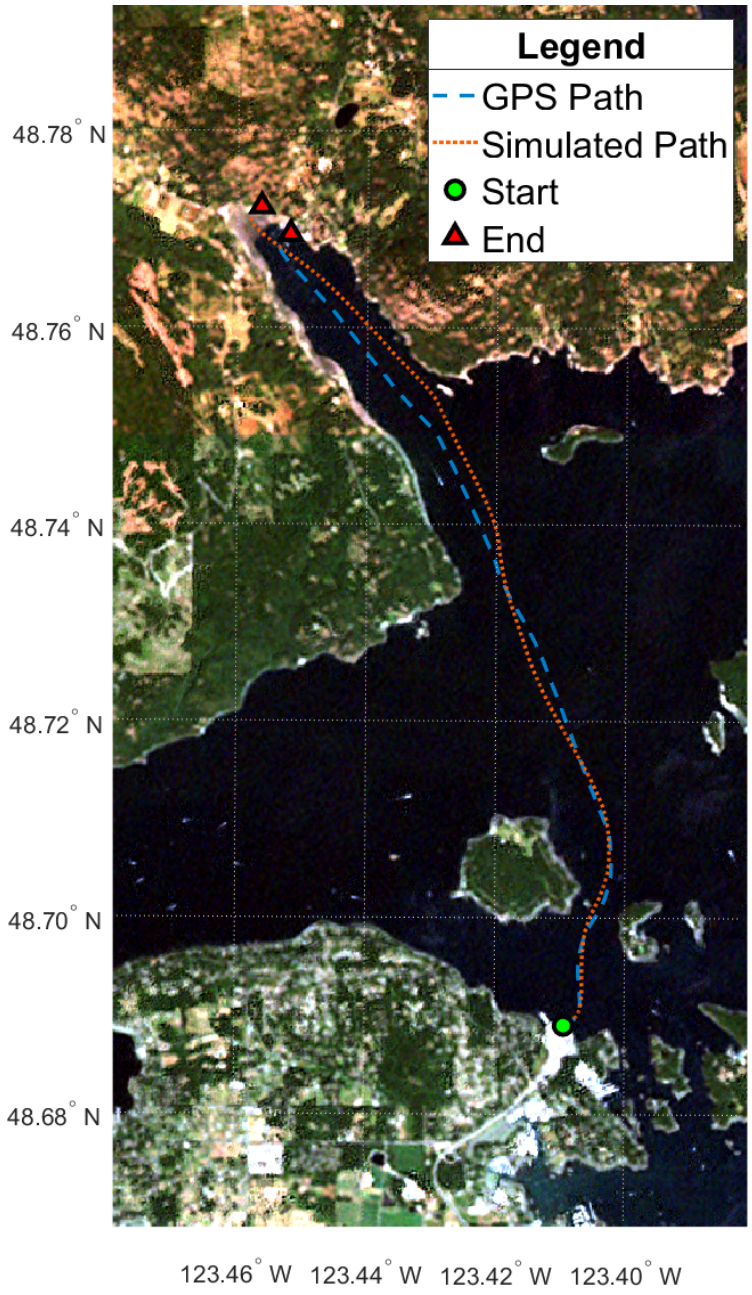

Figure 6.1: Vessel Path – Free-Running, Initial

It can be seen that the ship's simulated path tracks the ship's recorded GPS path well when considering that the calculated position is prone to errors from several sources including but not limited to:

1) Azimuth angle measurements

    a) Angle measurement tolerance

    b) Sensor to VDR lag

c) Signal recording frequency (1 Hz)

d) Data synchronization errors

2) Low resolution ocean current estimates

3) Simulated forces

a) Ship hydrodynamic forces

b) Propeller axial and transverse thrust

As the ship's simulated position is computed by integrating velocity over the duration of the simulation, small positional errors at each time-step compound over time and the error may be significant by the end of the simulation.

As indicated by the small overshoot in the vessel's position plot, the ship's speed-over-ground is slightly over-predicted when compared with the recorded data as shown in Figure 6.2. The over-predicted vessel speed is touched on later in this chapter and can be caused by under-predicted hull resistance, over-predicted thrust, or inaccurate ocean current estimates among other factors.

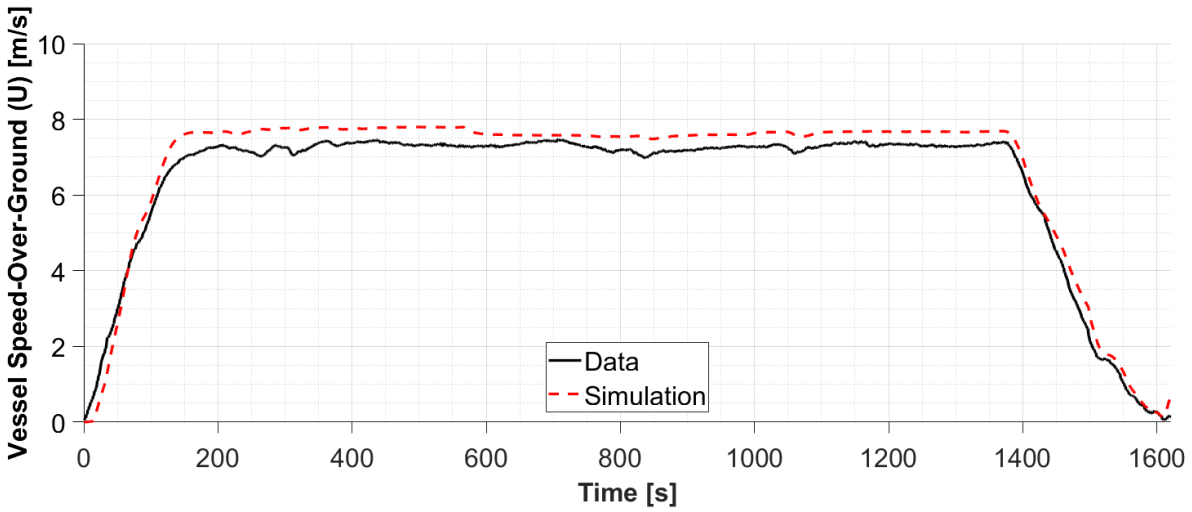

Figure 6.2: Vessel Speed – Free-Running, Initial

The vessel's simulated heading tracks the recorded GPS heading well, as shown in Figure 6.2.

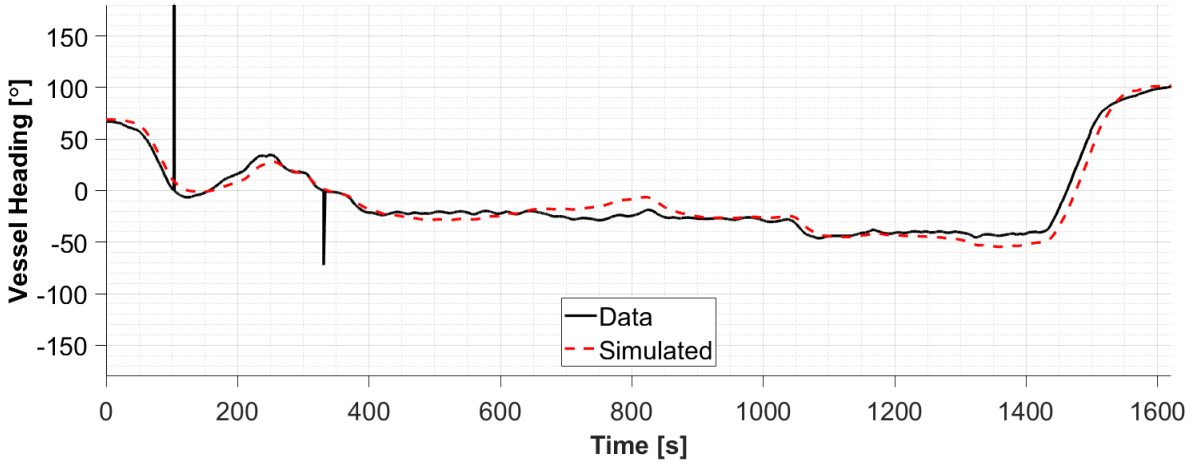

Figure 6.3: Vessel Heading – Free-Running, Initial

As with the vessel's path, the ship's simulated heading is computed by integrating the vessel's yaw rate over the duration of the simulation which compounds small positional errors at each time-step, potentially leading to a large error at the end of a simulation.

Before discussing simulated power results, a period termed the "cruising period" is introduced and is defined as the simulation *time between 200 and 1300 seconds* where vessel operation is steady and the ship's mean cruising velocity is $7.3m/s$.

$$cruising\ period: \ 200s \leq t \leq 1300s$$
$$mean\ cruising\ speed: \ \bar{U} = 7.3m/s$$

The simulated shaft powers are plotted alongside measured shaft powers as shown in Figures 6.4–6.7. Also plotted is a reference power from the *Skeena Queen*'s sea-trial report which is the propulsion power required to sustain a constant cruising speed of $7.3m/s$ (speed-over-water) as represented by the horizontal line [20]. The sea-trial power reference can be compared with simulated and measured power during the aforementioned cruising period between 200 and 1300 seconds when the vessel's mean speed is also $7.3m/s$.

It should be noted that as the ship was near-new when the sea-trial report was issued, the power reference does not factor in the effects of coating degradation, increased surface roughness, and fouling that may have led to increased power requirements over the following 20 years.

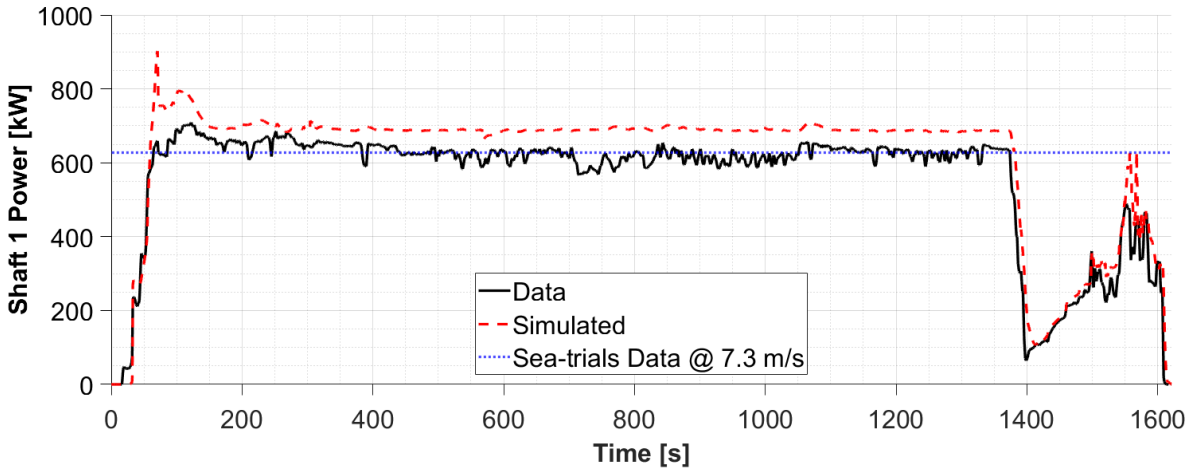

Figure 6.4: Shaft 1 Power – Free-Running, Initial

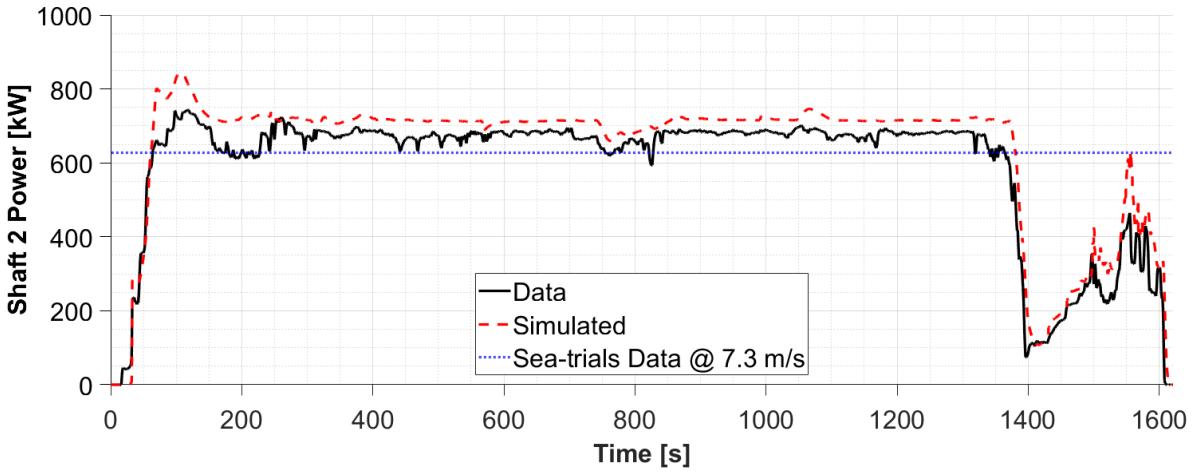

Figure 6.5: Shaft 2 Power – Free-Running, Initial

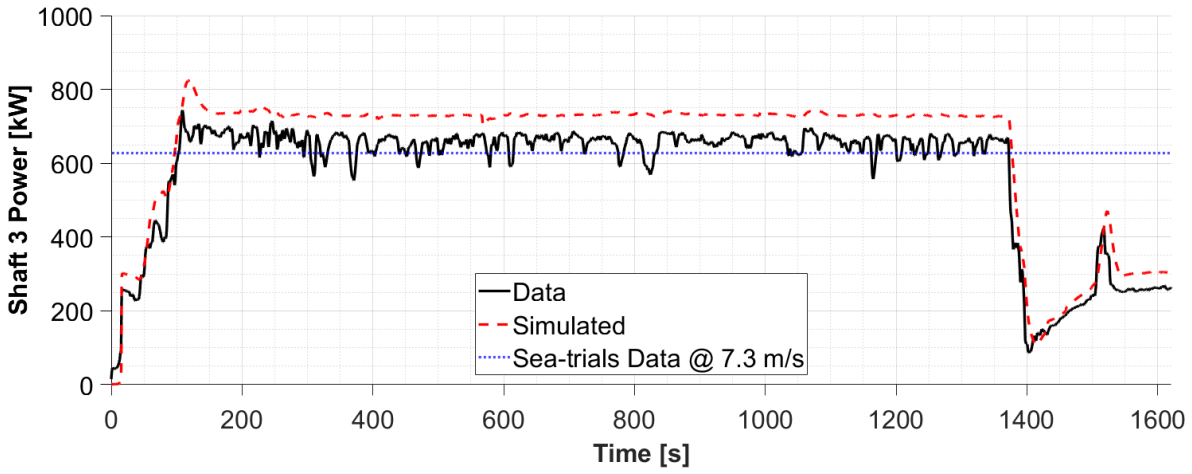

Figure 6.6: Shaft 3 Power – Free-Running, Initial

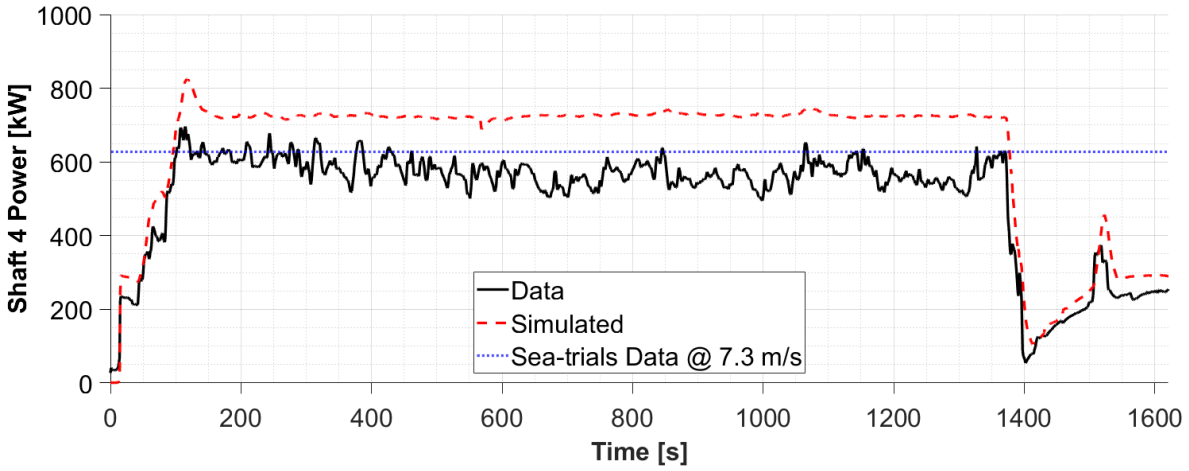

Figure 6.7: Shaft 4 Power – Free-Running, Initial

From the plots it can be seen that all of the shaft powers are slightly over-predicted, with shaft 4 being noticeably worse than the other three shafts. As previously mentioned, it is strongly suspected that the power measurements on shaft 4 were erroneously under-reported due to issues with strain gauge installation. This assertion is supported by comparing the power measurements on shaft 4 with the sea-trial reference power and noting that the measured power is less than the reference power.

The total energy consumed by the propulsion system as measured across the propeller shafts is shown in Figure 6.8.

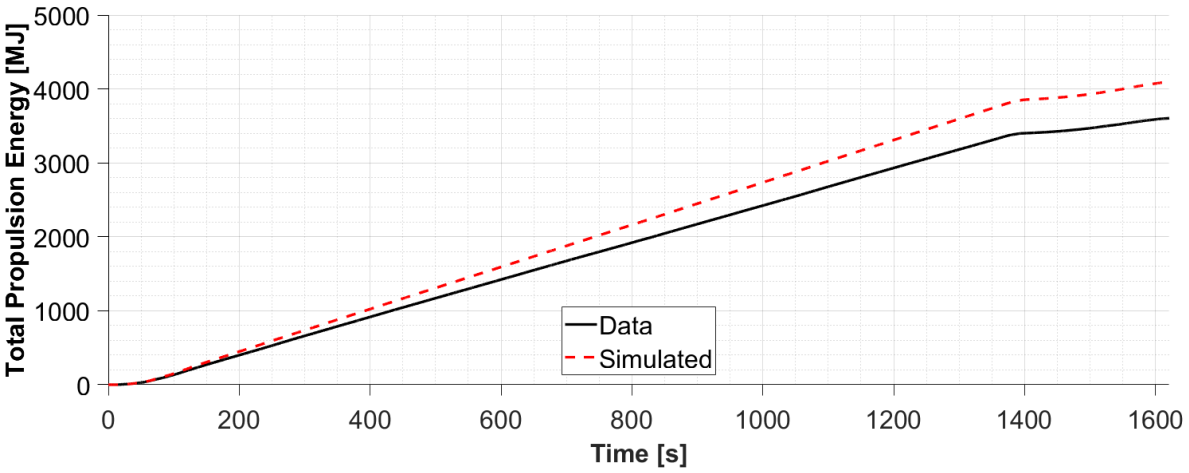

Figure 6.8: Total Propulsion Energy – Free-Running, Initial

With power being over-predicted on all shafts, it follows that propulsion energy will also be over-predicted, as is the case. It should be noted however, that if the shaft 4 power measurements were under-reported as suspected, the actual simulation error would be reduced.

Similar to other results, the simulated energy is computed by integrating power over the duration of the simulation and small energy errors at each time-step will compound over time and can grow large by the end of the simulation.

In conclusion the initial "free-running" simulation showed excellent agreement with the recorded data for vessel position, speed, and heading. The simulated shaft powers were also in close agreement with the measured data with the exception of shaft 4 which is suspected to have suffered from measurement error.

6.2 Simulation Results: Forced GPS Speed & Heading, Initial

While the initial simulation results were encouraging, an investigation was carried out to find the root-causes of the over-predicted vessel speed and shaft power.

One avenue of this investigation explored for errors within the propeller subsystem that may have been introduced through deviations in the propeller's CAD surface geometry and from the absence of the azimuth tower and duct struts during the propeller CFD analyses.

As mentioned in Section 4.2.1, the computed propeller model mass was 1.64% lighter than the mass stated on the propeller drawing, indicating that the propeller CAD model used to generate the thrust and torque look-up surfaces deviated from the true propeller geometry.

After performing a cross-section of the CAD propeller geometry, it can be seen that the modelled blade geometry departs somewhat from the design drawing. Perhaps the clearest deviation from the true geometry is visible near the root of the propeller where the rake in the design drawing is zero, but where the rake on the propeller model is non-zero as highlighted in Figure 6.9. This deviation was likely due to allowing the CAD software to fit the blade surface through the aerofoil contours without having provided additional guide curves. In future analyses, the accuracy of the propeller geometry can be improved with the simple addition of guide curves that better control the surfacing of the blade.

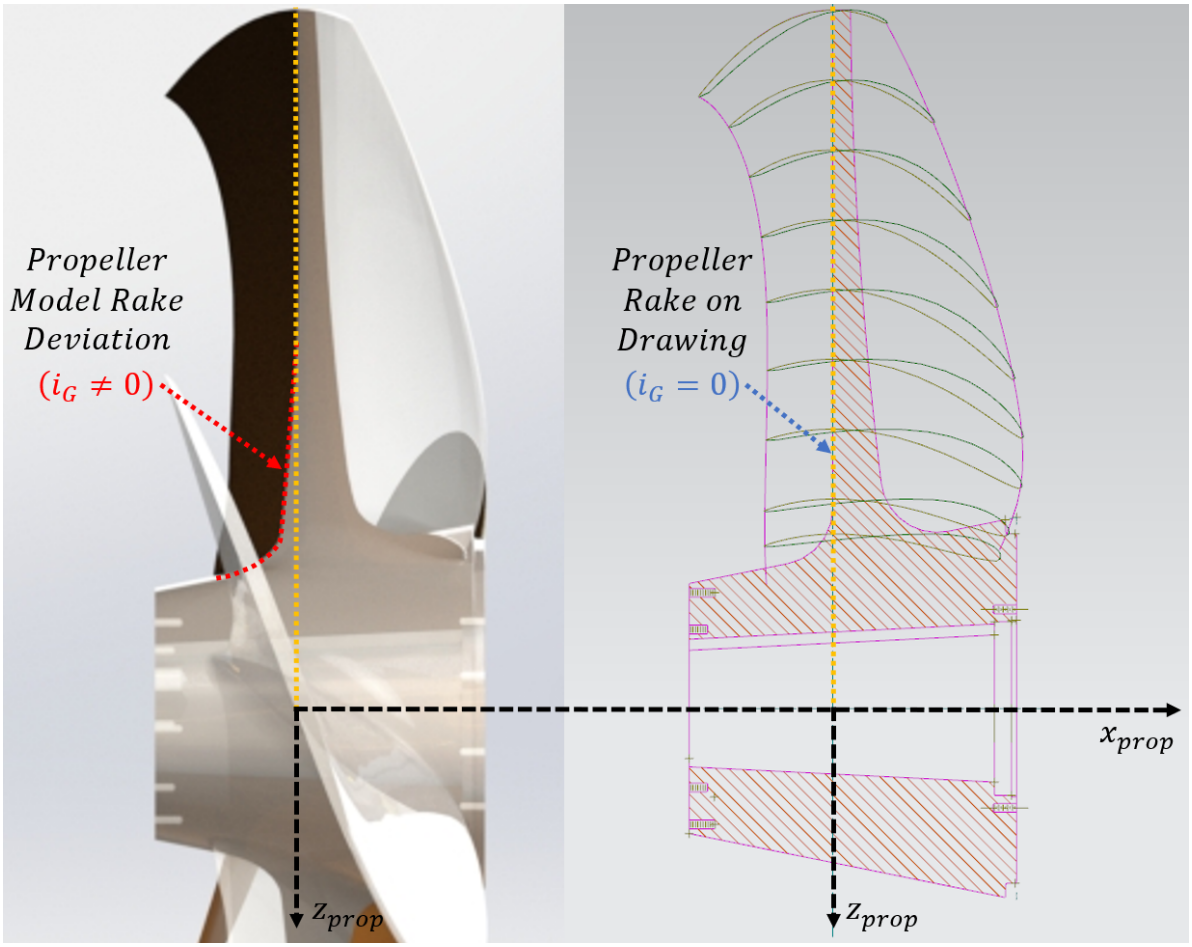

Figure 6.9: Propeller Geometry Deviation

Another possible cause of the over-predicted propeller torque and power was the use of modified thruster geometry in CFD. As shown in Figure 6.10, the propeller assembly's CFD geometry was modified to remove the azimuth tower as well as the duct struts that connect the duct to the tower (shown adjacent in Figure 6.11). It is unclear how these appendages would have altered the flow into the propeller and how large of an impact their removal may have had on the computed results.

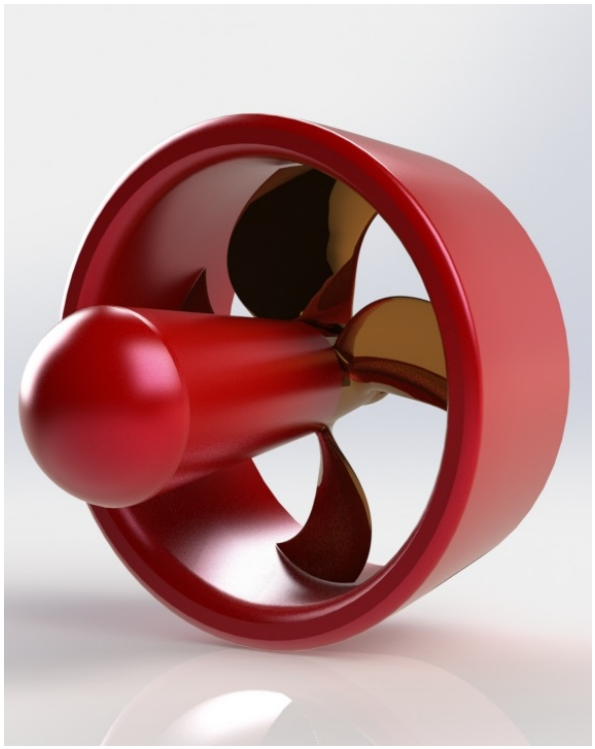

Figure 6.10: Propeller CFD Geometry without Azimuth Tower and Duct Struts

Figure 6.11: Propeller CAD Geometry with Azimuth Tower and Duct Struts

Finally, Figures 6.12–6.13 of the azimuth thruster show that the true duct geometry has a much shallower taper and larger blade clearance than the modelled duct geometry that was approximated from the *Skeena Queen*'s shafting arrangement drawing. Both of these deviations would have had an effect on computed thrust and torque [45–47].

Figure 6.12: Propeller Duct Actual Geometry – Back View

Figure 6.13: Propeller Duct Actual Geometry – Side View

Given that the propeller thrust and torque look-up tables were generated from CFD using the propeller assembly with multiple geometry deviations, it was suspected that this was a large contribution to the simulated power error.

To test this hypothesis, an attempt was made to isolate the propeller subsystem using a "forced GPS speed and heading" case to allow an assessment of the full extent of the error.

Unlike the initial "free-running" case where the vessel's velocity, position, and orientation were computed entirely by the simulation platform, the "forced GPS speed and heading" case intercepts the vessel's simulated velocity and heading and replaces them with the recorded GPS velocity and heading respectively. The "forced GPS speed and heading" case approximates the vessel's velocity expressed in the body-fixed frame as the recorded GPS speed-over-ground such that:

$$\boldsymbol{\nu}_{\boldsymbol{b/n}}^{\boldsymbol{b}} \approx \begin{bmatrix} U_{GPS} \\ 0 \\ 0 \end{bmatrix} \tag{6.1}$$

where U_{GPS} is the recorded GPS speed-over-ground.

This intervention has the effect of forcing the propeller's advance velocity ($J_{advance}$) and the inflow angle into the propeller ($\alpha_{advance}$) to be representative of the recorded data and isolates the propeller subsystem from inaccuracies that may be introduced by the vessel subsystem.

An updated simulation flow diagram for the "forced GPS speed and heading" case is shown in Figure 6.14.

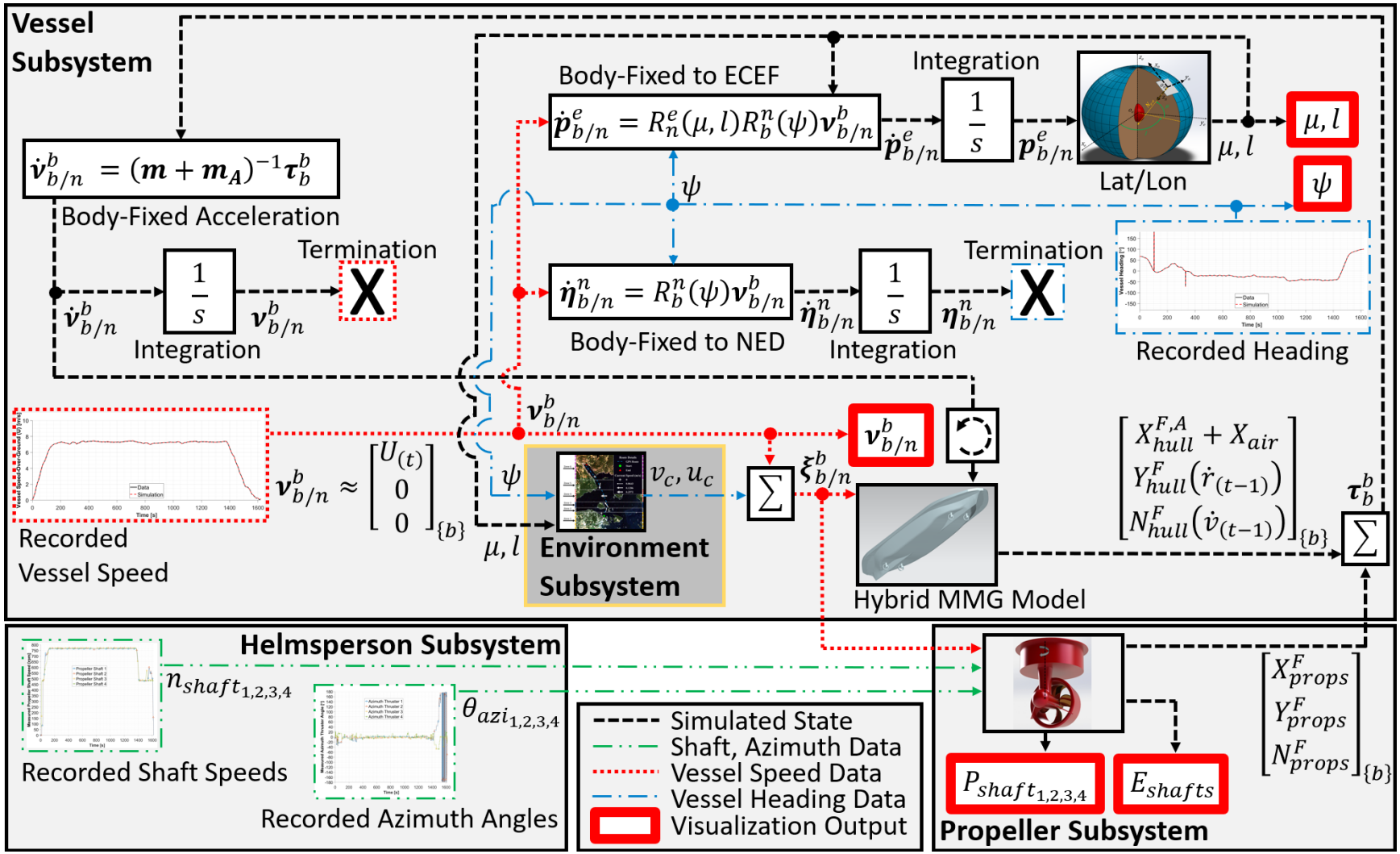

Figure 6.14: Simulation Flow Diagram – Forced GPS Speed & Heading, Initial

The simulation outputs are re-plotted for the "forced GPS speed and heading" case, beginning with vessel path, speed and heading in Figures 6.15–6.17.

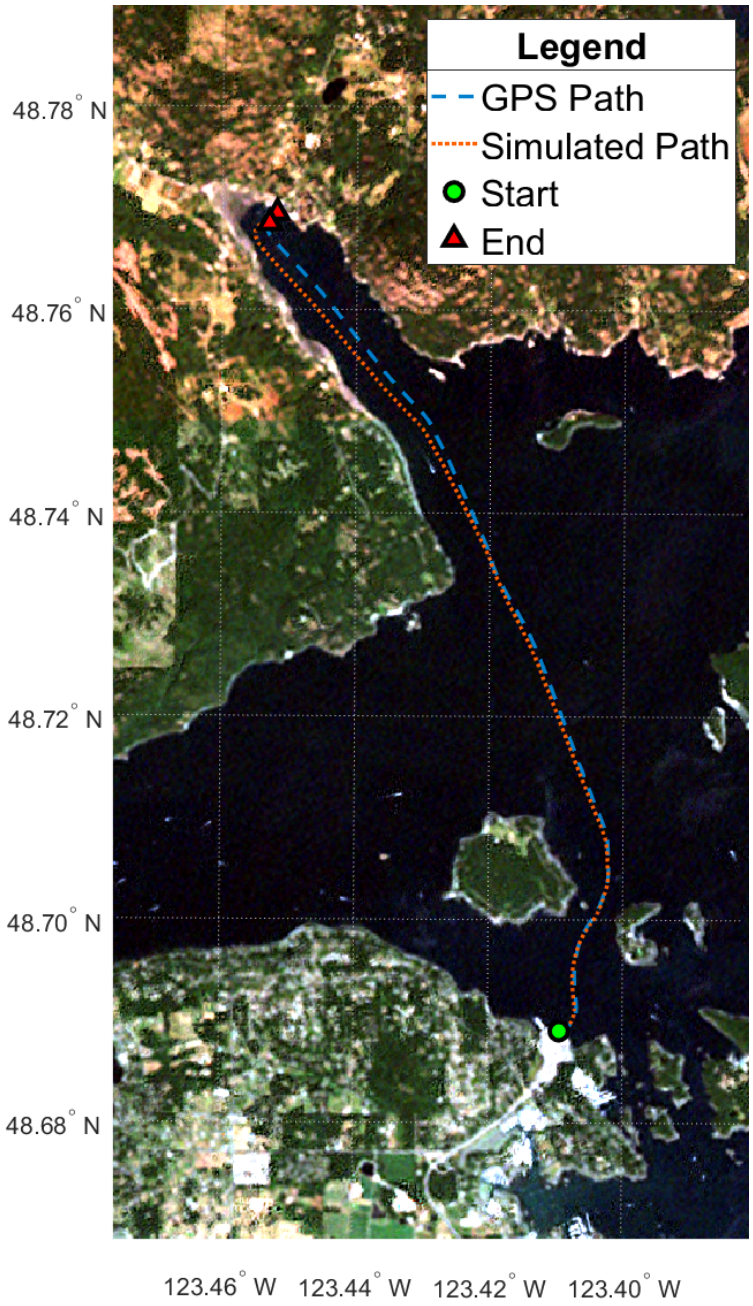

Figure 6.15: Vessel Path – Forced GPS Speed & Heading, Initial

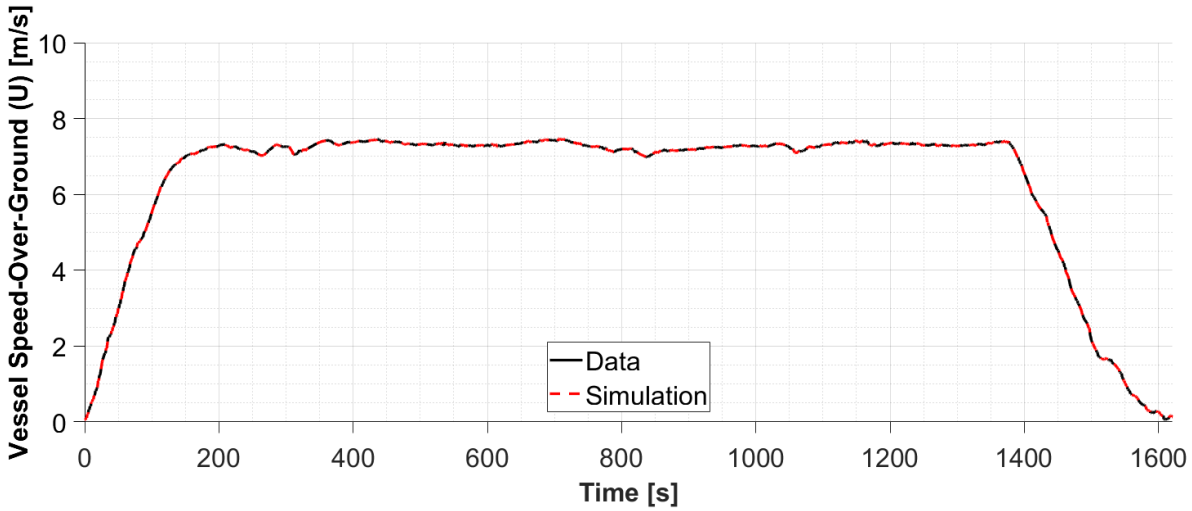

Figure 6.16: Vessel Speed – Forced GPS Speed & Heading, Initial

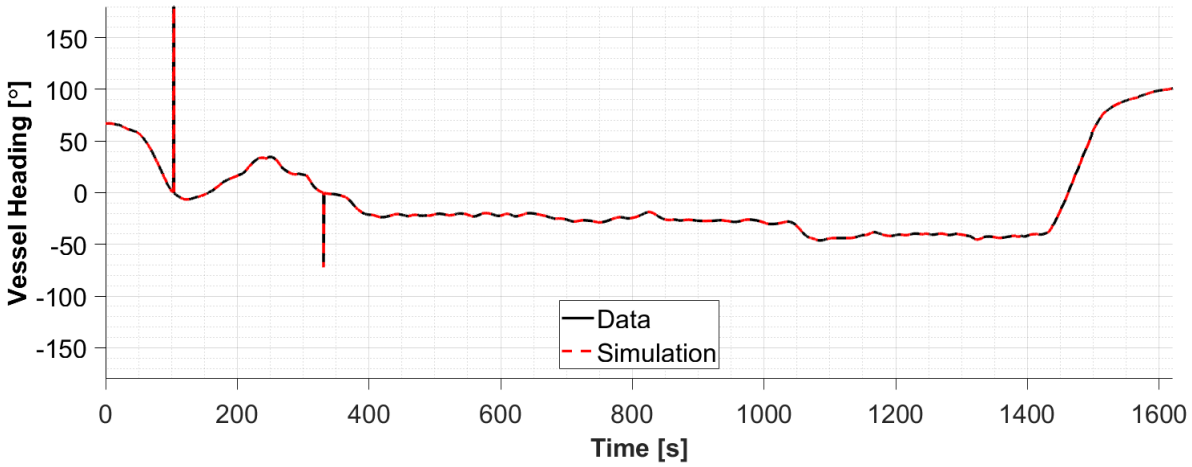

Figure 6.17: Vessel Heading – Forced GPS Speed & Heading, Initial

As expected, the vessel speed and heading outputs track the recorded data perfectly, and the vessel's path is off ever-so-slightly due a 1° difference in the estimated initial heading.

While the first three plots are extremely accurate, the shaft power and energy plots in Figures 6.18–6.22 show a different outcome.

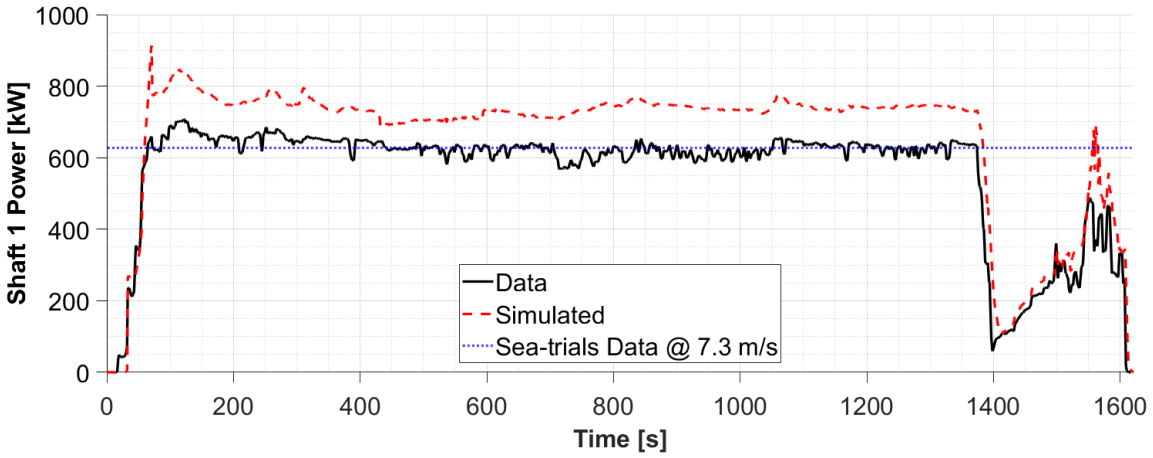

Figure 6.18: Shaft 1 Power – Forced GPS Speed & Heading, Initial

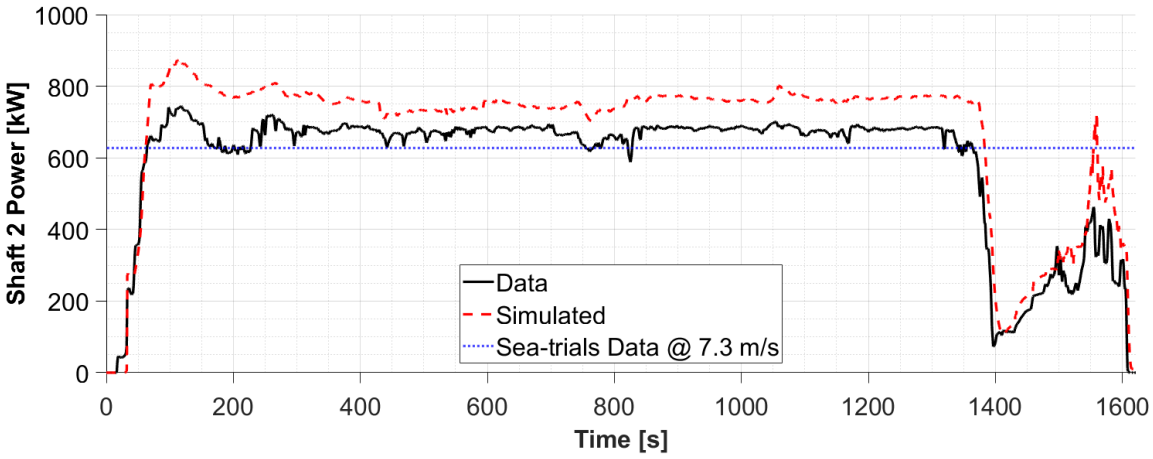

Figure 6.19: Shaft 2 Power – Forced GPS Speed & Heading, Initial

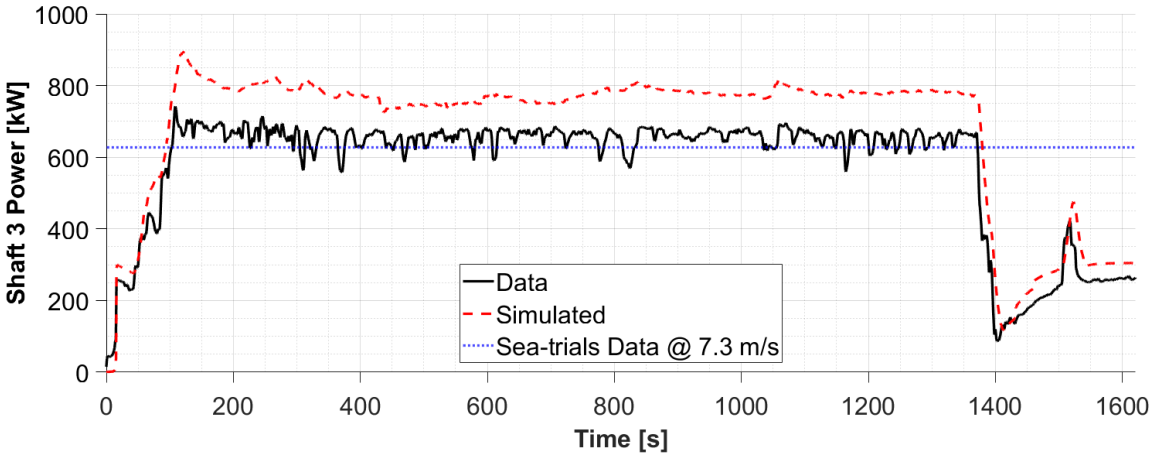

Figure 6.20: Shaft 3 Power – Forced GPS Speed & Heading, Initial

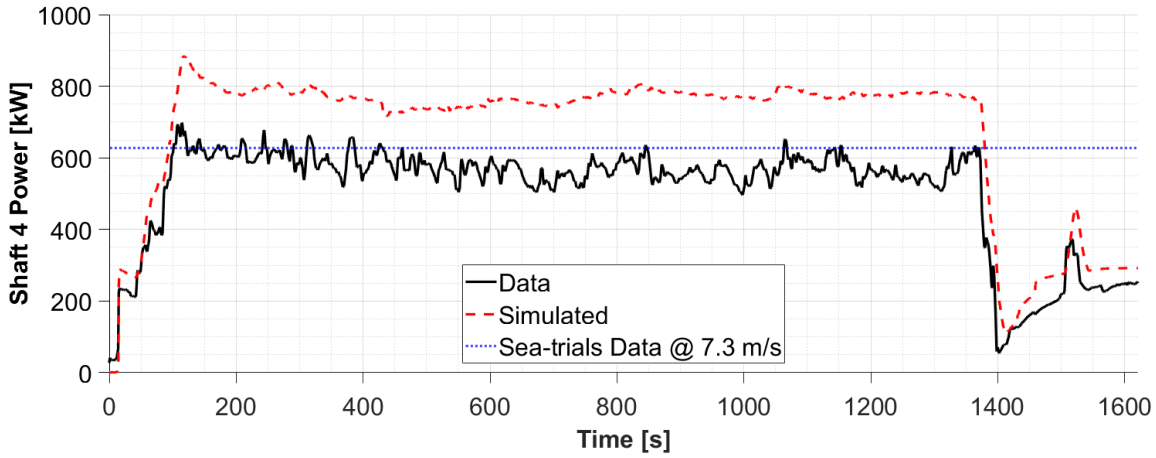

Figure 6.21: Shaft 4 Power – Forced GPS Speed & Heading, Initial

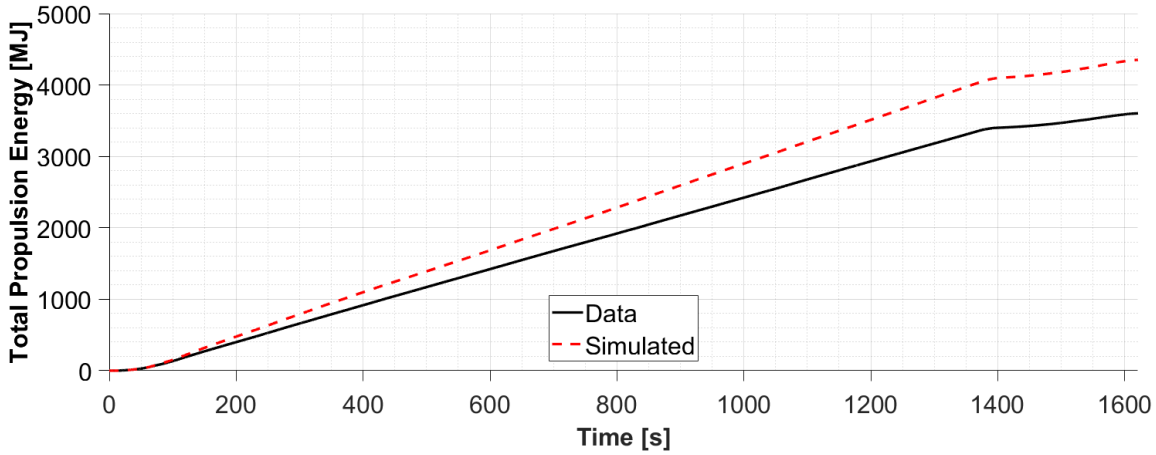

Figure 6.22: Total Propulsion Energy – Forced GPS Speed & Heading, Initial

The shaft power plots show that isolating the propeller subsystem by using the "forced GPS speed and heading" leads to increased error which can be explained when considering that the initial "free-running" simulation was inherently self-buffering by the following mechanism:

Consider that increases in propeller thrust, and by extension torque and power, have a tendency to increase hull velocity, but conversely the same increase in hull velocity leads to increased hull resistance that opposes the initial increase in hull velocity.

Simultaneously, an increase in hull velocity increases the propeller advance ratio which has a tendency to reduce propeller thrust, torque and power. This reduction in thrust also has the tendency to reduce hull velocity which again opposes the initial increase in hull velocity.

The opposite is true for a decrease in propeller thrust, and thus the nature of the "free-running" simulation is inherently self-buffering which explains the reduced extent of error in the original results.

In summary, by this mechanism, the over- or under-prediction of propeller thrust and by extension torque and power are compensated for by an increase or decrease in simulated vessel velocity, which in turn increases or decreases the propeller advance ratio to buffer the predicted torque and power.

In the "forced GPS speed and heading" case, the vessel is forced to travel at the recorded GPS velocity which effectively by-passes the simulation's buffering mechanism and reveals the true extent of the error introduced by the propeller thrust and torque look-up tables.

6.3 Simulation Results: Forced GPS Speed & Heading, Corrected

After establishing that deviations in propeller surface geometry had introduced error into the propeller CFD results and that this error propagated into the thrust and torque coefficient look-up tables and ultimately increased the error in simulated thrust and torque, a pair of geometry correction factors were introduced to correct the propeller coefficient look-up tables. One purpose of introducing geometry correction factors was to explore the extent of accuracy that the remaining portions of the simulation platform could have achieved had the propeller thrust and torque coefficient look-up tables been generated with a higher degree of accuracy.

As mentioned in the previous section, the simulation structure was temporarily altered to intercept the simulated ship speed and heading and replace these values with the recorded GPS speed and heading such that any error introduced by simulated ship motions could be eliminated. The use of GPS speed and heading to compute the advance ratio ($J_{advance}$) and inflow angle ($\alpha_{advance}$) input into the propeller thrust and torque coefficient look-up tables allowed for virtually all of the simulated propulsion power error to be isolated to the torque coefficient look-up table.

Once the true extent of the propulsion power error coming from the torque coefficient look-up table was known, the geometry correction factor was applied to tune the output of the look-up table such that the simulated propulsion power better reflected the measured power. The effect of this process was to emulate the integration of more accurately generated propeller thrust and torque coefficient look-up tables and should not be considered controversial due to the array of literature demonstrating that propeller torque and thrust

can be accurately predicted with CFD when more refined techniques are employed and when representative propeller surface geometry is used.

As this work aimed to introduce the methodology and concept of the proposed MBD marine simulation platform, the geometry correction factors were applied in lieu of running a rigorous CFD study to regenerate the propeller torque and thrust coefficient look-up tables with higher accuracy, a task that was made infeasible due to time and resource constraints.

The propeller geometry correction factors were applied to both thrust and torque with the assumption that the propeller's efficiency remained constant, where propeller efficiency is given as [21]:

$$\eta_{prop} = \frac{K_{Tx}}{K_Q}\frac{J_{advance}}{2\pi} \tag{6.2}$$

with η_{prop} being the propeller's efficiency.

In-line with keeping propeller efficiency constant, the geometry correction factors were applied equally to thrust and torque, or $K_{thrust_{geometry}} = K_{torque_{geometry}}$.

The equation for calculating thrust was modified to:

$$\begin{aligned} T^{F,G}_{prop_x} &= T^{F}_{prop_x} K_{thrust_{geometry}} \\ T^{F,G}_{prop_y} &= T^{F}_{prop_y} K_{thrust_{geometry}} \end{aligned} \tag{6.3}$$

where $T^{F,G}_{prop_x}$, and $T^{F,G}_{prop_y}$, are the axial and transverse thrusts after being corrected for both fouling and modelling geometry deviations.

With this modification, the propeller force and moment in surge, sway, and yaw expressed in the vessel's body-fixed frame become $X^{F,G}_{prop}$, $Y^{F,G}_{prop}$, and $N^{F,G}_{prop}$ respectively.

Similarly, the equation for calculating torque changes to:

$$Q^{F,G}_{prop} = Q^{F}_{prop} K_{torque_{geometry}} \tag{6.4}$$

where $Q^{F,G}_{prop}$ is the propeller torque after being corrected for both fouling and geometry.

The geometry correction factors were increased incrementally until the simulated power error in the "forced GPS speed and heading" case was reduced to an acceptable level. The resulting correction factors amounted to a 12% reduction, or $K_{thrust_{geometry}} = K_{torque_{geometry}} = 0.88$.

The resulting shaft power and energy plots for the corrected "forced GPS speed and heading" case are provided in Figures 6.23–6.27.

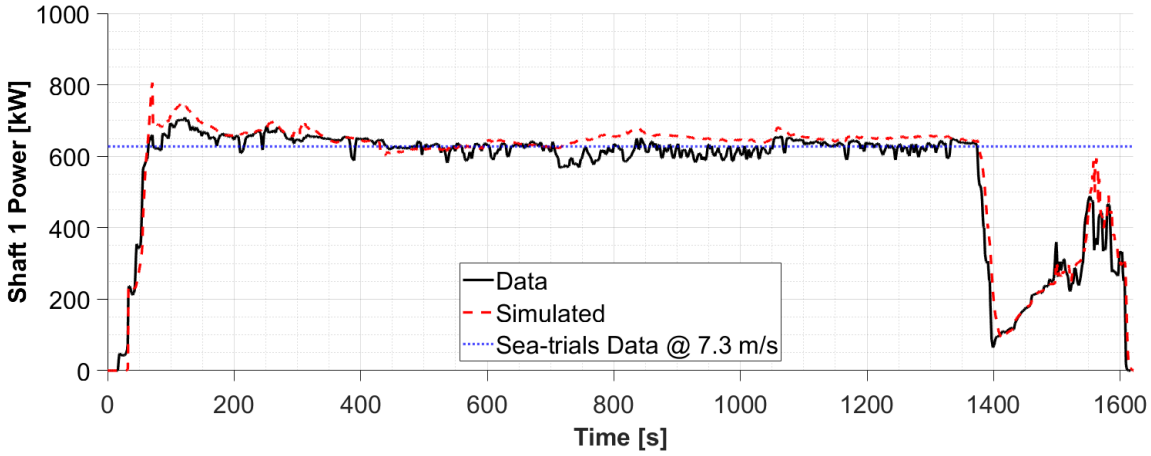

Figure 6.23: Shaft 1 Power – Forced GPS Speed & Heading, Corrected

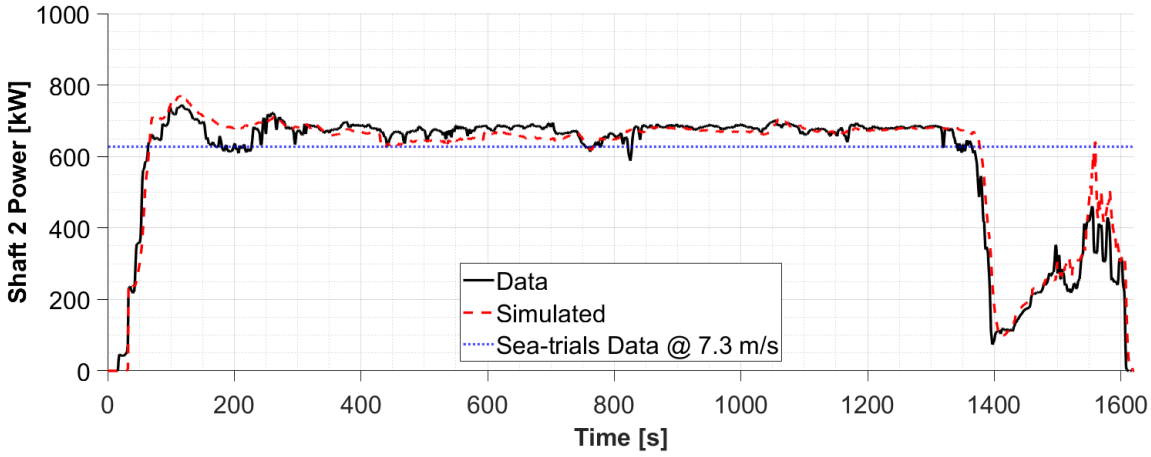

Figure 6.24: Shaft 2 Power – Forced GPS Speed & Heading, Corrected

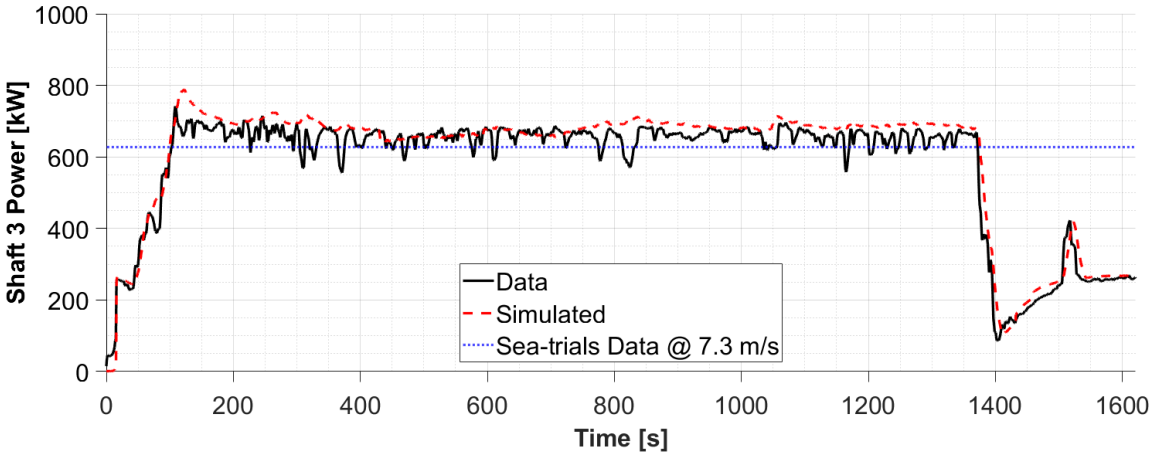

Figure 6.25: Shaft 3 Power – Forced GPS Speed & Heading, Corrected

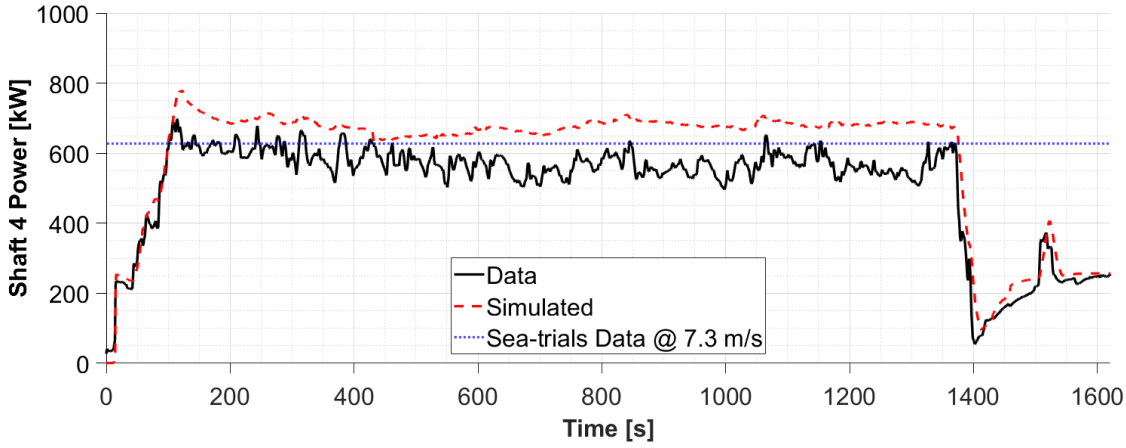

Figure 6.26: Shaft 4 Power – Forced GPS Speed & Heading, Corrected

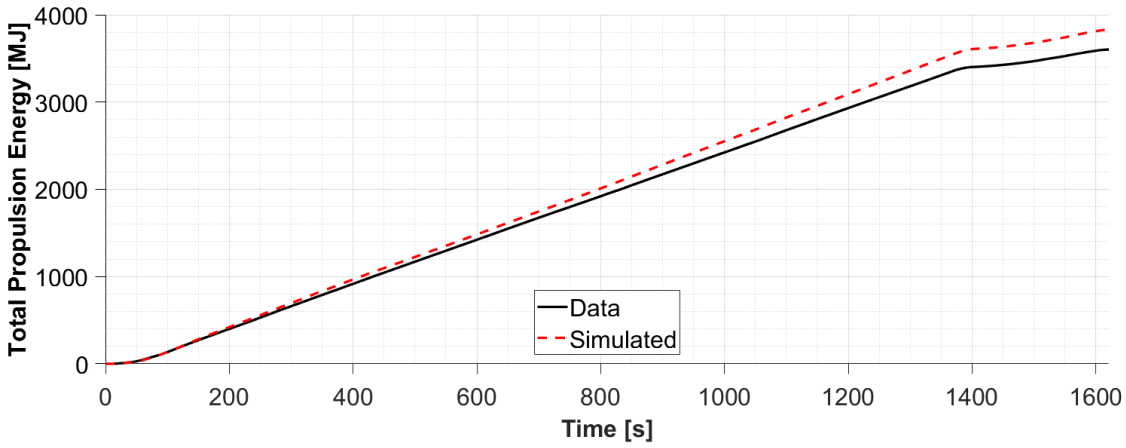

Figure 6.27: Total Propulsion Energy – Forced GPS Speed & Heading, Corrected

As expected, the simulated shaft powers are much closer to the measured powers, with the exception of shaft 4 for which there is evidence of measurement error caused by strain gauge installation issues.

It can also be seen that the cumulative propulsion energy error has significantly improved.

6.4 Simulation Results: Free-Running, Corrected

With propeller geometry correction factors having been introduced into the model and tuned with the isolated propeller subsystem in the "forced GPS speed and heading" case, the simulation was reverted back to the "free-running" configuration as shown in the simulation flow diagram provided in Figure 6.28.

The "free-running" simulation was re-run with the propeller geometry correction factors applied, and the results for vessel path, speed and heading can be seen in Figures 6.29–6.31.

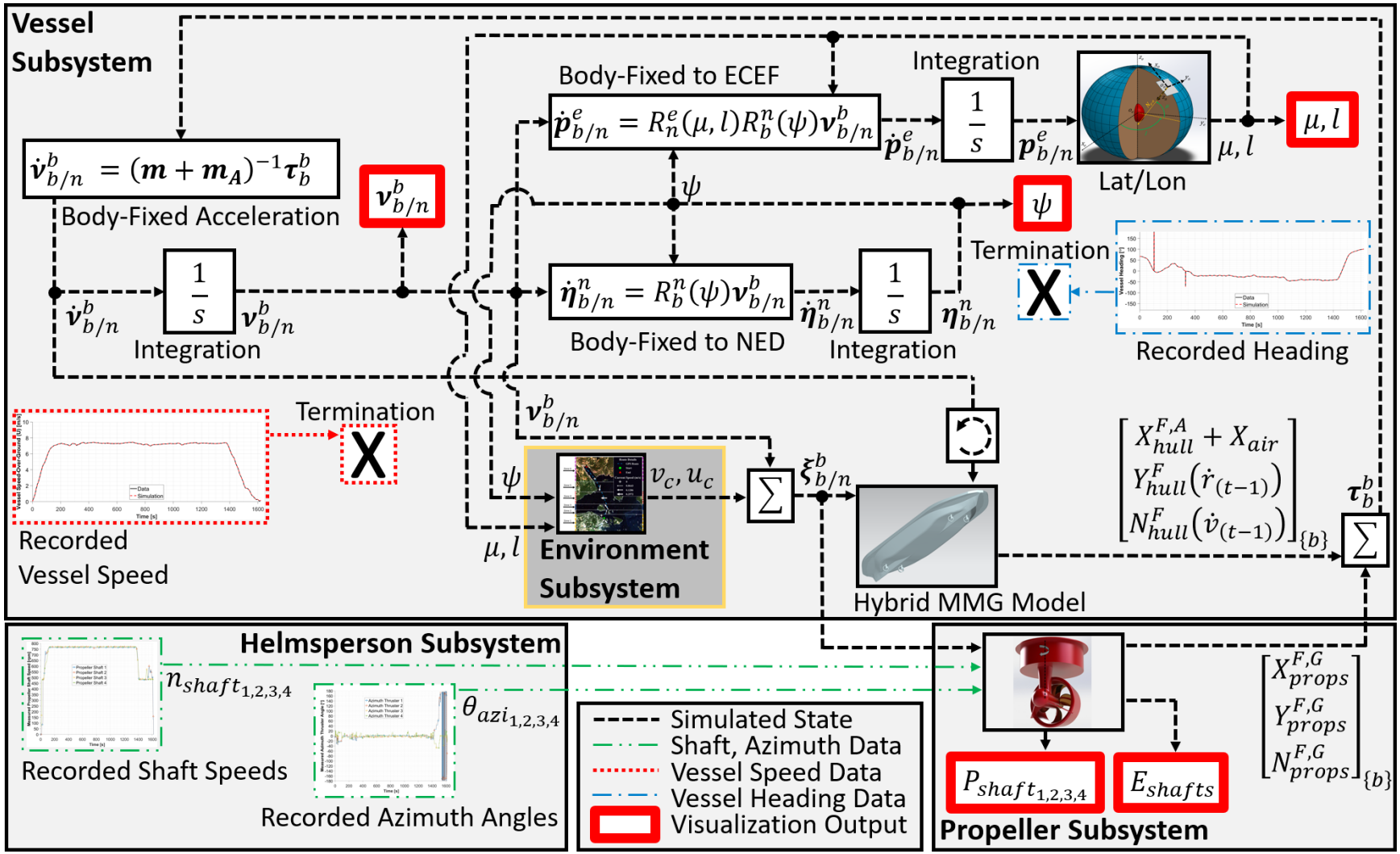

Figure 6.28: Simulation Flow Diagram – Free-Running, Corrected

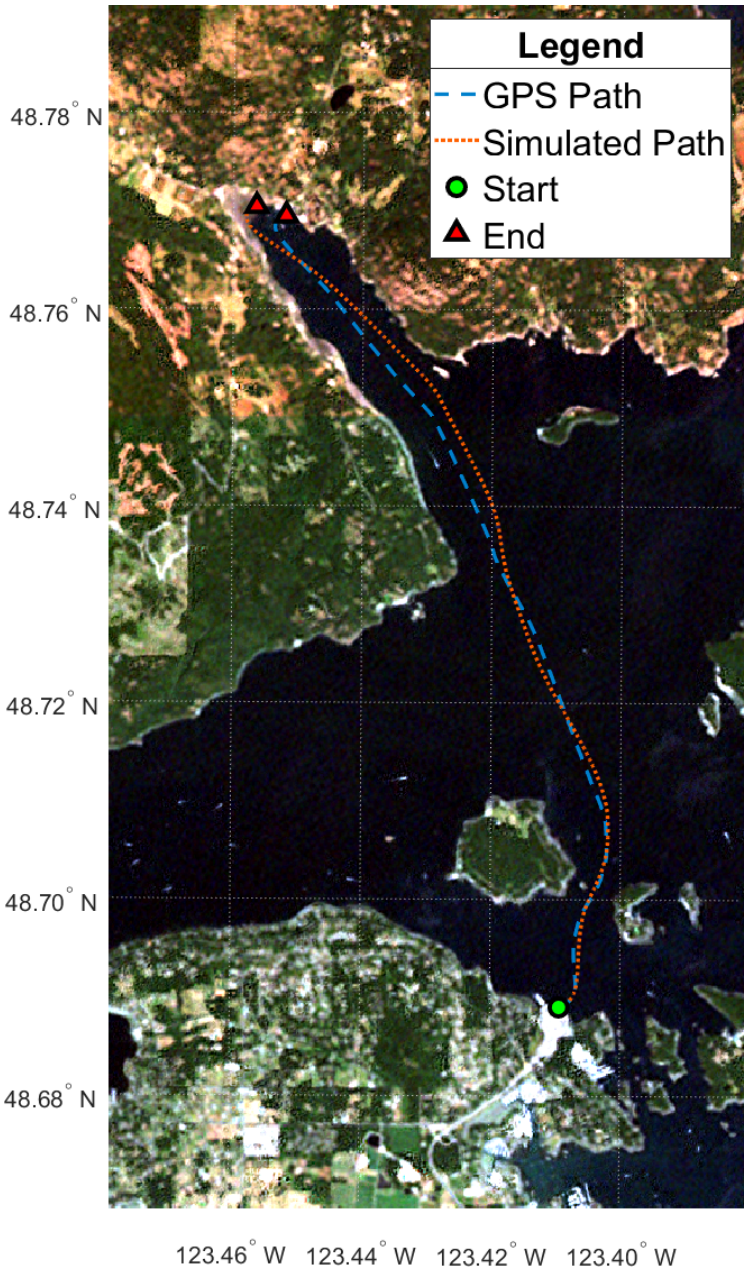

Figure 6.29: Vessel Path – Free-Running, Corrected

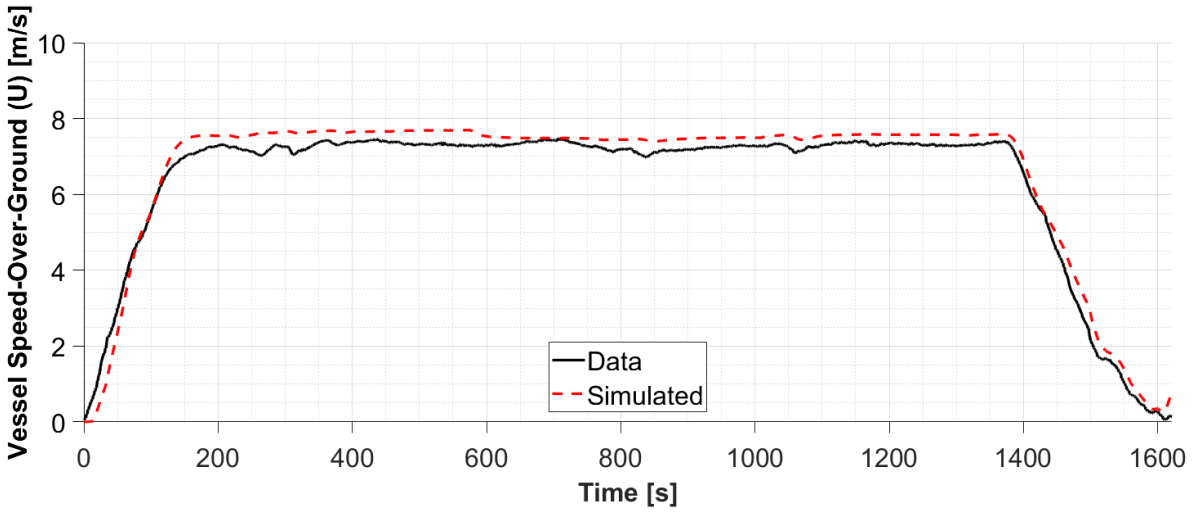

Figure 6.30: Vessel Speed – Free-Running, Corrected

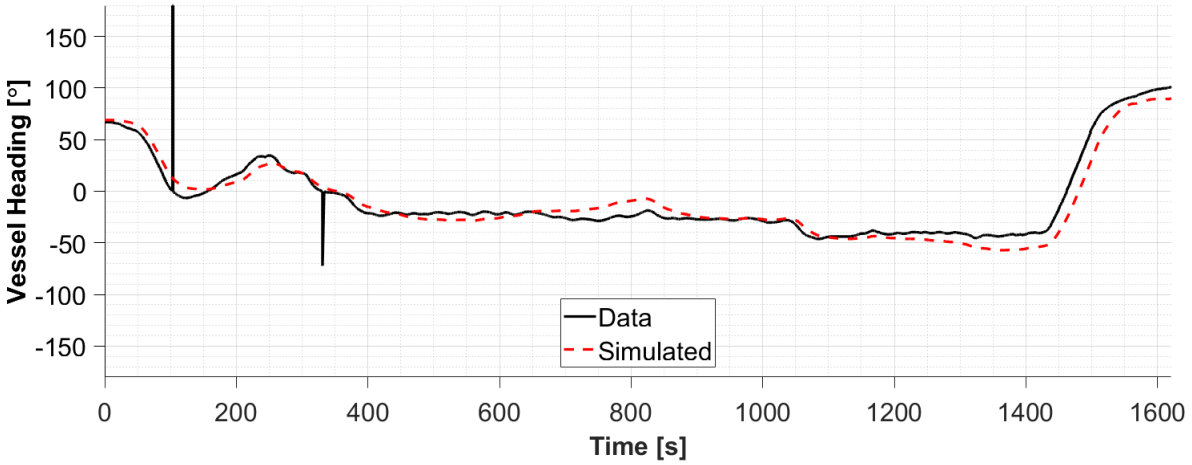

Figure 6.31: Vessel Heading – Free-Running, Corrected

The plots of vessel path, speed and heading show incremental improvement over the initial "free-running" simulation with a small reduction of the speed error resulting from the reduction of propeller thrust. As the vessel's speed is predicted more accurately, it also translates into a more accurately predicted vessel path.

The vessel's simulated shaft powers and energy are shown in Figures 6.32–6.36.

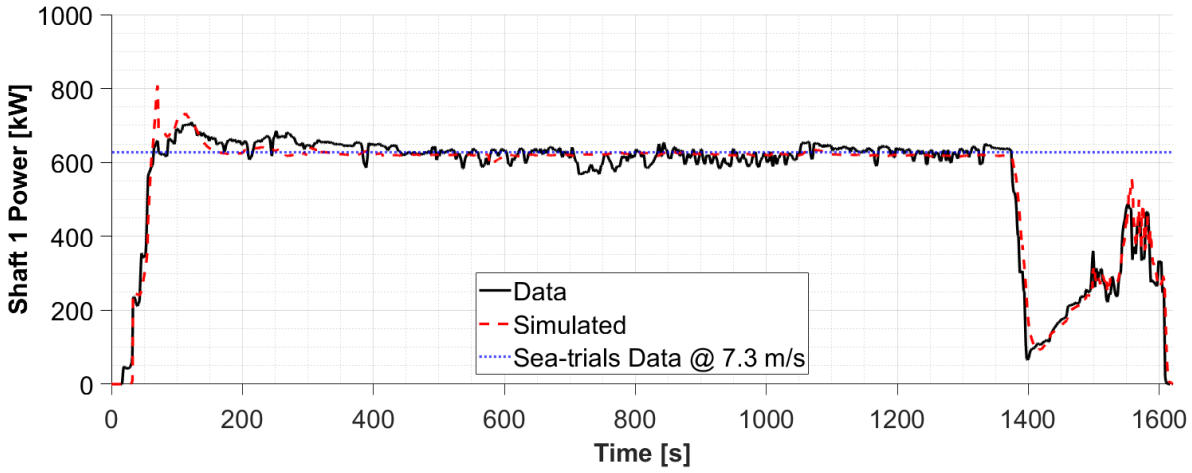

Figure 6.32: Shaft 1 Power – Free-Running, Corrected

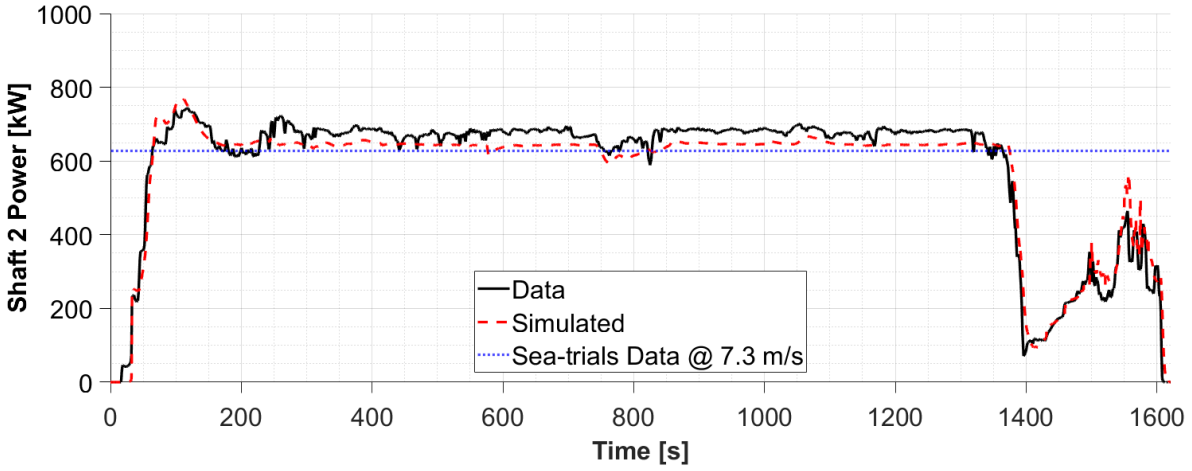

Figure 6.33: Shaft 2 Power – Free-Running, Corrected

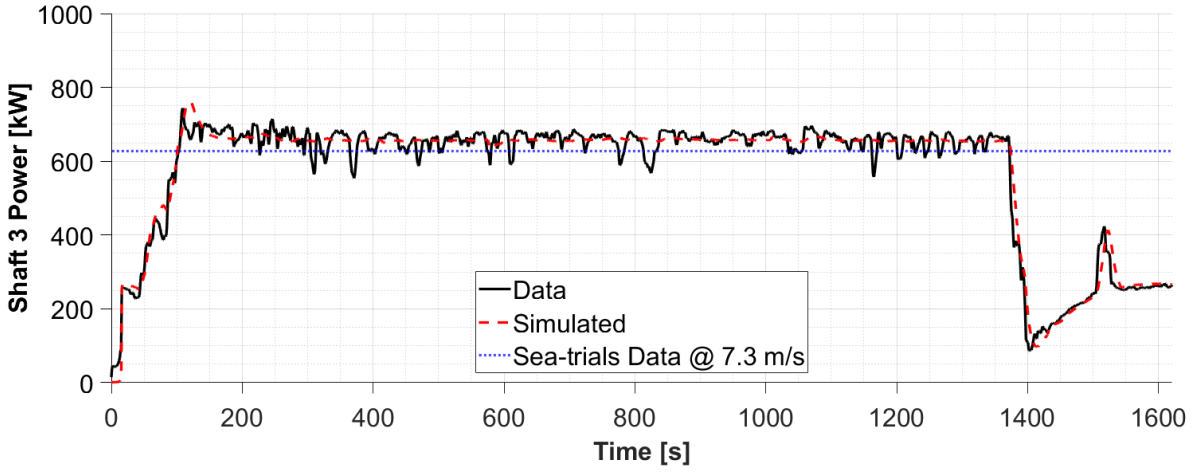

Figure 6.34: Shaft 3 Power – Free-Running, Corrected

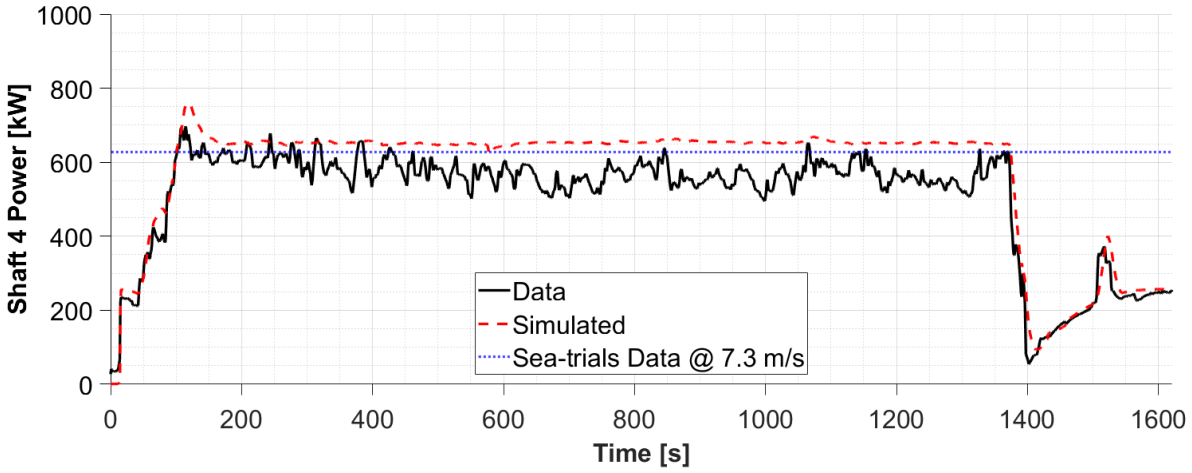

Figure 6.35: Shaft 4 Power – Free-Running, Corrected

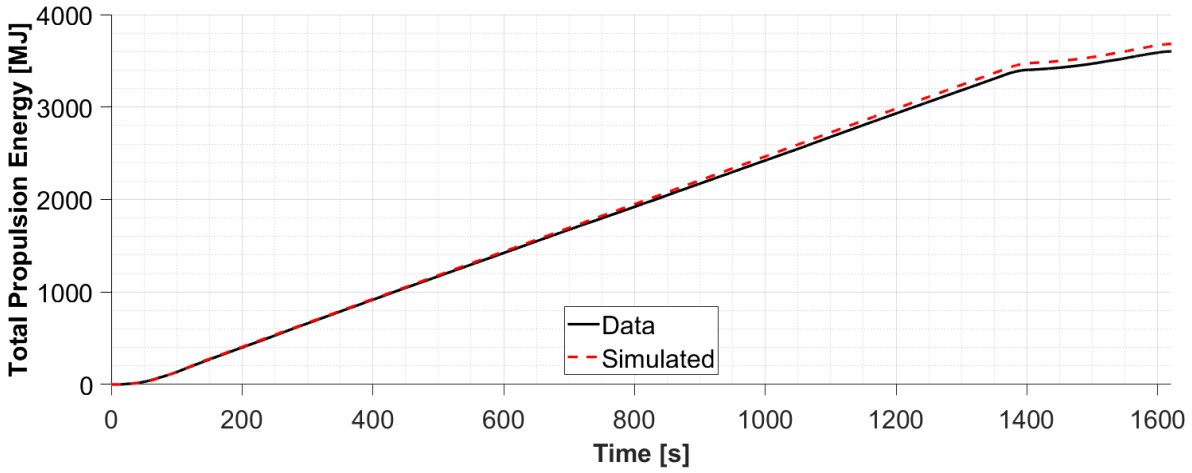

Figure 6.36: Total Propulsion Energy – Free-Running, Corrected

As expected, the plots of vessel shaft power and energy show meaningful improvement over the initial "free-running" simulation.

With the caveat that the results in the corrected "free-running" case have been tuned for accuracy, they serve to showcase the potential of the MBD marine simulation platform when provided with accurate inputs.

6.5 Simulation Results: Free-Running, Alternate Crossing, Corrected

With the model having been tuned for sufficient accuracy in the initial crossing, the simulation was trialled on a second alternate crossing between Swartz Bay and Fulford Harbour.

When preparing the simulation platform for the alternate crossing, the ocean current velocities were re-estimated at the alternate crossing time.

The alternate crossing simulation results for vessel path, speed and heading are provided in Figures 6.37–6.39.

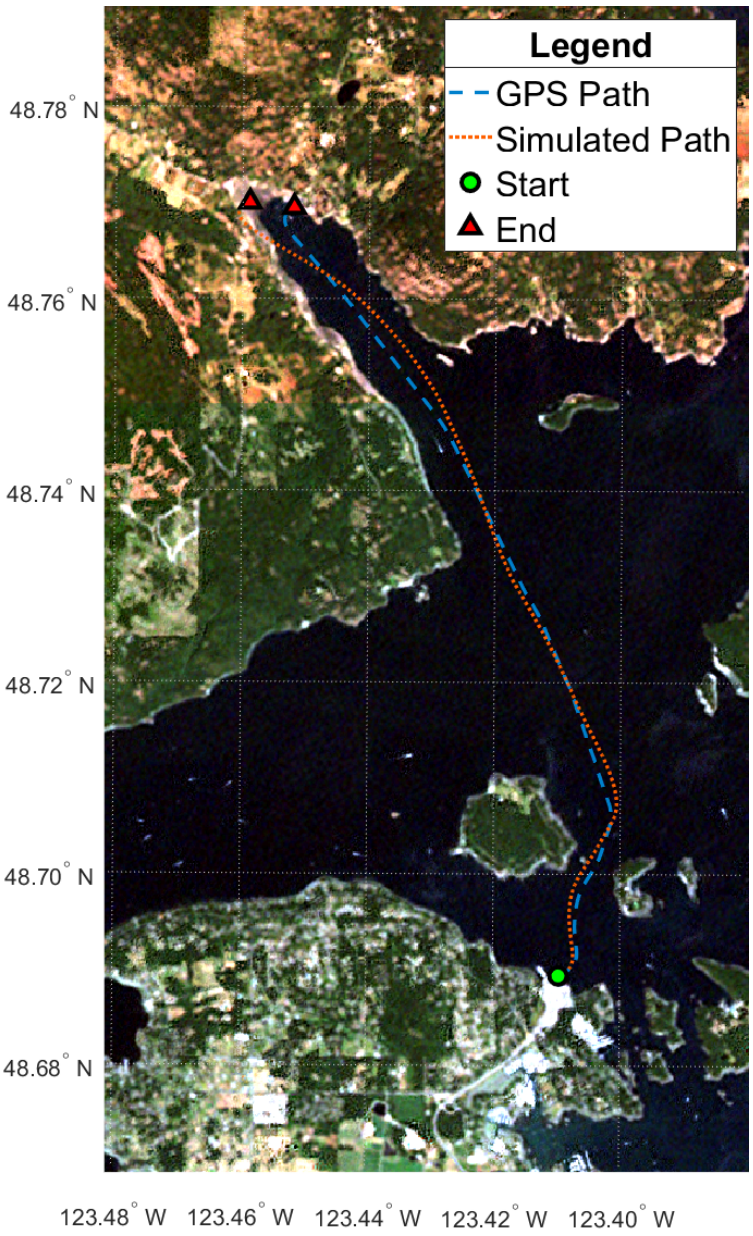

Figure 6.37: Vessel Path – Free-Running, Alternate Crossing, Corrected

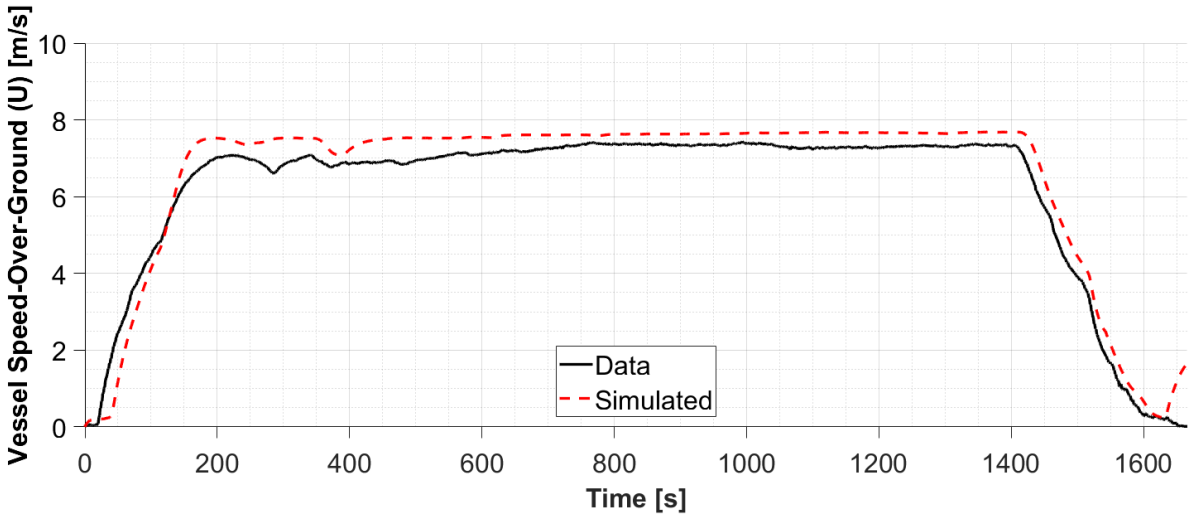

Figure 6.38: Vessel Speed – Free-Running, Alternate Crossing, Corrected

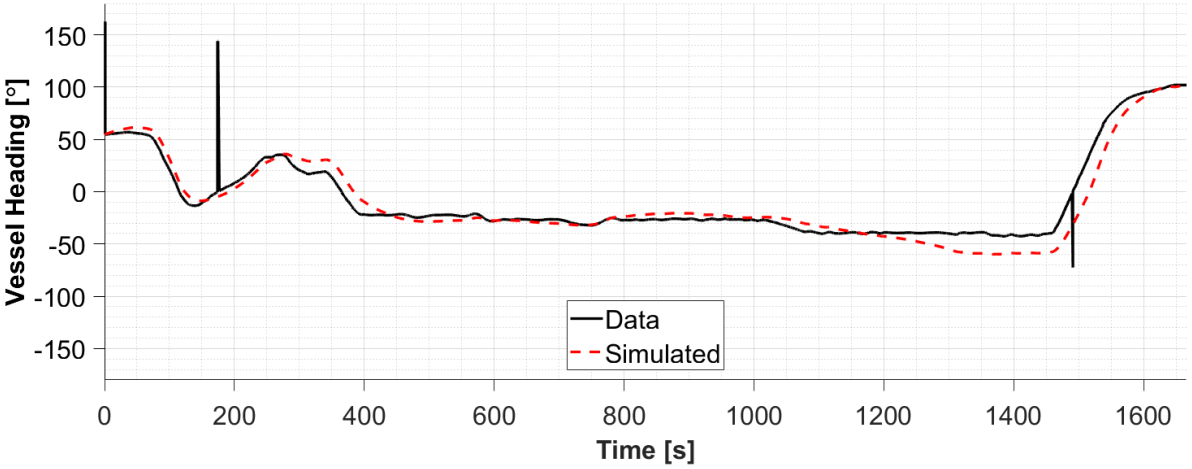

Figure 6.39: Vessel Heading – Free-Running, Alternate Crossing, Corrected

The predicted ship velocity in the alternate crossing tracks the recorded GPS speed well, but suffers somewhat between 200 and 400 seconds as the *Skeena Queen* manoeuvres between the nearby islands. As the currents are expected to be stronger and more chaotic during the alternate crossing, the increased speed error is likely due to the chaotic ocean currents that the vessel can encounter between these islands, currents which can exceed $0.5m/s$. Although the ocean current was approximated using a current atlas, the atlas did not provide a high enough resolution to adequately capture the nature of the current in this area.

Near the very end of the simulation, the predicted ship velocity can be seen to deviate from the measured velocity again. The cause of this deviation stems from the *Skeena Queen*'s number 3 and number 4 thrusters producing thrust to keep the vessel engaged with the berth during loading and unloading. In reality, the berth prevents the *Skeena Queen* from moving

forward, but there is no such restriction accounted for within the simulation and the vessel begins to accelerate again.

The vessel's simulated shaft powers and energy for the alternate crossing are shown in Figures 6.40–6.44.

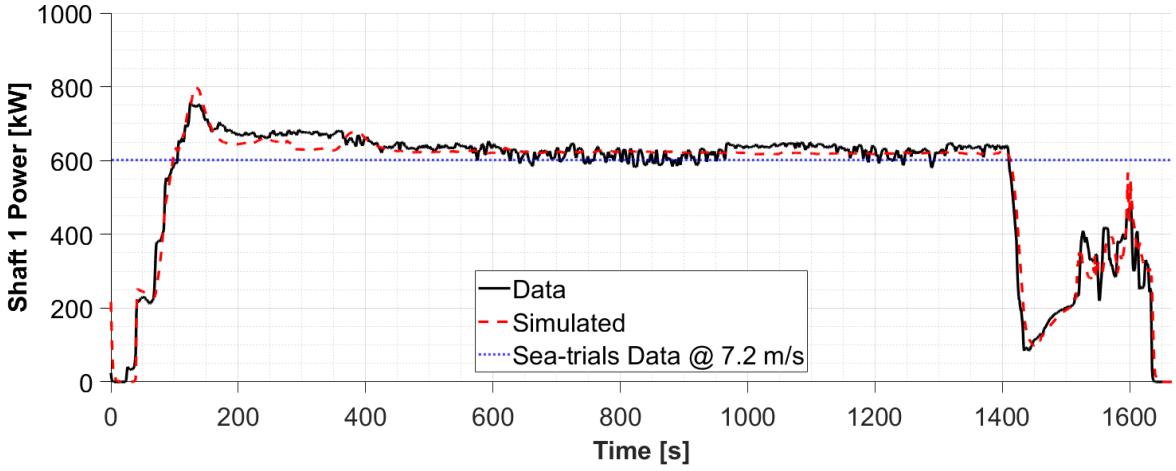

Figure 6.40: Shaft 1 Power – Free-Running, Alternate Crossing, Corrected

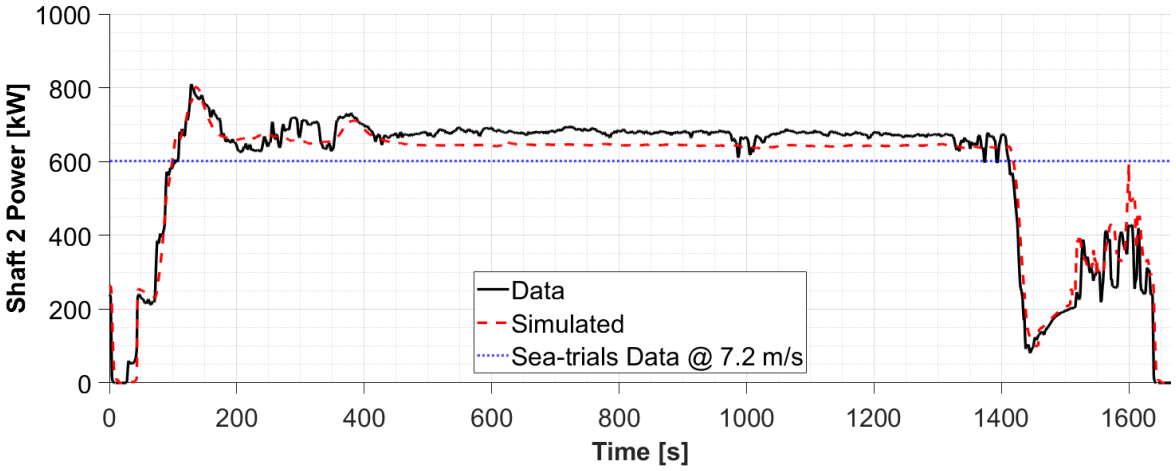

Figure 6.41: Shaft 2 Power – Free-Running, Alternate Crossing, Corrected

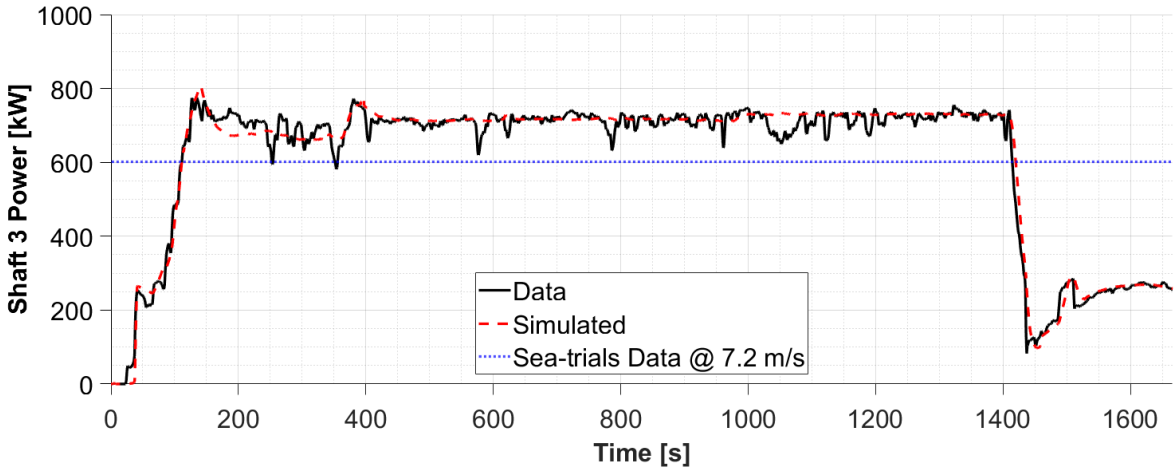

Figure 6.42: Shaft 3 Power – Free-Running, Alternate Crossing, Corrected

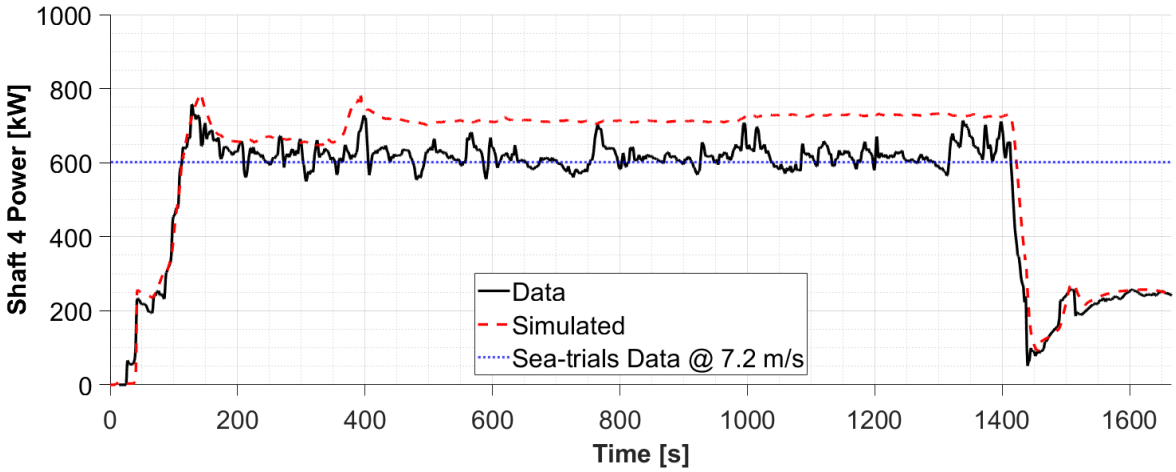

Figure 6.43: Shaft 4 Power – Free-Running, Alternate Crossing, Corrected

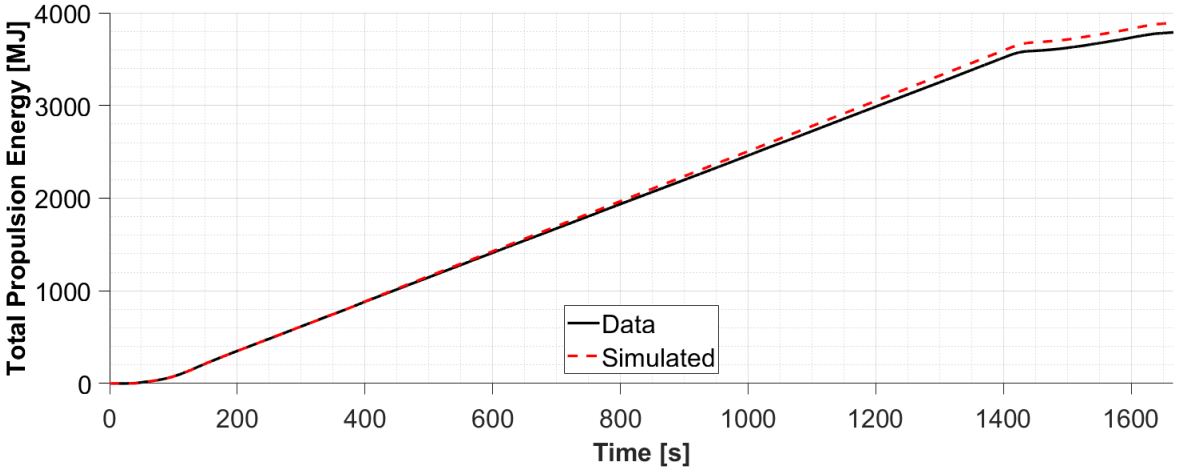

Figure 6.44: Total Propulsion Energy – Free-Running, Alternate Crossing, Corrected

Again, the plots of vessel shaft power and energy for the corrected, alternate "free-running" simulation show good agreement with measured results.

6.6 Simulation Results: Free-Running, Corrected, 1 DOF Motion

With similar works such as Andersen [8] having explored 1 DOF model formulations where vessel motion is restricted to the surge direction, the simulation platform herein was temporarily restricted to 1 DOF to assess the benefit of adding additional degrees of freedom.

In this simulation case, the vessel motions were restricted to surge by intercepting the forces computed in the sway and yaw directions and setting them to zero as follows:

$$\begin{bmatrix} \dot{u} \\ 0 \\ 0 \end{bmatrix}_{\{b\}} = (\boldsymbol{m} + \boldsymbol{m_A})^{-1} \begin{bmatrix} X^{F,A}_{hull} + X_{air} + X^{F,G}_{props} \\ \cancelto{0}{Y^{F}_{hull}} + \cancelto{0}{Y^{F,G}_{props}} \\ \cancelto{0}{N^{F}_{hull}} + \cancelto{0}{N^{F,G}_{props}} \end{bmatrix}_{\{b\}} \tag{6.5}$$

Although vessel motion is restricted to 1 DOF, the propeller forces are still calculated with respect to the azimuth angle, θ_{azi}, and values are yielded for both $T^{F,G}_{prop_x}$, and $T^{F,G}_{prop_y}$. After the propeller forces have been rotated into the body-fixed frame, the $X^{F,G}_{prop}$ component is extracted while the $Y^{F,G}_{prop}$ and $N^{F,G}_{prop}$ components are dropped.

Before running the corrected, "free-running", 1 DOF simulation, the initial vessel heading was changed to point in the general direction of Fulford Harbour.

The 1 DOF simulation results are plotted in Figures 6.45–6.52.

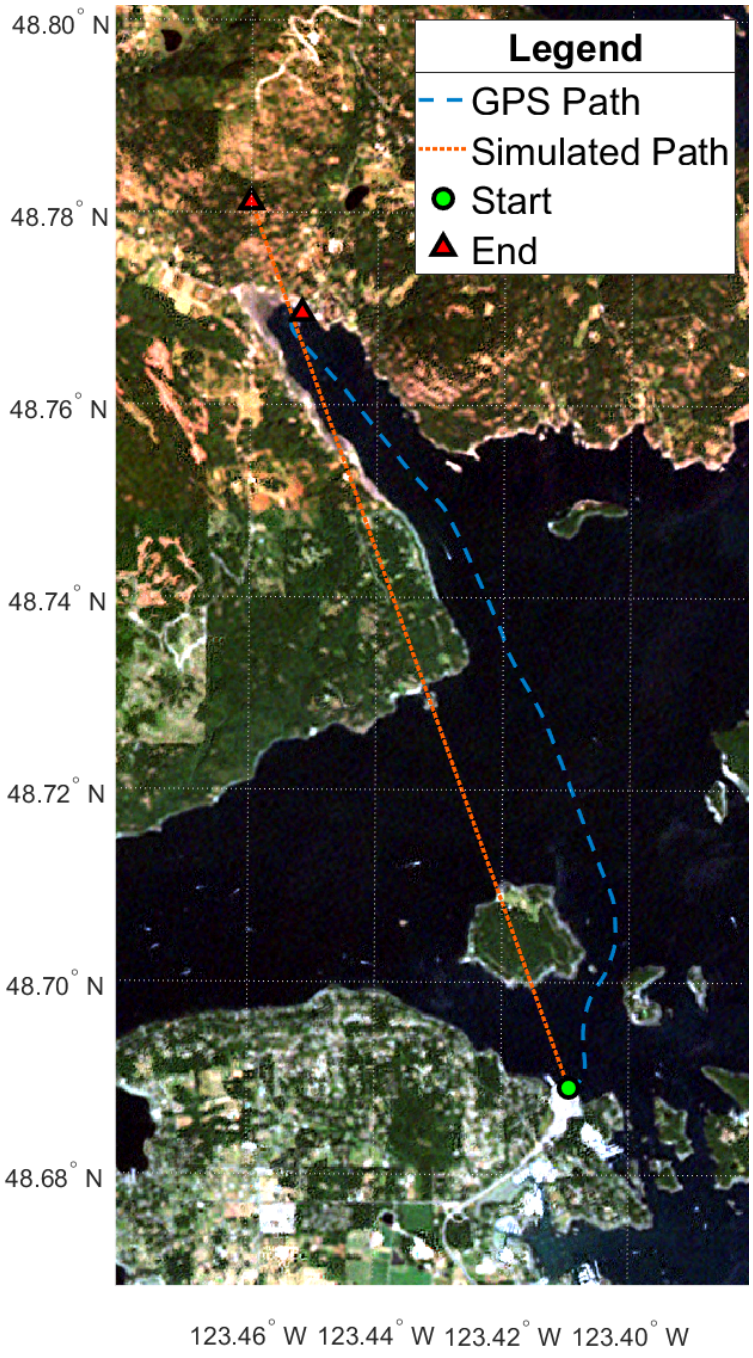

Figure 6.45: Vessel Path – Free-Running, Corrected, 1 DOF Motion

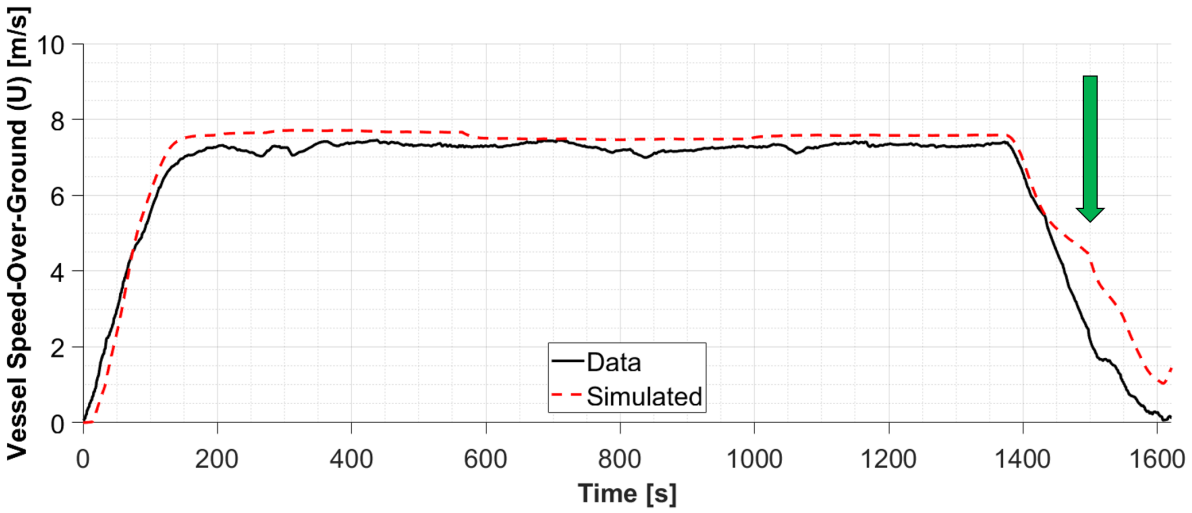

Figure 6.46: Vessel Speed – Free-Running, Corrected, 1 DOF Motion

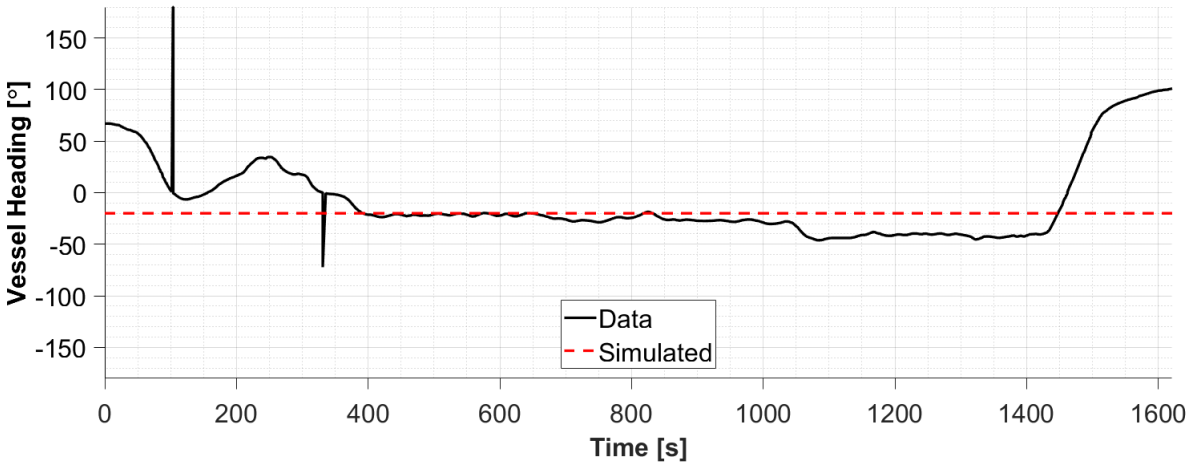

Figure 6.47: Vessel Heading – Free-Running, Corrected, 1 DOF Motion

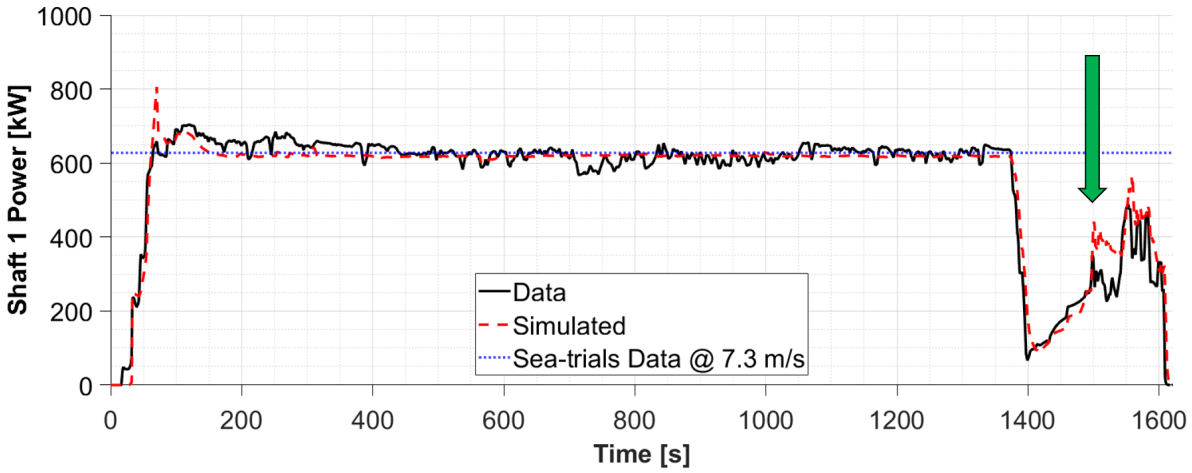

Figure 6.48: Shaft 1 Power – Free-Running, Corrected, 1 DOF Motion

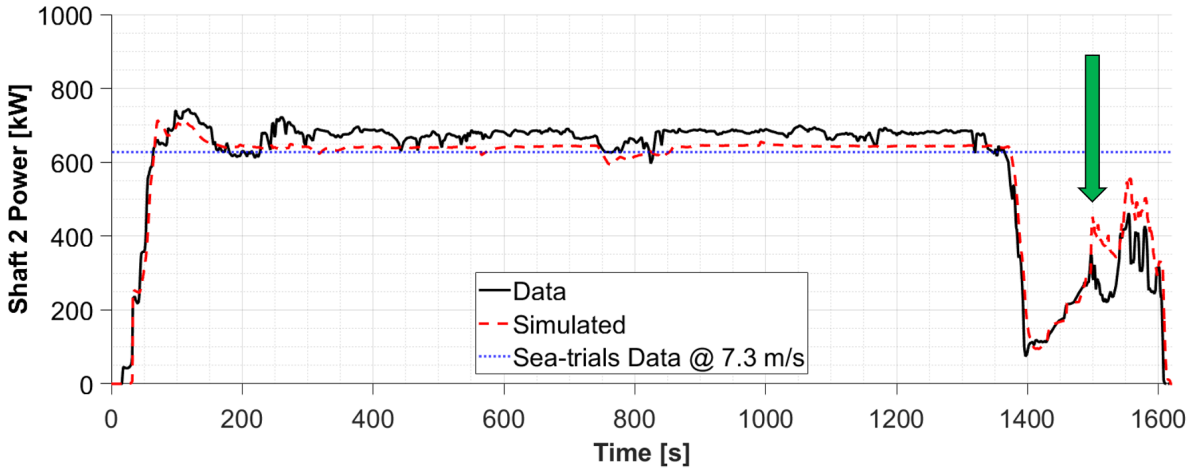

Figure 6.49: Shaft 2 Power – Free-Running, Corrected, 1 DOF Motion

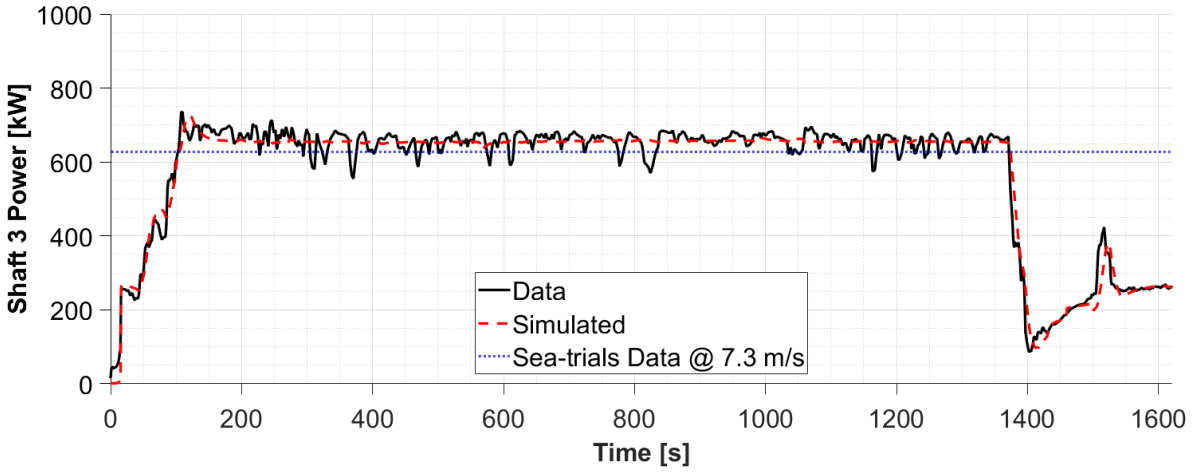

Figure 6.50: Shaft 3 Power – Free-Running, Corrected, 1 DOF Motion

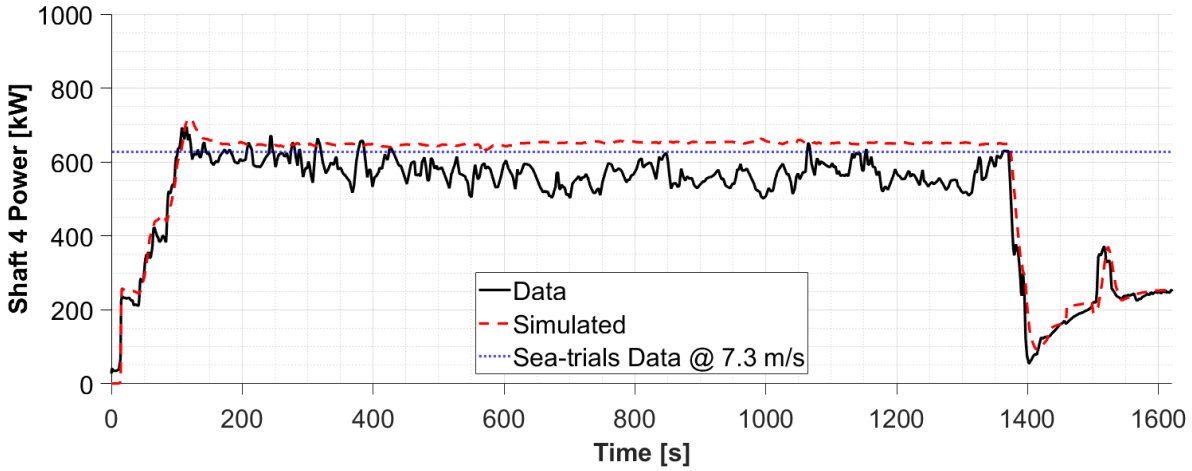

Figure 6.51: Shaft 4 Power – Free-Running, Corrected, 1 DOF Motion

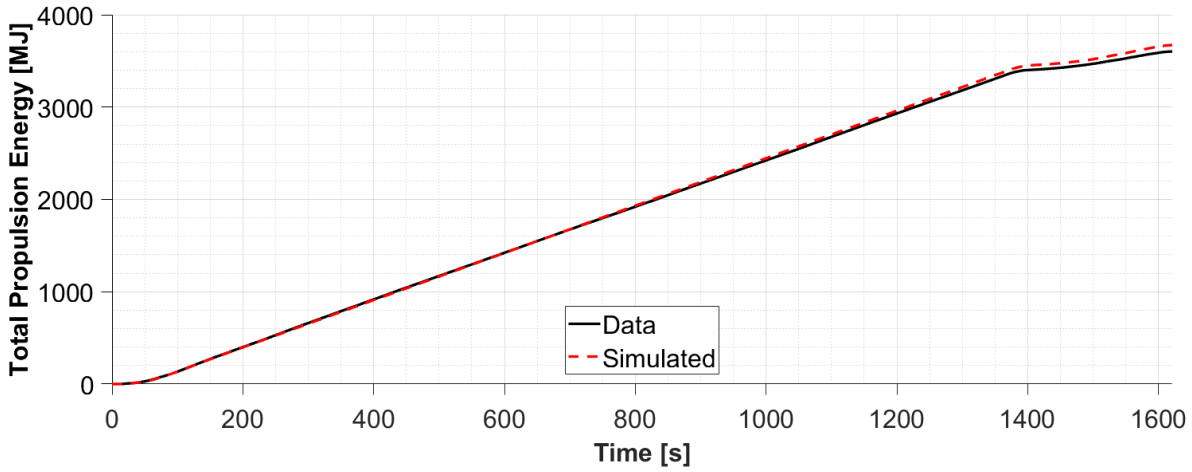

Figure 6.52: Total Propulsion Energy – Free-Running, Corrected, 1 DOF Motion

Overall, the 1 DOF simulation performed nearly as well as the 3 DOF simulation, especially during the cruising period between 200 and 1300 seconds. This can be explained when considering that the dominant source of the *Skeena Queen*'s hull resistance is coming from the resistance in surge due to motion in pure surge, $X_0^{F,A}$. It can be seen however, that the simulation with 1 DOF starts to under-perform during a dynamic manoeuvring sequence as the *Skeena Queen* approaches Fulford Harbour.

During the approach to Fulford Harbour, the plots show that the vessel's speed is significantly over-predicted in the 1 DOF simulation, as are the shaft powers on shafts 1 and 2 starting at 1500 seconds.

As the vessel manoeuvres, it begins to drift sideways through the water, which can be visualized analogously as a rally car drifting sideways through a muddy corner. When a

vessel drifts at an angle through the water, its hull resistance increases due to the changing angle of attack. This increase in resistance is captured in the 3 DOF simulation by the hybrid MMG model which estimates the drift forces as a function of drift angle (β) and yaw rate (r). The 1 DOF simulation fails to capture these additional drift forces as the vessel does not experience any motion in the sway and yaw directions. The difference can be seen when comparing the plotted surge force components with yaw rate, and in particular, $X^{F,A}_{MMG}$, in Figures 6.53–6.54.

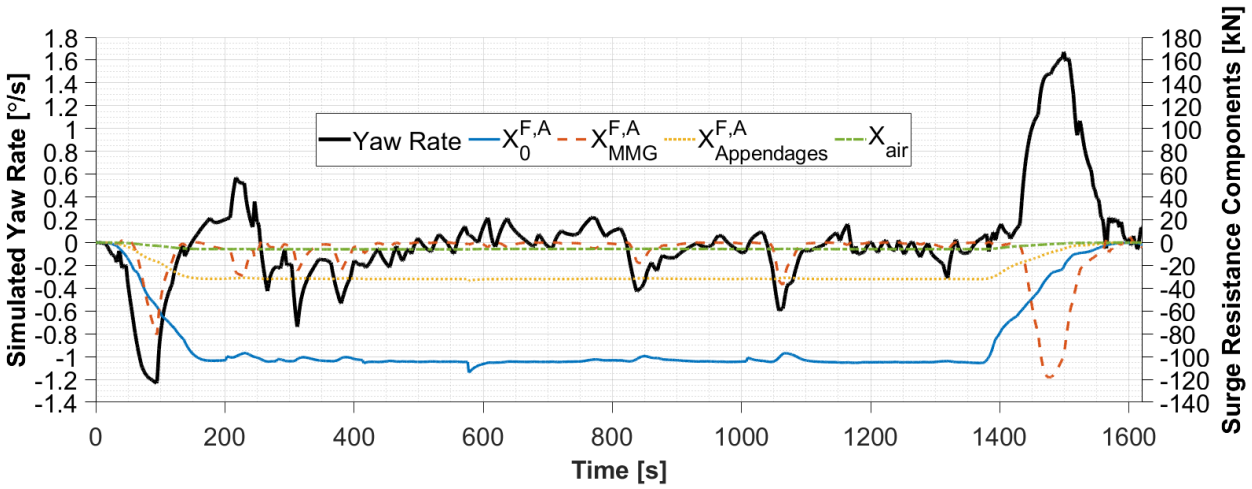

Figure 6.53: Surge Resistance Components – Free-Running, Corrected, 3 DOF Motion

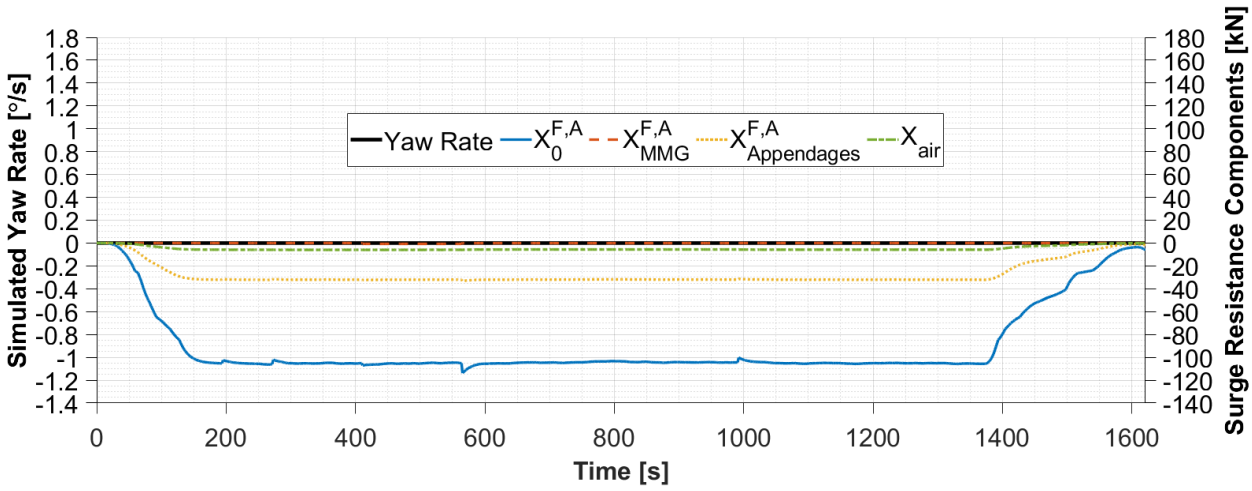

Figure 6.54: Surge Resistance Components – Free-Running, Corrected, 1 DOF Motion

6.7 Simulation Results: Summary and Discussion

A summary of simulation error is provided in Table 6.1 to allow for assessment and comparison of the simulation variants that were presented. The errors for speed and shaft power are provided both with respect to the total simulation, and again for just the cruising period between 200 and 1300 seconds. The energy error is provided at the final time-step of simulation.

Table 6.1: MBD Marine Simulation Platform Assessment

Simulation	Speed: Mean Error *Total/Cruise	Shaft 1 Power: Mean Error *Total/Cruise	Shaft 2 Power: Mean Error *Total/Cruise	Shaft 3 Power: Mean Error *Total/Cruise	Shaft 4 Power: Mean Error *Total/Cruise	Energy: Final Error
Free-Running, Initial	6.9%/5.2%	11.4%/10.0%	10.0%/5.9%	12.3%/11.4%	25.4%/26.6%	13.6%
Forced GPS Speed & Heading, Initial	0.0%/0.0%	18.3%/17.1%	17.1%/13.0%	19.3%/18.5%	32.4%/33.8%	20.8%
Forced GPS Speed & Heading, Corrected	0.0%/0.0%	4.2%/3.2%	2.8%/ − 0.8%	5.2%/4.4%	17.0%/18.0%	6.3%
Free-Running, Corrected	6.0%/3.8%	0.4%/ − 0.8%	−1.3%/ − 4.6%	0.9%/0.3%	12.8%/13.9%	2.2%
Free-Running, Alternate Crossing, Corrected	8.9%/5.4%	0.4%/ − 1.1%	1.1%/ − 3.8%	2.0%/1.1%	14.0%/14.6%	2.7%
Free-Running, Corrected, 1 DOF Motion	28.7%/4.1%	3.1%/ − 1.2%	2.3%/ − 5.2%	−0.2%/0.0%	11.6%/13.7%	1.9%

*Total error calculations neglect the initial and final few seconds of simulation time to avoid division by zero when one or more shaft speeds are zero

Prior to discussing the suitability of the proposed modelling approach, it needs to be re-stated that the mean power error associated with shaft 4 is consistently larger than for the other shafts. This discrepancy is suspected to stem from strain gauge installation issues on shaft 4, an assertion that is supported by independent sea-trial power measurements. It is suggested therefore, that any assessment of the suitability of the MBD marine simulation platform should look through the errors associated with shaft 4 and focus on the remaining error metrics.

Overall, the initial, uncorrected, "free-running" simulation results provide satisfactory accuracy and would be considered sufficient for making preliminary engineering decisions regarding propulsion system architecture and component sizing during the design phase. At first glance, double-digit errors may seem discouraging, but they are well within the 20%–40% margin of error that is often encountered during marine vessel simulation for commercial purposes [10].

The excellent accuracy of the corrected "free-running", and alternate-corrected "free-running" cases serve to showcase the potential of the MBD marine simulation platform to produce precise results that would be suitable for both hybrid propulsion component sizing and advanced energy management controller design.

With Simulink's default relative error tolerance of $1e^{-6}$, the simulation was run in "normal", "accelerator", and "parallel" simulation modes to assess total simulation time. The "parallel" mode consisted of 144 iterations of the same simulation being run simultaneously across 6 nodes. The purpose of running "parallel" mode was to obtain an idea of run-time for scenarios where an engineer may want to assess a vessel's performance across several drive-cycle variants, each with a unique vessel path and speed and/or with changing wind, wave and ocean current conditions. "Parallel" mode also enables the use of parallel optimization algorithms which may be compatible with certain MBD optimization processes.

The average total simulation run-times and time ratios for the roughly 27-minute crossing are given in Table 6.2.

Table 6.2: Average Simulation Time (Compilation + Execution)

Simulation Mode	**Average Simulation Run-time**	**Approximate Time Ratio**
Normal	$5.6s$	289 : 1
Accelerator	$2.4s$	675 : 1
Parallel	$0.9s$	1800 : 1

Overall, the simulation run times in all modes were excellent and the time-ratios compare well against the 12:1 time-ratio achieved in a similar work [10]. While the current implementation is quick, it remains to be seen how simulation run-times would be affected by the addition of an autopilot module that needs to solve for the magnitude and direction of thrust at each time-step.

Assessment of Proposed Method

When comparing the proposed method with existing semi-empirical and self-propelled CFD approaches, it can be seen that the new approach provides a significant speed advantage and strikes a balance between accuracy, complexity and cost as summarized in Table 6.3.

Table 6.3: Comparison of Proposed New Method vs. Existing Methods

Simulation Approach	**Estimated Simulation Time**	**Approximate Error**	**Computation Nodes**	**Relative Complexity**	**Relative Cost**
Proposed New Method	$0.9s - 5.6s$	$5\% - 15\%$	$1 - 6$	Med.	$$
Existing Semi-Empirical	$135s$ [10]	$20\% - 40\%$	1	Low	$
Self-Propelled CFD	$3.1e^5s - 6.4e^5s$ [48]	$3\% - 5\%$	$32 - 56$	High	$$$

When considering that a focus of this work was to enable advanced MBD processes that require a significant number of iterations, it is evident that self-propelled CFD methods are not practical or feasible due to the extensive simulation time required for a single iteration.

While the proposed new method and existing semi-empirical simulations enable MBD processes, the new method shows superior accuracy at the expense of increased complexity and cost. The increased complexity of the proposed new method stems from the need to pre-compute the propeller and hull look-up surfaces with CFD and requires about 1-2 weeks of total computation time on a common 6 node workstation. The increased cost associated with the new method is due to the multiple software licenses used in this work, although with some refinement this cost can be reduced through the consolidation of software packages and use of open-source software platforms as outlined in Section 7.3.

Chapter 7

Conclusion

7.1 Summary

This work described the motivation for applying vessel operational profiles to tune the design of hybrid electric marine propulsion systems and energy management strategies for individual vessels and their unique drive-cycles to result in reduced fuel consumption and emissions. New hybrid mathematical hull and propeller models were developed to predict ship motions and propulsion power demand with sufficient accuracy while remaining computationally efficient. A modular MBD marine simulation framework was proposed and applied to develop a vessel operational profile through virtual vessel simulation. Data was acquired from a benchmark vessel to validate the proposed simulation framework and the accuracy of its embedded models. Core subsystems of the modular simulation platform were constructed which produced initial simulation results that exceeded industry standards for accuracy while demonstrating fast execution times that are compatible with optimization processes. A root cause investigation isolated the propeller subsystem and revealed areas for refinement. The improved accuracy of subsequent revised simulation results served to showcase the potential of the proposed methodology.

7.2 Research Contributions

The key research contributions of the presented work are outlined in this section. In summary, this work:

- Introduced the method and procedure of data acquisition and computer modelling to establish vessel operational profiles that support the development of hybrid electric

marine propulsion systems and energy management strategies for reduced fuel consumption and emissions

- Proposed methods to generate hybrid mathematical hull and propeller models for predicting ship motions and propulsion power demand with sufficient accuracy while remaining computationally efficient to ensure compatibility with system design optimization
- Developed a modular MBD marine simulation framework for producing vessel operational profiles, which can be reconfigured with additional subsystems during later phases of vessel propulsion system design
- Built and tested the core subsystems of the modular simulation platform with initial simulation results exceeding industry norms for accuracy while demonstrating fast execution times
- Expanded the vessel and propeller subsystems from the 1 DOF approach used in similar works to a 3 DOF approach that provided improved accuracy during manoeuvring sequences [8, 9]
- Reduced execution time by up to $14,900\%$ when compared with similar works [10] and made it possible to integrate the marine vessel model with a hybrid electric marine propulsion system model to solve challenging MBD problems in MATLAB/Simulink
- Provided sufficient details such that this thesis can be used as a roadmap for reproducing an adapted simulation framework for future research

7.3 Possible Future Work

Autopilot Module

In terms of importance of further development, first and foremost is the addition of an autopilot module within the helmsperson subsystem. The current implementation which uses recorded control inputs from an existing ship is therefore limited to existing ship applications such as assessing the suitability of a hybrid propulsion system refit. By replacing the recorded helmsperson control inputs with a virtual autopilot that controls the magnitude and direction of thrust, vessel operational profiles can be generated for new virtual ships that are still in the design phase.

To this end, Fossen and Perez [43] present a general approach to the thrust allocation control problem for ships with multiple azimuthing thrusters such as the M.V. *Skeena Queen*.

Wave and Wind Modules

As previously mentioned, both wave and wind modules are absent from within the environment subsystem of the current simulation platform. The addition of wave and wind forces represent an important expansion of the capabilities of the platform such that new vessel types which operate in adverse environmental conditions with higher sea states can be simulated.

Expanded Validation

After incorporating lessons learned from this study, further validation of the proposed approach should be expanded to encompass new vessel types and drive cycles such that a better understanding of the applications and limitations of the proposed methodology can be obtained. Ultimately, once higher confidence is gained in the accuracy of propeller surfacing and CFD techniques, this framework can be incorporated into new vessel design processes.

Software Consolidation and Substitution

The presented approach made use of a number of commercial software licenses which added expense to the implementation. To reduce licensing costs, some programs can be eliminated or substituted with open source alternatives. Tentative suggestions to reduce the number of software licenses from six to two are as follows:

1) Rhinoceros 5→ no alternative identified:
    - Generates a meshed hull surface model for WAMIT
2) SolidWorks and Siemens NX → Rhinoceros 5 (consolidation):
    - Generates hull and propeller surface models for CFD
3) WAMIT → empirical added mass estimates [49–51]:
    - Provides vessel added masses and moments of inertia
    - WAMIT can also estimate wave response-amplitude operators (RAO) with MultiSurf
4) StarCCM+ → OpenFOAM (open source):
    - Generates the hull resistance look-up table
    - Generates the propeller torque and thrust look up tables

5) MATLAB/Simulink → Python (open source):

- Provides a development environment for simulation

References

[1] International Maritime Organization, "Third IMO GHG study 2014: executive summary and final report," tech. rep., London, UK, 2015. [Online]. Available: https://wwwcdn.imo.org/localresources/en/OurWork/Environment/Documents/Third%20Greenhouse%20Gas%20Study/GHG3%20Executive%20Summary%20and%20Report.pdf.

[2] International Maritime Organization, "Fourth IMO greenhouse gas study 2020: full report," tech. rep., London, UK, 2021. [Online]. Available: https://wwwcdn.imo.org/localresources/en/OurWork/Environment/Documents/Fourth%20IMO%20GHG%20Study%202020%20-%20Full%20report%20and%20annexes.pdf.

[3] O. Karabasoglu and J. Michalek, "Influence of driving patterns on life cycle cost and emissions of hybrid and plug-in electric vehicle powertrains," *Energy Policy*, vol. 60, pp. 445–461, 2013. [Online]. doi: https://doi.org/10.1016/j.enpol.2013.03.047.

[4] B. Manouchehrinia, "Modeling, optimization and environmental assessment of electrified marine vessels," Ph.D. dissertation, Dept. Mech. Eng., UVic, Victoria, B.C., 2018. [Online]. Available: https://dspace.library.uvic.ca/bitstream/handle/1828/10454/Manouchehrinia_Babak_PhD_2018.pdf?sequence=1&isAllowed=y.

[5] L. Chen, "Integrated design and control optimization of hybrid electric marine propulsion systems based on battery performance degradation model," Ph.D. dissertation, Dept. Mech. Eng., UVic, Victoria, B.C., 2019. [Online]. Available: https://dspace.library.uvic.ca/bitstream/handle/1828/11149/Chen_Li_PhD_2019.pdf?sequence=1&isAllowed=y.

[6] Y. Feng and Z. Dong, "Optimal control of natural gas compression engine hybrid electric mining trucks for balanced fuel efficiency and overall emission improvement," *Energy*, vol. 189, pp. 1–14, 2019. [Online]. doi: https://doi.org/10.1016/j.energy.2019.116276.

[7] H. Zhu, "Modelling, design and energy management of a hybrid electric ship – a case study," M.A.Sc. thesis, Dept. Mech. Eng., UVic, Victoria, B.C., 2020. [Online]. Available: https://dspace.library.uvic.ca/bitstream/handle/1828/11726/Zhu_Haijia_MASc_2020.pdf?sequence=1&isAllowed=y.

[8] K. Andersen, "Development of a time-domain modeling platform for hybrid marine propulsion systems," M.A.Sc. thesis, Dept. Mech. Eng., UVic, Victoria, B.C., 2016. [Online]. Available: https://dspace.library.uvic.ca//handle/1828/7245.

[9] S. Liu, "Model-based design of hybrid electric marine propulsion system using modified low-order ship hull resistance and propeller thrust models," M.A.Sc. thesis, Dept. Mech. Eng., UVic, Victoria, B.C., 2020. [Online]. Available: https://dspace.library.uvic.ca/bitstream/handle/1828/12518/Liu_Siyang_MASc_2020.pdf?sequence=1&isAllowed=y.

[10] W. A. Truelove, "A general methodology for generating representative load cycles for monohull surface vessels," M.A.Sc. thesis, Dept. Mech. Eng., UVic, Victoria, B.C., 2018. [Online]. Available: https://dspace.library.uvic.ca/bitstream/handle/1828/10434/Truelove_WilliamAnthony_MASc_2018.pdf?sequence=3&isAllowed=y.

[11] T. I. Fossen, *Handbook of Marine Craft Hydrodynamics and Motion Control*. Chichester, West Sussex, UK: John Wiley & Sons, Ltd., 1st ed., 2011.

[12] P. Grant and J. Grant, "Skeena Queen Embarking from Swartz Bay," 2021.

[13] STX Canada Marine Inc., *MV Skeena Queen: Trim and Stability Booklet*. Vancouver, BC, Canada: STX Canada Marine Inc., 2009.

[14] British Columbia Ferry Services Inc., "Our Fleet: Skeena Queen," 2021. [Online]. Available: https://www.bcferries.com/on-the-ferry/our-fleet/skeena-queen/SKEN.

[15] Mitsubishi Diesel Engines, "Mitsubishi Diesel Engine Technical Information: Specification Sheets of S6U-MPTK Engine," 2002. [Online]. Available: http://www.uspowerco.com/generator_attachments/8336-s6u_mptk.pdf.

[16] "Calculation formula of strain torque coefficient." BeeData TQ201H transmitter instruction manual, 2016.

[17] National Resources Canada, "SIDNEY canimage_092b11_tif," 2008. [Online]. Available: https://ftp.maps.canada.ca/pub/nrcan_rncan/vector/index/html/geospatial_product_index_en.html.

[18] National Resources Canada, "MAYNE ISLAND canimage_092b14_tif," 2008. [Online]. Available: https://ftp.maps.canada.ca/pub/nrcan_rncan/vector/index/html/geospatial_product_index_en.html.

[19] Canadian Hydrographic Service, *Current Atlas: Juan de Fuca Strait to Strait of Georgia*. Ottawa: Canadian Hydrographic Service, 2011.

[20] Allied Shipbuilders Ltd., *Hull No. 257 Century Class Ferry: Report on Propulsion Control Trial*. North Vancouver, British Columbia, CA, 1997.

[21] J. S. Carlton, *Marine Propellers and Propulsion*. Kidlington, Oxford, UK: Elsevier Ltd., 3rd ed., 2012.

[22] McLaren & Sons Naval Architects, "Century Class Ferry - MK. II Propeller Design." unpublished.

[23] McLaren & Sons Naval Architects, "Century Class Ferry - MK. II Shafting Arrangement." unpublished.

[24] M. Rahimpour, "Thrust and torque coefficient data for a century class ferry - MK. II propeller." Computational fluid dynamics results, StarCCM+.

[25] M. F. Islam, B. Veitch, A. Akinturk, N. Bose, and P. Liu, "Experiments with podded propulsors in static azimuthing conditions," in *8th Canadian Marine Hydromechanics and Structures Conference*, (St. John's, NL), 2007. [Online]. Available: https://www.researchgate.net/publication/44073512_Experiments_with_podded_propulsors_in_static_azimuthing_conditions.

[26] J. S. Carlton, "Podded propulsors: some results of recent research and full scale experience," *Journal of Marine Engineering & Technology*, vol. 7, no. 1, pp. 1–14, 2008. [Online]. doi: https://doi.org/10.1080/20464177.2008.11020208.

[27] S. Xingrong and C. Yuejin, "Study on hydrodynamic performance of podded propulsor at steering conditions," in *3rd International Symposium on Marine Propulsors smp'13*, (Launceston, Tasmania, Australia), May 2013. [Online]. Available: https://www.marinepropulsors.com/proceedings/2013/8A.3.pdf.

[28] B. Piaggio, M. Viviani, M. Martelli, and M. Figari, "Z-drive escort tub manoeuvrability model and simulation," *Ocean Engineering*, vol. 191, pp. 1–17, 2019. [Online]. doi: https://doi.org/10.1016/j.oceaneng.2019.106461.

[29] K. J. Rawon and E. C. Tupper, *Basic Ship Theory*. Jordan Hill, Oxford, UK: Butterworth Heinemann, 5th ed., 2001.

[30] V. Bertram, *Practical Ship Hydrodynamics*. Jordan Hill, Oxford, UK: Butterworth Heinemann, 1st ed., 2001.

[31] D. Owen, Y. K. Demirel, E. Oguz, T. Tezdogan, and A. Incecik, "Investigating the effect of biofouling on propeller characteristics using cfd," *Ocean Engineering*, vol. 159, pp. 505–516, 2018. [Online]. doi: https://doi.org/10.1016/j.oceaneng.2018.01.087.

[32] Y. Yoshimura and Y. Masumoto, "Hydrodyanmic force database with medium high speed merchant ships including fishing vessels and investigation into a maneuvering prediction method (translated by Y. Yoshimura from original paper in J. of JASNAOE)," *The Japan Society of Naval Architects and Ocean Engineers*, vol. 14, pp. 63–73, 2011. [Online]. doi: https://doi.org/10.2534/jjasnaoe.14.63.

[33] Dept. of Naval Arch. and Ocean Eng., United States Naval Academy, "Resistance and Powering of Ships." class notes for EN400 Principles of Ship Performance, [Online]. https://www.usna.edu/NAOE/_files/documents/Courses/EN400/02.07%20Chapter%207.pdf.

[34] A. F. Molland, S. R. Turnock, and D. A. Hudson, *Ship Resistance and Propulsion: Practiacal Estimation of Ship Propulsive Power*. New York, NY, USA: Cambridge University Press, 1st ed., 2011.

[35] *ITTC – Recommended Procedures and Guidelines: Numerical Simulation of Capsize Behaviour of Damaged Ships in Irregular Beam Seas*, 2017. [Online]. https://www.ittc.info/media/8149/75-02-07-044.pdf.

[36] M. Rahimpour, "Hull surge resistance data for a century class ferry." Computational fluid dynamics results, StarCCM+.

[37] WAMIT, Inc., *WAMIT User Manual Version 7.2*. Chestnut Hill, Maryland, USA: WAMIT, Inc., 2016.

[38] H. Yasukawa and Y. Yoshimura, "Introduction of mmg standard method for ship maneuvering predictions," *Journal of Marine Science and Technology*, vol. 20, pp. 37–52, 2015. [Online]. doi: https://doi.org/10.1007/s00773-014-0293-y.

[39] J. Holtrop and G. Mennen, "An approximate power prediction method," *International Shipbuilding Progress*, vol. 29, no. 335, 1982. [Online]. Available: http://resolver.tudelft.nl/uuid:ee370fed-4b4f-4a70-af77-e14c3e692fd4.

[40] M. Schultz, "Effects of coating roughness and biofouling on ship resistance and powering," *Biofouling*, vol. 23, pp. 331–341, 2007. [Online]. doi: https://doi.org/10.1080/08927010701461974.

[41] M. B. Flikkema, J. Holtrop, and T. J. C. van Terwisga, "A parametric power prediction model for tractor pods." Report No. 1545-P presented at the 2nd International T-POD Conference, 2006. [Online]. https://repository.tudelft.nl/islandora/object/uuid:eb3782fb-5972-489f-97b6-2f02c2e2f61f/datastream/OBJ/download.

[42] B. Hofmann-Wellenhof, H. Lichtenegger, and J. Collins, *Global Positioning System: Theory and Practice*. New York, NY, USA: Springer Verlag., 3rd ed., 1994.

[43] T. Perez and T. I. Fossen, *Motion control of marine craft.* In W. S. Levine, *The Control Systems Handbook: Control System Advanced Methods.* Boca Raton, Florida, USA: CRC Press, 2nd ed., 2011.

[44] Canadian Hydrographic Service, *Canadian Tide and Current Tables*, vol. 5. Ottawa: Canadian Hydrographic Service, 2017.

[45] F. Pacuraru, A. Lungu, C. Ungureanu, and O. Marcu, "Numerical simulation of flow around a steerable propulsion unit," in *25th IAHR Symposium on Hydraulic Machinery and Systems in IOP Conf. Ser.: Earth Environ. Sci.*, (Timisoara, Romania), September 2010. [Online]. Available: https://iopscience.iop.org/article/10.1088/1755-1315/12/1/012032/pdf.

[46] I. Funeno, "Influence of hydrodynamic interation between ducted propellers and struts on performance of azimuth thrusters," in *5th International Symposium on Marine Propulsors smp'17*, (Espoo, Finland), June 2017. [Online]. Available: https://www.marinepropulsors.com/proceedings/2017/THA2-1.pdf.

[47] F. Lemonakis, "Investigation of thrust deduction on azimuth thrusters in bollard pull condition using cfd," M.A.Sc. thesis, Dept. Mech. and Mar. Sci., Chalmers University of Technology, Gothenburg, Sweden, 2019. [Online]. Available: https://odr.chalmers.se/bitstream/20.500.12380/300590/5/Investigation%20of%20Thrust%20Deduction%20on%20Azimuth%20Thrusters%20in%20Bollard%20Pull%20Condition%20using%20CFD.pdf.

[48] V. Vukcevic, H. Jasak, I. Gatin, and T. Uroic, "Ship scale self propulsion cfd simulation results comapred to sea trial measurements," in *VII International Conference on Computational Methods in Marine Engineering*, (Nantes, France), 2017. [Online]. Available:

https://www.semanticscholar.org/paper/Ship-scale-self-propulsion-CFD-simulation-results-Vukcevic-Jasak/192c54ca6cb1c67af6d9ca03371d71f0759fe517.

[49] S. Motora, "On the measurement of added mass and added moment of inertia for ship motions," *Journal of The Society of Naval Architects of Japan*, vol. 105, pp. 83–92, 1959.

[50] S. Motora, "On the measurement of added mass and added moment of inertia for ship motions: part 2. added mass for longitudinal motions," *Journal of The Society of Naval Architects of Japan*, vol. 106, pp. 59–62, 1960.

[51] S. Motora, "On the measurement of added mass and added moment of inertia for ship motions: part 3. added mass for transverse motions," *Journal of The Society of Naval Architects of Japan*, vol. 106, pp. 63–68, 1960.